



Anechoic and Reverberation Chamber Design and Measurements

by

Qian Xu

Submitted in accordance with the requirements for the award of the
degree of Doctor of Philosophy of the University of Liverpool

September 2015

Copyright

Copyright © 2015 Qian Xu. All rights reserved.

The copyright of this thesis rests with the author. Copies (by any means) either in full, or of extracts, may not be made without prior written consent from the author.

To my parents and my wife: Thank you for your support.

Table of Contents

<i>Copyright</i>	<i>i</i>
<i>Table of Contents</i>	<i>iii</i>
<i>Acknowledgements</i>	<i>ix</i>
<i>List of Publications</i>	<i>x</i>
<i>Abstract</i>	<i>xiii</i>
Chapter 1: Introduction	1
1.1 Background	1
1.1.1 Anechoic Chamber Design	1
1.1.2 Reverberation Chamber	2
1.2 Organisation of the Thesis	3
1.3 References	4
Chapter 2: Theory for Anechoic Chamber Design	6
2.1 Introduction	6
2.2 GO Theory	6
2.2.1 GO from Maxwell Equations	6
2.2.2 Reflected Field from Curved Surface	7
2.2.3 Alternative GO Form	10
2.3 Anechoic Chamber Design Methods	12
2.4 Summary	14
2.5 References	14
Chapter 3: Computer Aided Anechoic Chamber Design	17
3.1 Introduction	17
3.2 Framework	17
3.3 Software Implementation	18
3.3.1 3D Model Description	18
3.3.2 Preprocessing	19
3.3.3 Far-field Data	21
3.3.4 Boundary Condition	22
3.3.5 RAM Definition	23
3.3.6 Forward Algorithm	26

3.3.7	Inverse Algorithm	30
3.3.8	Post Processing	33
3.4	Summary	34
3.5	References	34
Chapter 4:	Anechoic Chamber Characterisation and Verification	37
4.1	Introduction	37
4.2	NSA Measurement and Simulation	37
4.3	SVSWR Measurement and Simulation	49
4.4	FU Measurement and Simulation	53
4.5	Summary	57
4.6	References	58
Chapter 5:	New Measurement Methods in a Reverberation Chamber	59
5.1	Introduction	59
5.2	Antenna Radiation Efficiency Measurement in an RC	60
5.2.1	Method Using Reference Antenna	60
5.2.2	Method without Using a Reference Antenna	62
5.2.3	Modified Two-Antenna Method	65
5.2.4	Short Summary of Section 5.2	70
5.3	Diversity Gain Measurement in an RC	71
5.3.1	Traditional Diversity Gain Measurement Method	72
5.3.2	Diversity Gain Measurement without a Reference Antenna	74
5.3.3	Diversity Gain Measurement without Extra Antennas	80
5.3.4	Short Summary of Section 5.3	85
5.4	Radiated Emission Measurement in an RC	86
5.4.1	RE Measurement Method in the IEC Standard	87
5.4.2	RE Measurement Using a VNA and Two Antennas	88
5.4.3	RE Measurement Using a VNA and One Antenna	90
5.4.4	RE Validation Measurement	91
5.4.5	Short Summary of Section 5.4	95
5.5	Permittivity Measurement in an RC	96
5.5.1	Theory	97
5.5.2	Extracting the Permittivity and Conductivity	99
5.5.3	Short Summary of Section 5.5	105
5.6	Shielding Effectiveness Measurement in an RC	105
5.6.1	Theory	106

5.6.2	Measurement.....	109
5.6.3	Short Summary of Section 5.6.....	113
5.7	Volume Measurement.....	117
5.7.1	Calibration Process.....	118
5.7.2	Measurement Process.....	121
5.7.3	Short Summary of Section 5.7.....	125
5.8	Key Contributions.....	128
5.9	References.....	129
Chapter 6: B-Scan in a Reverberation Chamber.....		135
6.1	Introduction.....	135
6.2	B-Scan Measurement and Theory.....	136
6.2.1	Statistical Behaviour in the Time Domain.....	138
6.2.2	Stirrer Efficiency.....	139
6.2.3	Time-Gating Technique.....	140
6.3	Measurement Results.....	141
6.4	Discussion and Conclusions.....	151
6.5	Key Contributions.....	157
6.6	References.....	157
Chapter 7: Conclusions and Future Work.....		161
	References.....	164
Appendix A1.....		165
Appendix A2.....		170
Appendix A3.....		172

Acronyms

AC	Anechoic Chamber
ACS	Absorption Cross Section
AUT	Antenna under Test
BFS	Breadth-first Search
CAD	Computer-aided Design
CDF	Cumulative Distribution Function
CEM	Computational Electromagnetics
DG	Diversity Gain
EM	Electromagnetic
EMC	Electromagnetic Compatibility
EMI	Electromagnetic Interference
FDFD	Finite-difference Frequency-domain
FDTD	Finite-difference Time-domain
FEM	Finite Element Method
FFT	Fast Fourier Transform
FU	Field Uniformity
GO	Geometric Optics
GPU	Graphics Processor Unit
GUI	Graphical User Interface
IE	Integral Equation
IFFT	Inverse Fast Fourier Transform

LoS	Line of Sight
LUF	Lowest Usable Frequency
MIMO	Multiple Input Multiple Output
MoM	Method of Moment
NLoS	Non Line of Sight
NSA	Normalised Site Attenuation
OOP	Object-oriented Programming
OUT	Object under Test
P2A	Point-to-area
P2P	Point-to-point
PBC	Periodic Boundary Condition
PDF	Probability Density Function
PEC	Perfect Electric Conductor
PMC	Perfect Magnetic Conductor
PML	Perfectly Matched Layer
RAM	Radio Absorbing Material
RC	Reverberation Chamber
RE	Radiated Emission
SA	Site Attenuation/Spectrum Analyser
SE	Shielding Effectiveness
SG	Signal Generator
SNR	Signal to Noise Ratio
STL	Stereolithography

SVSWR	Site Voltage Standing Wave Ratio
TCS	Transmission Cross Section
TLM	Transmission Line Matrix
TSCS	Total Scattering Cross Section
UFA	Uniform Field Area
VNA	Vector Network Analyser

Acknowledgements

I would like to express my deepest gratitude to my supervisors Professor Yi Huang and Dr Xu Zhu. Without their guidance and persistent support this dissertation would not have been possible. I truly enjoyed working in a research environment that stimulates original idea and insightful thinking. Their skilful guidance, innovative ideas and great patience are much appreciated.

I would like to express my gratitude to my wife. I think I am lucky to be with you, providing me with inspirations, courage and love. I will always cherish the trust you gave me both on research and daily life.

I would also like to acknowledge important insights and suggestions from Professor Andy Marvin and Dr Jiafeng Zhou.

This work would not be completed without the financial support of CGE (Centre for Global Eco-Innovation), Rainford EMC Systems Ltd (Microwave Vision Group) and MPE Ltd. I would like to acknowledge the important roles of John Noonan, Paul Duxbury, Doug McInnes and Dr Matt Fulton.

Finally, I would like to thank my research lab colleagues and my friends: Shufeng Sun, Dr Stephen Boyes, Dr Neda Khiabani, Dr Ping Cao, Dr Jingwei Zhang, Sheng Yuan, Chaoyun Song, Zhihao Tian, Manoj Stanley, Zhouxiang Fei, Saqer Alja'afreh, Muayad Kod, Rula Alrawashdeh, Muaad Hussein, Aznida Abu Bakar Sajak, Amir Kotb, Abed Pour Sohrab, Anqi Chen, Yuan Zhuang, Umniyyah Ulfa, Saidatul Izyanie, Yukun Zhao, Shuang Li, Tingting Liu, Dr Wei Huang, Dr Tao Jin and Dr Junqing Zhang. I have enjoyed working with you all and I appreciate the ideas, help and good humour.

List of Publications

Journal Publications

- [1] **Q. Xu**, Y. Huang, X. Zhu, S. Alja'afreh, L. Xing and Z. Tian, "Diversity gain measurement in a reverberation chamber without extra antennas," *IEEE Antennas and Wireless Propagation Letters*, vol. 14, pp. 1666-1669, 2015.
- [2] **Q. Xu**, Y. Huang, X. Zhu, S. Alja'afreh and L. Xing, "A new antenna diversity gain measurement method using a reverberation chamber," *IEEE Antennas and Wireless Propagation Letters*, vol. 14, pp. 935-938, 2015.
- [3] **Q. Xu**, Y. Huang, X. Zhu, L. Xing, Z. Tian and C. Song, "A modified two-antenna method to measure the radiation efficiency of antennas in a reverberation chamber," *IEEE Antennas and Wireless Propagation Letters*, accepted, available online: 10.1109/LAWP.2015.2443987.
- [4] **Q. Xu**, Y. Huang, L. Xing and Z. Tian, "Extract the decay constant of a reverberation chamber without satisfying Nyquist criterion," *IEEE Microwave and Wireless Components Letters*, accepted.
- [5] **Q. Xu**, Y. Huang, X. Zhu, L. Xing, Z. Tian and C. Song, "Shielding effectiveness measurement of an electrically large enclosure using one antenna," *IEEE Transactions on Electromagnetic Compatibility*, vol. 57, no. 6, pp. 1466-1471, 2015.
- [6] **Q. Xu**, Y. Huang, L. Xing, Z. Tian, C. Song and M. Stanley, "The limit of the total scattering cross section of electrically large stirrers in a reverberation chamber," *IEEE Transactions on Electromagnetic Compatibility*, accepted.
- [7] **Q. Xu**, Y. Huang, L. Xing, Z. Tian, Z. Fei and L. Zheng, "A fast method to measure the volume of a large cavity," *IEEE Access*, vol. 3, pp. 1555-1561, 2015.
- [8] **Q. Xu**, Y. Huang, X. Zhu, L. Xing, P. Duxbury and J. Noonan, "A geometric optics based systematic solution for anechoic chamber design: theory, simulation, verification and measurements," *IEEE Antennas and Propagation Magazine*, accepted.
- [9] **Q. Xu**, Y. Huang, L. Xing, Z. Tian, M. Stanley and S. Yuan, "B-scan in a reverberation chamber," *IEEE Transactions on Antennas and Propagation*, accepted.
- [10] **Q. Xu**, Y. Huang, S. Yuan, L. Xing and Z. Tian, "Two alternative methods to measure the radiated emission in a reverberation chamber," *International Journal of Antennas and Propagation*, accepted.
- [11] S. Yuan, Y. Huang, J. Zhou, **Q. Xu**, C. Song and P. Thompson, "Magnetic field energy harvesting under overhead power lines," *IEEE Transactions on Power Electronics*, vol. 30, no. 11, pp. 6191-6202, 2015.
- [12] S. Alja'afreh, Y. Huang, L. Xing, **Q. Xu** and X. Zhu, "A low profile and wideband PILA-based antenna for handset diversity applications," *IEEE Antennas and Wireless Propagation Letters*, vol. 14, pp. 923-923, 2015.
- [13] L. Xing, Y. Huang, Y. Shen, S. Alja'afreh, **Q. Xu** and R. Alrawashdeh, "Further investigation on water antennas," *IET Microwave Antennas & Propagation*, vol. 9, no. 8, pp. 735-741, 2015.

- [14] L. Xing, Y. Huang, **Q. Xu** and S. Alja'afreh, "A transparent dielectric loaded reconfigurable antenna with a wide tuning range," *IEEE Antennas and Wireless Propagation Letters*, accepted.
- [15] L. Xing, Y. Huang, **Q. Xu** and S. Alja'afreh, "Wideband, hybrid rectangular water antenna for DVB-H applications," *Microwave and Optical Technology Letters*, vol. 57, no. 9, pp. 2160-2164, 2015.
- [16] L. Xing, Y. Huang, **Q. Xu**, S. Alja'afreh and T. Liu, "A broadband hybrid water antenna for hand-portable applications," *IEEE Antennas and Wireless Propagation Letters*, accepted, available online: 10.1109/LAWP.2015.2436692.
- [17] L. Xing, Y. Huang, **Q. Xu** and S. Alja'afreh, "A compact water loaded reconfigurable antenna for DVB-H applications," *Electronic Letters*, vol. 51, no. 24, pp. 1958-1960, 2015.
- [18] L. Xing, Y. Huang, **Q. Xu** and S. Alja'afreh, "A wideband hybrid water antenna with an F-shaped monopole," *IEEE Access*, vol. 3, pp. 1179-1187, 2015.
- [19] L. Xing, Y. Huang, **Q. Xu**, S. Alja'afreh and T. Liu, "Complex permittivity of water-based liquids for liquid antennas," *IEEE Antennas and Wireless Propagation Letter*, accepted.

Conference Publications

- [1] **Q. Xu**, Y. Huang, X. Zhu, L. Xing and Z. Tian, "Antenna radiation efficiency measurement in a reverberation chamber without the need for calibration," IEEE AP-S Symposium on Antennas and Propagation (APS), Vancouver, Canada, 2015.
- [2] **Q. Xu**, Y. Huang, J. Zhou, C. Song and L. Xing, "Field-circuit co-simulation of the Marx generator," European Conference on Antennas and Propagation (EuCAP), Lisbon, Portugal, 2015.
- [3] **Q. Xu**, Y. Huang, X. Zhu, L. Xing and Z. Tian, "Permittivity measurement of spherical objects using a reverberation chamber," Antennas and Propagation Conference (LAPC), Loughborough, 2014.
- [4] **Q. Xu**, Y. Huang, X. Zhu, L. Xing, P. Duxbury and J. Noonan, "NSA simulation in semi-anechoic chamber using ray tube tracing method," Ninth International Conference on Computation in Electromagnetics, London, 2014.
- [5] **Q. Xu**, Y. Huang, X. Zhu, L. Xing, P. Duxbury and J. Noonan, "An efficient method for the field uniformity analysis of anechoic chambers," IEEE AP-S Symposium on Antennas and Propagation (APS), Memphis, USA, 2014.
- [6] **Q. Xu**, Y. Huang, X. Zhu, L. Xing and A. A. B. Sajak, "Statistical electromagnetic analysis of PEC sphere scattering," International Conference on Engineering Technology & Technopreneurship (ICE2T), Kuala Lumpur, 2014.
- [7] **Q. Xu**, Y. Huang, X. Zhu, L. Xing, P. Duxbury and J. Noonan, "Anechoic chamber design and antenna measurements in reverberation chamber," COST 6th WG Meeting & Technical Workshop, Madrid, Spain, 2014.
- [8] Z. Tian, Y. Huang and **Q. Xu**, "Stirring effectiveness characterization based on Doppler spread in a reverberation chamber," European Conference on Antennas and Propagation (EuCAP), Davos, Switzerland, 2016.

- [9] M. Stanley, Y. Huang, H. Wang, S. Alja'afreh, **Q. Xu** and L. Xing, "LTE MIMO antenna using unbroken metallic rim and non-resonant CCE element," European Conference on Antennas and Propagation (EuCAP), Davos, Switzerland, 2016.
- [10] L. Xing, Y. Huang, **Q. Xu**, and S. Alja'afreh, "Overview of water antenna designs for wireless communications," IEEE Asia-Pacific Conference on Antennas and Propagation (APCAP), Bali Island, Indonesia, 2015.
- [11] C. Song, Y. Huang, **Q. Xu** and U. Umniyyah, "A broadband circularly polarized cross-dipole antenna for GNSS applications," Antennas and Propagation Conference (LAPC), Loughborough, 2015.
- [12] C. Li, T. Loh, Z. Tian, **Q. Xu** and Y. Huang, "A comparison of antenna efficiency measurements performed in two reverberation chambers using non-reference antenna methods," Antennas and Propagation Conference (LAPC), Loughborough, 2015.
- [13] Z. Tian, Y. Huang and **Q. Xu**, "A further investigation of the source stirred chamber method for antenna efficiency measurements," 8th UK, Europe, China Conference on Millimeter Waves and Terahertz Technologies, Cardiff, UK, 2015.
- [14] C. Song, Y. Huang, J. Zhou, S. Yuan, **Q. Xu** and P. Carter, "A broadband efficient rectenna array for wireless energy harvesting," European Conference on Antennas and Propagation (EuCAP), Lisbon, Portugal, 2015.
- [15] L. Xing, Y. Huang, S. Alja'afreh, **Q. Xu**, M. Kod and C. Song, "Reconfigurable 3D folded monopole antenna design for DVB-H applications," Antennas and Propagation Conference (LAPC), Loughborough, 2014.
- [16] Z. Tian, Y. Huang, Y. Shen and **Q. Xu**, "An electrical stirring method for a reverberation chamber," Antennas and Propagation Conference (LAPC), Loughborough, 2014.
- [17] L. Xing, Y. Huang, Y. C. Shen, S. Alja'afreh, **Q. Xu** and R. Alrawashdeh, "Broadband U-shaped water antenna for DVB-H applications," IEEE International Symposium on Antennas and Propagation, Memphis, USA, 2014.
- [18] N. Khiabani, Y. Huang, Y. Shen, S. Boyes and **Q. Xu**, "A novel simulation method for THz photoconductive antenna characterizations," European Conference on Antennas and Propagation (EuCAP), Gothenburg, Sweden, 2013.

Abstract

Two different chambers are studied in this thesis: the anechoic chamber (AC) and the reverberation chamber (RC). The AC has been developed for many years, while in the past few years RC has emerged as a promising facility not just in electromagnetic compatibility (EMC) measurements but also as a multi-disciplinary research facility in various areas.

For the anechoic chamber, a CAD tool is developed to aid the design of an anechoic chamber. The objective is to estimate the chamber performance accurately. The ultimate goal is to minimise the cost but optimise the chamber performance for given conditions and specifications. This is very important for a commercial company. The CAD tool is developed based on the GO theory, two different algorithms are realised, acceleration techniques are applied, and measurements are performed to validate the CAD tool.

For the reverberation chamber, a series of new measurement methods in the RC are developed including antenna radiation efficiency measurement, diversity gain measurement, radiated emission measurement, material characterisation, shielding effectiveness, volume measurement, *etc.* Finally, we apply the B-scan in an RC to characterise the behaviour of the electric field in the time domain. Statistical characterisation of the electric field in the time domain is given, stirrer efficiency is quantified based on the total scattering cross section (TSCS) of stirrers, and time gating technique in the RC is introduced. It has been found that the stirrer efficiency can be well-quantified in the time domain and the definition of stirrer efficiency in this thesis provides a universal and quantitative way to compare the performance between different RCs or different stirrer designs in one RC.

Chapter 1: Introduction

1.1 Background

In this chapter, we introduce the background information of this thesis. This thesis is focused on two different chambers: the anechoic chamber and reverberation chamber. For the anechoic chamber, we focus on the design procedure of it since the applications of the anechoic chamber are well developed. For the reverberation chamber, there are still many scopes to be explored, a series of new methods and applications are proposed, and finally the characterisation of the RC is investigated using B-scan results. Guidelines for the reverberation chamber design are also discussed.

1.1.1 Anechoic Chamber Design

An anechoic chamber (AC) [1] is a large room lined with radio absorbing materials (RAMs) on the walls, floor and ceiling to simulate the free space environment (Fig. 1.1) – no echoes are generated, thus all outdoor electromagnetic measurements can be conducted inside such a comfortable indoor environment which is not subject to any interference. It is therefore widely used in electrical and electronics industry.

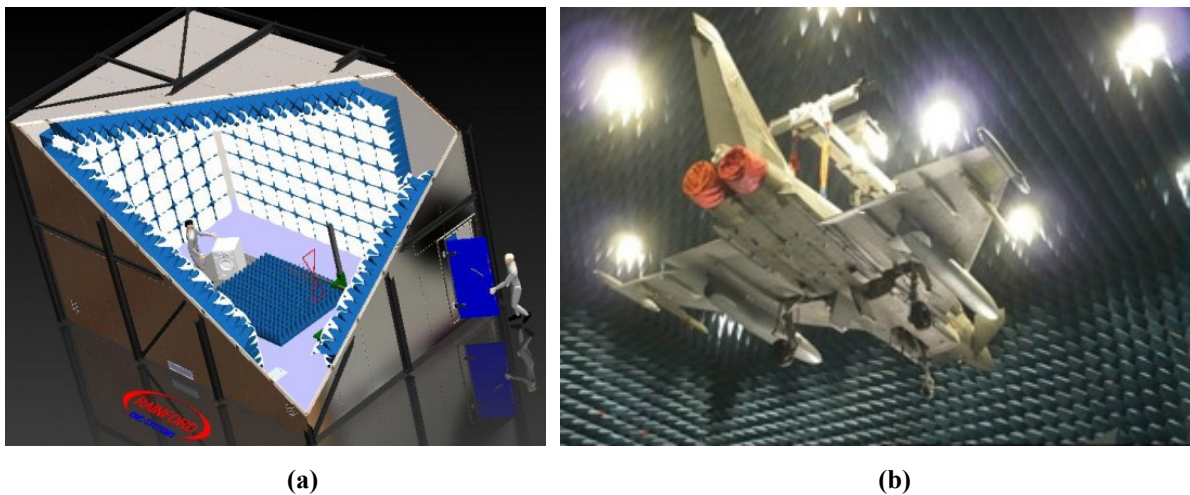


Fig. 1.1. Anechoic chamber (a) 3D model, (b) measurement with an aircraft inside an anechoic chamber (pictures from Rainford EMC Systems Ltd).

A problem is how to optimise the performance of such a chamber for a given chamber size using the least amount of RAM (cost-effectively). The cost of the RAM depends on the size and type of it. How to choose the RAM and arrange them properly is the key problem. Currently, the design of the chamber depends on the designer's experience and sometimes who needs to take a try-and-error

approach or use a large safe margin [2]. Thus, we need a scientific and objective way to find the best solution.

Normally, a large safe margin is built in to ensure the good performance of the chamber. There is a trade-off between the performance and the cost, the better RAM (thus better chamber performance) normally means more expensive and a larger RAM size (thus less space for measurements). At the moment, there are no proper chamber design tools available; all chambers are basically designed using some guidelines (including in-house simple tools) and experience. Part objective of this thesis is to develop an efficient and systematic solution for anechoic chamber design which will help the designer to estimate the chamber performance accurately during the design process. The ultimate goal is to minimise the cost but optimise the chamber performance for given conditions and specifications.

The chamber may have various forms in applications, such as tapered chambers [3], compact chambers with reflectors [4], double horn chambers [5], [6], *etc.* There are many ways and parameters to characterise the chamber performance: site attenuation (SA, or normalised SA), site voltage standing wave ratio (SVSWR) and field uniformity (FU) are the three key parameters which are normally employed in the chamber related standards [7], [8] to evaluate the chamber performance.

1.1.2 Reverberation Chamber

A reverberation chamber (RC) is an electrically large screened room with electrically large stirrers used to stir the field inside the chamber [9] (Fig. 1.2). We can consider the RC as an opposite environment against the anechoic chamber:

The wall of the AC absorbs the electromagnetic waves while the wall of RC reflects them mostly (each time);

The AC is a deterministic environment while the RC is a statistical environment: in the AC, the deterministic theory is used while in the RC the statistical theory is applied.

The AC can be considered as an ideal Gaussian channel, while the RC can be considered as a Rayleigh channel or Rician channel (rich multipath channel).

The RC has been used for a wide range of measurement applications related to such as radiated immunity, radiated emission, shielding effectiveness, antenna efficiency, channel emulation, material characterisation, biological effects, *etc.* Although a lot of applications have been developed, there are still new methods and applications to explore. In this thesis, we focus on the new methods of the RC, a series of new measurement methods are developed. The time domain behaviour of the RC is also

investigated which gives a further understanding of the RC. The stirrer efficiency is quantified based on the B-scan results.



Fig. 1.2. Reverberation chamber at the University of Liverpool.

1.2 Organisation of the Thesis

There are seven chapters in this thesis. In Chapter 1, a brief introduction is given; Chapter 2 to Chapter 4 are mainly focused on the anechoic chamber, while Chapter 5 and Chapter 6 are about reverberation chamber. The summary of the thesis is given in Chapter 7.

In Chapter 2, we review the theory for the anechoic chamber design, GO theory is presented; two forms of GO theory are given, a number of computational electromagnetics (CEM) algorithms are discussed and compared for anechoic chamber simulation.

In Chapter 3, the development details of the CAD tool for the anechoic chamber design are given, including 3D model description, preprocessing, material definition, boundary definition, post processing, etc. Two algorithms (forward and inverse) are developed with acceleration techniques respectively. Adaptive octree is proposed in the forward algorithm, and convex acceleration technique is proposed in the inverse algorithm. Both these two techniques improve the computation efficiency significantly.

In Chapter 4, definitions of NSA, SVSWR, FU are given, and the measurement methods are introduced, the measurement figures of NSA, SVSWR and FU are given, results from measurement and simulation are compared. Good agreements are obtained. Discussion and conclusions are given.

In Chapter 5, the applications of the reverberation chamber are reviewed, a series of measurement methods in the RC are developed including antenna radiation efficiency measurement, diversity gain measurement, radiated emission measurement, material characterisation, shielding effectiveness, volume measurement, *etc.* The new methods are detailed in each subsection with theories and measurement verifications.

In Chapter 6, B-scan has been performed in an RC, the electric field behaviour inside the RC in the time domain is investigated, statistical characterisation in the time domain is given, stirrer efficiency is quantified, and time-gating technique in the RC is introduced. It has been found that the stirrer efficiency can be well-defined by using the total scattering cross section of the stirrers, and this definition is not sensitive to the antenna position and the load in the RC.

In Chapter 7, we summarise all the work in this thesis and identify key contributions, potential problems and future work are also discussed.

1.3 References

- [1] W. H. Emerson, "Electromagnetic wave absorbers and anechoic chamber through the years," *IEEE Trans. Antennas Propagat.*, vol. 21, no. 4, pp. 484–490, Jul. 1973.
- [2] L. H. Hemming, *Electromagnetic Anechoic Chambers: A Fundamental Design and Specification Guide*, New York: Wiley-IEEE Press, 2002.
- [3] H. E. King, F. I. Shimabukuro and J. L. Wong, "Characteristics of a tapered anechoic chamber," *IEEE Trans. Antennas Propagat.*, vol. 15, no. 3, pp. 488–490, May 1967.
- [4] V. Galindo-Israel, S. R. Rengarajan, W. A. Imbriale and R. Mittra, "Offset dual-shaped reflectors for dual chamber compact ranges," *IEEE Trans. Antennas Propagat.*, vol. 39, no. 7, pp. 1007–1013, Jul. 1991.
- [5] L. H. Hemming, "Anechoic chamber," U.S. Patent 4 507 660, March 26, 1985.
- [6] G. A. Sanchez, "Geometrically optimized anechoic chamber," U.S. Patent 5 631 661, May 20, 1997.
- [7] CISPR 16-1-4: Specification for radio disturbance and immunity measuring apparatus and methods - Part 1-4: Radio disturbance and immunity measuring apparatus - Antennas and test sites for radiated disturbance measurements, IEC Standard, Ed 3.1, Jul. 2012.

- [8] IEC 61000-4-3: Electromagnetic compatibility (EMC) - Part 4-3: Testing and measurement techniques - Radiated, radio-frequency, electromagnetic field immunity test, IEC Standard, Ed 3.1, Apr. 2008.
- [9] Available online: https://en.wikipedia.org/wiki/Electromagnetic_reverberation_chamber

Chapter 2: Theory for Anechoic Chamber Design

2.1 Introduction

In this chapter, the theory used for the anechoic chamber design is introduced – geometric optics (GO). GO is normally related with ray tracing or imaging method. From analytical point of view, GO is an intuitive theory and easy to understand. However, when realising it the problem is not just an electromagnetic problem but also highly related to computer graphics. The realisation of GO and its application will be presented in the next chapter. In this chapter, we focus on the theory part of GO and do not consider the complexity during realisation. To have a quick overview, publication numbers related to GO in each year are shown in Fig. 2.1 (raw data from IEEE Xplorer®). It can be seen that, since 1980, there has been increasing interest on it (the number of year 2015 is not complete).

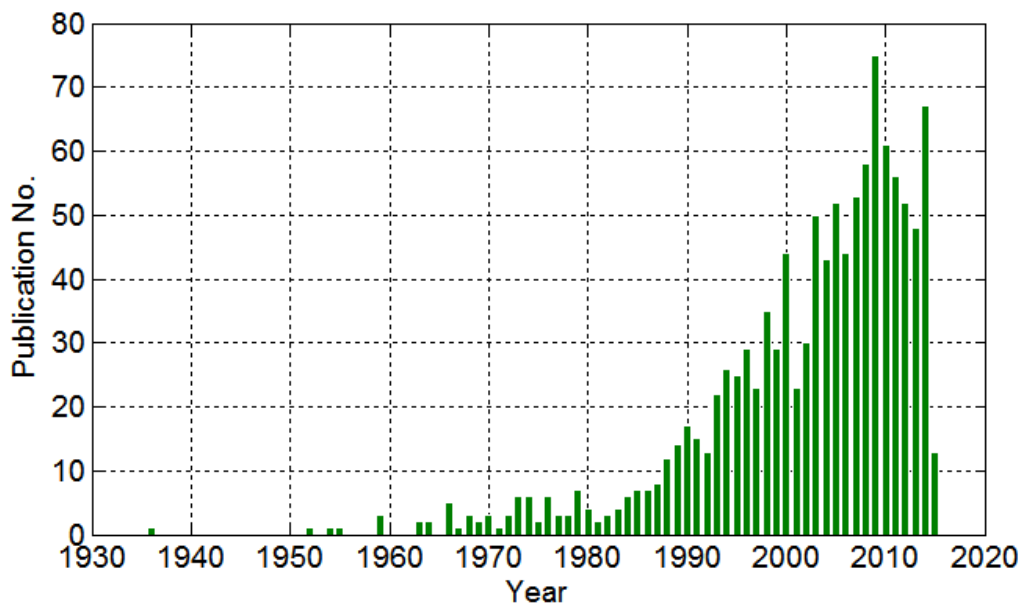


Fig. 2.1. Publication number every year (key words: *geometric optics*)

2.2 GO Theory

We first introduce the derivation of GO from Maxwell equations and then present how to obtain the reflected E-field from the incident E-field.

2.2.1 GO from Maxwell Equations

Geometrical optics can be treated as an extreme case of very high frequency approximation in Maxwell's theory [1], consider the solution

$$\vec{E}(\vec{r}) = \vec{E}e^{-jk_0L(\vec{r})} \quad (2.1)$$

$$\vec{H}(\vec{r}) = \vec{H}e^{-jk_0L(\vec{r})} \quad (2.2)$$

where $k_0 = \omega/c$ is the free space wave number, ω is the angular frequency, c is the speed of light, let $k_0 \rightarrow \infty$. Substituting in the source-free Maxwell equations we have [1]

$$\nabla L(\vec{r}) \times \vec{H} + \frac{n}{\eta} \vec{E} = \frac{-j}{k_0} \nabla \times \vec{H} \quad (2.3)$$

$$\nabla L(\vec{r}) \times \vec{E} - n\eta \vec{H} = \frac{-j}{k_0} \nabla \times \vec{E} \quad (2.4)$$

$$\nabla L(\vec{r}) \cdot \vec{E} = \frac{-j}{k_0} \nabla \cdot \vec{E} \quad (2.5)$$

$$\nabla L(\vec{r}) \cdot \vec{H} = \frac{-j}{k_0} \nabla \cdot \vec{H} \quad (2.6)$$

where $n = c\sqrt{\mu\varepsilon}$ is the refractive index, ε , μ are the permittivity and permeability respectively, $\eta = \sqrt{\mu/\varepsilon}$ is the characteristic impedance of the media. In the high-frequency limit we omit the right-hand sides of (2.3)-(2.6) and obtain the governing equations for geometrical optics [1]

$$\nabla L(\vec{r}) \times \vec{H} + \frac{n}{\eta} \vec{E} = 0 \quad (2.7)$$

$$\nabla L(\vec{r}) \times \vec{E} - n\eta \vec{H} = 0 \quad (2.8)$$

$$\nabla L(\vec{r}) \cdot \vec{E} = 0 \quad (2.9)$$

$$\nabla L(\vec{r}) \cdot \vec{H} = 0 \quad (2.10)$$

Substituting (2.8) in (2.7) and making use of (2.9) we obtain geometrical optics [1]

$$|\nabla L(\vec{r})|^2 = n^2 \quad (2.11)$$

2.2.2 Reflected Field from Curved Surface

It is easy to obtain the reflected wave from an infinite large plane surface, but the reflected wave from a curved surface is not that easy. The theory has been given in [2], results are summarised here.

For an incident wave $\vec{E}^i(Q_R)$ shown in Fig. 2.2, the reflected wave can be obtained from [2]

$$\vec{E}^r(s) = \vec{E}^i(Q_R) \bar{R} \sqrt{\frac{\rho_1^r \rho_2^r}{(\rho_1^r + s)(\rho_2^r + s)}} e^{-j\beta s} \quad (2.12)$$

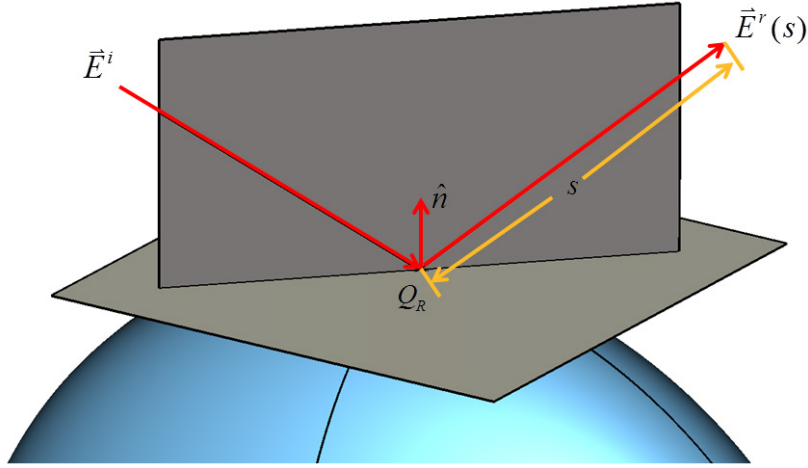


Fig. 2.2. Incident and reflected wave for a curved surface.

\bar{R} is the dyadic reflection coefficient, ρ_1^r, ρ_2^r are the principal radii of curvature of the reflected wave front at the point of reflection [2], shown in Fig. 2.3 and Fig. 2.4, β is the propagation constant.

$$\rho_1^r = \left[\frac{1}{2} \left(\frac{1}{\rho_1^i} + \frac{1}{\rho_2^i} \right) + \frac{1}{f_1} \right]^{-1} \quad (2.13)$$

$$\rho_2^r = \left[\frac{1}{2} \left(\frac{1}{\rho_1^i} + \frac{1}{\rho_2^i} \right) + \frac{1}{f_2} \right]^{-1} \quad (2.14)$$

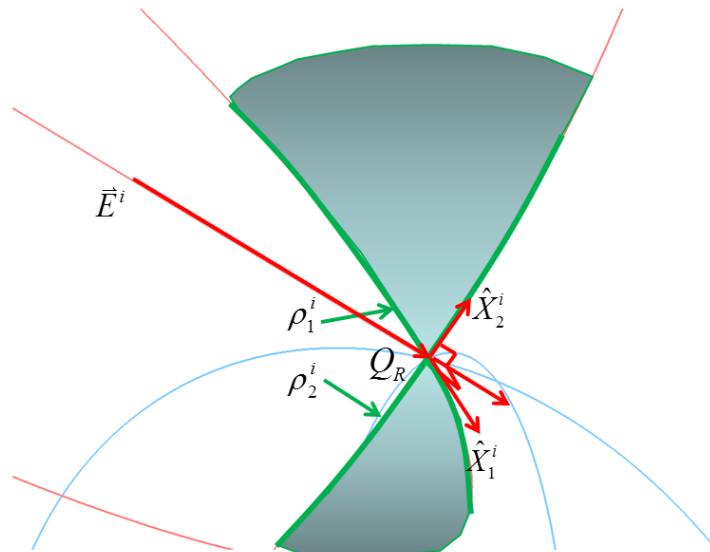


Fig. 2.3. Incident wave front.

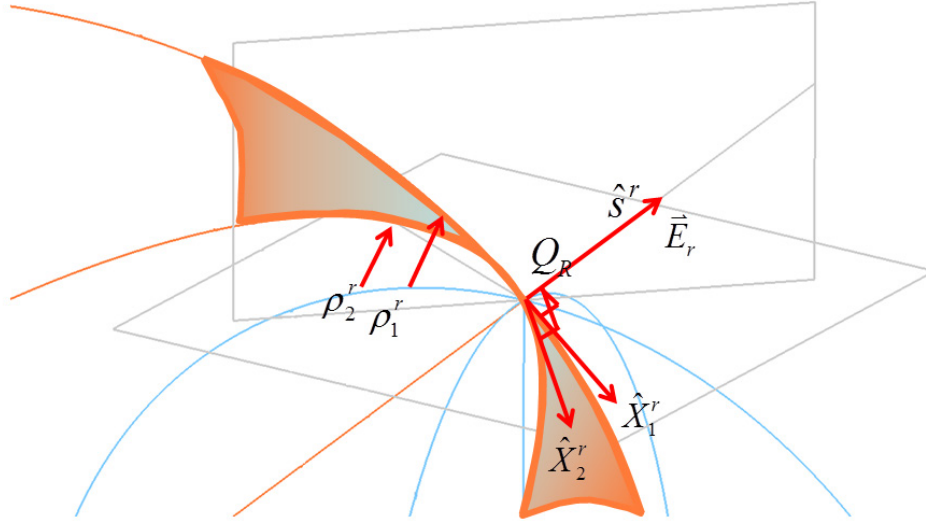


Fig. 2.4. Reflected wave front.

where

$$\begin{aligned} \frac{1}{f_{1(2)}} &= \frac{\cos\theta_i}{|\boldsymbol{\theta}|^2} \left(\frac{\theta_{22}^2 + \theta_{12}^2}{R_1} + \frac{\theta_{21}^2 + \theta_{11}^2}{R_2} \right) \\ &\pm \frac{1}{2} \left\{ \left(\frac{1}{\rho_1^i} - \frac{1}{\rho_2^i} \right)^2 + \left(\frac{1}{\rho_1^i} - \frac{1}{\rho_2^i} \right) \frac{4\cos\theta_i}{|\boldsymbol{\theta}|^2} \left(\frac{\theta_{22}^2 - \theta_{12}^2}{R_1} + \frac{\theta_{21}^2 - \theta_{11}^2}{R_2} \right) \right. \\ &\quad \left. + \frac{4\cos^2\theta_i}{|\boldsymbol{\theta}|^4} \left[\left(\frac{\theta_{22}^2 + \theta_{12}^2}{R_1} + \frac{\theta_{21}^2 + \theta_{11}^2}{R_2} \right)^2 - \frac{4|\boldsymbol{\theta}|^2}{R_1 R_2} \right] \right\}^{1/2} \end{aligned} \quad (2.15)$$

where + is used for f_1 and the minus for f_2 . In (2.15), $|\boldsymbol{\theta}|$ is the determinant of

$$[\boldsymbol{\theta}] = \begin{bmatrix} \hat{\mathbf{X}}_1^i \cdot \hat{\mathbf{u}}_1 & \hat{\mathbf{X}}_1^i \cdot \hat{\mathbf{u}}_2 \\ \hat{\mathbf{X}}_2^i \cdot \hat{\mathbf{u}}_1 & \hat{\mathbf{X}}_2^i \cdot \hat{\mathbf{u}}_2 \end{bmatrix} \quad (2.16)$$

or

$$|\boldsymbol{\theta}| = (\hat{\mathbf{X}}_1^i \cdot \hat{\mathbf{u}}_1)(\hat{\mathbf{X}}_2^i \cdot \hat{\mathbf{u}}_2) - (\hat{\mathbf{X}}_2^i \cdot \hat{\mathbf{u}}_1)(\hat{\mathbf{X}}_1^i \cdot \hat{\mathbf{u}}_2) \quad (2.17)$$

and

$$\theta_{jk} = \hat{\mathbf{X}}_j^i \cdot \hat{\mathbf{u}}_k \quad (2.18)$$

The vectors $\hat{\mathbf{X}}_1^i$ and $\hat{\mathbf{X}}_2^i$ represent the principal direction of the incident wave front at the reflection point Q_R with principal radii of curvature ρ_1^i and ρ_2^i . To define $\hat{\mathbf{X}}_1^r$ and $\hat{\mathbf{X}}_2^r$, we first introduce [2]

$$\mathbf{Q}^r = \begin{bmatrix} Q_{11}^r & Q_{12}^r \\ Q_{12}^r & Q_{22}^r \end{bmatrix} \quad (2.19)$$

where \mathbf{Q}^r is defined as the curvature matrix for the reflected wave front whose entries are [2]

$$Q_{11}^r = \frac{1}{\rho_1^i} + \frac{2\cos\theta_i}{|\boldsymbol{\theta}|^2} \left(\frac{\theta_{22}^2}{R_1} + \frac{\theta_{21}^2}{R_2} \right) \quad (2.20)$$

$$Q_{12}^r = -\frac{2\cos\theta_i}{|\boldsymbol{\theta}|^2} \left(\frac{\theta_{22}\theta_{11}}{R_1} + \frac{\theta_{11}\theta_{21}}{R_2} \right) \quad (2.21)$$

$$Q_{22}^r = \frac{1}{\rho_2^i} + \frac{2\cos\theta_i}{|\boldsymbol{\theta}|^2} \left(\frac{\theta_{12}^2}{R_1} + \frac{\theta_{11}^2}{R_2} \right) \quad (2.22)$$

$\hat{\mathbf{X}}_1^r$ and $\hat{\mathbf{X}}_2^r$ can be written as [2]

$$\hat{\mathbf{X}}_1^r = \frac{\left(Q_{22}^r - \frac{1}{\rho_1^r} \right) \hat{\mathbf{x}}_1^r - Q_{12}^r \hat{\mathbf{x}}_2^r}{\sqrt{\left(Q_{22}^r - \frac{1}{\rho_1^r} \right)^2 + (Q_{12}^r)^2}} \quad (2.23)$$

$$\hat{\mathbf{X}}_2^r = -\hat{s}^r \times \hat{\mathbf{X}}_1^r \quad (2.24)$$

where $\hat{\mathbf{x}}_1^r$ and $\hat{\mathbf{x}}_2^r$ are unit vectors perpendicular to the reflected ray, and can be obtained using [2]

$$\hat{\mathbf{x}}_1^r = \hat{\mathbf{X}}_1^i - 2(\hat{\mathbf{n}} \cdot \hat{\mathbf{X}}_1^i) \hat{\mathbf{n}} \quad (2.25)$$

$$\hat{\mathbf{x}}_2^r = \hat{\mathbf{X}}_2^i - 2(\hat{\mathbf{n}} \cdot \hat{\mathbf{X}}_2^i) \hat{\mathbf{n}} \quad (2.26)$$

$\hat{\mathbf{n}}$ is the unit vector normal to the surface at the reflection point.

2.2.3 Alternative GO Form

In the previous section, the analytical form of GO has been given. To obtain the reflected field analytically, the surface equation $z(x, y)$ must be known. In practice, the surface could not be expressed analytically. Thus, an alternative form is needed to make the GO easy to implement numerically.

An alternative form of GO can be expressed as [3]

$$\vec{E} = \vec{E}_0 \cdot \left\{ \prod \bar{R}_i \right\} \cdot \left\{ \prod \bar{T}_i \right\} \cdot \left\{ \prod e^{-\gamma_i l_i} \right\} \cdot SF \quad (2.27)$$

where the E-field is assumed to propagate like the light as shown in Fig. 2.5 where A_0 and A are the cross-sectional area of the ray tubes at the source point and field point of interest, they will be used to calculate the spreading factor ($SF = \sqrt{A_0}/\sqrt{A}$). \vec{E}_0 is the E-field at the source point (reference point), \vec{E} is the E-field at the field point. $\prod \bar{\bar{R}}_i$ and $\prod \bar{\bar{T}}_i$ are the reflection and transmission coefficient dyads along the whole ray path, $\prod e^{-\gamma_i l_i}$ is the total phase variations and losses along the whole path.

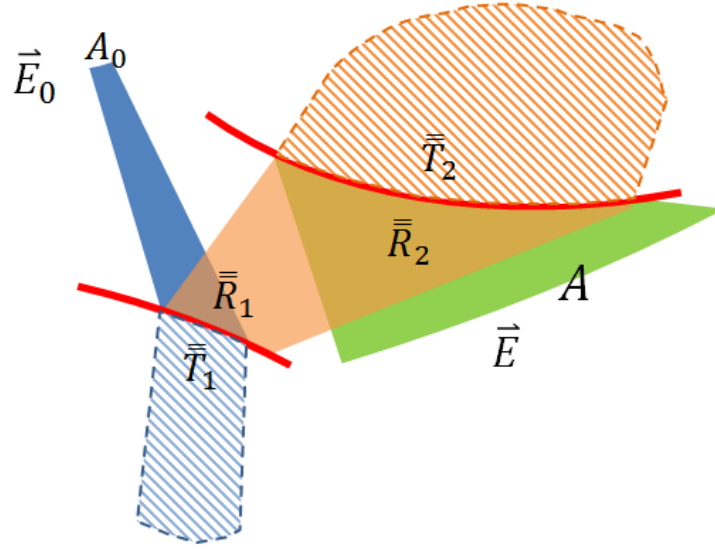


Fig. 2.5. Radio wave propagation in GO.

It can be seen from Fig. 2.5 that once the ray path is obtained, it is easy to calculate the E-field at the field point. For the anechoic chamber simulation, no transmission coefficient needs to be considered, this simplifies (2.27) as

$$\vec{E} = \vec{E}_0 \cdot \left\{ \prod \bar{\bar{R}}_i \right\} \cdot \left\{ \prod e^{-\gamma_i l_i} \right\} \cdot SF \quad (2.28)$$

where $\bar{\bar{R}}$ relates the incident field \vec{E}^i and reflected field \vec{E}^r as

$$\vec{E}^r = \begin{bmatrix} E_{\parallel}^r \\ E_{\perp}^r \end{bmatrix} = \bar{\bar{R}} \cdot \vec{E}^i = \begin{bmatrix} R_{\parallel\parallel} & R_{\parallel\perp} \\ R_{\perp\parallel} & R_{\perp\perp} \end{bmatrix} \begin{bmatrix} E_{\parallel}^i \\ E_{\perp}^i \end{bmatrix} \quad (2.29)$$

where E_{\parallel} and E_{\perp} are the decomposed parallel component and perpendicular component of the E-field shown in Fig. 2.6.

Equation (2.28) also simplifies the data structure for the CAD tool. In the simulation, this procedure requires a stack to store the rays, once the first ray of the stack is popped and traced, two rays are pushed back to the stack, this process will continue until the stack depth becomes zero. Without

considering the transmission rays, the total ray number is not changed during the simulation; the rays can be stored in arrays.

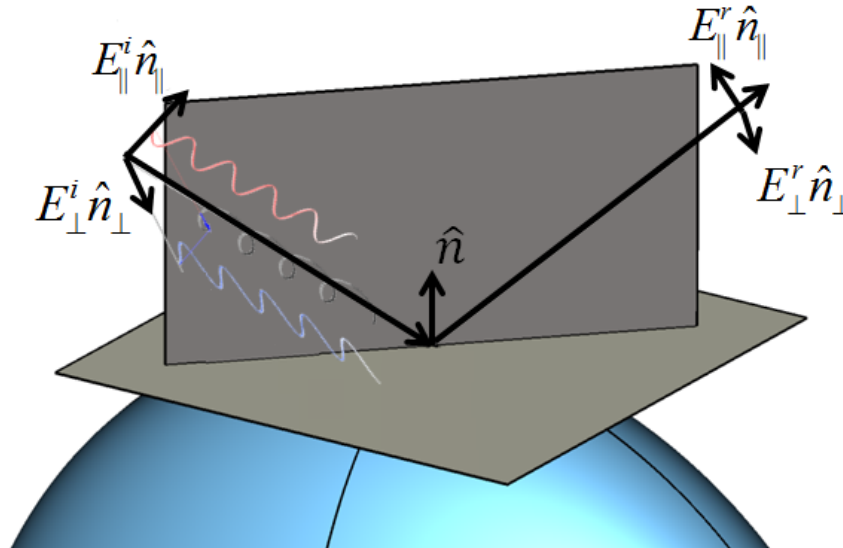


Fig. 2.6. Definition of the incident and reflected wave.

2.3 Anechoic Chamber Design Methods

A number of computational electromagnetics (CEM) modelling methods have been employed for chamber simulation, and they can be divided into two classes: the micro level and macro level.

At the micro level, the RAM reflectivity is related to the shape, permittivity and permeability of the RAM, full wave methods such as the finite-difference time-domain (FDTD) [4], frequency-domain finite-difference (FDFD) [5], finite element method (FEM) [6], and integral equation (IE) [7, 8] have been applied to the simulation and optimisation of the RAM. By taking advantage of the periodic boundary condition, the mesh number and memory requirement can be reduced significantly. Other methods used for this problem, like the transmission line method [9], homogenisation method [10-12] and rigorous coupled-wave analysis [13], simplify the RAM structure under certain assumptions. These methods may combine the analytical and numerical strategies together to further reduce the memory and time consumption with the expense of accuracy.

At the macro level, the whole chamber performance is considered. Full wave methods have also been applied, because of the complexity and the large electrical size of the whole chamber, simplifications have been made to increase the efficiency and reduce the time and memory requirement. For example, in [14], to avoid the calculation of the Green's function in such a complex environment, conductive wire meshes have been used to imitate the RAM in the moment method (MoM); in [15], large cells

were introduced to increase the time step and reduce the memory requirement in the FDTD method; the homogenisation method can also be combined with the transmission line matrix (TLM) to boost the efficiency [16]. Brute-force full-wave models without any simplifications have been applied as well, such as the TLM [17], hybrid MoM/FEM [18] and FDTD [19]. Even with a high performance computer, large electrical size problems with complex material scenarios are not easy to solve due to the large memory and time requirements.

High frequency approximation methods such as GO have been proven to be a fast and efficient way to simulate the macro level problem [20-25]. However, RAM modelling at the system level is normally simplified by using a cosine approximation [21], an effective medium [26], a homogenisation model [10], [11] or a multi-layer model [22]. Thus, the RAM is not fully described and to find an accurate equivalent analytical model over a wide frequency range and a wide incident angle is challenging.

The mesh type, complexity and the electrical size for different CEM methods are summarised in Fig. 2.7, where N means the number of freedoms/unknowns. It can be found that using only one method to simulate the wave propagation in an anechoic chamber could be too complex or too simple. In this thesis, to balance these two levels, at the macro level we apply the GO algorithm while at the micro level the full wave method FEM is applied. The connection between the GO and FEM is realised by using $\bar{\bar{R}}$. Software implementations are given in the next chapter.

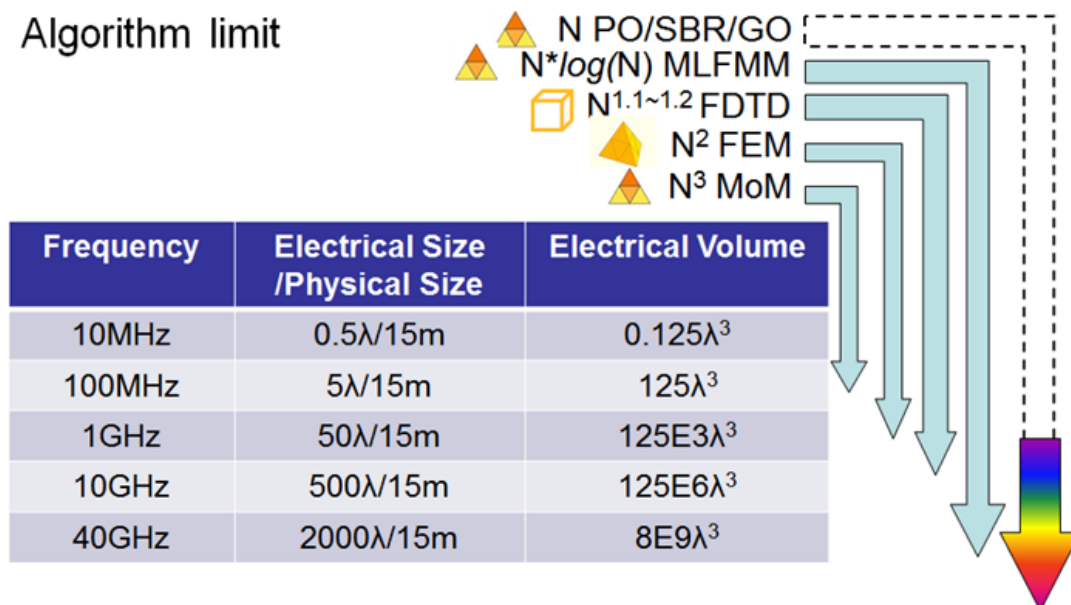


Fig. 2.7. Comparison of different CEM methods; PO: physical optics, SBR: shooting bouncing ray, GO: geometric optics, MLFMM: multilevel fast multipole algorithm, FDTD: finite-difference time-domain, FEM: finite element method, MoM: method of moment. (Part of the information in this picture is from CST China brochure)

2.4 Summary

In this chapter, we have considered the AC design problem from the theoretical point of view, and the theory for the anechoic chamber design has been reviewed. Two forms of GO are given. A number of computational electromagnetics (CEM) modelling methods have been compared for chamber simulation. To have an efficient solution, an appropriate CEM algorithm needs to be chosen; we consider the combination of the FEM and GO method as the proposed solution. The implementation and realisation of the proposed solution are given in the next chapter.

2.5 References

- [1] J. A. Kong, *Electromagnetic wave theory*, EMW, Cambridge, 2008.
- [2] C. A. Balanis, *Advanced engineering electromagnetics*, 2nd ed, Wiley, 2012.
- [3] C. Yang, B. Wu and C. Ko, "A ray-tracing method for modeling indoor wave propagation and penetration," *IEEE Trans. Antennas Propagat.*, vol. 46, no. 6, pp. 907–919, Jun. 1998.
- [4] K. Elmahgoub, F. Yang, A. Z. Elsherbeni, V. Demir and J. Chen, "FDTD analysis of periodic structures with arbitrary skewed grid," *IEEE Trans. Antennas Propagat.*, vol. 58, no. 8, pp. 2649–2657, Aug. 2010.
- [5] W. Sun, K. Liu and C. A. Balanis, "Analysis of singly and doubly periodic absorbers by frequency-domain finite-difference method," *IEEE Trans. Antennas Propagat.*, vol. 44, no. 6, pp. 798–805, Jun. 1996.
- [6] Y. Jiang and A. Q. Martin, "The design of microwave absorbers with high order hybrid finite element method," in *IEEE Antennas and Propagation Society International Symposium*, Orlando, 1999, vol. 4, pp. 2622–2625.
- [7] R. Janaswamy, "Oblique scattering from lossy periodic surfaces with application to anechoic chamber absorbers," *IEEE Trans. Antennas Propagat.*, vol. 40, no. 2, pp. 162–169, Feb. 1992.
- [8] N. Marly, B. Baekelandt, D. D. Zutter and H. F. Poes, "Integral equation modeling of the scattering and absorption of multilayered doubly-periodic lossy structures," *IEEE Trans. Antennas Propagat.*, vol. 43, no. 11, pp. 1281–1287, Nov. 1995.
- [9] V. Kubytzkyi, B. Sapoval, G. Dun and J. Rosnarho, "Fast optimization of microwave absorbers," *Microwave and Optical Technology Letters*, vol. 54, no. 11, pp. 2472–2477, Nov. 2012.
- [10] E. F. Kuester and C. L. Holloway, "A low-frequency model for wedge or pyramid absorber arrays-I: theory," *IEEE Trans. Electromagnetic Compatibility*, vol. 36, no. 4, pp. 300–306, Nov. 1994.

-
- [11] C. L. Holloway and E. F. Kuester, "A low-frequency model for wedge or pyramid absorber arrays-II: computed and measured results," *IEEE Trans. Electromagnetic Compatibility*, vol. 36, no. 4, pp. 307-313, Nov. 1994.
- [12] A. Khajepour and S. A. Mirtaheri, "Analysis of pyramid EM wave absorber by FDTD method and comparing with capacitance and homogenization methods," *Progress In Electromagnetics Research Letters*, vol. 3, pp. 123-131, 2008.
- [13] M. G. Moharam, D. A. Pommet, E. B. Grann and T. K. Gaylord, "Stable implementation of the rigorous coupled-wave analysis for surface-relief gratings: enhanced transmittance matrix approach," *Journal of the Optical Society of America A*, vol. 12, iss. 6, pp. 1077-1086, 1995.
- [14] T. Sasaki, Y. Watanabe and M. Tokuda, "NSA calculation of anechoic chamber using method of moment," in *Progress In Electromagnetics Research Symposium*, Cambridge, 2006, pp. 200-205.
- [15] M. Kawabata, Y. Shimada, K. Shmada and N. Kuwabara, "FDTD method for site attenuation analysis of compact anechoic chamber using large-cell concept," *Electrical Engineering in Japan*, vol. 162, iss. 4, pp. 9-16. 2008.
- [16] F. Bellamine, "Simulation of anechoic chamber using a combined TLM and homogenization method in the frequency range 30-200 MHz," in *First European Conference on Antennas and Propagation (EuCAP)*, Nice, pp. 1-6, 2006.
- [17] Available:<https://www.cst.com/Applications/Article/Intelligent-Representation-Of-Anechoic-Chamber-Wall-Cuts-Electromagnetic-Simulation-Time-95>.
- [18] D. Campbell, G. Gampala, C. J. Reddy, M. Winebrand and J. Aubin, "Modeling and analysis of anechoic chamber using CEM tools," in *Proceedings of AMTA Conference*, Bellevue, 2012.
- [19] N. V. Kantartzis and T. D. Tsiboukis, "Wideband numerical modelling and performance optimisation of arbitrarily-shaped anechoic chambers via an unconditionally stable time-domain technique," *Electrical Engineering*, vol. 88, iss. 1, pp. 55-81, Nov. 2005.
- [20] B. K. Chung, C. H. The and H. T. Chuah, "Modeling of anechoic chamber using a beam-tracing technique," *Progress In Electromagnetics Research (PIER)*, vol. 49, pp. 23-38, 2004.
- [21] S. R. Mishra and T. J. F. Pavlasek, "Design of absorber-lined chamber for EMC measurements using a geometrical optics approach," *IEEE Trans. Electromagnetic Compatibility*, vol. EMC-26, no. 3, pp. 111-119, Aug. 1984.
- [22] M. K. Mansour and J. Jarem, "Anechoic chamber design using ray tracing and theory of images," in *IEEE Southeastcon '90 Proceedings*, New Orleans, 1990, pp. 689-695.
- [23] C. L. Holloway and E. F. Kuester, "Modeling semi-anechoic electromagnetic measurement chambers," *IEEE Trans. Electromagnetic Compatibility*, vol. 38, no. 1, pp. 79-94, Feb. 1996.

-
- [24] M. Lin, J. Ji, C. G. Hsu and H. Hsieh, "Simulation and analysis of EMC chambers by ray tracing method," in *IEEE International Symposium on Electromagnetic Compatibility*, Honolulu, 2007, pp. 1-4.
- [25] S. M. J. Razavi, M. Khalaj-Amirhosseini and A. Cheldavi, "Minimum usage of ferrite tiles in anechoic chambers," *Progress In Electromagnetics Research B (PIER B)*, vol. 19, pp. 367-383, 2010.
- [26] B. K. Chung, H. T. Chuah, "Modeling of RF absorber for application in the design of anechoic chamber," *Progress In Electromagnetics Research*, (PIER), vol. 43, pp. 273-285, 2003.

Chapter 3: Computer Aided Anechoic Chamber Design

3.1 Introduction

In this chapter, we focus on the software implementation of the anechoic chamber design. When we model an electromagnetic (EM) problem using a computer, the first thing is to define the problem and identify what information is needed. Similar to the existing commercial CAD tools, to define an EM problem, we need to digitise a 3D model, define the material properties, assign boundary conditions, define the excitation source, choose the right solver and post process the results. These are detailed in this chapter: the framework of the tool is first given and then followed by the detailed techniques. It is shown in this chapter that the development of the CAD tool is not just an electromagnetic problem but a multi-disciplinary project which involves electromagnetics, software engineering and computer graphics.

3.2 Framework

The framework is shown in Fig. 3.1, it includes four parts from the top to the bottom. We name the software based on this solution as the *fast anechoic chamber evaluation tool* (FACET). The graphical user interface (GUI) is developed by using Microsoft Visual Basic .NET and the computational engine is developed by using MATLAB. They are connected using component object model technology. Like other CEM tools, it includes preprocessing, simulation and post processing parts. The two different algorithms share the same preprocessing but different post processing part. Each part will be explained in details.

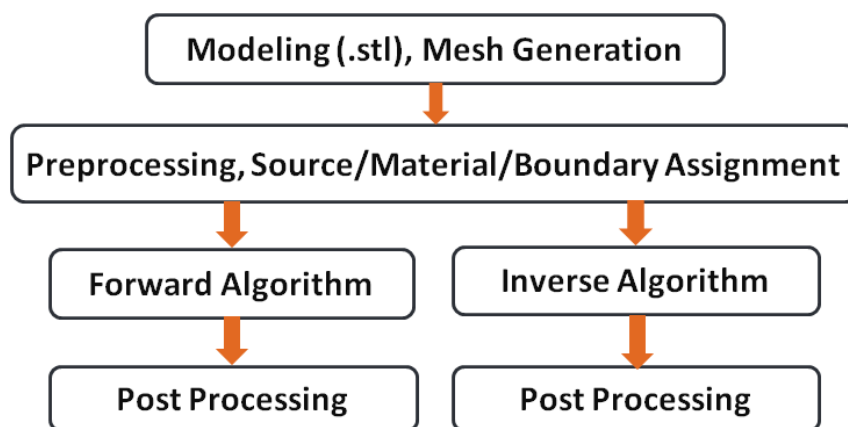


Fig. 3.1. Block diagram of the CAD tool.

3.3 Software Implementation

3.3.1 3D Model Description

To model the anechoic chamber by using a computer, the first thing we need to do is to describe the 3D structure of the chamber. To make it compatible with other 3D modelling software, the STL file is chosen to describe the 3D model. The STL file has two formats: the ASCII format and the binary format. We use the ASCII format since it is more direct [1]. A typical ASCII STL format is shown in Fig. 3.2.

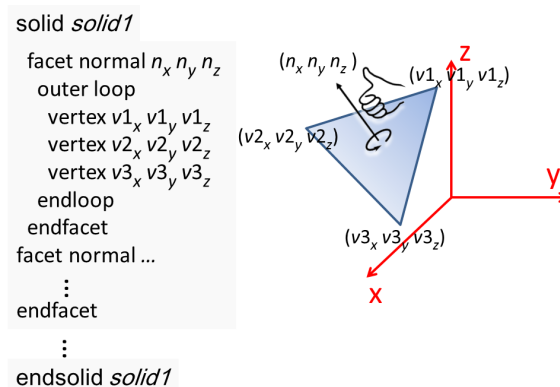


Fig. 3.2. A typical ASCII STL file format.

The model is discretised into triangular meshes. An ASCII STL file begins with key word *solid*, and then the name of the model is given (*solid1* in Fig. 3.2). The file continues with any number of triangles (shown in the right-hand side of Fig. 3.2), *facet normal* means the normal vector (n_x, n_y, n_z) of the triangle; the coordinates of the vertices of each triangle are given after *vertex* ($(v1_x, v1_y, v1_z)$, $(v2_x, v2_y, v2_z)$ and $(v3_x, v3_y, v3_z)$). The normal vector and vertices are ordered by the right-hand rule shown in Fig. 3.2 [1].

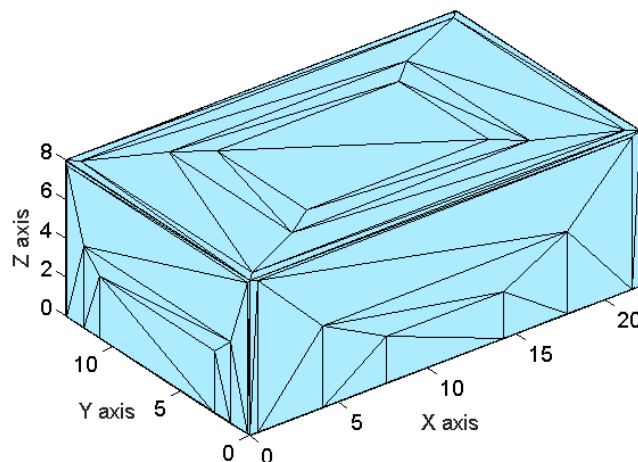


Fig. 3.3. Discretised chamber model represented by triangles, unit: metre.

The ASCII STL file can be imported into MATLAB and is shown in Fig. 3.3. The triangle surface mesh will be used to determine the intersection point between the ray and the model.

3.3.2 Preprocessing

There are two algorithms to realise the GO method: forward and inverse algorithm. In computer graphics community, GO is also called ray tracing [2]. Since the preprocessing part for the forward and inverse algorithm is different, we first review the forward and inverse algorithm respectively. An intuitive understanding is shown in Fig. 3.4.

For the forward algorithm, the E-field on a predefined monitor plane is recorded, it can deal with point-to-area (P2A) problems but the inverse algorithm is more efficient for point-to-point (P2P) problems, only the E-field of the predefined points is recorded [3]. In Fig. 3.4(a), a monitor plane is defined to intercept the rays pass through it; rays are launched from the source to all directions. The bottleneck for the forward algorithm is the speed in finding the intersection point between the ray and model. For a single ray, the complexity is $O(NM)$ (N is the number of patches describing the model, M is the reflection order) without using an acceleration technique. It can be reduced to $O(NM/2^H)$ (H is the depth of octree) by using octree [4], or $O(M \log_2 N)$ by using kd-tree technique [5], and it can be further reduced by taking the advantage of ray coherence theorem [3], [6]. Other techniques include parallelisation with graphics processing unit (GPU) [7] and multi-resolution grid to reduce the total ray number [8]. In Fig. 3.4(b), both source point and field point are defined; triangles are tested to check if there are visible paths connect these two points. The bottleneck for the inverse algorithm is finding the path that connects the source and field points with different orders, the maximum complexity is $O(N^M)$ [9].

It is important to note that the complexity discussed above is for a single ray. If we consider the ray number T related with the electrical area S of the chamber as $T \sim O(S^2) \sim O(f^2)$ (f is the frequency of interest), and the frequency sweep with F points the complexity of the forward algorithm needs to be multiplied by a factor of $O(Ff^2)$. However, for the inverse algorithm, the ray path between the source point and the field point can be recorded after path finding, this makes it nearly independent of F and f , and the complexity will not be affected too much.

In this thesis, both algorithms are developed with the acceleration techniques; the chamber designer can choose the suitable one for a specific problem. If the field distribution in a specific region is of interest, the forward algorithm is preferred, if only the field at some discrete points need to be known, the inverse algorithm is more efficient. Different from other full-wave methods, the beauty of GO is

that the fields contributed by different orders can be separated. The designer can identify where the unexpected field comes from by analysing the field with different orders.

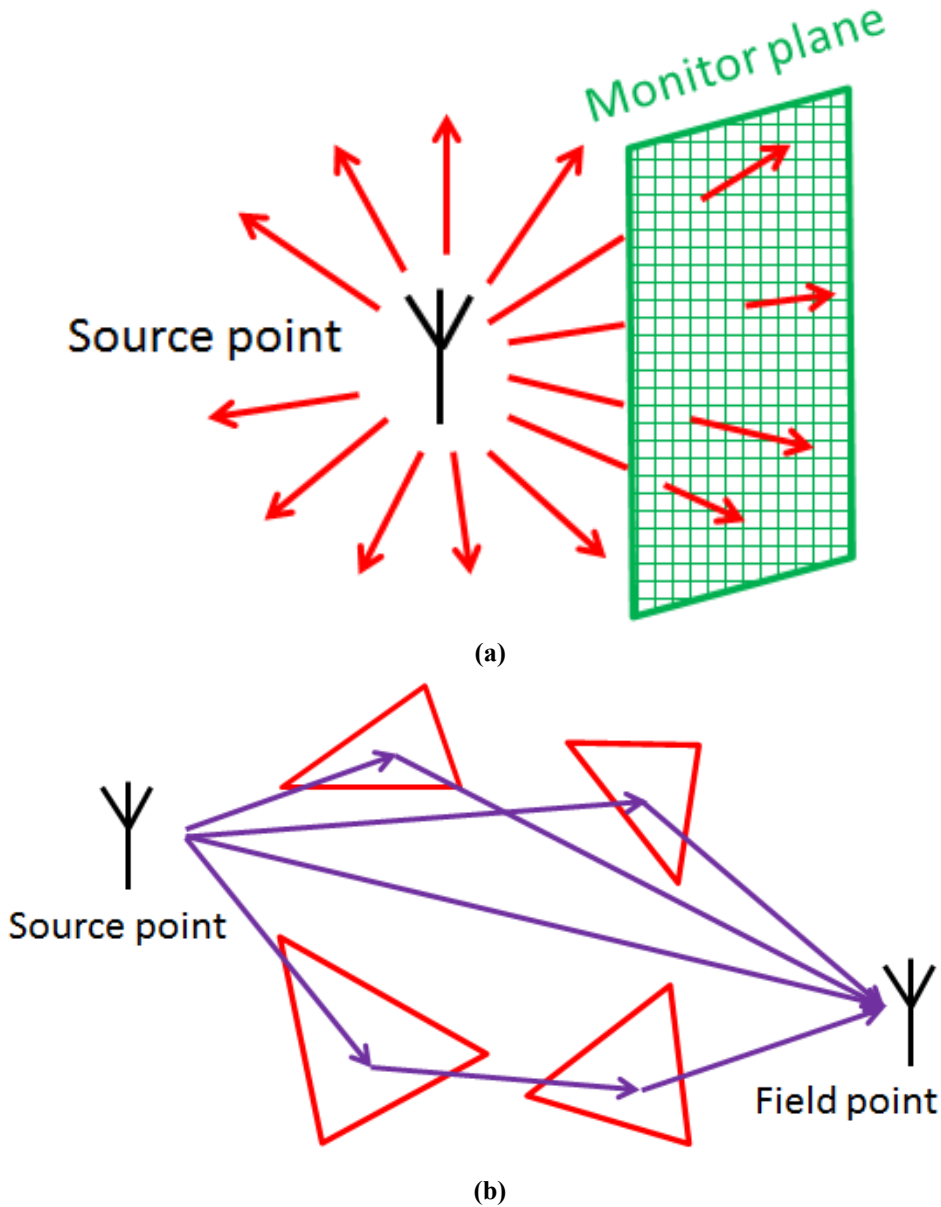


Fig. 3.4. Two different approaches in ray tracing: (a) forward algorithm, (b) inverse algorithm.

To find the intersection point between the ray and the triangle meshes, an important data structure is the octree. We follow the same process given in [4]. But different from [4], we propose an adaptive octree depth instead of a fixed depth octree. The depth (D) is given as

$$D = 1 + \left\lceil \log_2 \frac{\max(W, H, L)}{\text{mean}(\text{Triangle edge length})} \right\rceil \quad (3.1)$$

where W , H and L represent the width, height and length of the chamber respectively, the mean value of all triangle edge length is used to determine the depth of the octree. The complexity of the octree

building process is $O(ND)$, no acceleration technique is necessary, and the octree only needs to be built once.

3.3.3 Far-field Data

The antenna far-field pattern is considered as the excitation source of the chamber; the E-field at 3 m distance is calculated as \vec{E}_0 in (2.28). As we can see, the structure of the antenna is encapsulated; only the far-field data is needed, which can be obtained from either simulation or measurement of the antenna. To make it reusable, once the far-field pattern is obtained, it will be saved into a library/database which can be reused for future simulations. Four matrices are used to save the complex electric far-field at each frequency. They are $[E_{\theta mag}]$, $[E_{\theta phase}]$, $[E_{\phi mag}]$ and $[E_{\phi phase}]$ with dimension $R \times C$ where R is number of points in φ (azimuthal angle) direction, C is the number of points in θ (polar angle) direction. A typical farfield data file is shown in Fig. 3.5: the first two columns (Theta and Phi) show the angles in spherical coordinates, the third column (Abs(E)) gives the magnitude of the farfield at a certain distance, followed by the magnitude and phase in θ component (Abs(Theta) and Phase(Theta)) and φ component (Abs(Phi) and Phase(Phi)), the last column is the axial ration (Ax. Ratio).

Theta [deg.]	Phi [deg.]	Abs(E) [V/m]	Abs(Theta) [V/m]	Phase(Theta) [deg.]	Abs(Phi) [V/m]	Phase(Phi) [deg.]	Ax.Ratio
0.000	0.000	7.337e-002	7.337e-002	28.881	2.512e-008	36.434	3.162e+002
5.000	0.000	4.709e-002	4.709e-002	26.636	1.505e-008	43.821	3.162e+002
10.000	0.000	1.977e-002	1.977e-002	33.050	1.364e-008	49.507	3.162e+002
15.000	0.000	1.640e-002	1.640e-002	156.417	1.264e-008	56.211	3.162e+002
20.000	0.000	5.592e-002	5.592e-002	169.012	1.205e-008	63.552	3.162e+002
25.000	0.000	1.076e-001	1.076e-001	166.429	1.186e-008	70.509	3.162e+002
30.000	0.000	1.728e-001	1.728e-001	162.372	1.197e-008	75.510	3.162e+002
35.000	0.000	2.530e-001	2.530e-001	158.262	1.221e-008	76.959	3.162e+002

Fig. 3.5. A typical far-field data file.

We also need to consider the rotation of the antenna shown in Fig. 3.6. Suppose the far-field is rotated around z-axis with angle φ , then around y-axis with angle θ , then around x-axis with angle γ .

The vector in the transformed coordinate system can be expressed as

$$Q_3 Q_2 Q_1 \begin{bmatrix} A_x \\ A_y \\ A_z \end{bmatrix} = \begin{bmatrix} T_x \\ T_y \\ T_z \end{bmatrix} \quad (3.2)$$

where $\vec{A} = [A_x \ A_y \ A_z]^T$ is the vector in the original coordinate system, $\vec{T} = [T_x \ T_y \ T_z]^T$ is the vector in the transformed coordinate system,

$$Q_1 = \begin{bmatrix} \cos\varphi & \sin\varphi & 0 \\ -\sin\varphi & \cos\varphi & 0 \\ 0 & 0 & 1 \end{bmatrix} \quad (3.3)$$

$$Q_2 = \begin{bmatrix} \cos\theta & 0 & \sin\theta \\ 0 & 1 & 0 \\ -\sin\theta & 0 & \cos\theta \end{bmatrix} \quad (3.4)$$

$$Q_3 = \begin{bmatrix} 1 & 0 & 0 \\ 0 & \cos\gamma & \sin\gamma \\ 0 & -\sin\gamma & \cos\gamma \end{bmatrix} \quad (3.5)$$

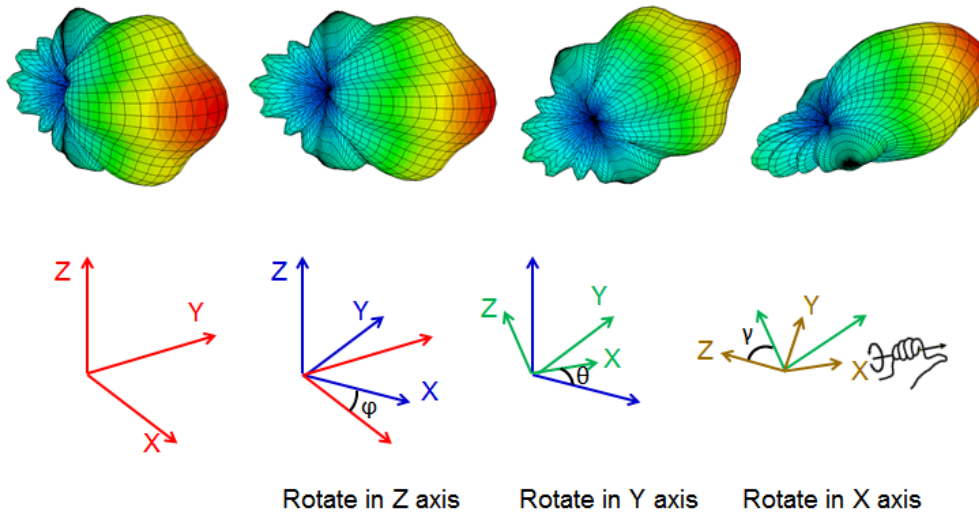


Fig. 3.6. Far-field transformation.

3.3.4 Boundary Condition

If we borrow the philosophy of the OOP (object-oriented programming), each triangle can be considered as an object in programming and the type of RAM on it can be considered as its property. Different triangles may have different kinds of RAM, as shown in Fig. 3.3.

The boundary conditions in the full wave simulation normally include the perfect electric conductor (PEC), perfect magnetic conductor (PMC), radiation condition or perfect matched layer (PML), *etc.* In GO we can also emulate these kinds of boundary conditions by assigning suitable values to the reflection coefficient matrix $\bar{\bar{R}}$ which has taken the wave polarisation into account as shown in (2.29). The coordinates are defined in Fig. 2.6. The $\bar{\bar{R}}$ for the PEC is

$$\bar{\bar{R}} = \begin{bmatrix} R_{\parallel\parallel} & R_{\parallel\perp} \\ R_{\perp\parallel} & R_{\perp\perp} \end{bmatrix} = \begin{bmatrix} 1 & 0 \\ 0 & -1 \end{bmatrix} \quad (3.6)$$

For the PML, there are two ways to treat it, we can either set the reflection coefficient to a very small value (e.g. -200 dB) or mark it a special type. We can also set the RAM type index as -1, which can

make it faster in ray tracing, and all rays that hit on the PML do not need to be traced for the next order reflection.

3.3.5 RAM Definition

A full numerical model is applied to describe the reflection coefficient of the RAM, the reflection coefficient dyad $\bar{\bar{R}}$ includes 4 elements: $R_{\parallel\parallel}$, $R_{\parallel\perp}$, $R_{\perp\parallel}$ and $R_{\perp\perp}$, all of them are dependent on the incident angle and frequency, $R_{ij} = R_{ij}(\theta, \varphi, f)$ (i, j can be \parallel or \perp), a 3D matrix as shown in Fig. 3.7 is used to save each type of RAM.

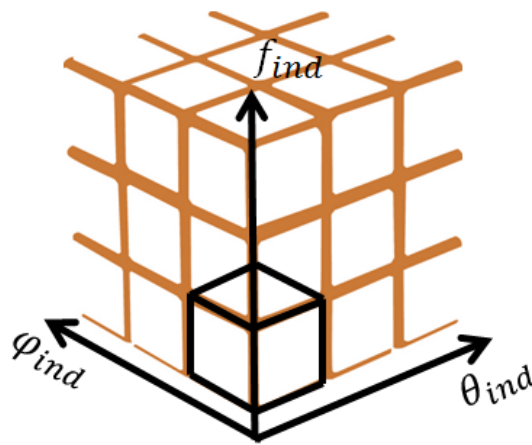


Fig. 3.7. Data structure of the reflection coefficient.

Compared with the traditional simplified models [10-13], this approach needs more memory (10 MB/each RAM type) but much faster than the simplified models which need more operations to calculate the reflection coefficient for each reflection (while the proposed approach only needs interpolation). Also the proposed numerical model encapsulates the detailed information of RAM which can be obtained from either simulation [10-19] or the arch method in measurements [20]. The information is saved in a library/database to make it reusable. Each type of RAM corresponds to four 3D matrices; once they are obtained we do not need to know the micro level properties of the RAM (permittivity and shape). This is a general extraction procedure and can be used to any type of RAM.

A typical FEM analysis of RAM unit can be performed with periodic boundary conditions (PBCs), shown in Fig. 3.8. For each incident angle, two orthogonal incident waves/modes need to be analysed, shown in Fig. 3.9. Frequency sweep is adopted for each incident angle. When all the simulation/measurements are finished, $\bar{\bar{R}}$ is ready. Since we can only simulate some discrete incident angles, for an arbitrary incident angle, the reflection coefficient can be obtained using interpolation.

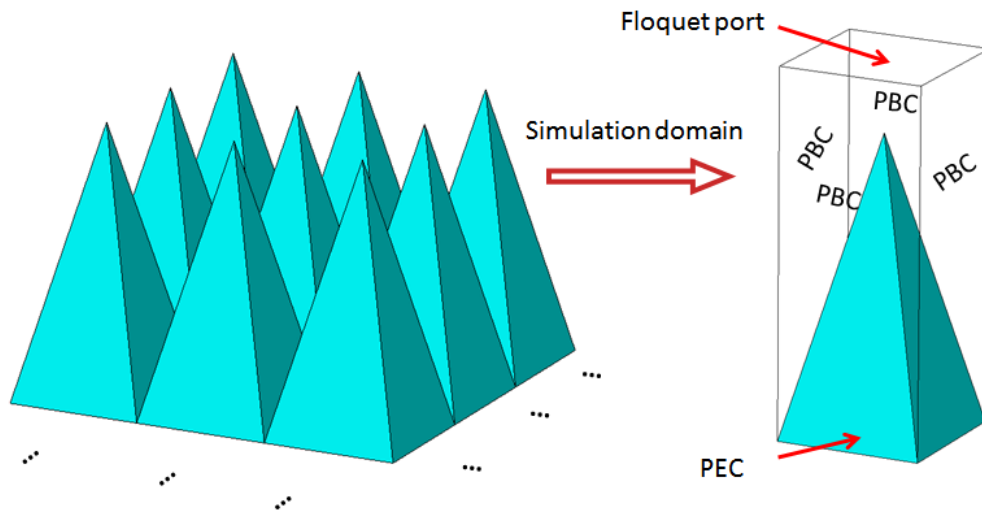


Fig. 3.8. The simulation model of the pyramid absorber.

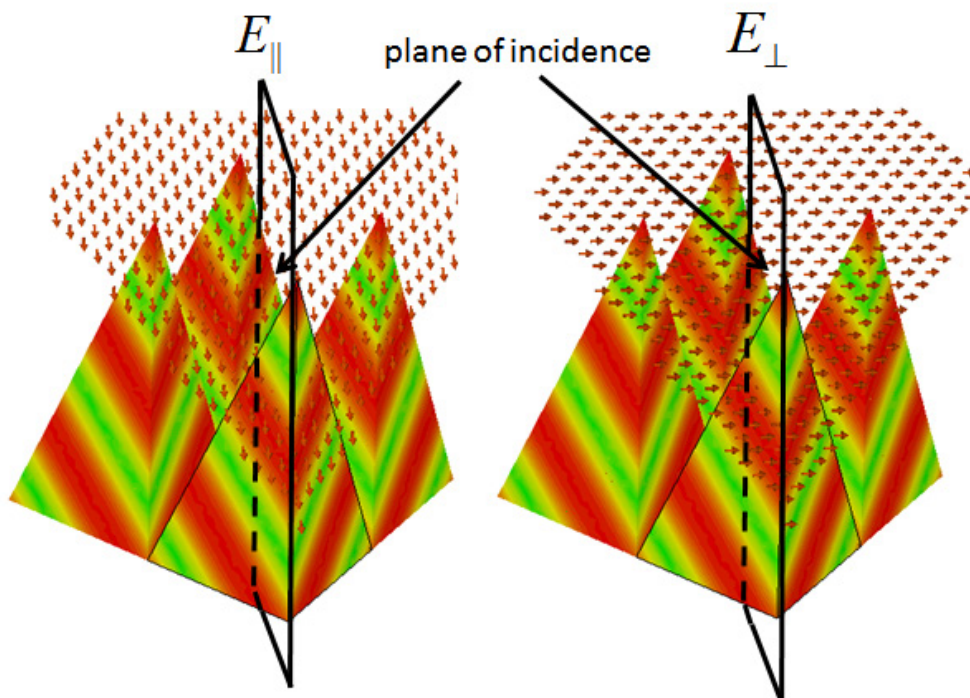


Fig. 3.9. Two orthogonal incident waves/modes.

A typical value of \bar{R} at 3 GHz is shown in Fig. 3.10 (magnitude) and Fig. 3.11 (phase) with different incident angles. A 5° step is used for both polar angle θ and azimuthal angle φ , for other values 2D interpolation is used, note that at the edge of the figure (large incident angle) the transition is not very smooth, this is because we have used the nearest available value to interpolate it. As can be seen, in Fig. 3.10, the cross-polarisation $R_{\perp\perp}$, $R_{\perp\parallel}$ are very small and $R_{\parallel\parallel}$, $R_{\perp\perp}$ are not sensitive to azimuthal angle φ since pyramid is a relatively symmetric shape. For small angles of θ , $R_{\parallel\parallel}$ and $R_{\perp\perp}$ are very small ($\sim -20\text{dB}$), when θ increase they decrease first and increase quickly with large θ angles. There is an optimised angle ($\theta \approx 60^\circ$) which has relatively small reflection coefficient compare with other

angles. Note this is not general conclusion; this angle depends on the shape and material property of the RAM.

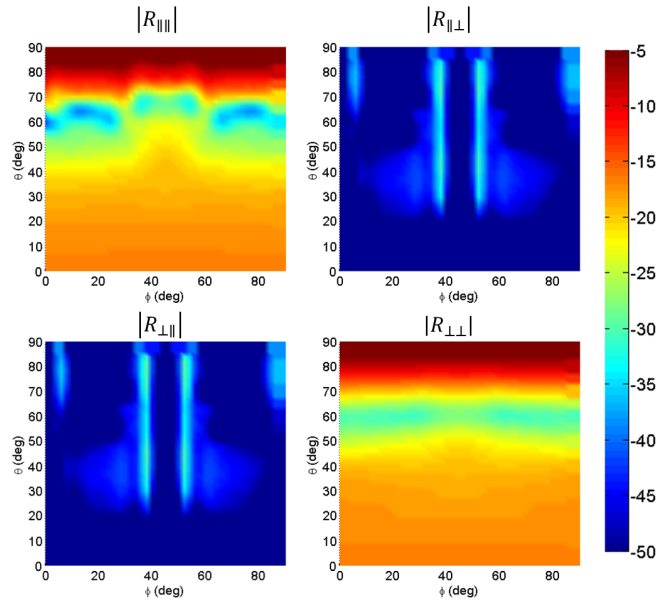


Fig. 3.10. Typical magnitude values of each element of \bar{R} , unit: dB.

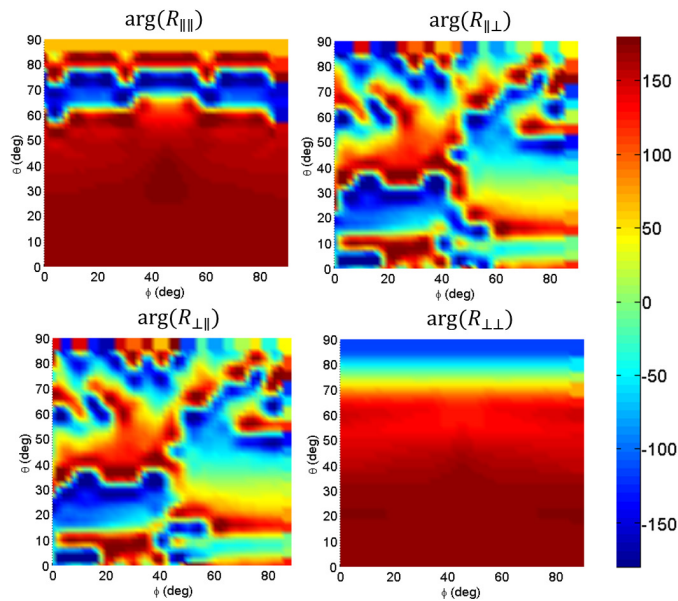


Fig. 3.11. Typical phase values of each element of \bar{R} , the phase reference plane is chosen at the bottom of the RAM, unit: degree.

The RAM layout definition process is the same as the boundary condition definition. The type index is used to mark the RAM type on each triangle. The rotation of RAM is considered by applying an angle offset to R_{ij} with $\Delta\varphi$ ($R_{ij}(\theta, \varphi + \Delta\varphi, f)$).

3.3.6 Forward Algorithm

In this section, the forward algorithm is detailed with the acceleration techniques. First, the rays are launched from the source point, and then reflected and intercepted by the monitor plane as shown in Fig. 3.4; finally, results from different reflection orders are superimposed to obtain the total E-field.

To start the ray tracing procedure, the initial value of the E-field and the cross-sectional area need to be known. The sphere surrounding the source point is divided into triangular patches as shown in Fig. 3.12. The vertices of the patch and the centre of sphere form a tetrahedron, as shown in Fig. 3.13. The initial value \vec{E}_0 is determined by the E-field on the sphere using 2D interpolation of $[E_{\theta mag}]$, $[E_{\phi phase}]$, $[E_{\phi mag}]$ and $[E_{\theta phase}]$, the radius of the sphere can be an arbitrary value, we use 3 m. The initial cross-sectional area is the triangular area A_0 which will be used to calculate SF later; different from the pyramid ray tube in [21], the tetrahedral ray tube is used. For a pyramid ray tube, the wave front is quadrilateral, there is a potential risk that the wave front will be distorted and self-intersected after reflecting by the model, but for the tetrahedral ray tube, the wave front is always kept the shape of triangle. After the ray and ray tube is traced, \vec{E} at the field point is determined using (2.28).

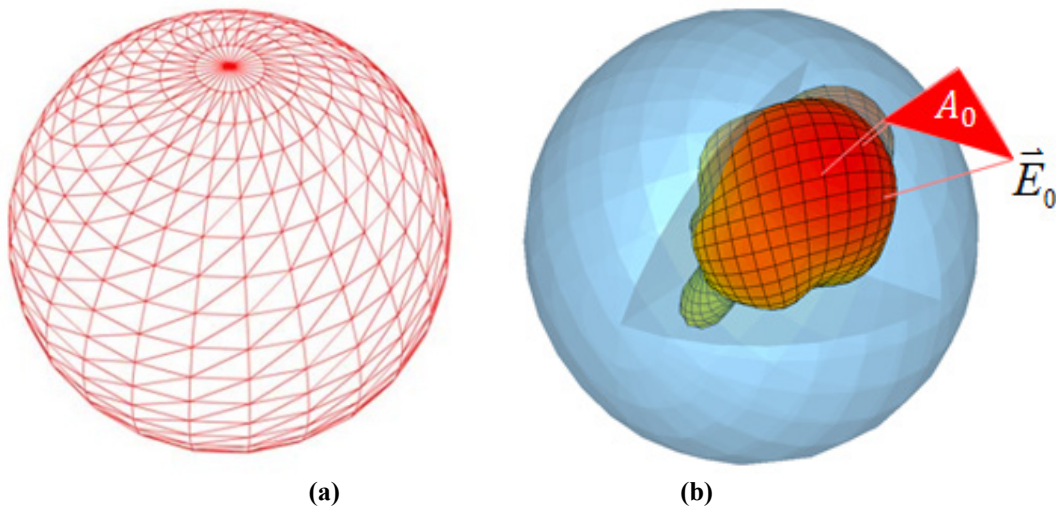


Fig. 3.12. (a) Sphere division and (b) initial values.

It is interesting to note that each tube shares the same vertex with its neighbour, but the SF can be different after the tube interacts with the model, this will make the E-field at the vertices ambiguous. To eliminate this ambiguity, we only use the vertices to carry the information of SF , the E-field is defined at the sample points inside each patch, as shown in Table 3.1, the tube triangle is divided into different orders, and the sample points are chosen to be the centre of each triangle.

After the initial value of the E-field is determined, rays need to be traced and recorded at the monitor plane. Since the adaptive octree has been built in the pre-processing part, we use the famous breadth-

first search (BFS) algorithm [22] to find the intersection point between the ray and the model. The searching process of BFS algorithm is given in Fig. 3.14.

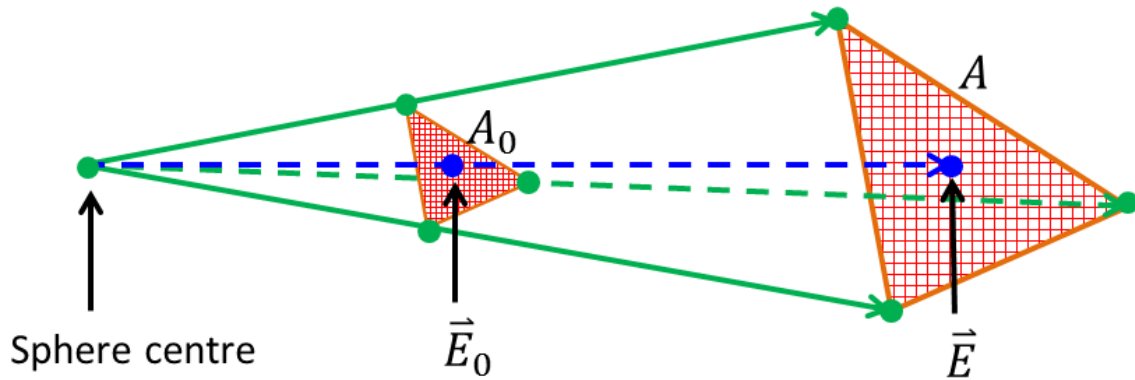
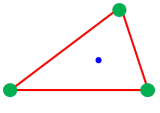
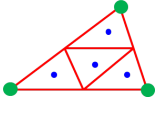
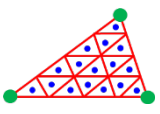
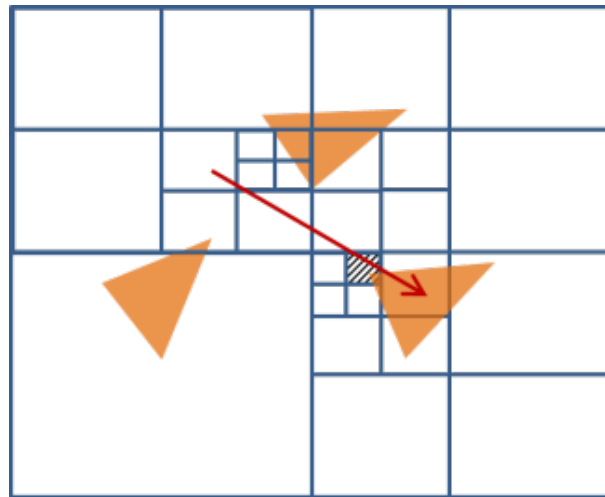


Fig. 3.13. E-field along the ray.

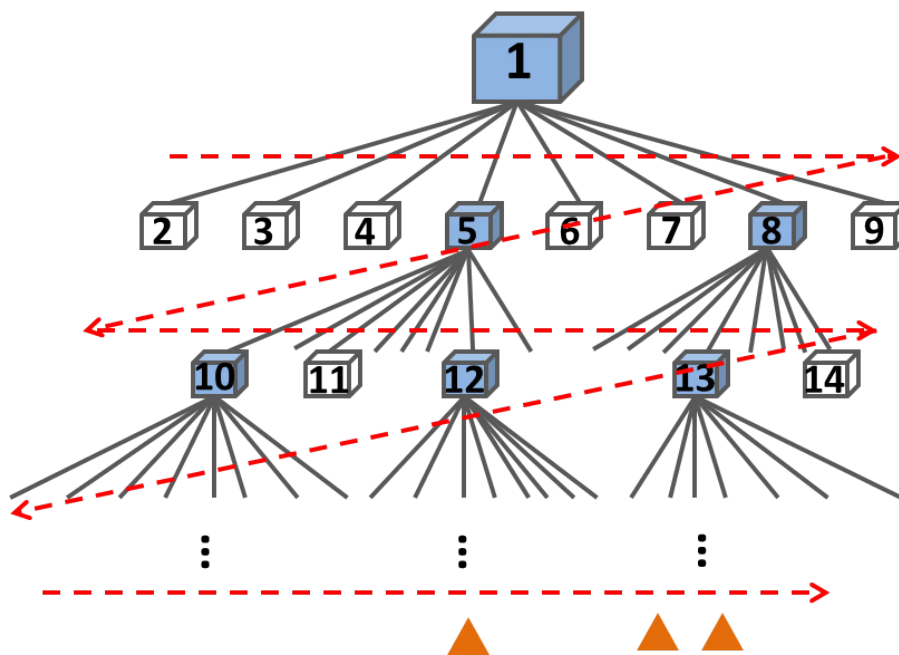
Table 3.1: Triangle with different division order

Division Order	Number of Sample Points	Triangle Division
1	1	
2	4	
3	16	
⋮	⋮	⋮
n	4^{n-1}	⋮

The model is divided into boxes with hierarchy, the ray can be launched from anywhere in the model. The boxes at the top level are first checked. If the ray intersects with it, check the sub level boxes. In the last level, the intersection between the ray and triangle is checked (the shaded area in Fig. 3.14(a)), because the ray-box intersection check is much faster than the ray-triangle check. Fig. 3.14(b) gives the searching direction and sequence number, the shaded area means the box containing triangles that may potentially intersect with the ray.



(a)



(b)

Fig. 3.14. BFS searching algorithm: (a) geometrical view, (b) hierarchical view.

It is important to note that: if the model is over-divided by octree (the octree level is too deep), the searching speed will deteriorate. The ray-triangle and the ray-box checking numbers with different octree depths are given in Fig. 3.15. The model contains 768 triangle meshes, 1000 random rays are launched to perform the benchmark. When the octree depth is 1, the model is not divided into an octree; the ray-box checking number is zero. As can be seen in Fig. 3.15, although deeper octree reduces the ray-triangle checking number, it increases the ray-box checking number thus more time is

wasted on the ray-box intersection check. That is the reason why the adaptive octree has been proposed.

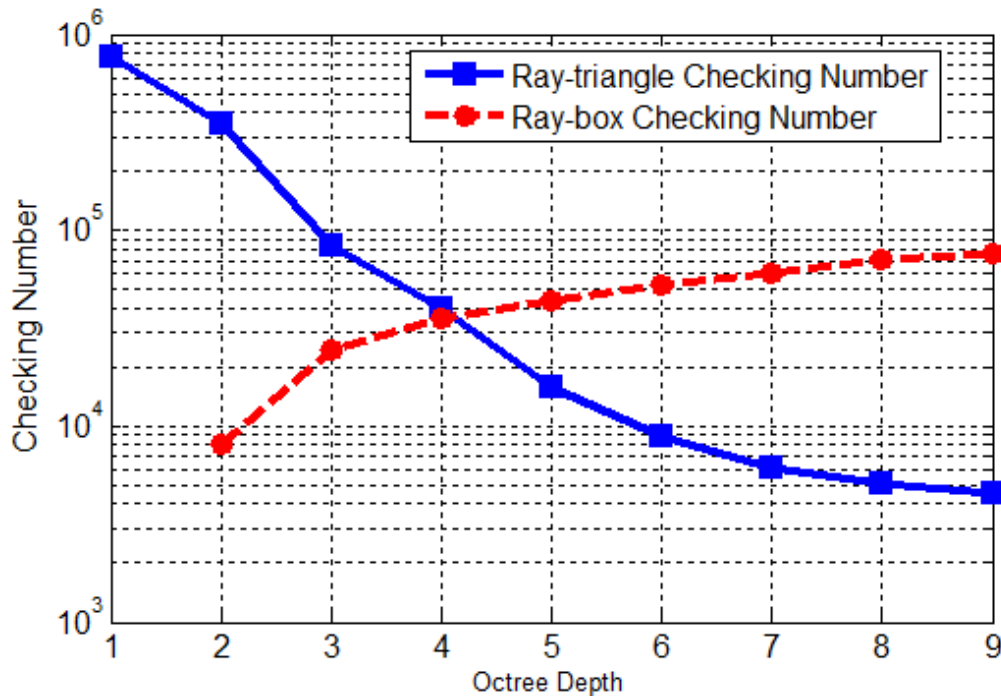


Fig. 3.15. Ray-triangle and ray-box checking numbers with different octree depth.

Once the intersection point between the ray and the triangle is found, equation (2.29) is used to calculate the reflected E-field and update the initial value and the wave front area A_0 for the next trace. Because the incident angle can be of an arbitrary value and the frequency of interest may not be exactly the same as the sample frequency in the full numerical model of RAM (where a set of frequencies are used), 1D and 2D interpolation are used to obtain the reflection coefficient value. First, each matrix in $\bar{\bar{R}}$ is interpolated with the frequency of interest, since each element in the matrix needs to be interpolated, it is time consuming to do it in the ray tracing loop. This procedure can be moved out of the ray tracing loop and it only needs to be calculated once for each frequency of interest. Then, the 2D angle interpolation is applied to each matrix in $\bar{\bar{R}}$. Considering the magnitude and phase, this makes only eight 2D interpolations for each ray-triangle intersection, which is much faster than the traditional RAM model.

One of the advantages of GO is that it is easy to parallelise. We have already used the octree algorithm to accelerate the intersection checking process. Further acceleration techniques are also considered, both the distributed computing and multithreading techniques are employed to divide the sphere in Fig. 3.12(a) into sub regions; rays in different sub regions are traced simultaneously in a different computing engine, and finally the results are combined. Two methods are used to reduce the

number of the total rays: one method is to set a threshold for the E-field value (e.g. -30 dB of the peak value). The rays below the threshold will be skipped. Another method is to limit the ray launching region; we rarely need to consider the rays close to the polar points in Fig. 3.12(a). By combining these two methods the speed can be improved significantly.

After the monitor plane is defined, the plane needs to be discretized into meshes. The mesh size is normally chosen $\leq \lambda/10$ (λ is the wavelength of the frequency of interest). Fig. 3.16(a) gives the procedure for the value assignment in each tube: the values on each grid are first initialised as zero, after the ray tube is intercepted by the monitor plane, the grid points in the tubes are checked, the distance between the grid points and the sample points are calculated, the E-field of the nearest sample point is chosen to be the value of the grid point. Fig. 3.16(b) shows the superposition of the field values between two tubes, the field value on the grid points shared by different tubes are superimposed.

Finally, the E-field from different orders needs to be superimposed to obtain the total value.

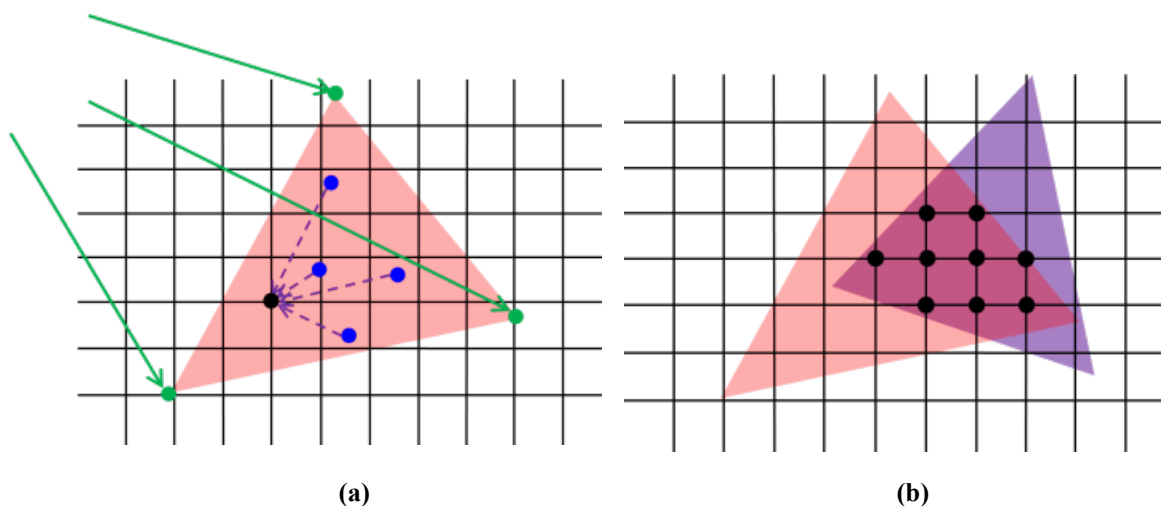


Fig. 3.16. Superposition of the E-field in different tubes: (a) value assignment in each tube, (b) value update for the grid points shared by different tubes.

3.3.7 Inverse Algorithm

Different from launching the rays in all directions in the forward algorithm, the inverse algorithm finds the path that connects the source point and the field point which is called path finding. After the paths are found and saved, the initial value and the reflection coefficient can be obtained in the same way as in the forward algorithm, the final E-field with different orders can also be easily superimposed.

Each triangle has a unique index number; the possible paths to be checked are shown in Fig. 3.17. For the rays reflected once from source point (S) to field point (F), the possible paths are S -1- F , S -2- F , S -3- F and S -4- F . As can be seen in Fig. 3.17(a), only 2 paths are practical (visible), other images are invisible because the intersection points are outside the triangle. The same thing happens to the 2nd order rays in Fig. 3.17(b), the number of paths to be checked becomes 12. Generally, for the model with N triangles, the number of M th order paths to be checked is $N(N-1)^{M-1}$ [9], [23]. It is important to note that without any acceleration strategy, it could be very time consuming to check the images one by one when N and M are large numbers.

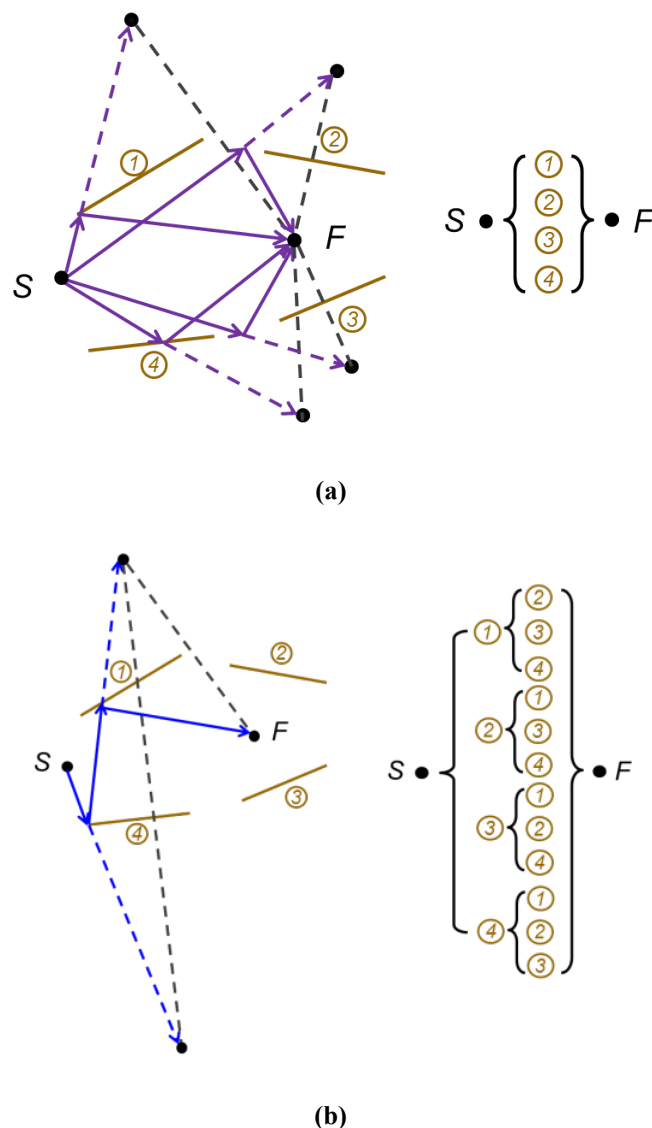


Fig. 3.17. Path finding in the inverse algorithm: (a) paths with the 1st order, (b) paths with the 2nd order.

Parallelisation is used as shown in Fig. 3.18. The engine can be a distributed computer or a thread in a single computer. The whole path tree is split into different parts which are checked by different engines simultaneously.

An additional strategy which takes advantage of the chamber shape is proposed and called convex acceleration. In topology, the 3D model can be divided into two categories: the concave and the convex as shown in Fig. 3.19.

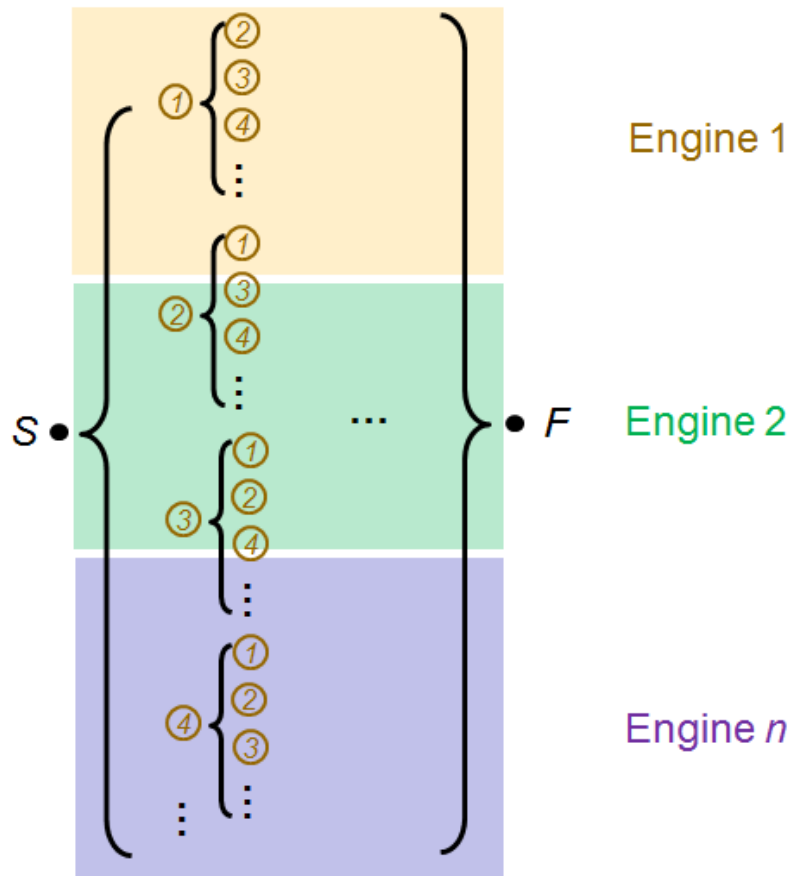


Fig. 3.18. Parallel path finding.

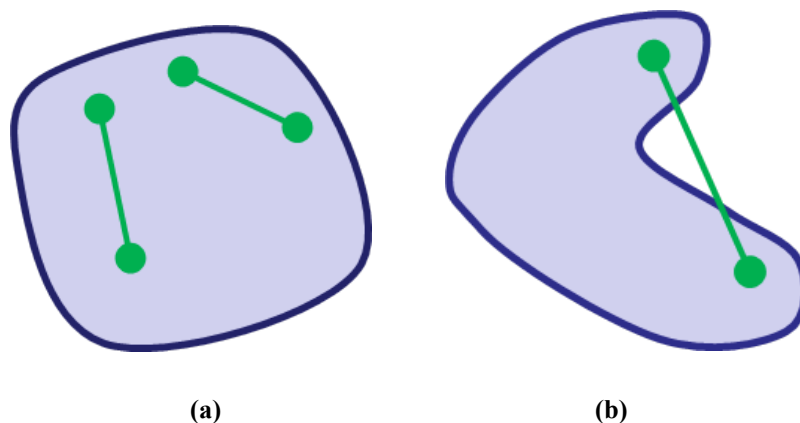


Fig. 3.19. Topology of the model: (a) convex shape, (b) concave shape.

For a convex shape, all line segments connecting any pair of points are inside the shape. For a concave shape, there is a possibility that the line segments will be intercepted by the model itself. This offers an opportunity to accelerate the path finding process. Generally speaking, each path needs to be

checked to make sure it is not intercepted by the other triangles of the model, but for a convex model, this checking procedure is not necessary since most of the chambers are convex shape. The benchmark has been performed to validate the convex acceleration: for a model with 116 triangles, 1 thread is used, and only the 1st order reflection is considered, we found that the speed with convex acceleration is 28 times faster than the general algorithm.

3.3.8 Post Processing

The post processing is to process the results and calculate the figures of merit such as the SA in a fully anechoic chamber, or NSA in a semi-anechoic chamber, SVSWR and FU. All of these values are extracted from the E-field distribution in the post processing part. If the transmitting (Tx) antenna is well matched and the input power is normalised to 1 W, the NSA value can be calculated by using [24]

$$NSA(dB) = 46.76 + G - 20\log f - 20\log E_{max} \quad (3.7)$$

where G is the gain of the Tx antenna in free space in dBi, f is the frequency of interest in MHz, E_{max} is the maximum E-field value in V/m measured by the receiving (Rx) antenna, when the height is scanning from 1 m to 4 m.

The site attenuation is defined as the ratio of the power input to a matched and balanced lossless tuned dipole radiator to that at the output of a similarly balanced matched lossless tuned dipole receiving antenna. *Normalise* means the site attenuation is normalised to the transmitting and receiving antenna factors (chapter 5 in [24]). The definitions of SVSWR and FU can be found in [25], [26].

For a semi-anechoic chamber, the NSA is required to be in the range of ± 4 dB of the values given in the standard [25], the SVSWR is required to be ≤ 6 dB and the FU is required to be in the range of 0 dB to +6 dB for 75% of the sample points for each frequency (shown in Table 3.2).

Table 3.2: Acceptability Criterion

Test Performed	Acceptability Criterion	Reference
NSA	± 4 dB	[25]
SVSWR	≤ 6 dB	[25]
FU	-0 dB, +6 dB for 75%	[26]

The cost of RAM used in the chamber can be obtained by

$$Cost_{RAM} = \sum Area_i \times Price_i \quad (3.8)$$

which is the summation of the price for all the RAMs used in the chamber, where i means the type index of the RAM. The cost is a vital parameter for a business, especially when the chamber is large. The proposed solution can optimise a chamber for given specs.

3.4 Summary

In this chapter, the software implementation of the CAD tool has been detailed. Two different algorithms have been developed: a forward algorithm and an inverse algorithm. They share the same pre-processing part, but different post processing part. The complexity and parallelisation have also been discussed respectively. The forward algorithm is more efficient for P2A problems while the inverse algorithm is more suitable for P2P problems. The corresponding acceleration strategies have been proposed, developed and discussed in details. The adaptive octree has been proposed for the forward algorithm, and a new acceleration strategy named convex acceleration has also been proposed for the inverse algorithm. Both have improved the efficiency significantly.

We have also borrowed the philosophy from software engineering: considering the RAM and the antenna as objects and the properties (reflection coefficient, position, radiation pattern, *etc.*) are encapsulated. This approach does not require the antenna and RAM detailed information which is normally not available. It provides a seamless connection between the micro level and the macro level designs, which makes the design procedure systematically. Although compared with the traditional analytical model, the proposed RAM model requires more memory to save it (10 MB/each type, it is still very small for computers nowadays) which is a trade-off of the proposed approach.

3.5 References

- [1] Available: [https://en.wikipedia.org/wiki/STL_\(file_format\)](https://en.wikipedia.org/wiki/STL_(file_format)).
- [2] A. S. Glassner, *An Introduction to Ray Tracing*, Morgan Kaufmann, 1989.
- [3] C. Saeidi, A. Fard and F. Hodjatkashani, "Full three-dimensional radio wave propagation prediction model," *IEEE Trans. Antennas Propagat.*, vol. 60, no. 5, pp. 2462–2471, May 2012.
- [4] K. Jin, T. Suh, S. Suk, B. Kim and H. Kim "Fast ray tracing using a space-division algorithm for RCS prediction," *Journal of Electromagnetic Waves and Applications*, vol. 20, no. 1, pp. 119-126, 2006.

-
- [5] Y. Tao, H. Lin and H. Bao, "Kd-tree based fast ray tracing for RCS prediction," *Progress In Electromagnetics Research, (PIER)*, vol. 81, pp. 329-341, 2008.
- [6] M. Ohta and M. Maekawa, "Ray coherence theorem and constant time ray tracing algorithm," *Computer Graphics*, pp. 303-314, 1987.
- [7] J. Bang and B. Kim "Time consumption reduction of ray tracing for RCS prediction using efficient grid division and space division algorithms," *Journal of Electromagnetic Waves and Applications*, vol. 21, no. 6, pp. 829-840, 2007.
- [8] H. Meng, "Acceleration of asymptotic computational electromagnetics physical optics – shooting and bouncing ray (PO-SBR) method using CUDA," M.S. thesis, Dept. Electrical and Computer Eng., University of Illinois at Urbana-Champaign., Illinois, USA, 2011.
- [9] J. W. McKown and R. L. Hamilton , "Ray tracing as a design tool for radio networks," *IEEE Network*, vol. 5, no. 6, pp. 27-30, Nov. 1991.
- [10] V. Kubytyski, B. Sapoval, G. Dun and J. Rosnarho, "Fast optimization of microwave absorbers," *Microwave and Optical Technology Letters*, vol. 54, no. 11, pp. 2472-2477, Nov. 2012.
- [11] E. F. Kuester and C. L. Holloway, "A low-frequency model for wedge or pyramid absorber arrays-I: theory," *IEEE Trans. Electromagnetic Compatibility*, vol. 36, no. 4, pp. 300-306, Nov. 1994.
- [12] C. L. Holloway and E. F. Kuester, "A low-frequency model for wedge or pyramid absorber arrays-II: computed and measured results," *IEEE Trans. Electromagnetic Compatibility*, vol. 36, no. 4, pp. 307-313, Nov. 1994.
- [13] A. Khajepour and S. A. Mirtaheri, "Analysis of pyramid EM wave absorber by FDTD method and comparing with capacitance and homogenization methods," *Progress In Electromagnetics Research Letters*, vol. 3, pp. 123-131, 2008.
- [14] K. Elmahgoub, F. Yang, A. Z. Elsherbeni, V. Demir and J. Chen, "FDTD analysis of periodic structures with arbitrary skewed grid," *IEEE Trans. Antennas Propagat.*, vol. 58, no. 8, pp. 2649–2657, Aug. 2010.
- [15] W. Sun, K. Liu and C. A. Balanis, "Analysis of singly and doubly periodic absorbers by frequency-domain finite-difference method," *IEEE Trans. Antennas Propagat.*, vol. 44, no. 6, pp. 798–805, Jun. 1996.
- [16] Y. Jiang and A. Q. Martin, "The design of microwave absorbers with high order hybrid finite element method," in *IEEE Antennas and Propagation Society International Symposium*, Orlando, 1999, vol. 4, pp. 2622–2625.
- [17] R. Janaswamy, "Oblique scattering from lossy periodic surfaces with application to anechoic chamber absorbers," *IEEE Trans. Antennas Propagat.*, vol. 40, no. 2, pp. 162–169, Feb. 1992.

-
- [18] N. Marly, B. Baekelandt, D. D. Zutter and H. F. Pues, "Integral equation modeling of the scattering and absorption of multilayered doubly-periodic lossy structures," *IEEE Trans. Antennas Propagat.*, vol. 43, no. 11, pp. 1281–1287, Nov. 1995.
- [19] V. Kubytzkyi, B. Sapoval, G. Dun and J. Rosnarho, "Fast optimization of microwave absorbers," *Microwave and Optical Technology Letters*, vol. 54, no. 11, pp. 2472-2477, Nov. 2012.
- [20] IEEE Std 1128-1998: IEEE Recommended Practice for Radio-Frequency (RF) Absorber Evaluation in the Range of 30 MHz to 5 GHz, IEEE Standard, Apr. 1998.
- [21] C. Yang, B. Wu and C. Ko "A ray-tracing method for modeling indoor wave propagation and penetration," *IEEE Trans. Antennas Propagat.*, vol. 46, no. 6, pp. 907–919, Jun. 1998.
- [22] T. H. Cormen, C. E. Leiserson, R. L. Rivest and C. Stein, *Introduction to Algorithms*, 3rd Ed, The MIT Press, 2009.
- [23] M. F. Catedra, J. Perez, F. Saez de Adana and O. Gutierrez, "Efficient ray-tracing techniques for three-dimensional analyses of propagation in mobile communications: application to picocell and microcell scenarios," *IEEE Antennas and Propagation Magazine*, vol. 40, no. 2, pp. 15-28, Apr. 1998.
- [24] V. P. Kodali, *Engineering Electromagnetic Compatibility: Principles, Measurements, Technologies, and Computer Models*, 2nd Ed, New York: Wiley-IEEE Press, 2001
- [25] CISPR 16-1-4: Specification for radio disturbance and immunity measuring apparatus and methods - Part 1-4: Radio disturbance and immunity measuring apparatus - Antennas and test sites for radiated disturbance measurements, IEC Standard, Ed 3.1, Jul. 2012.
- [26] IEC 61000-4-3: Electromagnetic compatibility (EMC) - Part 4-3: Testing and measurement techniques - Radiated, radio-frequency, electromagnetic field immunity test, IEC Standard, Ed 3.1, Apr. 2008.

Chapter 4: Anechoic Chamber Characterisation and Verification

4.1 Introduction

The anechoic chamber may have various forms in applications, such as tapered chambers [1], compact chambers with reflectors [2], double horn chambers [3], [4], *etc.* There are many ways and parameters to characterise the chamber performance: the site attenuation (SA, or normalised SA), site voltage standing wave ratio (SVSWR) and field uniformity (FU) are the three key parameters which are normally employed in the chamber related standards [5], [6] to evaluate the chamber performance.

In this chapter, NSA, SVSWR and FU measurement methods are introduced first, and then we compare the measurement results and the simulation results obtained from our developed CAD tool. Discussions and conclusions are also given.

4.2 NSA Measurement and Simulation

The measurement is performed in a semi-anechoic chamber (ground plane is metallic, walls and ceilings are lined with RAMs) and a schematic plot is shown in Fig. 4.1. The measurement distance is can be 3 m, 10 m or 30 m, depending on the relevant standards and the size of the object under test.

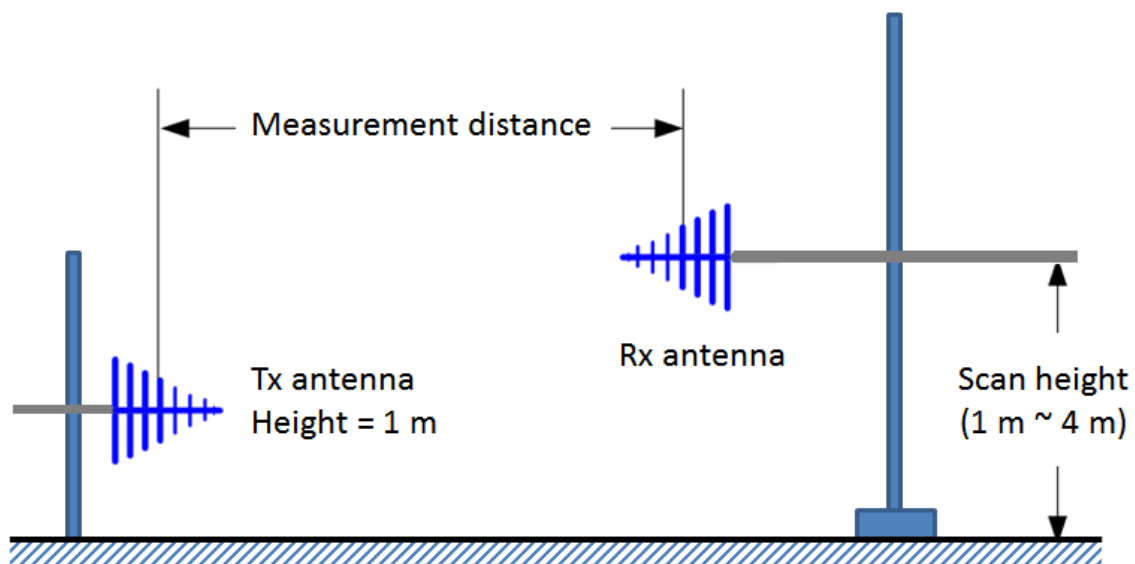


Fig. 4.1. NSA measurement setup.

In the measurement, the Tx antenna is connected to a signal generator and the Rx antenna is connected to a spectrum analyser (or a voltage meter). All measurements are performed in 50 Ohm

system. The Rx antenna is scanned in height from 1m to 4m (could be different for different type of antenna [5]), the maximum signal V_{site} is measured. Then the reading of V_{direct} is taken with two coaxial cables disconnected from the two antennas and connected to each other via an adapter. The NSA value can be obtained using [5], all units are in dB.

$$NSA = V_{direct} - V_{site} - AF_T - AF_R - \Delta AF_{TOT} \quad (4.1)$$

where AF_T is the antenna factor of the transmitting antenna (dB/m), AF_R is the antenna factor of the receiving antenna (dB/m), ΔAF_{TOT} is the mutual impedance correction factor (dB). For a semi-anechoic chamber, the NSA value is required to be in the range of ± 4 dB of the values given in the standard [5].

The NSA value can also be obtained from the E-field. If the transmitting antenna is well-matched and the input power is normalised to 1 W, the NSA value can be calculated using [7]

$$NSA(dB) = 46.76 + G - 20 \log f - 20 \log E_{max} \quad (4.2)$$

where G is the gain of the Tx antenna in free space in dBi, f is the frequency of interest in MHz, E_{max} is the maximum E-field value in V/m measured by the receiving antenna when the height is scanning from 1 m to 4 m. (4.1) and (4.2) are equivalent, in practice, (4.1) is easy to use since the loss of cables can be corrected by measuring V_{direct} , but in simulation, (4.2) is more convenient since it is easy to force/normalise the radiation power to 1 W for all frequencies.

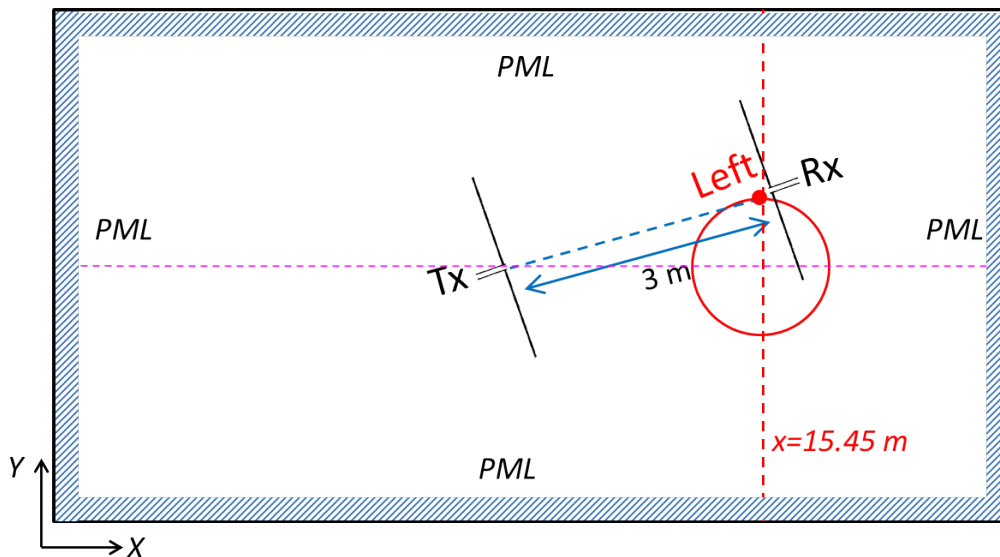


Fig. 4.2. A cross-section (horizontal) view of an ideal semi-anechoic chamber, the ground plane is set as PEC where other planes are set as PML.

We first simulate an ideal semi-anechoic chamber (the RAMs absorb waves perfectly) and then move on to a real scenario. A semi-anechoic chamber as shown in Fig. 4.2 is used for evaluation. The size

of the chamber is $22 \text{ m} \times 13.5 \text{ m} \times 8 \text{ m}$ ($L \times W \times H$). The Rx antenna is positioned at the left side in the test region, the Tx antenna is 3 m away from the Rx antenna, the height is 2 m, the coordinate is (12.62, 6.745, 2). Both Rx and Tx antennas are half-wave dipoles. All the boundary conditions are set as PML except the ground plane (set as PEC). A monitor plane is set at $x = 15.45 \text{ m}$ across the centre of the test region (red circle) to record the E-field.

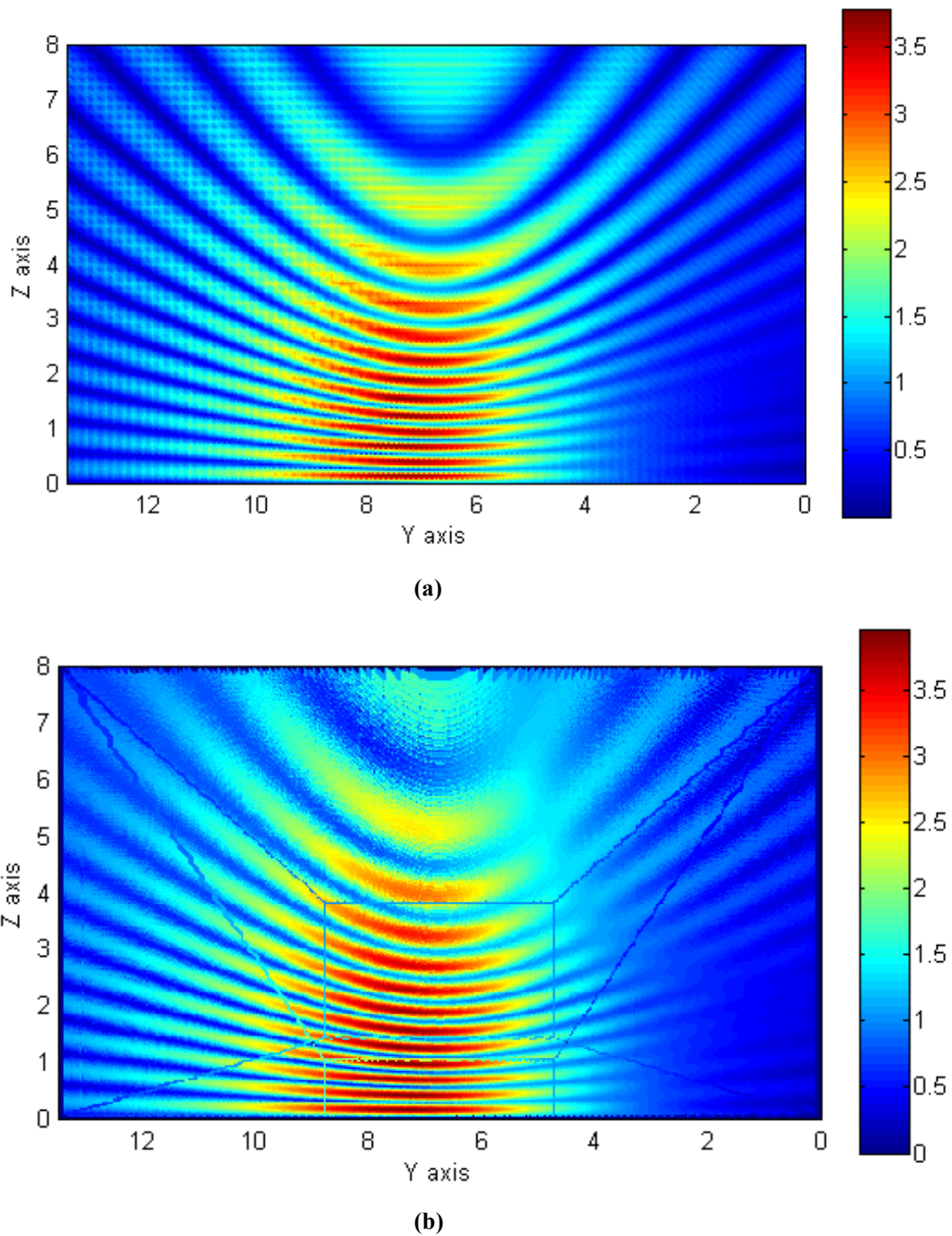


Fig. 4.3 Total E-field in the semi-anechoic chamber on the monitor plane at 1 GHz: (a) obtained by using MoM method, (b) obtained by using the forward algorithm, unit: V/m.

Since this is a perfect half-space problem, and the Green's function for the half space is well-known, only the Tx antenna needs to be discretised and the MoM is used to simulate it. The far-field data is exported to FACET to predict the chamber performance; the results obtained from FACET and MoM method are compared to verify the accuracy of the proposed solution. The magnitude of the total E-field on the monitor plane at 1 GHz is shown in Fig. 4.3. As can be seen, they are in good agreement.

The small difference between Fig. 4.3(a) and Fig. 4.3(b) is due to the mutual coupling of the image antenna (because of the ground plane). The mutual coupling between the Tx antenna and its image was considered in MoM, but not in FACET. A unique feature of GO is that the fields with different order of reflection can be viewed separately as shown in Fig. 4.4. The superposition of the zero order and first order E-field makes the total E-field in Fig. 4.3(b). It is important to note that when the ray tubes hit the corners of the chamber, the wave front distorts drastically which may produce unreasonable values for the further rays, thus these ray tubes are filtered and may result in small errors.

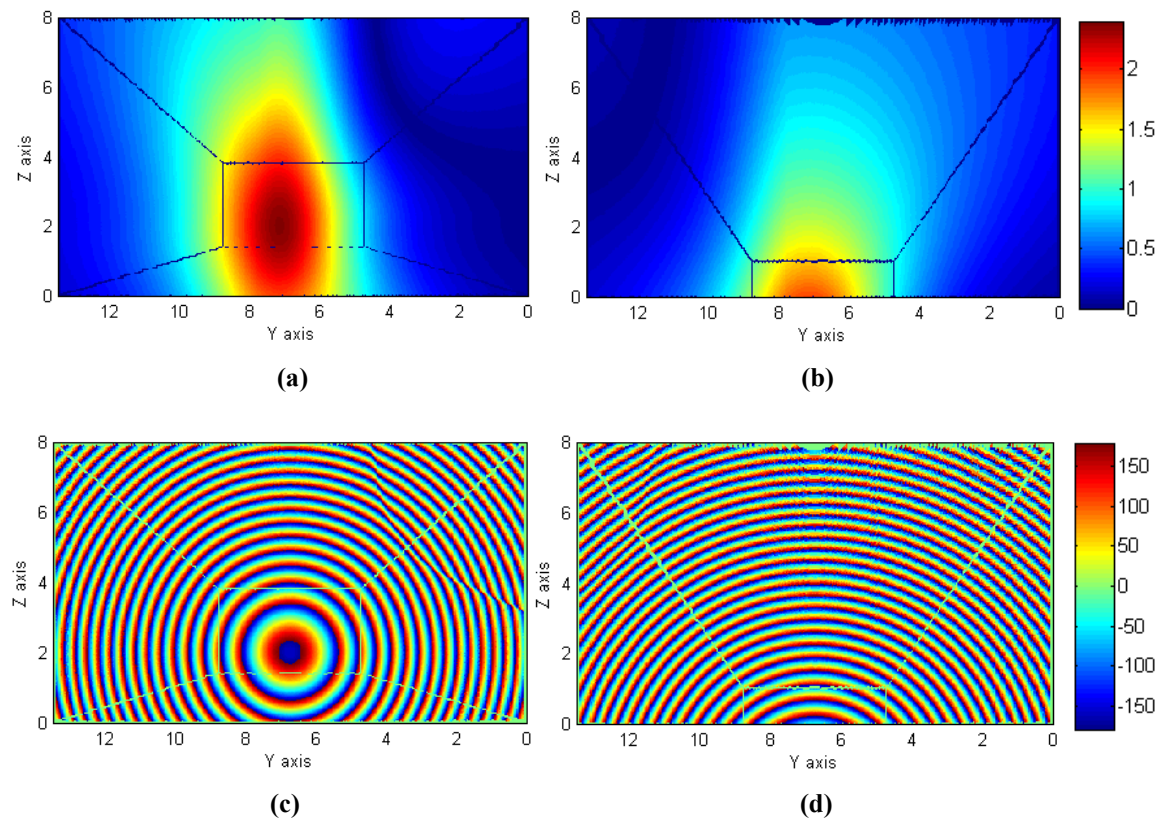


Fig. 4.4 *y*-polarized E-field with different reflective orders: (a) zero order magnitude, (b) first order magnitude, unit: V/m, (c) zero order phase, (d) first order phase, unit: degree.

By using the inverse algorithm, the paths with less than the 2nd orders are shown in Fig. 4.5, higher order rays do not exist for the ideal semi-anechoic chamber. Actually only the zero and first order rays contribute to the field superposition, higher order rays are absorbed by the PML boundary.

The E-field values are extracted with the height scanning from 0 ~ 4 m at the centre of the test region. Both the forward and inverse algorithms are used; results are compared and shown in Fig. 4.6. It can be seen that all the results are in good agreement except the height is close to the ceiling, this is because for the forward algorithm, the ray tubes hit the corners are filtered, the values become inaccurate when close to the corner (the height is 8 meters).

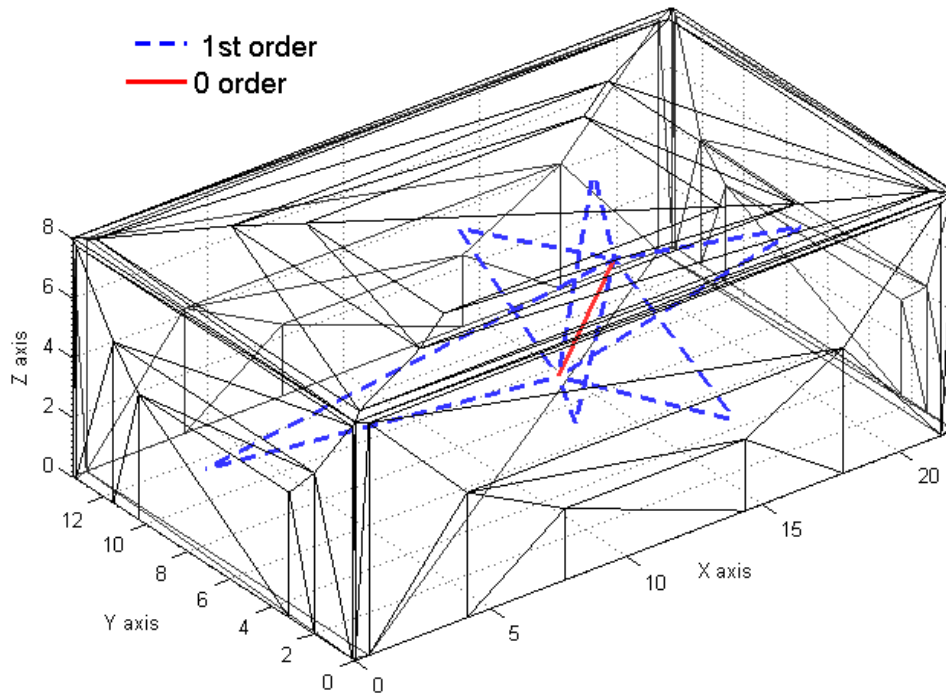


Fig. 4.5 Paths connect the source point and the field point with different orders: 1 ray with zero order and 6 rays with the first order.

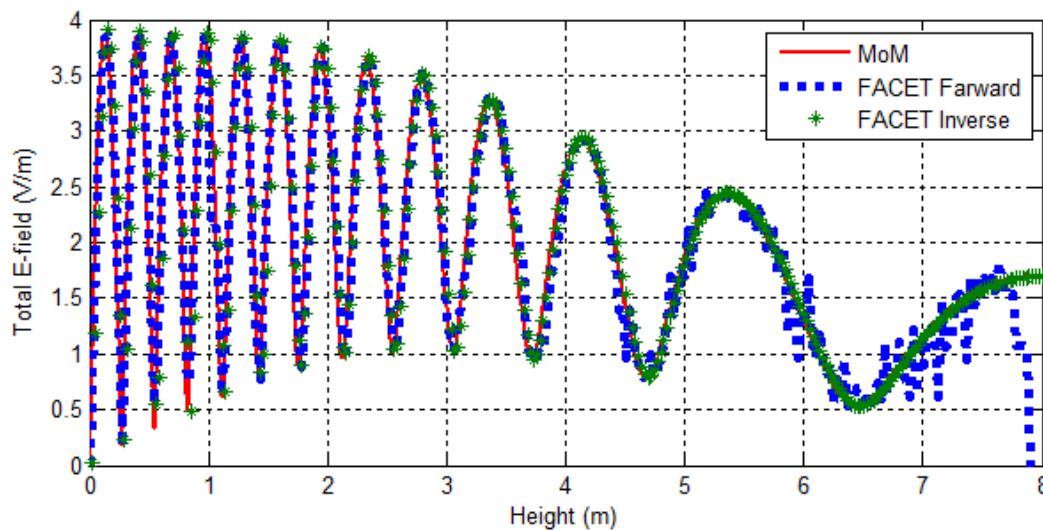


Fig. 4.6 Total E-field comparison by using different methods.

After the E-field values are extracted, (4.2) is used to obtain the NSA values. The same procedure is repeated for each frequency of interest, Fig. 4.7 gives the results obtained from the CISPR standard [5], the MoM method and FACET. It is important to note that when we use the half-wave dipole antenna, mutual coupling correction factors should be used. As can be seen in Fig. 4.7, all the curves agree well with each other. The difference (mainly at lower frequencies) between the MoM and the other two is mainly due to the non-typical balun of the Tx antenna as already stated in [5]. Also GO is a high frequency method: at lower frequencies, the accuracy of the proposed GO-based method is reduced.

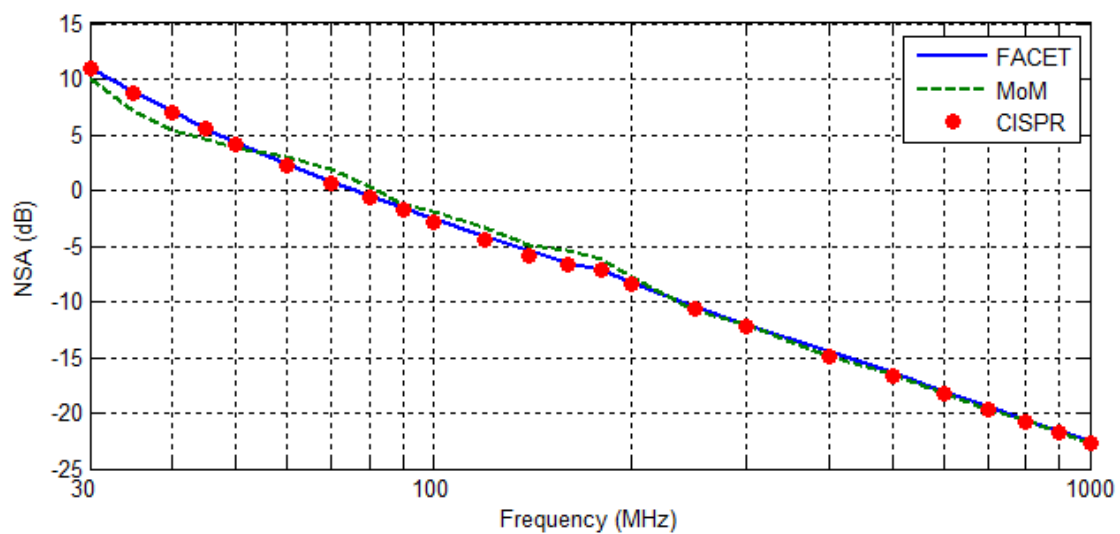
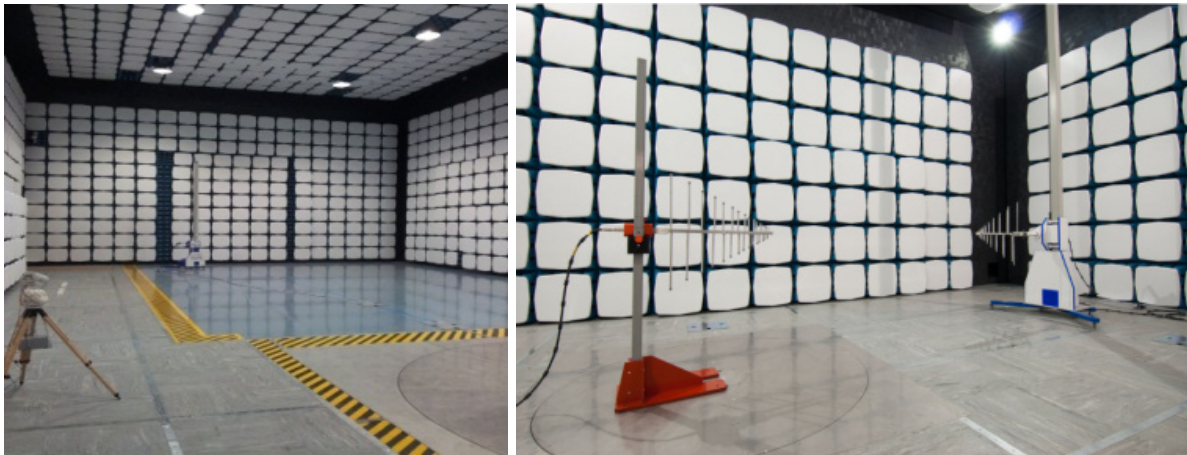


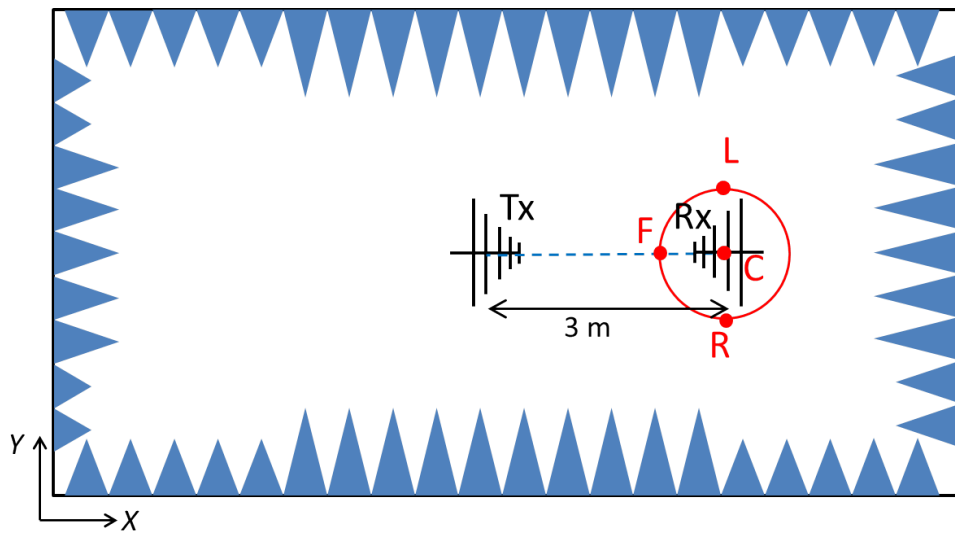
Fig. 4.7 NSA comparison of the reference semi-anechoic chamber.

For this scenario, the overall simulation time using FACET for each polarisation is less than 1 minute with a standard PC. The results validate the proposed method with confidence. It should be noted that for a practical chamber it is not realistic to simulate it using MoM (a huge amount of memory requirement and complex material definition which is sometimes not known). Next we compare the simulation and measurement results for a practical semi-anechoic chamber.

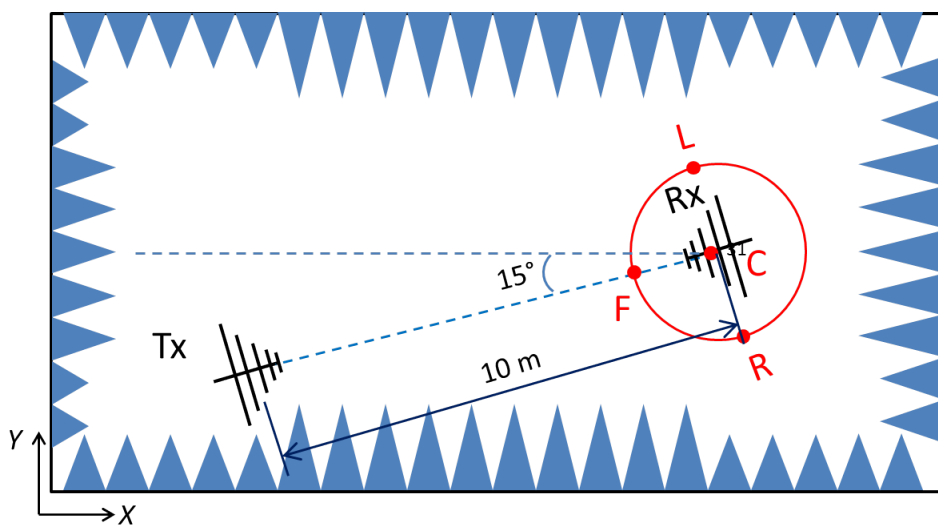
For measurement comparison, a semi-anechoic chamber is selected as shown in Fig. 4.8. The size is $22 \text{ m} \times 13.5 \text{ m} \times 8 \text{ m}$ ($L \times W \times H$). Both 3 m and 10 m NSA values are measured following the standard steps in [5]. Four different locations of the Rx antenna in the turntable region are tested: left (L), right (R), front (F) and centre (C). For each location, there are two height values and two polarisations for the Tx antenna. These make $2 \times 2 \times 4 = 16$ cases for each distance as shown in Table 4.1. A biconical antenna is used in the frequency range of 30 MHz ~ 200 MHz and a log-periodic antenna (LPDA) is used in the frequency range of 200 MHz ~ 1 GHz. For the 10 m case, the Tx antenna is chosen to be 15° off the axis to test a more general scenario.



(a)



(b)



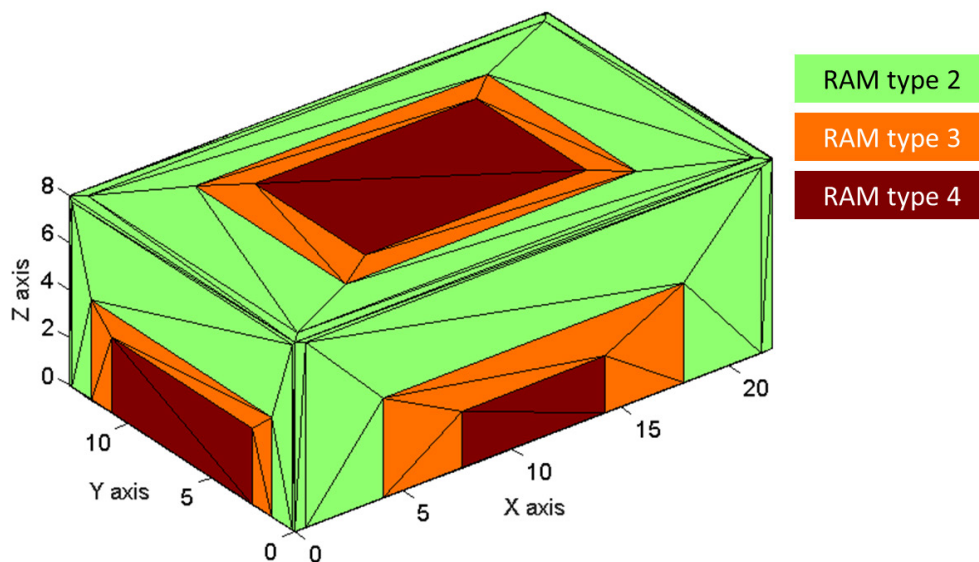
(c)

Fig. 4.8. NSA measurement scenario: (a) chamber under test (pictures from Rainford EMC Systems Ltd), (b) 3 m NSA, (c) 10 m NSA.

Table 4.1: NSA Test Scenarios

Polarisation	Tx Height	Rx Location
Horizontal (H)	Lower (L)	Left (L)
		Right (R)
Vertical (V)	Upper (U)	Front (F)
		Centre (C)

The layout of the RAM is given in Fig. 4.9, the colour represents the RAM type. Each RAM was characterised and the complex reflection coefficients for different angles were obtained. The magnitude of the normal reflection coefficient is shown in Fig. 4.10. The paths with different orders for one of the receiving points are shown in Fig. 4.11. 100 sample points are used for the 1 m to 4 m height scanning. The rays up to the 2nd order are considered, and the convex acceleration is used. For each scenario, the resource consumption using the inverse algorithm is shown in Table 4.2. The resource consumption using the traditional FDTD has also been estimated and given in the table. It can be seen that the full wave method takes 8 hours and 10 GB memory to complete the simulation and is not a good choice for a chamber designer. For the frequency higher than 1 GHz or a larger chamber the problem will become even worse.

**Fig. 4.9 Discretised chamber model with different RAMs (represented by the colours in different regions).**

The measurement results for the 3 m NSA values deviated from the CISRP standard [5] are shown in Fig. 4.12(a) ~ Fig. 4.12(d), the simulation results using FACET are shown in Fig. 4.12(e) ~ Fig. 4.12(h). The measured and simulated results agree well with each other, the spikes in the measurement results may be due to the unexpected scatters from the complex environment (cables,

masts, imperfect ground); Fig. 4.13 gives the measured and simulated 10 m NSA deviation. It can be seen that they are correlated; the peak value may have a slight shift in frequency which is due to the phase error at lower frequencies (mutual coupling, near-field effect). The differences between the simulation and measurement values are within ± 2 dB.

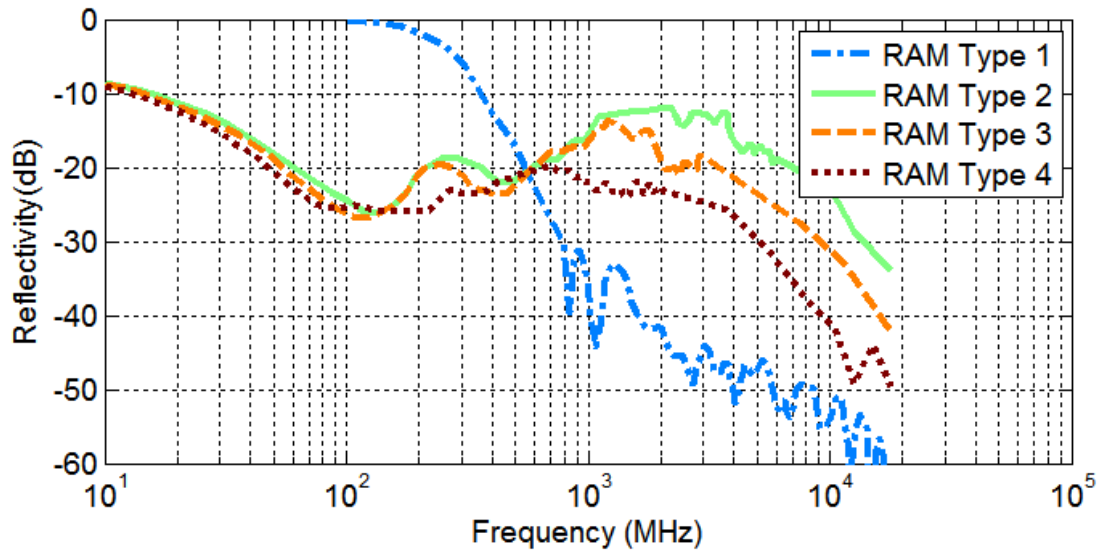


Fig. 4.10 Normal reflection coefficient for different types of RAM.

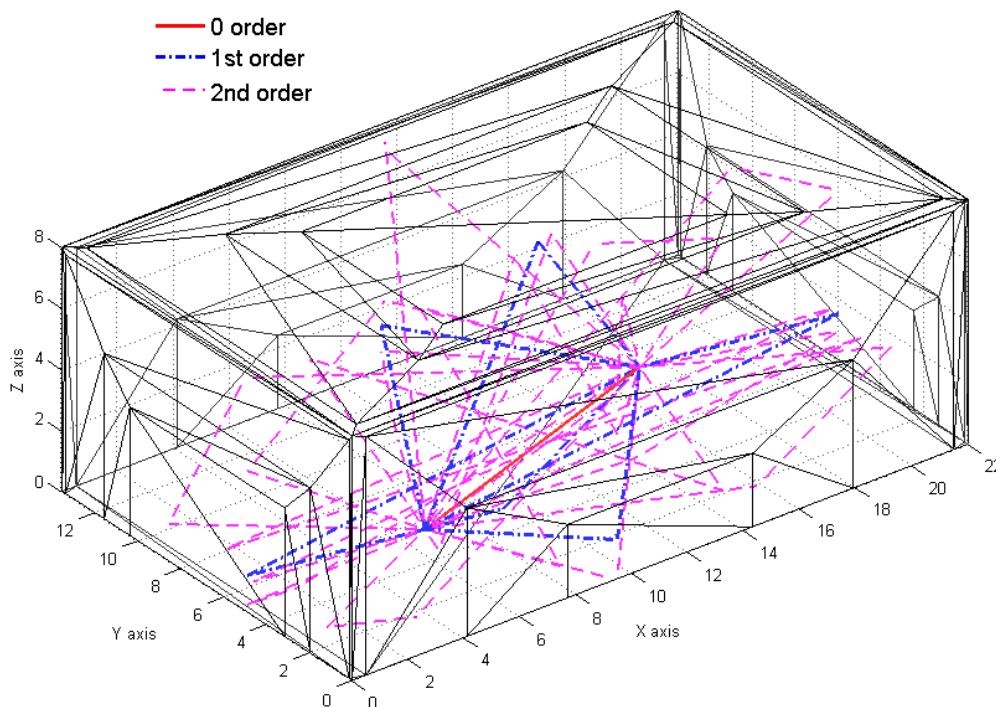
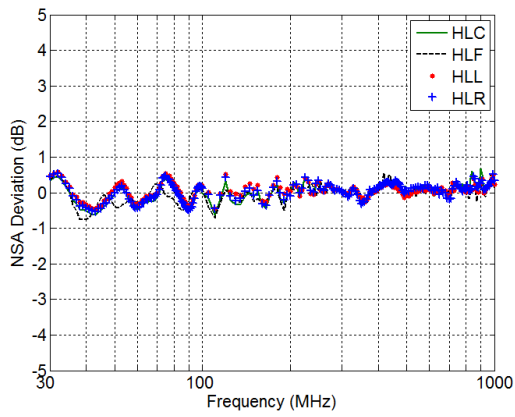
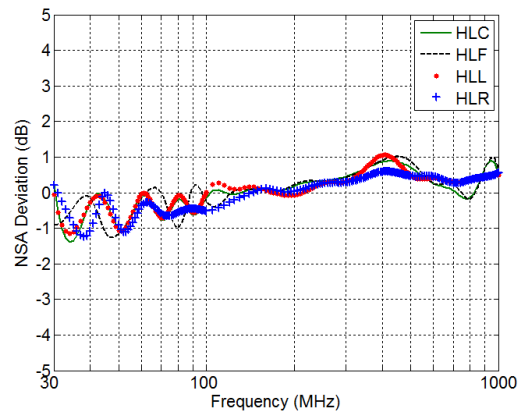
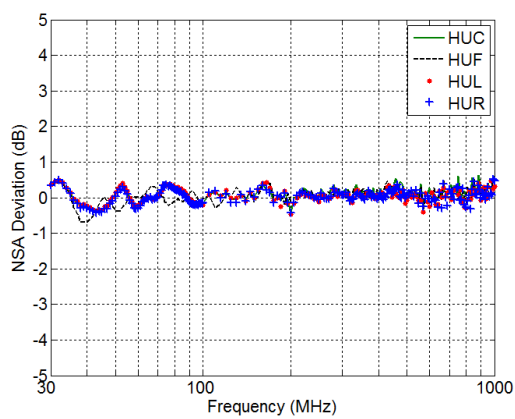
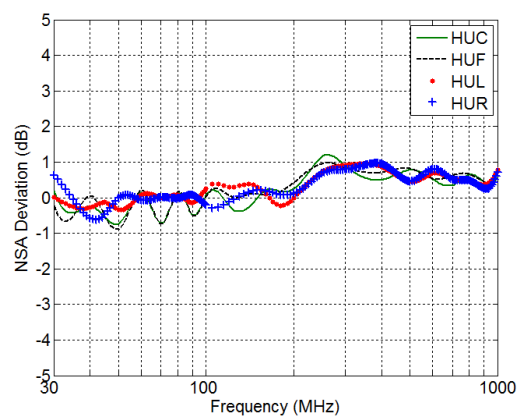


Fig. 4.11 Paths connect the source point and the field point with different orders: 1 ray with zero order, 6 rays with first order and 18 rays with second order.

Table 4.2: Resource Comparison

	CPU	Mesh No.	Memory Requirement	Simulation Time
GO Inverse Algorithm	2.33GHz 2 threads	116 Triangles	~ 200 MB	2.5 mins
FDTD	3.0 GHz 4 threads	~ 90 million Hexahedra	~ 10 GB	~ 8 hrs

**(a)****(e)****(b)****(f)**

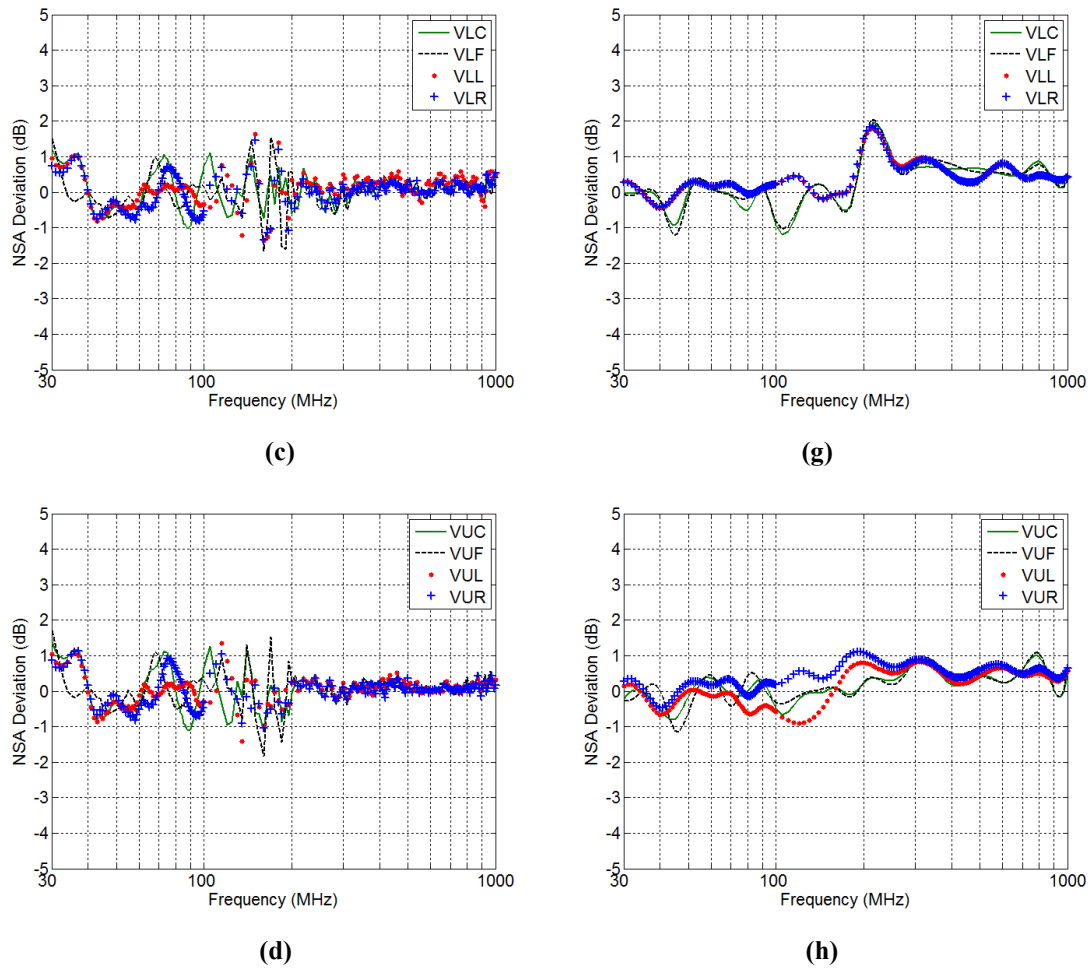
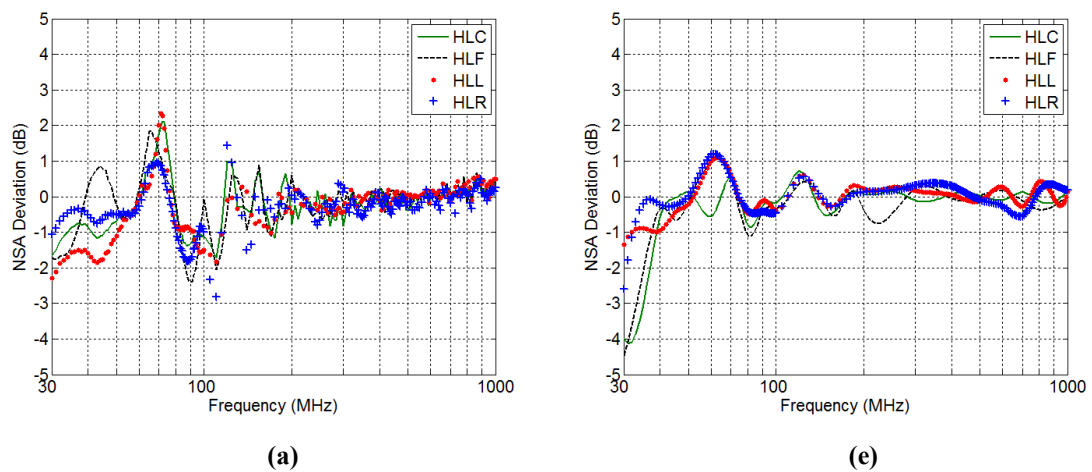


Fig. 4.12 3 m NSA deviation values: (a) ~ (d) measurement results, (e) ~ (h) simulation results. The notations are explained in Table 4.1, e.g. HLC stands for horizontal polarisation (H), the Tx antenna at the lower (L) height and the Rx antenna is located at the centre (C) of the test region (measurement results from Rainford EMC Systems Ltd).



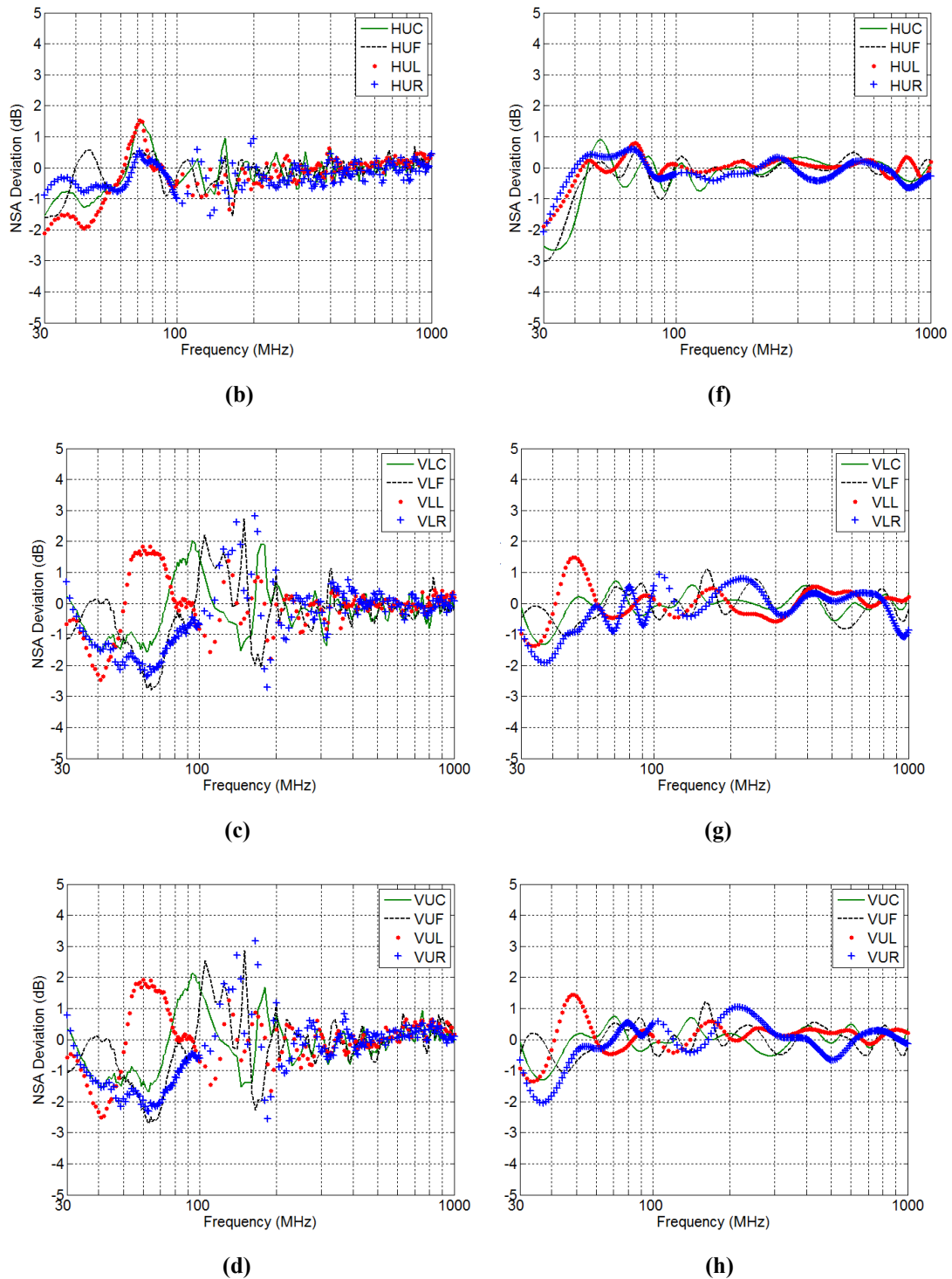
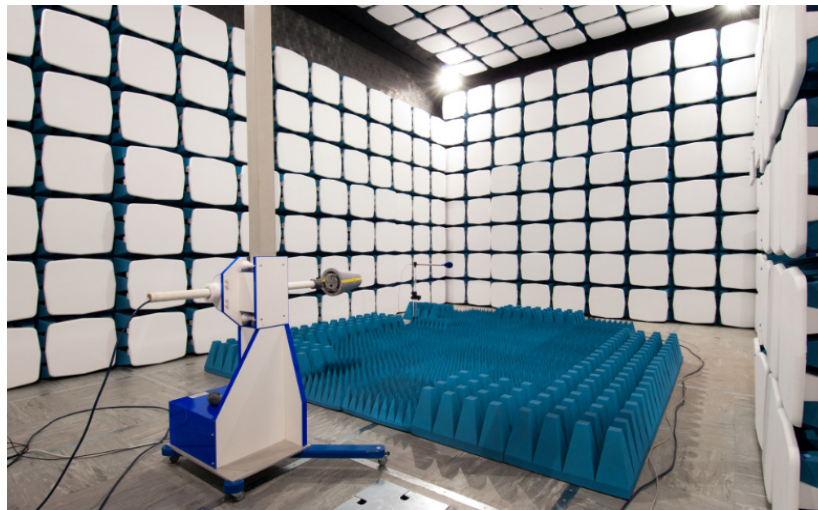


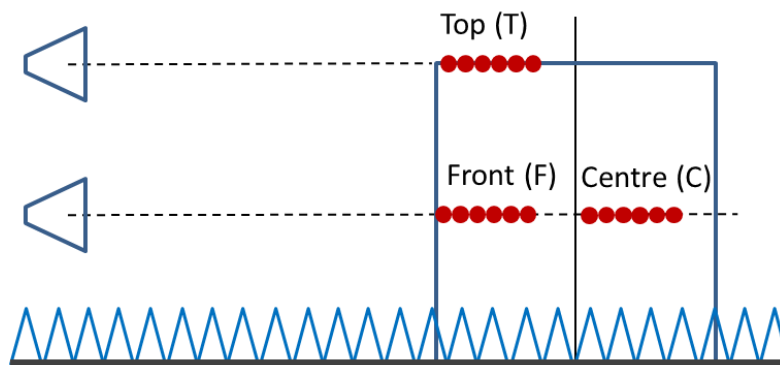
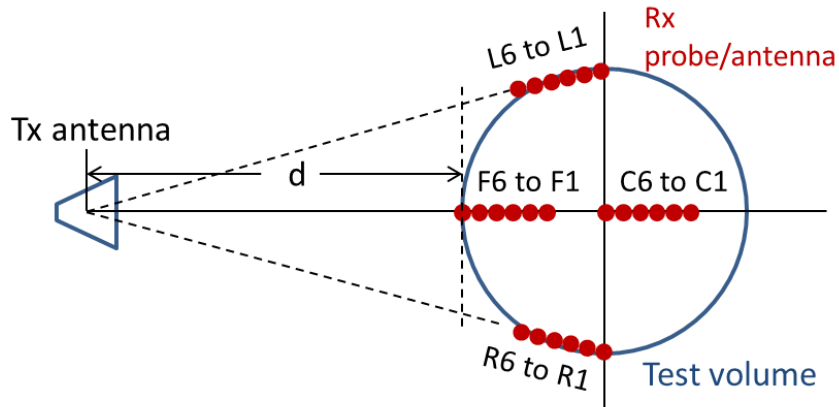
Fig. 4.13 10 m NSA deviation values: (a) ~ (d) measurement results, (e) ~ (h) simulation results (measurement results from Rainford EMC Systems Ltd).

4.3 SVSWR Measurement and Simulation

The measurement scenario is shown in Fig. 4.14. The E-field at the sample points (red dots in Fig. 4.14(b)) are recorded in the frequency range of 1 GHz ~ 18 GHz. The Tx probe/antenna is swept along the measurement axis.



(a)



(b)

Fig. 4.14 SVSWR measurement setup. (a) picture from Rainford EMC Systems Ltd.

Take F1 ~ F6 as an example, F5 and F1 are measured relative to F6 as follows, moving away from the Tx antenna [5]:

- 1) F5 = F6 + 2 cm away from the Tx antenna
- 2) F4 = F6 + 10 cm away from the Tx antenna
- 3) F3 = F6 + 18 cm away from the Tx antenna
- 4) F2 = F6 + 30 cm away from the Tx antenna
- 5) F1 = F6 + 40 cm away from the Tx antenna.

It should be noted that the distance among them are not uniform. This is because we need to sample the E-field in a very wide frequency range, if they are sampled uniformly, the recorded E-field could be always at the peak or trough points of the standing wave at some frequencies. Suppose E_{max} and E_{min} are the measured maximum and minimum E-fields along the axis respectively. The SVSWR can be obtained from

$$S_{VSWR} = \frac{E'_{max}}{E'_{min}} = \frac{V'_{max}}{V'_{min}} \quad (4.3)$$

where E'_{max} (V'_{max}), E'_{min} (V'_{min}) are the normalised measured E-field (voltage)

$$E'_* = E_* \frac{d_{TxRx}}{d_{ref}} \quad (4.4)$$

Because the free-space attenuation ($E \propto d^{-1}$) will not be accounted for the calculation of S_{VSWR} , d_{ref} can be chosen as the distance between the Tx antenna and the first receive point.

Table 4.3: SVSWR Test Scenarios

Polarisation	Rx Position
Horizontal (H)	Front (F)
	Centre (C)
	Right (R)
Vertical (V)	Left (L)
	Top (T)

The simulation model is shown in Fig. 4.15, the size of the chamber is 9 m × 6 m × 6 m ($L \times W \times H$). To reduce reflections from the ground plane, part of the ground is covered by RAMs. After applying the inverse method, the rays connect the Tx and Rx antenna can be found, shown in Fig.

4.16. By repeating the procedure for all the scenarios listed in Table 4.3, comparisons between the measurement and simulation results are shown in Fig. 4.17.

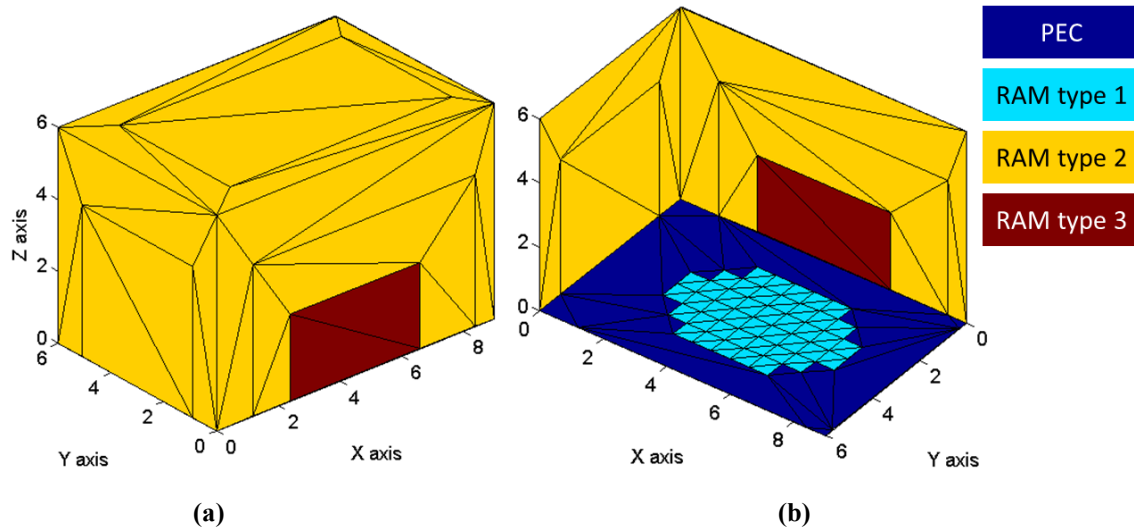


Fig. 4.15 Simulation model, different colour represents different type of RAM, (a) top view, (b) bottom view.

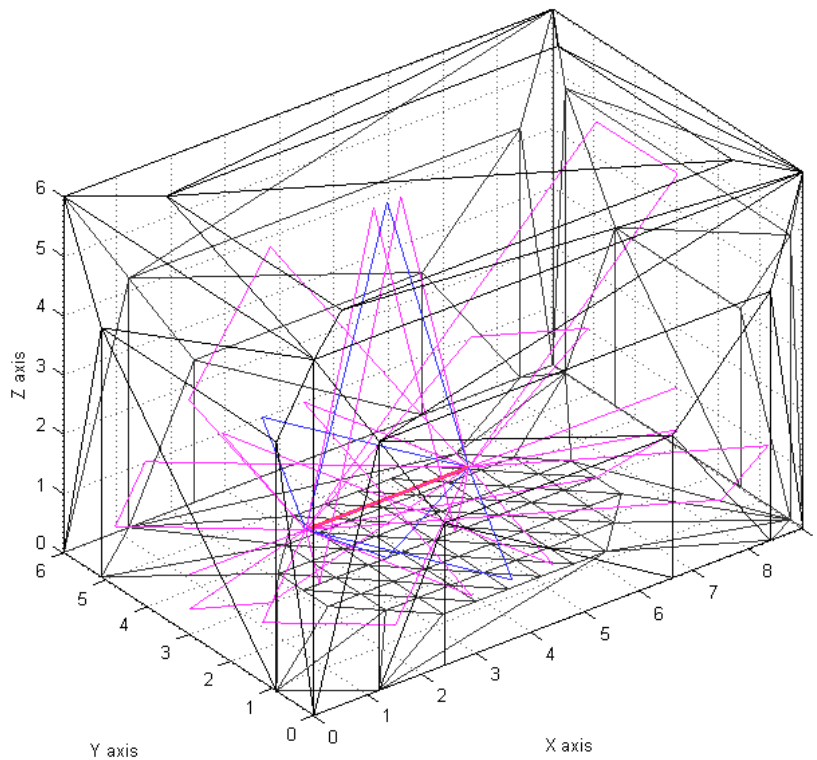
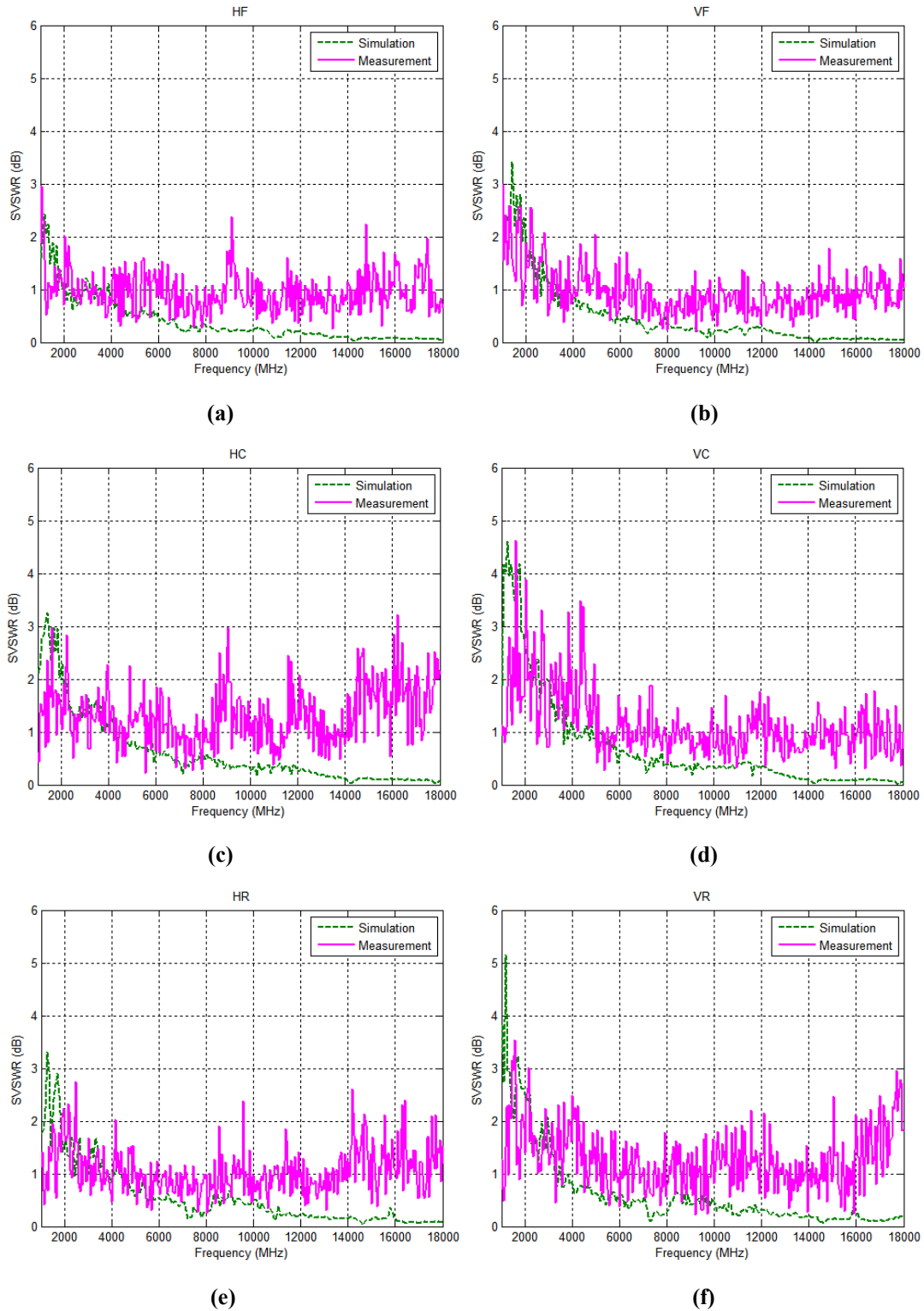


Fig. 4.16 Rays with different orders.

It can be seen that the simulated SVSWR is much smaller than the measured value at higher frequencies. This is because, at higher frequencies, the radiation pattern may not be exactly the same as in the simulation, the tip scattering of RAM could be significant and hard to predict, the reflection

coefficient is more sensitive to material properties, and also the supporting objects used in the measurement could become potential scattering sources. It can be seen that, when frequency is smaller than 8 GHz, the differences between the measured values and simulated values are smaller than 2 dB.



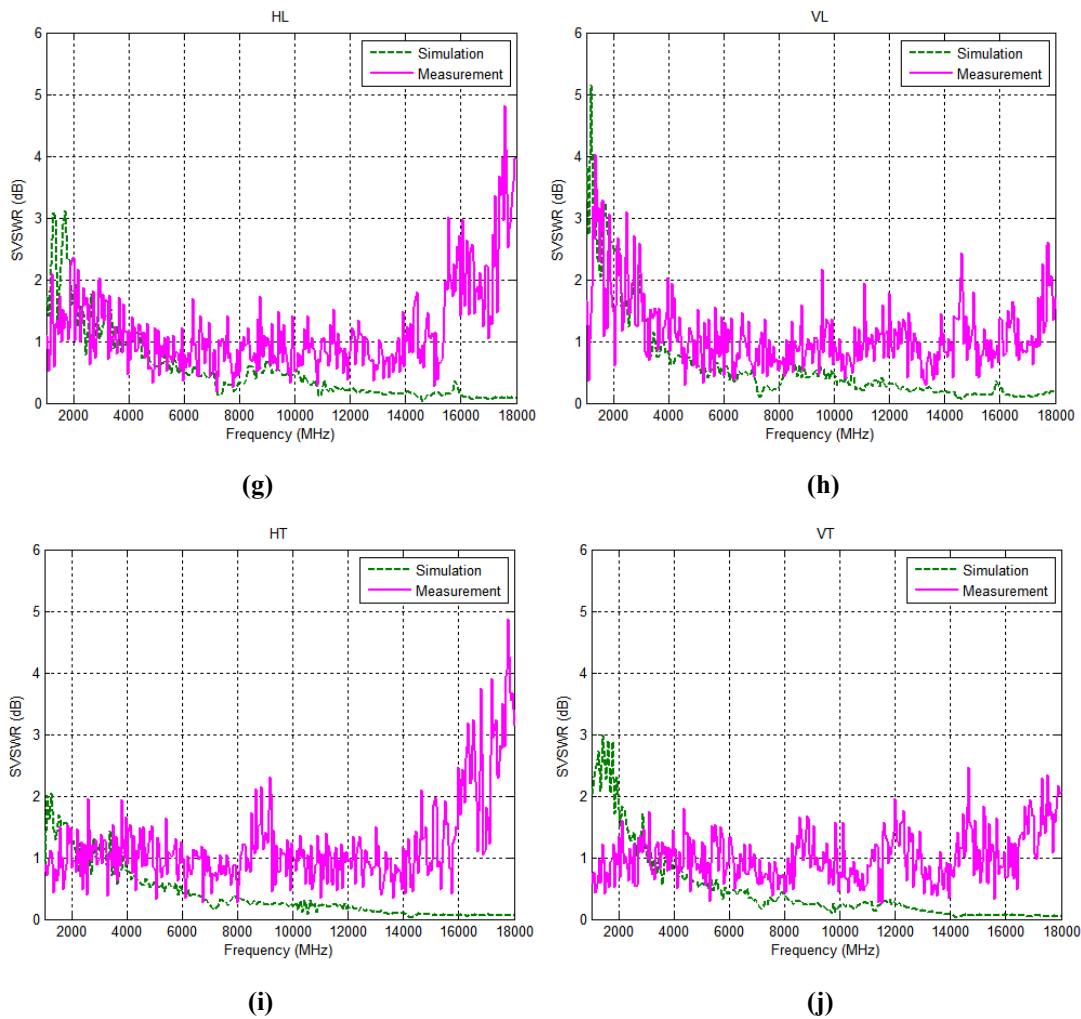


Fig. 4.17 Simulated and measured SVSWR, HF means the Tx antenna is horizontal polarisation and the Rx is chosen at front position in Table 4.3 (measurement results from Rainford EMC Systems Ltd).

4.4 FU Measurement and Simulation

The FU measurement is performed by measuring the E-field magnitude at 16 points in the uniform field area at each frequency, as shown in Fig. 4.18. The transmitting antenna is placed at a distance of 3 m from the uniform field area (UFA) plane with a height of 1.55 m. The E-field magnitude for at least 12 points (75%, sometimes 100%) of the 16 points of the UFA are required to be within the tolerance of $\pm_6^0 dB$ [6]. The measurement scenario is shown in Fig. 4.19, to improve the FU, part of the ground is covered with RAMs (according to the standard [6]) to reduce the reflection from the ground.

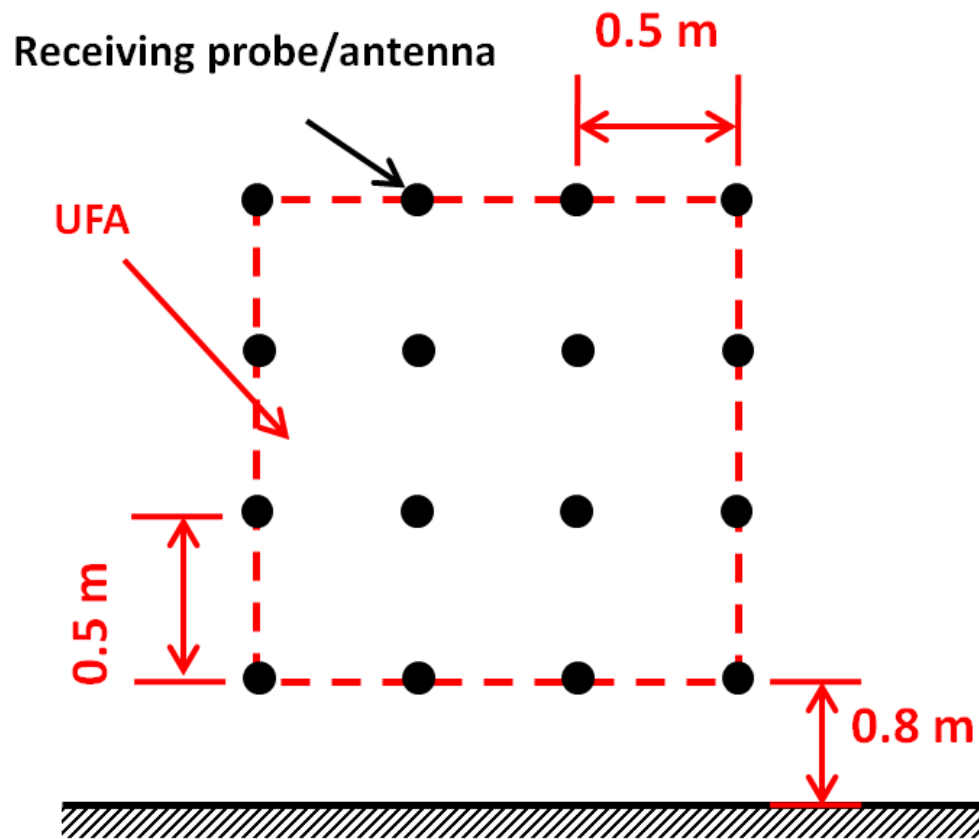


Fig. 4.18 FU sample points of the UFA.

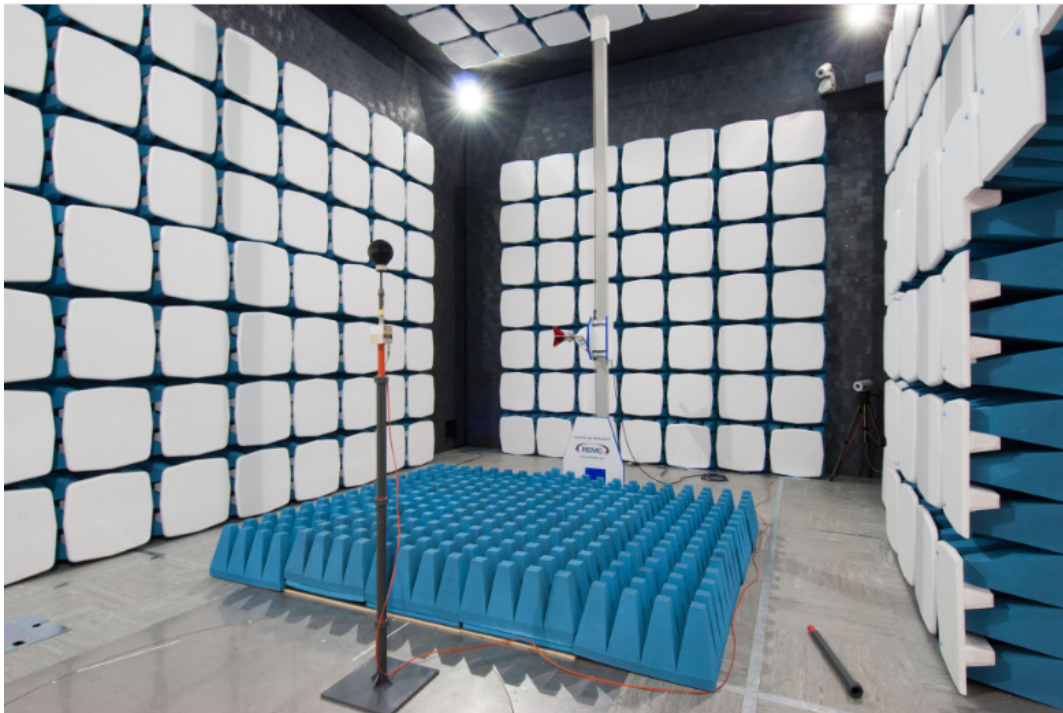


Fig. 4.19 FU measurement scenario (picture from Rainford EMC Systems Ltd).

The simulation model is shown in Fig. 4.20, as can be seen, part of the ground is covered by RAMs. The rays connect the Tx and Rx antennas are shown in Fig. 4.21. The measurement and simulation are repeated for horizontal and vertical polarisations. Comparisons are given in Fig. 4.22 with 75% sample points and 100% sample points in the frequency range of 80 MHz to 18 GHz. Note when 75% sample points fall in the range of $\pm 6dB$, but not for 100% sample points. This is acceptable according to the standard, since in practice the size of EUT may not be the same as UFA and not all the surface need to be illuminated (only electronic devices). However, nowadays 100% sample points are also required which normally means a stricter standard defined by customer.

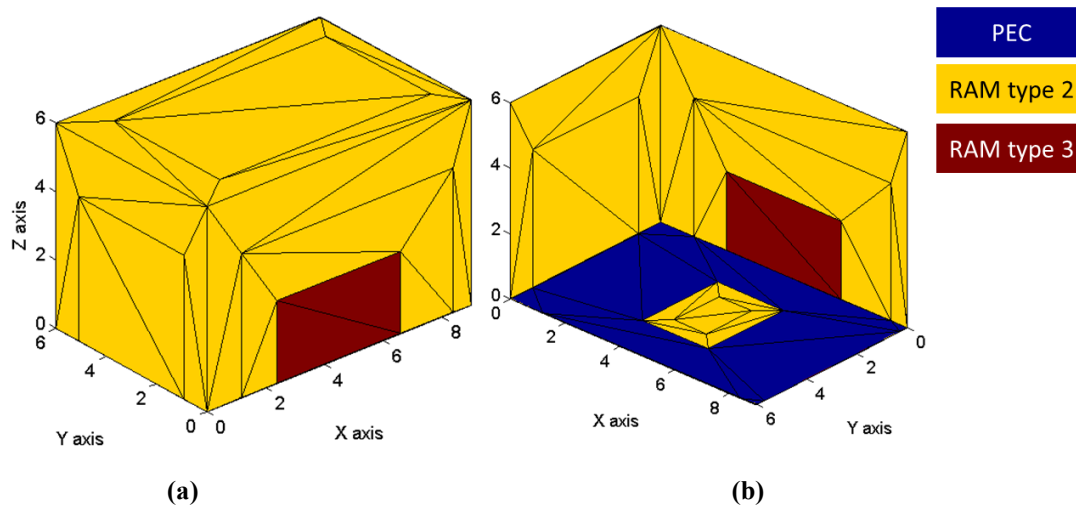


Fig. 4.20 Simulation model, different colour represents different type of RAM, (a) top view, (b) bottom view.

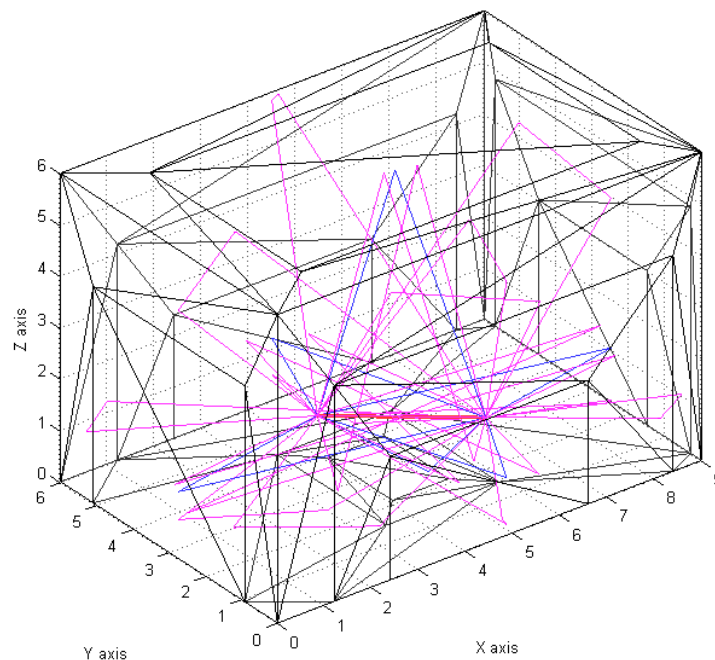
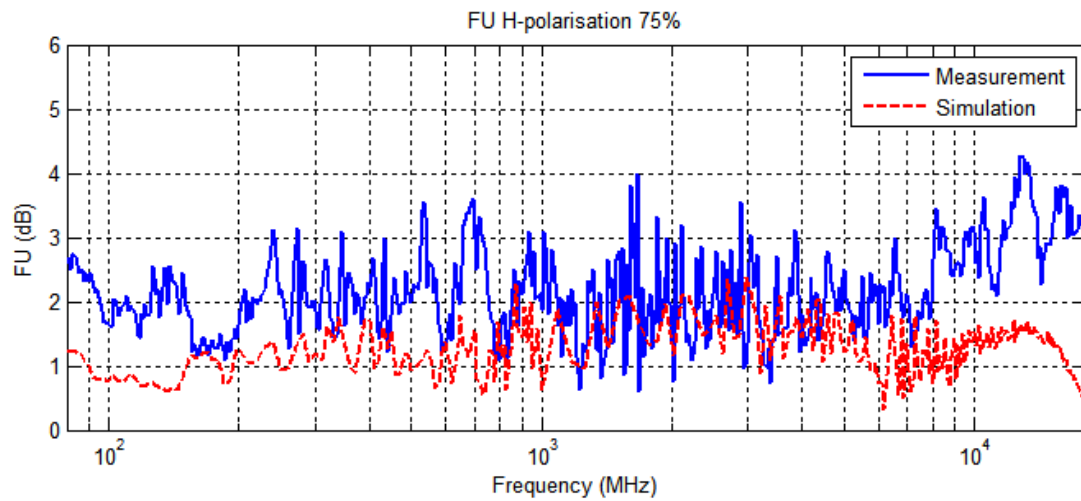
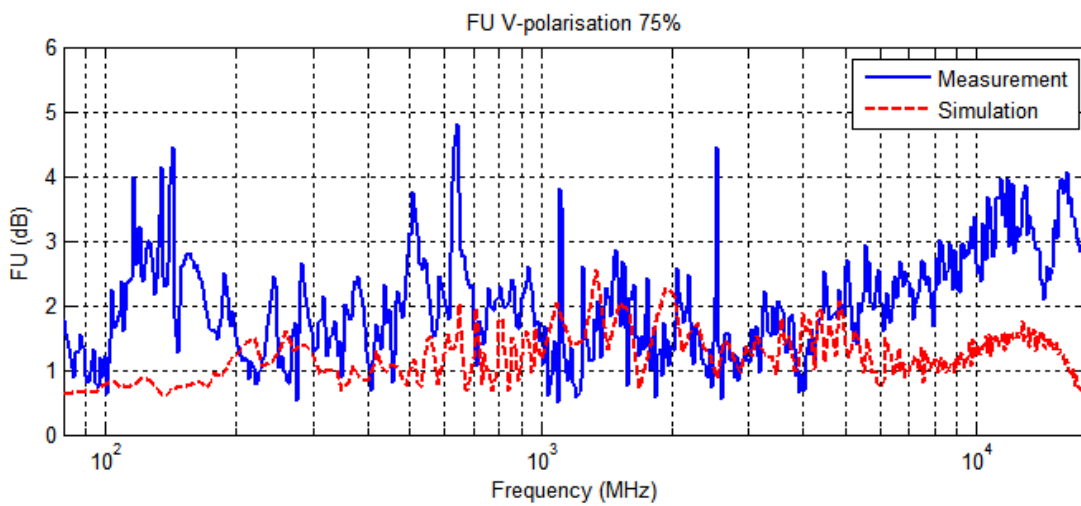


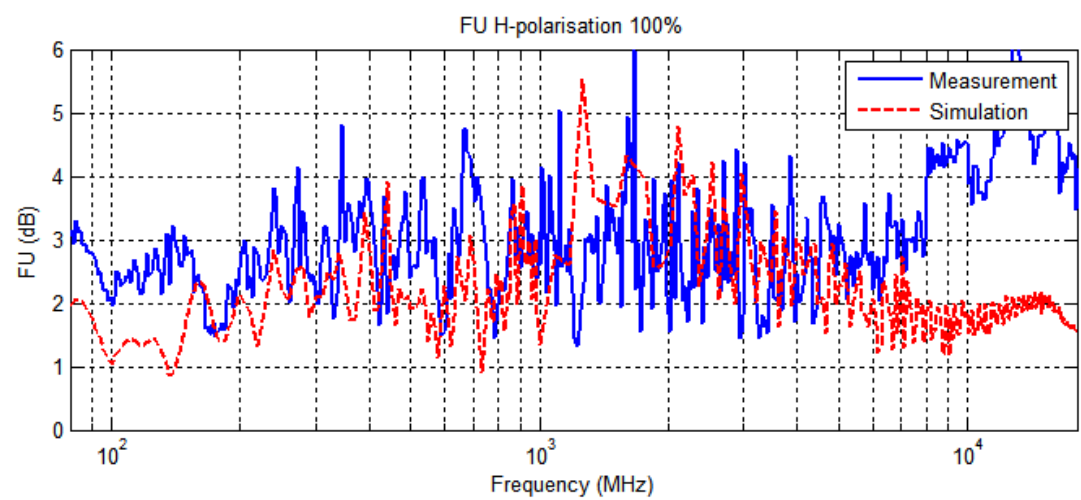
Fig. 4.21 Rays with different orders.



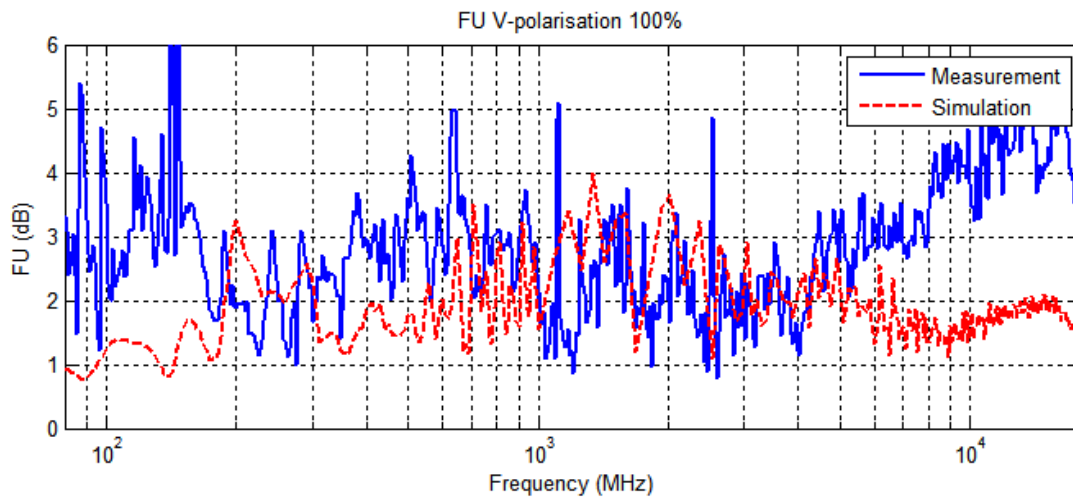
(a)



(b)



(c)



(d)

Fig. 4.22 Simulated and measured FU (a) horizontal polarisation FU with 75% sample points, (b) vertical polarisation FU with 75% sample points, (c) horizontal polarisation FU with 100% sample points, (d) vertical polarisation FU with 100% sample points (measurement results from Rainford EMC Systems Ltd).

The results show that: for the frequencies higher than 200 MHz and lower than 8 GHz, the difference is smaller than 2 dB for both polarisations. For the frequencies lower than 200 MHz, the error could be due to the high frequency approximation of the GO method. For the frequencies higher than 8 GHz, the error could be due to the difference between the simulation and measurement: radiation pattern of the antenna, material property of the RAM, scattering/reflections from masts and cables, also the tip scattering of the RAM is not considered in simulation.

4.5 Summary

In this chapter, the definitions of NSA, SVSWR and FU have been given; measurement results and simulation results obtained from the developed CAD tool have been compared. For the NSA values, the difference between the simulated values and measurement values can be smaller than ± 2 dB in the whole frequency range (30 MHz ~ 1 GHz). For the SVSWR values, a good agreement has been obtained when the frequency is between 1 GHz ~ 14 GHz, and the difference is smaller than 2 dB when frequency is lower than 8 GHz. For the FU values, the difference is smaller than 2 dB in the frequency range of 300 MHz ~ 8 GHz.

It is important to note that the GO is a high frequency approximation method, in the measurement part we have compared the simulation and measurement results which are in good agreement. A potential problem is: at lower frequencies, the near field mutual coupling and diffraction may affect the results (the prediction accuracy is expected to be reduced using the GO method). Another issue is that the tip

scattering of RAM at higher frequencies becomes significant and it is not considered in this model, when the tip scattering becomes the major contribution for the unexpected field (in millimetre wave), it will limit the boundary of the high frequency of this method. This could be in the region of statistical electromagnetics but not deterministic electromagnetics. There are also detailed structures which could not be included in the simulation because of the complexity of the measurement scenario (masts, cables, *etc.*).

4.6 References

- [1] H. E. King, F. I. Shimabukuro and J. L. Wong, “Characteristics of a tapered anechoic chamber,” *IEEE Trans. Antennas Propagat.*, vol. 15, no. 3, pp. 488–490, May 1967.
- [2] V. Galindo-Israel, S. R. Rengarajan, W. A. Imbriale and R. Mittra, “Offset dual-shaped reflectors for dual chamber compact ranges,” *IEEE Trans. Antennas Propagat.*, vol. 39, no. 7, pp. 1007–1013, Jul. 1991.
- [3] L. H. Hemming, “Anechoic chamber,” U.S. Patent 4 507 660, March 26, 1985.
- [4] G. A. Sanchez, “Geometrically optimized anechoic chamber,” U.S. Patent 5 631 661, May 20, 1997.
- [5] CISPR 16-1-4: Specification for radio disturbance and immunity measuring apparatus and methods - Part 1-4: Radio disturbance and immunity measuring apparatus - Antennas and test sites for radiated disturbance measurements, IEC Standard, Ed 3.1, Jul. 2012.
- [6] IEC 61000-4-3: Electromagnetic compatibility (EMC) - Part 4-3: Testing and measurement techniques - Radiated, radio-frequency, electromagnetic field immunity test, IEC Standard, Ed 3.1, Apr. 2008.
- [7] V. P. Kodali, *Engineering Electromagnetic Compatibility: Principles, Measurements, Technologies, and Computer Models*, 2nd Ed, New York: Wiley-IEEE Press, 2001

Chapter 5: New Measurement Methods in a Reverberation Chamber

5.1 Introduction

From this chapter, we focus on the reverberation chamber (RC). In the electromagnetics (EM) community, an RC is normally an electrically large room which is designed to make the field therein as diffused as possible [1]. While anechoic chamber (AC) can be regarded as a useful facility to study the deterministic electromagnetics, a reverberation chamber can be considered as an important facility to investigate statistical electromagnetics (SEM). In the past few years, the applications of the RC have been extended from EMC community to various areas. Publication numbers related to the reverberation chamber in each year are shown in Fig. 5.1 (raw data from IEEE Xplorer®). As can be seen, since 1990, there has been a significant increasing interest in this area. The statistics in 2015 is not complete, that is the reason why the publication number is small.

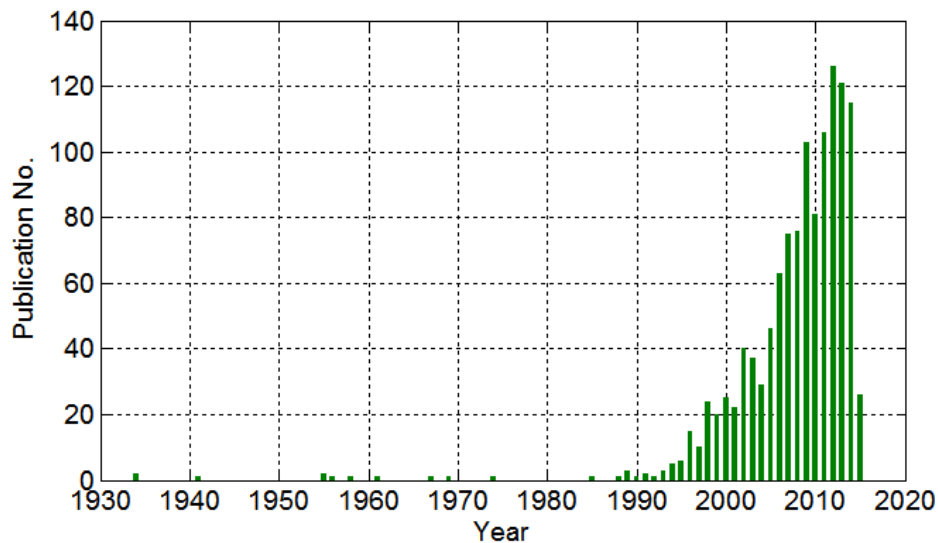


Fig. 5.1. Publication number every year (key words: *reverberation chamber*)

To review the applications of the RC systematically, we list some typical applications in Table 5.1 and related references.

The purpose of this chapter is to present new measurement methods in an RC. The measurement data normally contains more information than we expected. How to extract the useful information as much as possible is an important topic. In this chapter we present new measurement methods for antenna radiation efficiency, diversity gain, radiated emission, material permittivity and shielding effectiveness measurements. It is interesting to note that these measurement methods are not isolated;

they are inter-related. For example, when measuring the diversity gain, we need to consider the radiation efficiency of antennas. Actually, in most measurements in an RC, the antenna effect should be taken into account since it acts as a radiating source and a load in the RC simultaneously.

Table 5.1: Typical applications of an RC

Applications	References
Free space S -parameters	[2]
Antenna radiation efficiency	[1, 3-13]
Antenna directivity/pattern/gain	[14-17]
Radiated emission	[1, 18]
Radiated immunity	[1, 19]
Shielding effectiveness	[1, 20-24]
Diversity gain/channel capacity	[25-28]
MIMO channel emulation	[29-33]
Bit error rate	[34]
Doppler effect	[35-37]
Total isotropic sensitivity	[38-39]
Absorption cross section	[40-45]
Material permittivity	[45]
Scattering cross section	[46-49]

5.2 Antenna Radiation Efficiency Measurement in an RC

There are many ways to measure the radiation efficiency of antennas in an RC. First, we present the measurement method with reference antenna and then study the methods without reference antenna.

5.2.1 Method Using Reference Antenna

We start from the method given in IEC 61000-4-21 [1]. As shown in Fig. 5.2, the computer controls the operation of the stirrers and collects the S -parameters from the VNA for each stirrer position.

Suppose antenna 2 is the AUT, and the *Ref Ant* is the reference antenna with known radiation efficiency. The measurement procedure is given as follows.

Step 1) Calibrate the VNA (the reference plane is calibrated at the end of the cable).

Step 2) Place all the antennas inside the RC to ensure that the chamber Q factor does not change during the whole measurement, and the main beams of the each antenna are not directed to each other to reduce the unstirred part.

Step 3) Connect antenna 1 to the VNA port 1 and antenna 2 to port 2, the reference antenna is loaded with a 50 Ohm termination. Collect the complex S -parameters S_{A22} , S_{a21} for each stirrer position (S_{A*} means the S -parameters with AUT).

Step 4) Connect the reference antenna to port 2 of the VNA and load the AUT with a 50 Ohm termination. Collect the complex S -parameters S_{R22} , S_{R21} for each stirrer position (S_{R*} means the S -parameters with the reference antenna).

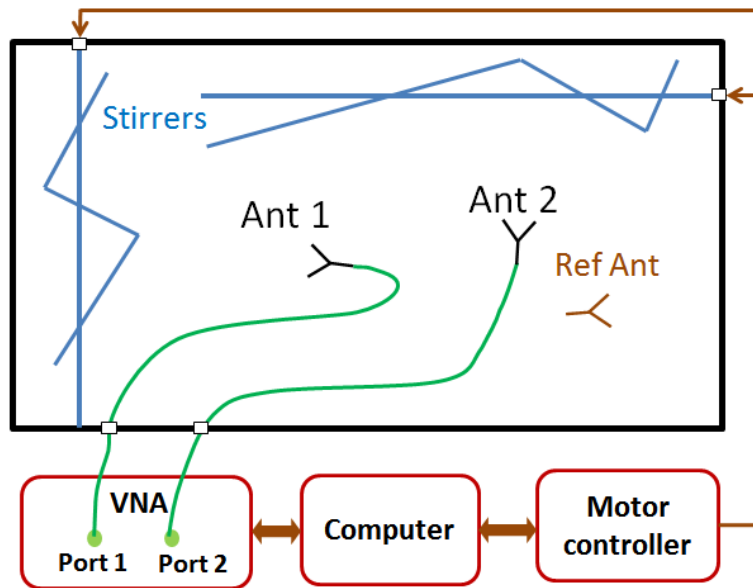


Fig. 5.2. Radiation efficiency measurement setup using a reference antenna.

If the RC has good field uniformity, which means the chamber transfer function from antenna 1 to the AUT and antenna 1 to the reference antenna are the same

$$\frac{\langle |S_{A21,s}|^2 \rangle}{(1 - \langle |S_{A22}|^2 \rangle) \eta_A} = T_{A21} = T_{R21} = \frac{\langle |S_{R21,s}|^2 \rangle}{(1 - \langle |S_{R22}|^2 \rangle) \eta_R} \quad (5.1)$$

where $S_{A21,s}$ is the stirred part of the S -parameters [3]

$$S_{*,s} = S_* - \langle S_* \rangle \quad (5.2)$$

$\langle * \rangle$ means the average value of the S -parameter using any stirring method (e.g. mechanical stir, frequency stir, polarisation stir, source stir, etc.). $\langle S_{*22} \rangle$ can also be obtained from anechoic chamber, since $\langle S_{*22} \rangle = S_{*,22 \text{ freespace}}$ [2, 9]. The radiation efficiency of AUT can be obtained as

$$\eta_A = \frac{\langle |S_{A21,s}|^2 \rangle (1 - \langle |S_{R22}|^2 \rangle)}{\langle |S_{R21,s}|^2 \rangle (1 - \langle |S_{A22}|^2 \rangle)} \eta_R \quad (5.3)$$

The *total* efficiency (include the mismatching of the antenna) will be

$$\eta_{\text{Tot}} = \eta_A (1 - \langle |S_{A22}|^2 \rangle) = \frac{\langle |S_{A21,s}|^2 \rangle}{\langle |S_{R21,s}|^2 \rangle} \eta_{\text{Rtot}} \quad (5.4)$$

The *radiation efficiency* in this thesis is defined as the ratio of the total power radiated by an antenna to the *net power* accepted by the antenna from the connected transmitter, while the total efficiency includes the mismatch of the antenna. It can be seen that, this method is direct and easy to understand. However, the problem is that we need an antenna with known radiation efficiency; this could be a problem in practice. If the accuracy requirement is not high, a well-matched horn antenna can be used as the reference antenna, an estimation value 95% ($\pm 5\%$) can be used as a reference value [1].

5.2.2 Method without Using a Reference Antenna

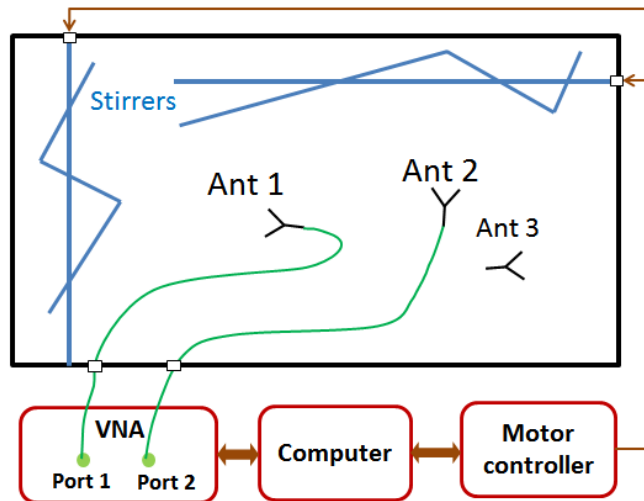


Fig. 5.3. Radiation efficiency measurement without reference antenna.

Recently, Holloway *et al* developed new methods to measure the radiation efficiency of antennas without involving a reference antenna [3]. The methods based on the difference of Q factor measured

from frequency domain and time domain. The measurement setup is shown in Fig. 5.3, as can be seen, no reference antenna is needed.

In the frequency domain, when the antennas are idea antennas (well-matched, 100% radiation efficiency) and no line-of-sight, the Q factor can be obtained from [3]

$$Q_{FD} = C_{RC} \langle |S_{21}|^2 \rangle \quad (5.5)$$

where C_{RC} is the chamber constant [3]

$$C_{RC} = \frac{16\pi^2 V}{\lambda^3} \quad (5.6)$$

V is the volume of the chamber, and λ is the free-space wavelength. If we correct the antenna efficiency, and consider the line-of-sight component, the corrected Q_{FD} becomes [3]

$$Q_{FDCor} = \frac{C_{RC} \langle |S_{21,s}|^2 \rangle}{\eta_{1tot} \eta_{2tot}} \quad (5.7)$$

where $S_{21,s}$ is the stirred part of the S -parameters [3]

$$S_{*,s} = S_* - \langle S_* \rangle \quad (5.8)$$

Meanwhile, the Q factor can be obtained from time domain [3]

$$Q_{TD} = \omega \tau_{RC} \quad (5.9)$$

where τ_{RC} is the chamber decay constant which can be extracted from time domain response of the chamber [34], τ_{RC} describes how fast the power profile decays in the time domain ($e^{-t/\tau_{RC}}$). Because the Q factor obtained from should be the same, thus $Q_{FDCor} = Q_{TD}$, we have [3]

$$\eta_{1tot} \eta_{2tot} = \frac{C_{RC} \langle |S_{21,s}|^2 \rangle}{\omega \tau_{RC}} \quad (5.10)$$

Now we only have only one equation for two variables η_{1tot} and η_{2tot} which cannot be solved. It is important to note that the S -parameters can be related using enhanced back scatter constant [3]

$$e_b = \frac{\sqrt{\langle |S_{11,s}|^2 \rangle \langle |S_{22,s}|^2 \rangle}}{\langle |S_{21,s}|^2 \rangle} \quad (5.11)$$

For a well-stirred RC, $e_b = 2$ [50], if only one antenna is used (the one-antenna method in [3]), which means the transmitting antenna and receiving antenna are the same, $\langle |S_{11,s}|^2 \rangle = \langle |S_{22,s}|^2 \rangle$. From (5.10) and (5.11) (details can be found in Appendix A2), the radiation efficiency of antennas can be expressed as [3]

$$\eta_i = \frac{1}{(1 - \langle |S_{ii}|^2 \rangle)} \sqrt{\frac{C_{RC}}{2\omega\tau_{RC}} \langle |S_{ii,s}|^2 \rangle} \quad (i = 1 \text{ or } 2) \quad (5.12)$$

If both antennas are used, we do not need $e_b = 2$ to solve (5.10) and (5.11), but need e_b to be identical for two antennas, we have (the two-antenna method in [3])

$$\eta_i = \frac{1}{(1 - \langle |S_{ii}|^2 \rangle)} \sqrt{\frac{C_{RC}}{\omega e_b \tau_{RC}} \langle |S_{ii,s}|^2 \rangle} \quad (i = 1 \text{ or } 2) \quad (5.13)$$

If three antennas are used, there is no requirement for e_b , we have (the three-antenna method in [3])

$$\eta_1 = \frac{1}{(1 - \langle |S_{11}|^2 \rangle)} \sqrt{\frac{C_{RC}}{\omega\tau_{RC}} \frac{\langle |S_{21,s}|^2 \rangle \langle |S_{31,s}|^2 \rangle}{\langle |S_{32,s}|^2 \rangle}} \quad (5.14)$$

$$\eta_2 = \frac{1}{(1 - \langle |S_{22}|^2 \rangle)} \sqrt{\frac{C_{RC}}{\omega\tau_{RC}} \frac{\langle |S_{21,s}|^2 \rangle \langle |S_{32,s}|^2 \rangle}{\langle |S_{31,s}|^2 \rangle}} \quad (5.15)$$

$$\eta_3 = \frac{1}{(1 - \langle |S_{33}|^2 \rangle)} \sqrt{\frac{C_{RC}}{\omega\tau_{RC}} \frac{\langle |S_{31,s}|^2 \rangle \langle |S_{32,s}|^2 \rangle}{\langle |S_{21,s}|^2 \rangle}} \quad (5.16)$$

The two-antenna method works well for high efficiency antennas. However, when the AUT is very lossy (radiation efficiency is very small), $S_{ii,s}$ could be outside the dynamic range of VNA. In this case, we may need a power amplifier to increase the transmitting power. But when the power amplifier is involved, the reverse signal from the output to the input is not allowed. This makes $S_{ii,s}$ hard to measure when it is very small. Thus we need an alternative method which can use the information of S_{21} (like the gain measurement in an anechoic chamber), and when the signal amplitude is small we can use a power amplifier to increase the dynamic range. In the following part of this section, we propose a modified two-antenna method to solve this problem.

5.2.3 Modified Two-Antenna Method

The measurement scenario is illustrated in Fig. 5.4. In this method, we need at least one antenna of high radiation efficiency, to make sure that the time domain response from this antenna can be used to extract the chamber decay time and the $S_{11,s}$ for this antenna is in the dynamic range of VNA. Here we assume that the radiation efficiency of antenna 2 in Fig. 5.4 is high, thus the one-antenna method in [3] can be applied to antenna 2. Antenna 1 is assumed to be the AUT.

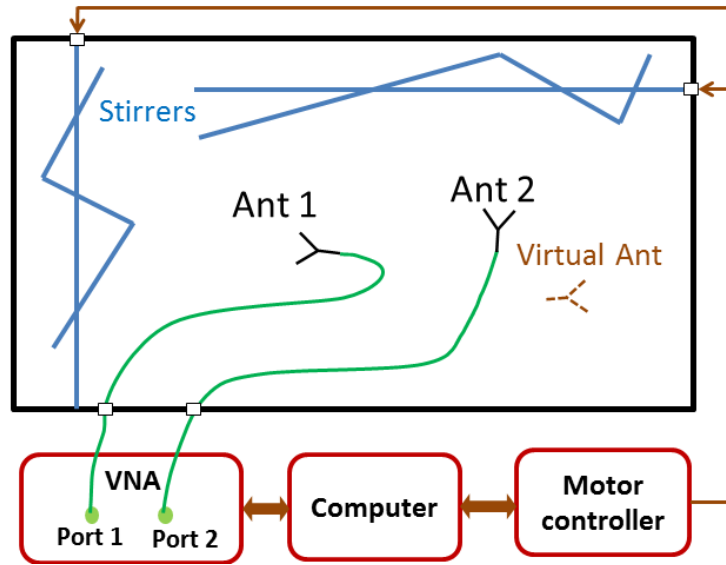


Fig. 5.4. The radiation efficiency measurement setup in an RC (modified two-antenna method).

It has been shown that the radiation efficiency of antenna 2 can be obtained using one-antenna method equation (5.12)

$$\eta_2 = \frac{1}{(1 - \langle |S_{22}|^2 \rangle)} \sqrt{\frac{C_{RC}}{2\omega\tau_{RC}} \langle |S_{22,s}|^2 \rangle} \quad (5.17)$$

It is helpful to introduce a virtual antenna to understand the enhanced backscatter effect. Assume that the virtual antenna in Fig. 5.4 is exactly the same as antenna 2. When the chamber is well-stirred, the enhanced backscatter constant brings the stirred S -parameters between antenna 2 and the virtual antenna together by the following equation [3]

$$e_b = \frac{\sqrt{\langle |S_{22,s}|^2 \rangle \langle |S_{vv,s}|^2 \rangle}}{\langle |S_{2v,s}|^2 \rangle} = 2 \quad (5.18)$$

It should be noted that $e_b = 2$ is an assumption for a well-stirred RC, e_b depends on the dimensions of the problem (e.g. $e_b = 1.5$ for 1D and $e_b = 2.25$ for 2D), it could also be affected by the directivity of the antenna (at high frequencies, it may not be 2). Currently experimental results were given and empirical conclusions were obtained, but there is still a lack of rigorous theory to characterise what factors could affect e_b and how [63].

Because the virtual antenna is assumed to be exactly the same as antenna 2. We have $\langle |S_{22,s}|^2 \rangle = \langle |S_{vv,s}|^2 \rangle$, thus

$$\langle |S_{2v,s}|^2 \rangle = \frac{\langle |S_{22,s}|^2 \rangle}{2} \quad (5.19)$$

In the Section 5.2.1, the chamber transfer function between antenna 2 and the virtual antenna can be written as

$$\begin{aligned} T_{2v} &= \frac{\langle |S_{2v,s}|^2 \rangle}{(1 - \langle |S_{22}|^2 \rangle)(1 - \langle |S_{vv}|^2 \rangle)\eta_2\eta_v} \\ &= \frac{\langle |S_{22,s}|^2 \rangle}{2(1 - \langle |S_{22}|^2 \rangle)^2\eta_2^2} \end{aligned} \quad (5.20)$$

The chamber transfer function between the AUT and antenna 2 is

$$T_{21} = \frac{\langle |S_{21,s}|^2 \rangle}{(1 - \langle |S_{22}|^2 \rangle)(1 - \langle |S_{11}|^2 \rangle)\eta_2\eta_1} \quad (5.21)$$

If the RC is well-stirred and has a good field uniformity, $T_{2v} = T_{21}$, substitute (5.17) to (5.21) to obtain η_1

$$\eta_1 = \frac{\langle |S_{21,s}|^2 \rangle}{(1 - \langle |S_{11}|^2 \rangle)} \sqrt{\frac{2C_{RC}}{\omega\tau_{RC} \langle |S_{22,s}|^2 \rangle}} \quad (5.22)$$

This is the efficiency of the AUT using the proposed method. Vice versa, if antenna 1 is a highly efficient antenna, we can obtain the radiation efficiency of the AUT (antenna 2) as

$$\eta_2 = \frac{\langle |S_{21,s}|^2 \rangle}{(1 - \langle |S_{22}|^2 \rangle)} \sqrt{\frac{2C_{RC}}{\omega\tau_{RC} \langle |S_{11,s}|^2 \rangle}} \quad (5.23)$$

If we compare (5.22) with the two-antenna method (5.13), it can be found that, while the proposed method requires $e_b = 2$ for antenna 2 and the RC is well-stirred (spatially uniform), (5.13) does not

require $e_b = 2$ but needs e_b to be identical for the two antennas. In order to verify the proposed method, measurements are conducted.

To verify the effectiveness of the proposed method, an antenna with known low radiation efficiency is needed. It is not easy to find a very lossy antenna with known radiation efficiency, so we use an attenuator connected to an antenna and consider the attenuator as part of the antenna. We know how much radiation efficiency is reduced by introducing the attenuator, but in the measurement, no special treatment is required, the attenuator and the antenna become an integrated AUT. This offers an opportunity to verify the proposed method.

The measurement scenario is shown in Fig. 5.5(a) and the size of the RC is $3.6 \text{ m} \times 4 \text{ m} \times 5.8 \text{ m}$. After the VNA was calibrated, antenna 1 (Rohde & Schwarz® HF 906) and antenna 2 (SATIMO® SH 2000) were connected to port 1 and port 2, respectively, with no line-of-sight, 359 stirrer locations with a step size of 1 degree for the stirrers and 10,001 points were set for the range of 2.8 GHz ~ 4.2 GHz which means that the inverse fast Fourier transform (IFFT) of the collected S -parameters has a time domain response of 7,140 ns in length with a time step resolution of 0.24 ns.

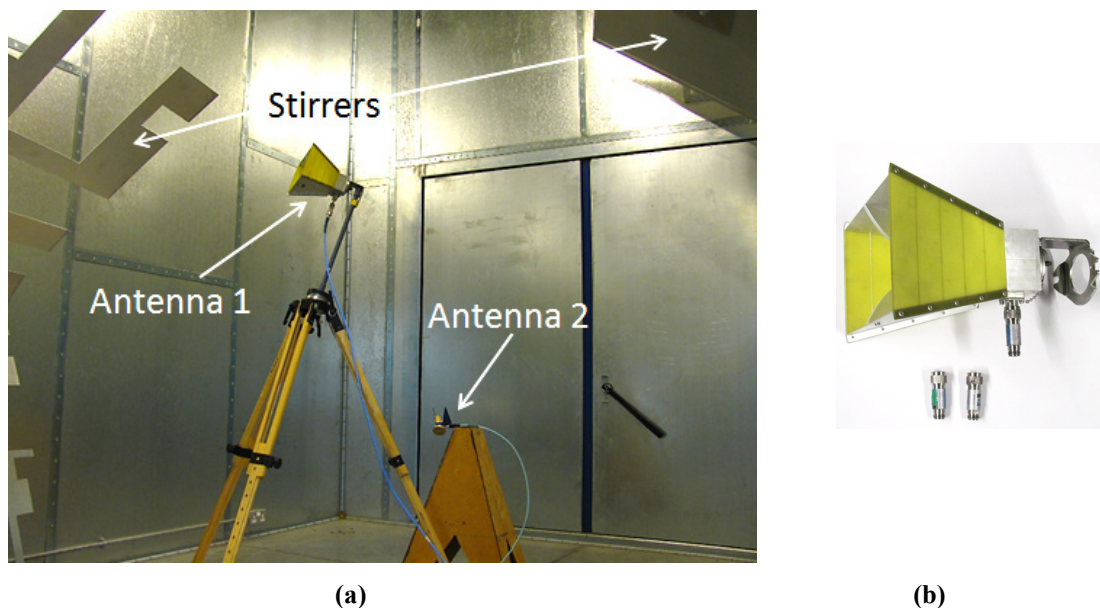


Fig. 5.5. (a) The radiation efficiency measurement setup in an RC (modified two-antenna method), (b) AUT with different attenuators.

The measured S -parameters of antenna 1 with different attenuators are shown in Fig. 5.6. It can be seen that when the attenuation is large, the effect of RC could become too small to be detected in the dynamic range of the VNA. The corresponding $\ln(\text{IFFT}(S)^2)$ are shown in Fig. 5.7, which can be regarded as the measured power signal in the time domain. It can be found that the reflected signal is so small that it quickly drops below the noise level and cannot be detected in the limited dynamic range.

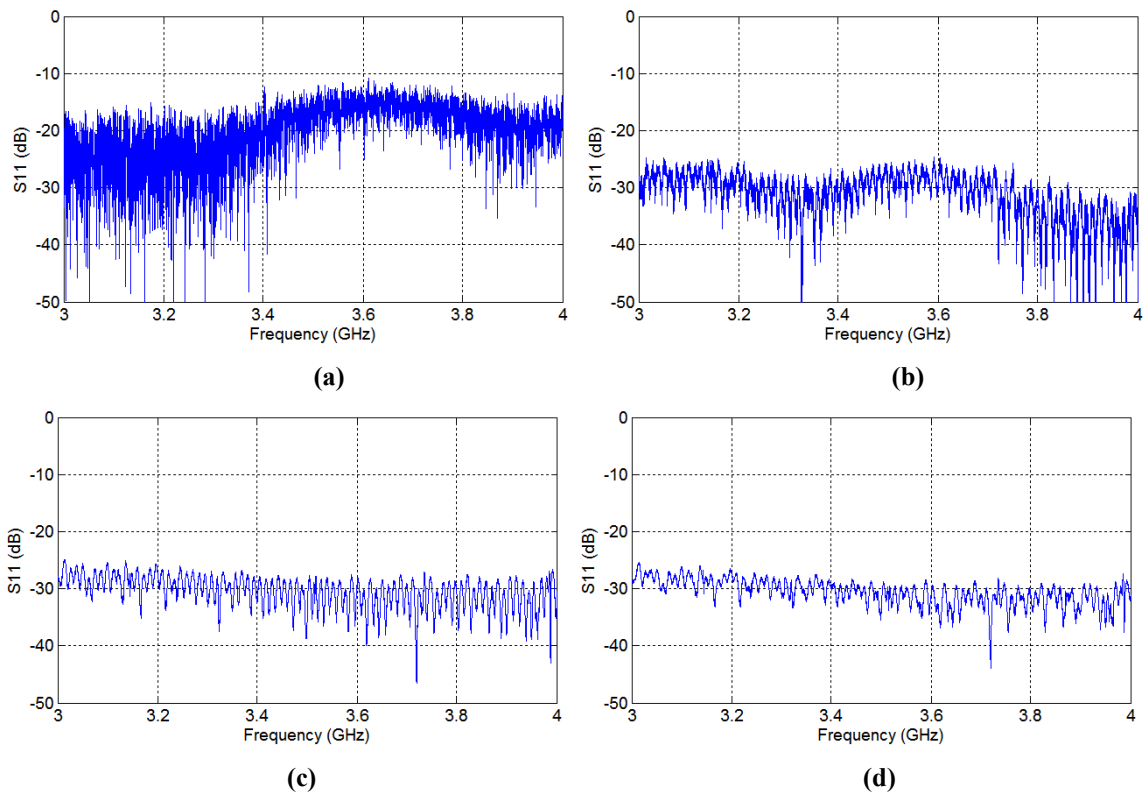


Fig. 5.6. Typical measured S -parameters with different attenuators (a) 0dB, (b) 10 dB, (c) 20 dB, (d) 30 dB.

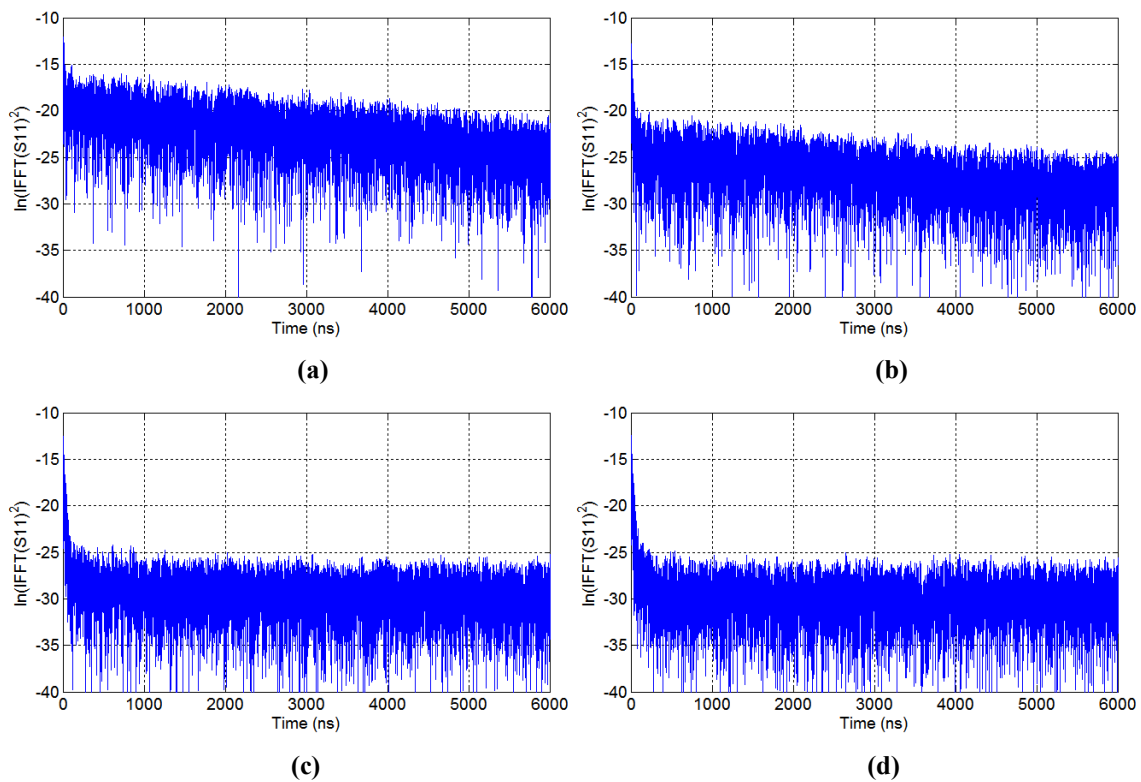


Fig. 5.7. $\ln(\text{IFFT}(S)^2)$ of the typical measured S -parameters with different attenuators (a) 0 dB, (b) 10 dB, (c) 20 dB, (d) 30 dB.

Because the power decay in the RC follows $P_0 e^{-t/\tau_{RC}}$, τ is the measured decay time which can be obtained from the slope (k) of $\ln(\text{IFFT}(S)^2)$, which is $\tau_{RC} = -1/k$ [51]. When the attenuation of antenna 1 is large we cannot extract τ_{RC} from $\ln(\text{IFFT}(S_{11})^2)$ so we use τ obtained from $\ln(\text{IFFT}(S_{22})^2)$, since antenna 2 is a highly efficient antenna and the time domain response has a better signal to noise ratio (SNR) over the time period of interest, the chamber decay time τ_{RC} becomes easy to extract. Since τ_{RC} is frequency dependent, an elliptic band-pass filter with 200 MHz bandwidth was used to obtain τ_{RC} for different centre frequency [34, 51]. The averaged τ_{RC} obtained from 359 stirrer locations is shown in Fig. 5.8.

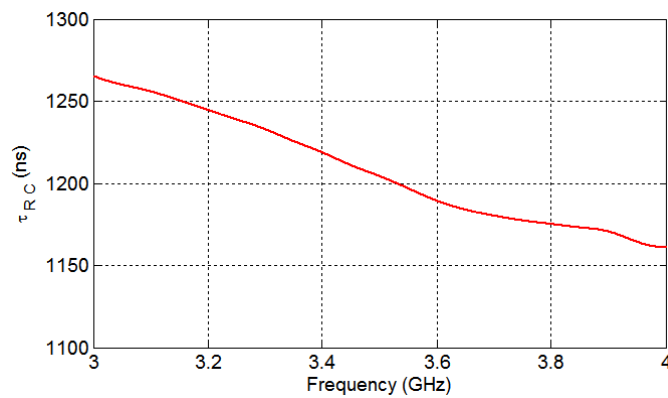


Fig. 5.8 τ_{RC} extracted from $\ln(\text{IFFT}(S_{22})^2)$.

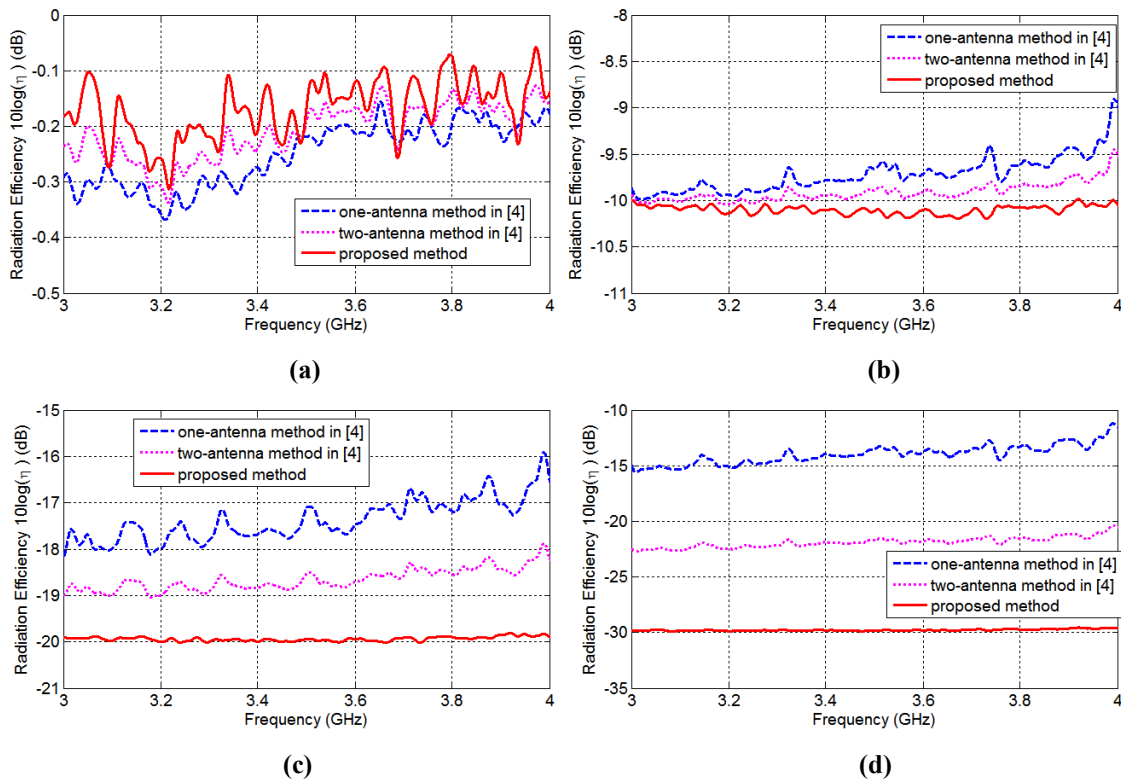


Fig. 5.9. The measured radiation efficiency of antenna 1 with different attenuators. (a) 0 dB attenuator, (b) 10 dB attenuator, (c) 20 dB, (d) 30 dB.

Three methods have been used to process the collected S -parameters: the proposed method using (5.22), the one-antenna method, and the two-antenna method in [3]. The frequency stir with 100 sample points were also used (14 MHz bandwidth) to provide an averaged result for each frequency - this makes $359 \times 100 = 35,900$ samples at each frequency, the measured results are given in Fig. 5.9.

As expected, when the antenna radiation efficiency is high, the results from 3 methods are in a good agreement, even when the radiation efficiency is close to -10 dB, the results are still very similar. However, when the radiation efficiency decreases to -20 dB or -30 dB the one-antenna and two-antenna methods give inaccurate prediction but the proposed method still has a good performance. This problem was not caused by τ_{RC} but from $S_{11,s}$, because τ_{RC} was extracted from S_{22} . As discussed before, when antenna 1 is very lossy, the magnitude of the reflected signal can be very small (outside the dynamic range of the VNA after calibration and poor SNR), this is easy to understand, when a 30 dB attenuator is connected and the chamber loss is around 20 dB, the received signal will be around $30 + 20 + 30 = 80$ dB smaller than the transmitted signal, which is most likely comparable with noise. Also note that the error from the one-antenna method is larger than that from the two-antenna method, this was also found in [3], this is understandable from mathematical point of view, since the precondition $e_{b1} = e_{b2} = 2$ for one-antenna method is stricter than $e_{b1} = e_{b2}$ for two-antenna method, thus two-antenna method has smaller deviation.

5.2.4 Short Summary of Section 5.2

A modified two-antenna method to measure the radiation efficiency of antennas in an RC has been proposed. The conventional method [1] requires a reference antenna, the one-antenna method and two-antenna method in [3] require no reference antenna, but the loss of the antenna must be much smaller than the loss of the RC. The method proposed in this chapter does not need a reference antenna with known efficiency and the loss of the AUT can be arbitrary. The proposed method offers an opportunity to measure the antenna with very low radiation efficiency (e.g. implantable antenna with η around 0.3% [52-53]) in the RC. The proposed method can also be generalised to nonreciprocal antennas (active antennas). If the transmitting (Tx) efficiency and receiving (Rx) efficiency of the AUT are different (nonreciprocal), the total Tx efficiency (at certain Tx power) and total Rx efficiency (at certain Rx signal strength) will be

$$\eta_{tot1Tx} = \langle |S_{21,s}|^2 \rangle \sqrt{2C_{RC} / [\omega\tau_{RC} \langle |S_{22,s}|^2 \rangle]} \quad (5.24)$$

$$\eta_{tot1Rx} = \langle |S_{12,s}|^2 \rangle \sqrt{2C_{RC} / [\omega\tau_{RC} \langle |S_{22,s}|^2 \rangle]} \quad (5.25)$$

Some issues should be noted when applying this method:

- 1) The RC must be well-stirred. The enhanced back scatter effect is invalid when the RC is not well-stirred and the e_b will not be 2, this is the fundamental assumption of the proposed method.
- 2) The assumption of *antenna 2 being a highly efficient antenna* is to make sure that $S_{22,s}$ is in the dynamic range of the VNA. The measured η_1 does not depend on the radiation efficiency of antenna 2. Antenna 2 is used to extract the chamber transfer function and τ_{RC} , as long as η_2 can be measured accurately using one-antenna method, the radiation efficiency of antenna 2 can be arbitrary. From Fig. 5.9(b), it can be seen that there is 1 dB error at 4 GHz for the one-antenna method. In this scenario, as long as η_2 is larger than 10%, the error caused by η_2 will be smaller than 1 dB.
- 3) As can be seen in (5.22) and (5.23), τ_{RC} obtained from antenna 2 affects the results directly, thus τ_{RC} should be carefully measured, and antenna 2 must be an efficient antenna. It should be noted that the chamber decay time is an intrinsic value related with the RC (including load), however, in practice, when it is measured using very lossy antennas, the time domain response is affected by the antenna, this was also pointed out in [3]. The attenuators do not change τ_{RC} , but affect the time domain response (extracted from $IFFT(S_{11})$) which makes τ_{RC} hard to be extracted (because of the noise level/dynamic range). τ_{RC} is determined by the chamber loss and all the loading effect, including the antennas.
- 4) If the radiation efficiency is so small that the $S_{21,s}$ in (5.22) or (5.23) is outside the dynamic range of VNA, an amplifier can be used, the original $S_{21,s}$ can be obtained by adding the offset.

5.3 Diversity Gain Measurement in an RC

Reverberation chambers (RCs) have been used to emulate the multipath propagation channel in mobile communications in indoor and outdoor environments [34]. To mitigate the fading in the multipath environment, more than one antenna is used to transmit and receive the radio signal so as to increase the channel capacity and improve the signal-to-noise ratio (SNR) in a MIMO system. The received signals from different channels are combined with a specific strategy such as the switching, selection combining or maximum combining schemes. The *diversity gain* (DG) is an important figure of merit to measure the MIMO system performance, which normally gives a direct understanding of how the MIMO system outperforms the single channel system.

The definition of DG may have different forms depending on the reference used. The *apparent* DG is the measured data relative to the branch with the strongest power level at a given level of the

cumulative distribution function (CDF) of the received signal while the *effective* DG uses the ideal reference antenna at a given CDF level and the *actual* DG uses the single antenna as the reference at a given CDF level [26, 27]. The effective DG corrects the impedance mismatch with the transmission line and the dissipative loss and is widely used to characterise the performance of the MIMO antenna.

Traditionally, in addition to the AUT, two extra antennas are needed: one is used as the transmit (Tx) antenna, the other is used as a reference antenna which must have known radiation efficiency. This could be a problem for some labs. The measured channel samples are normalised using the radiation efficiency of the reference antenna and the chamber transfer function. The CDF of the normalised samples can be obtained and the DG value can be read directly from the CDF figure [25-27].

In this research, a 2-branch MIMO antenna is used to demonstrate the proposed method which can be extended to any number of branches. The proposed method incorporates the one- or two-antenna method for radiation efficiency measurement [3]. The measurements and verifications of the proposed method are given; conclusions are drawn in the final section.

5.3.1 Traditional Diversity Gain Measurement Method

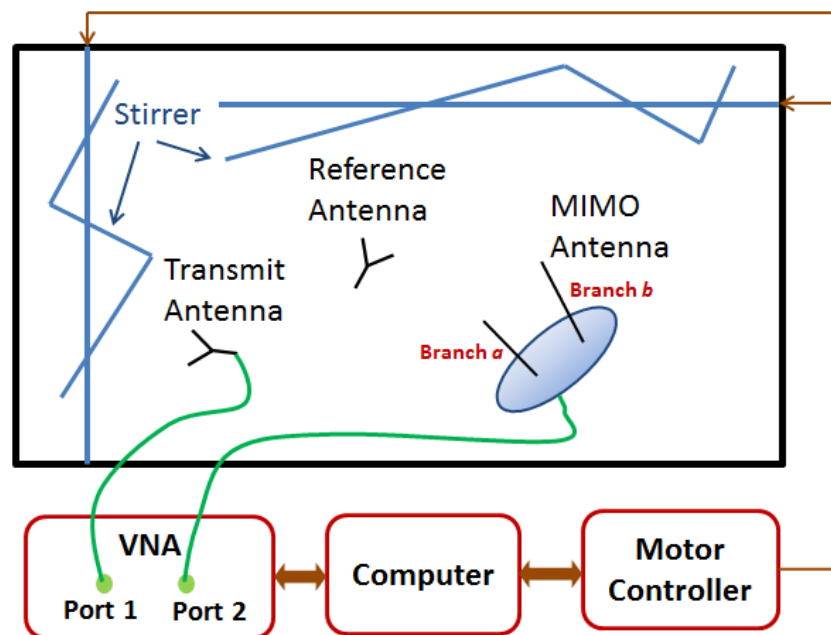


Fig. 5.10. MIMO antenna measurement system using an RC.

The MIMO antenna measurement system in a RC is given in Fig. 5.10 where the computer controls the operation of the stirrers and collects the S -parameters from the vector network analyser (VNA) for each stirrer position. Step motors are used to drive the stirrers and ensure the repeatability of the stirrers. The measurement procedure is given as follows:

Step 1) Calibrate the VNA including the cables used to connect the antennas.

Step 2) Place all the antennas inside the chamber to keep the chamber Q factor constant.

Step 3) Connect the Tx antenna to the VNA port 1 and the reference antenna to port 2, load the AUT with a 50 Ohm termination, and collect the full S -parameters (S_{11Tx} , S_{21Ref} , S_{22Ref}) for each stirrer position.

Step 4) Connect the AUT branch a to port 2, load the reference antenna and AUT branch b with a 50 Ohm termination, collect S -parameters S_{21a} for each stirrer position.

Step 5) Repeat Step 4) with port 2 connected to the AUT branch b while AUT branch a with a 50 Ohm termination and collect S -parameters S_{21b} for each stirrer position.

It is necessary to note that in Step 4) and Step 5), the stirrer position must be the same to make sure that the environment is unchanged, an alternative way is to use an RF switch to select the channel from port a or b or use VNA with more than two ports [54]. Otherwise the received signals from different branches are decorrelated and independent which has no meaning of diversity gain.

After all the S -parameters are collected, the normalized channel samples for branches a and b are

$$h_{21a} = |S_{21a,s}| \sqrt{\frac{\eta_{Ref}(1 - \langle |S_{11Tx}|^2 \rangle)}{T_{Ref}}} \quad (5.26)$$

$$h_{21b} = |S_{21b,s}| \sqrt{\frac{\eta_{Ref}(1 - \langle |S_{11Tx}|^2 \rangle)}{T_{Ref}}} \quad (5.27)$$

where η_{Ref} is the radiation efficiency of the reference antenna, T_{Ref} is the chamber transfer function measured by using the reference antenna, the definition is

$$T_{Ref} = \frac{\langle |S_{21Ref,s}|^2 \rangle}{(1 - \langle |S_{11Tx}|^2 \rangle)(1 - \langle |S_{22Ref}|^2 \rangle)} \quad (5.28)$$

$S_{*,s}$ is the stirred part of the S -parameter [3] defined in (5.8), Different from [26] we use the magnitude of the S -parameter while the direct coupling part is removed by using the well-known vector average subtraction in (25).

If we choose the maximum value of these two branches, the combined samples are

$$h_{comb} = \max(h_{21a}, h_{21b}) \quad (5.29)$$

Other strategies are also applicable for the method proposed. From the CDF plot of h_{21a} , h_{21b} and h_{comb} the diversity gain value can be obtained.

5.3.2 Diversity Gain Measurement without a Reference Antenna

The radiation efficiency measurement in a RC without a reference antenna has been investigated [3]. Checking (5.26) - (5.28) carefully, we have found that the chamber transfer function T_{Ref} can actually be obtained from one branch of AUT and this branch can be used as the reference antenna at the same time. Thus the reference antenna is not necessary and Step 3) in the traditional procedure can be skipped. And in Steps 4) and 5) all S -parameters need to be collected. To validate this idea, let us assume that branch a of the AUT is used as the reference antenna, if the two-antenna method is used, the radiation efficiency of branch a will be [3]

$$\eta_{Ref} = \eta_a = \sqrt{\frac{C_{RC} \langle |S_{22a,s}|^2 \rangle_{cor}}{\omega e_b \tau_{RC}}} \quad (5.30)$$

where C_{RC} is the chamber constant defined in (5.6), $\omega = 2\pi f$ is the angular frequency, τ_{RC} is the chamber decay time which can be obtained from the inverse Fourier transform (IFFT) of S -parameters [3, 34], e_b is the enhanced back scatter constant [50]

$$e_b = \frac{\sqrt{\langle |S_{11Tx,s}|^2 \rangle \langle |S_{22a,s}|^2 \rangle}}{\langle |S_{21a,s}|^2 \rangle} \quad (5.31)$$

$\langle |S_{22a,s}|^2 \rangle_{cor}$ is the corrected S -parameter

$$\langle |S_{22a,s}|^2 \rangle_{cor} = \frac{\langle |S_{22a,s}|^2 \rangle}{(1 - \langle |S_{22a}|^2 \rangle)^2} \quad (5.32)$$

The chamber transfer function can be written as

$$T_{Ref} = \frac{\langle |S_{21a,s}|^2 \rangle}{(1 - \langle |S_{11Tx}|^2 \rangle)(1 - \langle |S_{22a}|^2 \rangle)} \quad (5.33)$$

By substituting (5.30) into (5.26) and (5.27), replacing (5.28) with (5.33), the reference antenna is eliminated, thus the proposed method is mathematically proved.

$$h_{21a} = |S_{21a,s}|(1 - |\langle S_{11Tx} \rangle|^2) \sqrt{\frac{C_{RC} \langle |S_{22a,s}|^2 \rangle}{\omega e_b \tau_{RC}}} \sqrt{\frac{1}{\langle |S_{21a,s}|^2 \rangle}} \quad (5.34)$$

$$h_{21b} = |S_{21b,s}|(1 - |\langle S_{11Tx} \rangle|^2) \sqrt{\frac{C_{RC} \langle |S_{22a,s}|^2 \rangle}{\omega e_b \tau_{RC}}} \sqrt{\frac{1}{\langle |S_{21a,s}|^2 \rangle}} \quad (5.35)$$

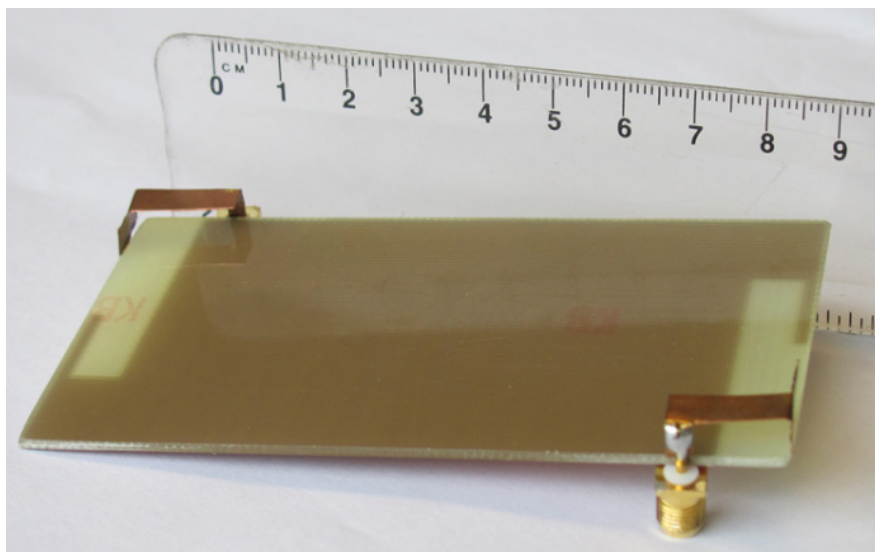
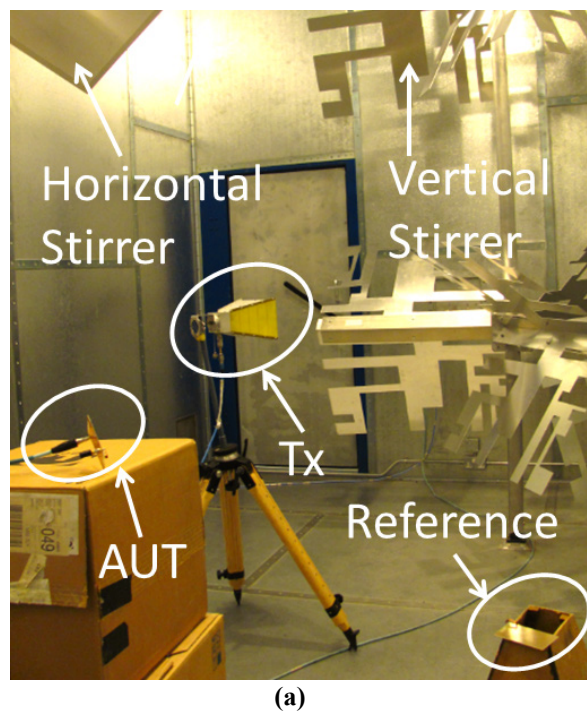


Fig. 5.11. Measurement setup in RC using traditional method: (a) the system view, (b) the AUT.

To validate the proposed new method, we employ both the traditional method and the proposed method for MIMO antenna measurements. We first apply the traditional DG measurement method. The measurement setup is shown in Fig. 5.11(a); empty cartons are used to support the AUT for the simplicity reason. The size of the RC is $3.6 \text{ m} \times 4 \text{ m} \times 5.8 \text{ m}$. The frequency setting of the VNA is $1 \text{ GHz} \sim 4 \text{ GHz}$ with 10,001 sample points. The reason for having chosen so many points is that we need to calculate the chamber decay time τ_{RC} from the IFFT of S -parameter, under this setting, the resolution time step of IFFT is 0.25 ns and the total time is 2,500 ns. The AUT is shown in Fig. 5.11(b), the Tx antenna is a double-ridged waveguide horn antenna (Rohde & Schwarz® HF906). The reference antenna is a homemade planar inverted-L antenna (PILA) and the detailed dimensions are given in [55]. The mechanical stirring sample number is 360 with 1° step size.

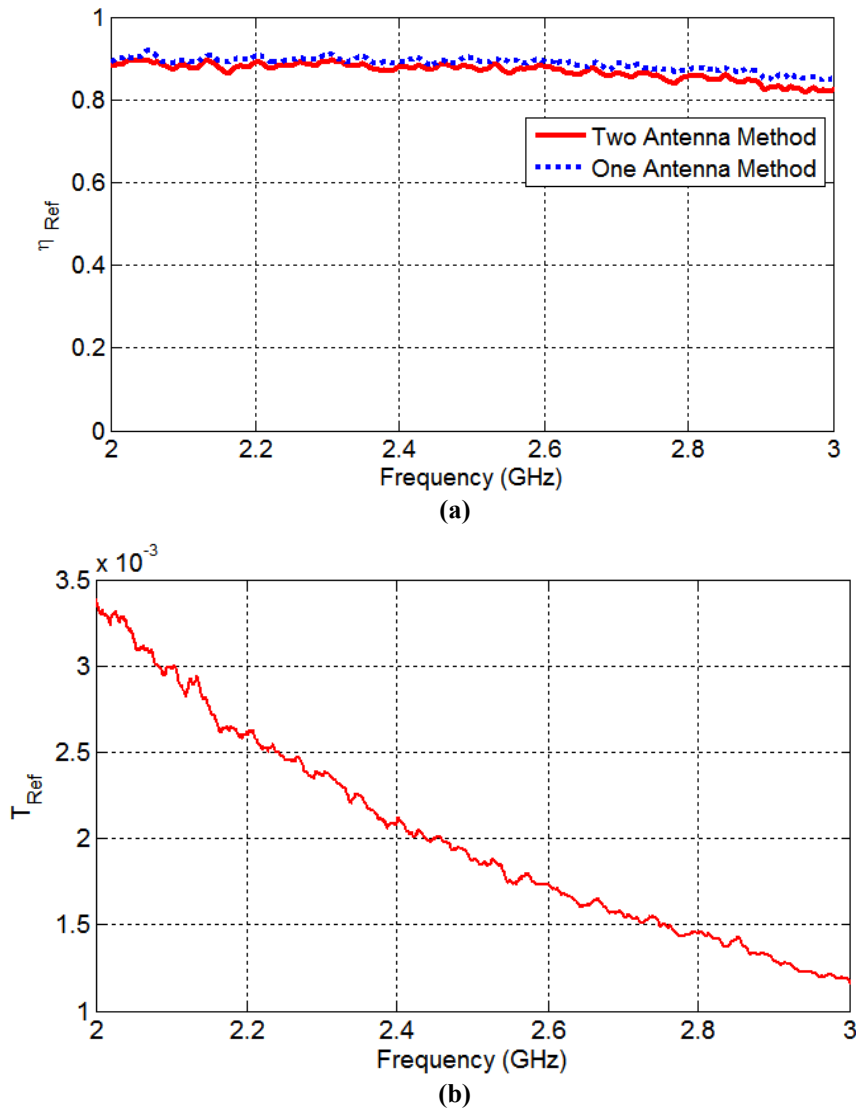


Fig. 5.12. (a) Radiation efficiency of the reference antenna (PILA) by using one- and two-antenna methods, (b) chamber transfer function obtained from the reference antenna (PILA).

The radiation efficiency of the PILA is obtained by using one- and two- antenna methods [3], including mechanical stir, frequency stir with nearest 50 frequency samples are used, this means $360 \times 50 = 18,000$ samples for each frequency. The radiation efficiency results are shown in Fig. 5.12(a). As can be seen, a good agreement is obtained between one- and two- antenna methods. We use the values from the two-antenna method to calculate the normalized samples, since it has a smaller uncertainty [3]. The chamber transfer function T_{Ref} has also been calculated using (5.28) and the result is given in Fig. 5.12(b).

All the samples between 2 GHz ~ 3 GHz (the working frequency of the AUT) are used to plot the CDF. This means $360 \times 3,335 = 1,200,600$ samples for each branch. The results are given in Fig. 5.13. Because the antennas for the two branches are the same, the CDFs from the two branches are the same. The apparent DG and the effective DG at 1% can be obtained from Fig. 5.13 as $-11.05 + 21.24 = 10.19$ dB and $-11.05 + 20.33 = 9.28$ dB, respectively.

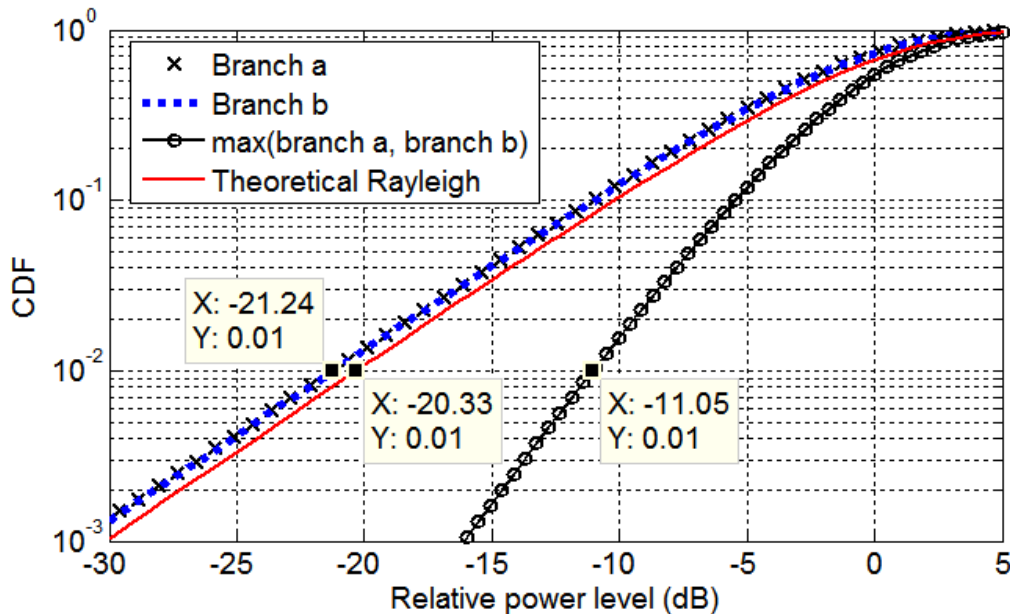


Fig. 5.13. CDF plot of both branches and the combined signal, theoretical Rayleigh distribution is also given.

As discussed before, if we treat branch *a* as the reference antenna, the reference antenna PILA is now not needed. The chamber decay time τ_{RC} can be extracted from the *S*-parameters, as shown in Fig. 5.14. Since τ_{RC} can be extracted from any of the *S*-parameters [3], the average value is used. It can be seen that they are very similar and we use the average value to calculate η_{Ref} in (5.30). The enhanced back scatter constant in (5.31) are extracted from the *S*-parameters and shown in Fig. 5.15, it is very close to 2 which means the RC is well stirred [3]. Thus, the radiation efficiency of the branch *a* antenna can be obtained using (5.30) which is shown in Fig. 5.16(a). In addition, Fig. 5.16(b) gives

the chamber transfer function calculated using (5.33), which agrees well with that obtained using the traditional method in Fig. 5.12(b).

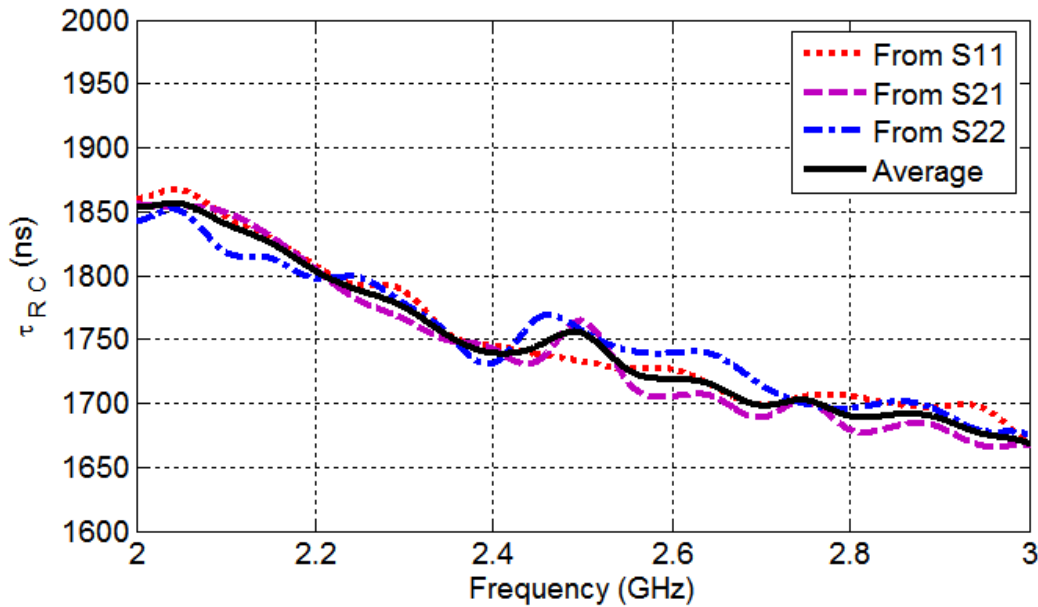


Fig. 5.14. Chamber decay time extracted from S -parameters.

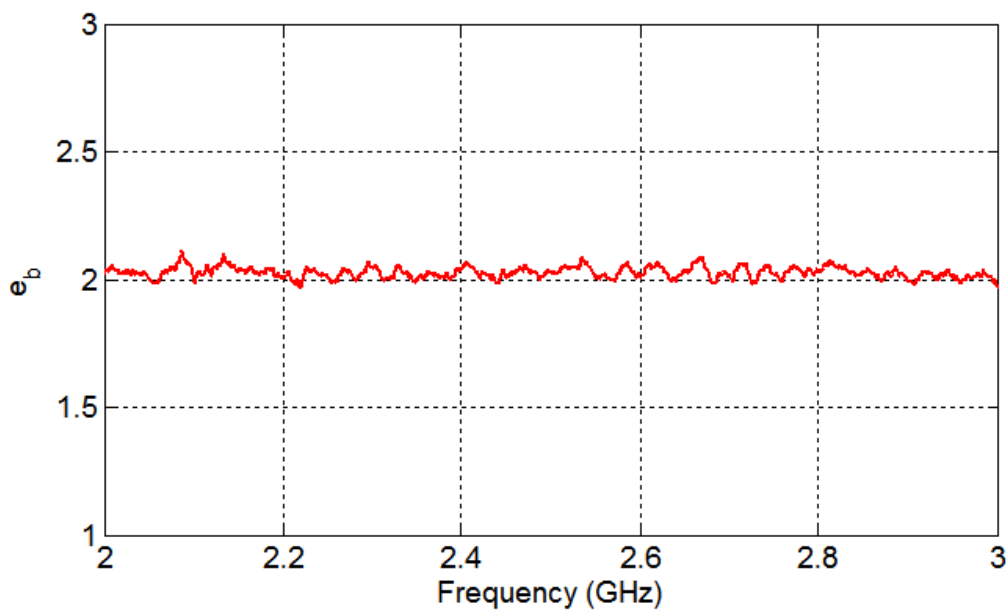


Fig. 5.15. Enhanced back scatter constant extracted from S -parameters.

Finally, we use the same sample number as in the traditional method to generate the CDF which is given in Fig. 5.17. The apparent DG and the effective DG at 1% are 10.19 dB and 9.15 dB, correspondingly, which are very close to the traditional measurement results. Because the DG is frequency dependent, we have also divided the working frequency range 2 GHz ~ 3 GHz into 10 bands (100 MHz each) and verified the DG values using both the traditional and proposed methods.

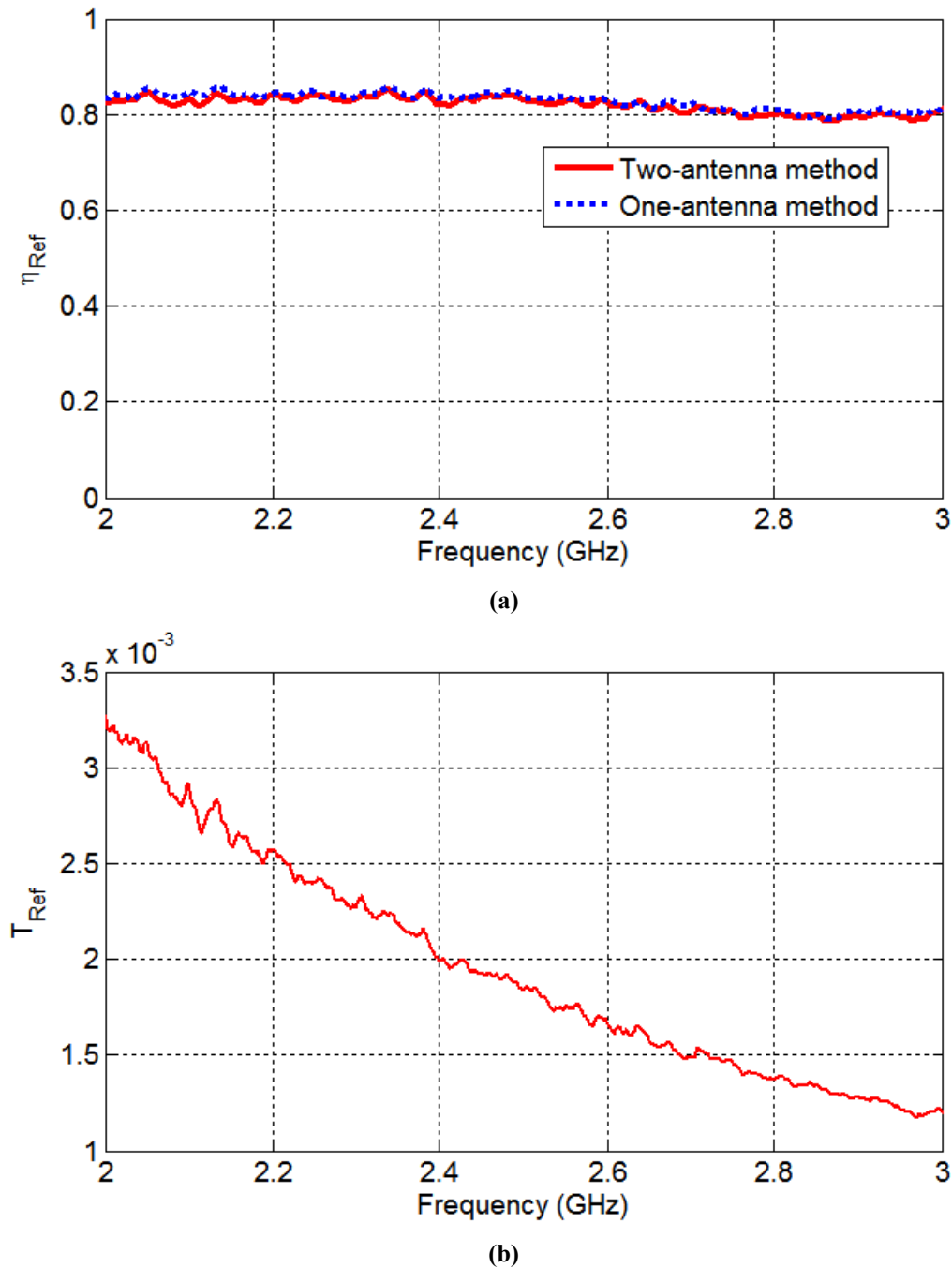


Fig. 5.16. (a) Radiation efficiency of the reference antenna (branch *a*) by using one and two antenna method, (b) chamber transfer function obtained from the branch *a*.

The results are also in a very good agreement (Appendix A1). It can be seen that, how the frequency band is allocated will not affect both the traditional and the proposed method.

The results from the two methods are summarised in Table 5.2, (at the centre frequency 2.5 GHz with 1 GHz bandwidth). They are in good agreement. The biggest difference is 0.13 dB which is quite small, thus this has proved the validity of the proposed method.

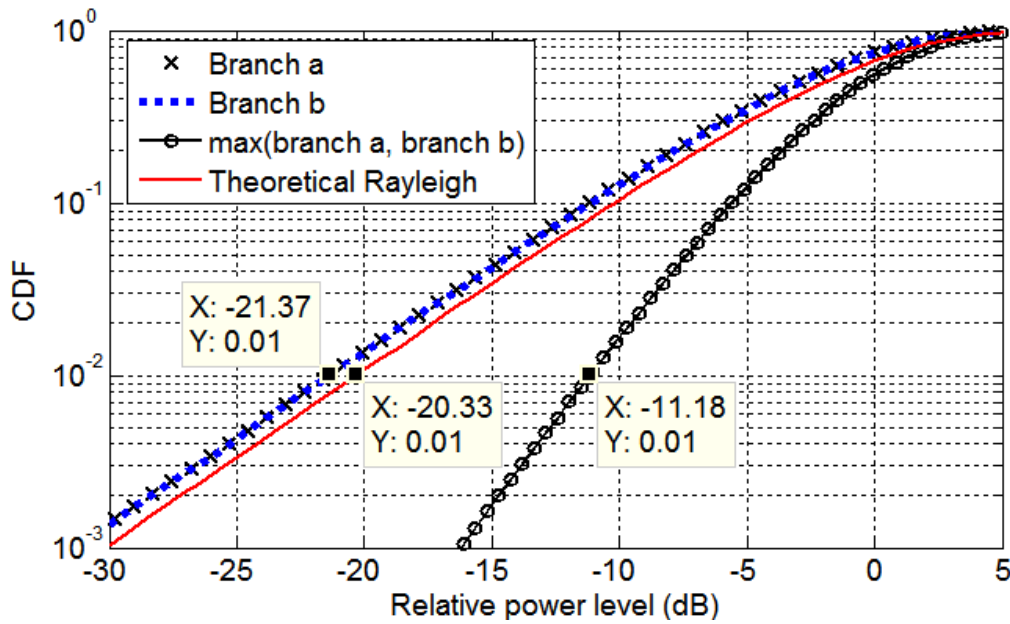


Fig. 5.17. CDF plot of both branches and the combined signal using method without reference antenna.

Table 5.2: DG Results Comparison

Apparent DG (dB)	Effective DG (dB)	Method
10.19	9.28	Traditional method
10.19	9.15	Proposed method

5.3.3 Diversity Gain Measurement without Extra Antennas

We showed that by incorporating the one- or two-antenna method for antenna efficiency measurement into the DG measurement, the reference antenna is not needed and one of the branches of the MIMO antenna can be used as the reference antenna. This can simplify the measurement setup greatly.

Further study suggests that the Tx antenna can also be eliminated by taking advantage of the enhanced back scattering effect and introducing a virtual antenna, one branch of the MIMO antenna can be treated as the Tx antenna, this leads a new measurement method without the need for any additional antenna. Only the antenna under test (AUT) is required. The measurement setup is given in Fig. 5.18.

Assume that port 1 is connected to branch *a* and port 2 is connected to branch *b* of the AUT. If branch *a* is treated as the reference antenna, the radiation efficiency of branch *a* becomes

$$\eta_{Ref} = \eta_a = \sqrt{\frac{C_{RC} \langle |S_{11a,s}|^2 \rangle_{cor}}{\omega e_b \tau_{RC}}} \quad (5.36)$$

which eliminates the need for a reference antenna, where C_{RC} is the chamber constant defined in (5.6), the chamber transfer function in (5.28) can now be written as

$$T_{Ref} = \frac{\langle |S_{21ab,s}|^2 \rangle}{(1 - \langle |S_{11a}|^2 \rangle)(1 - \langle |S_{22b}|^2 \rangle)} \quad (5.37)$$

and (5.27) becomes

$$h_{21ab} = |S_{21ab,s}| \sqrt{\frac{\eta_{Ref}(1 - \langle |S_{11a}|^2 \rangle)}{T_{Ref}}} \quad (5.38)$$

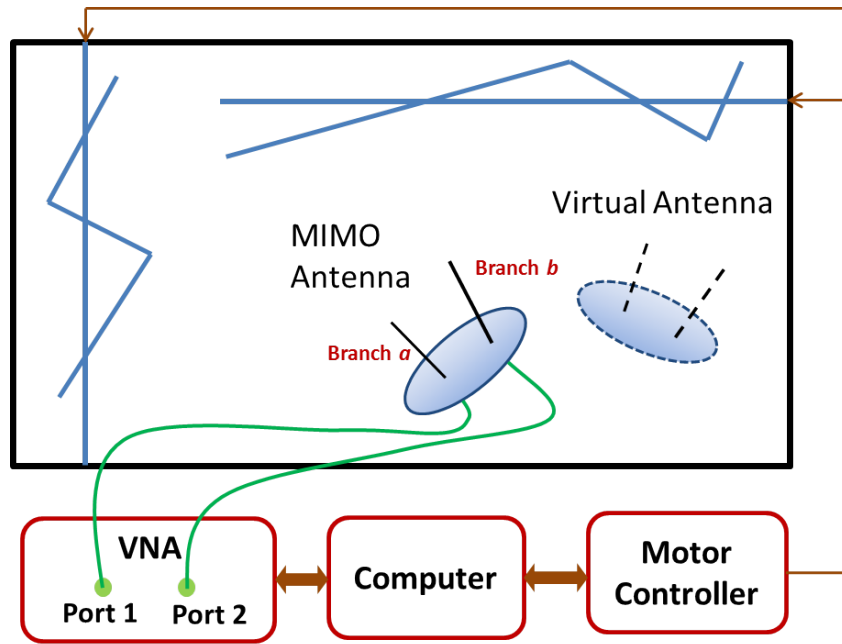


Fig. 5.18. Introduce a virtual antenna which is the same as AUT.

Equation (5.38) can be regarded as an alternative form of (5.27) if we treat branch a as the Tx antenna. Next we need to extract the receiving samples in (5.26) from S_{11a} . Like the one-antenna method in [3], we introduce a virtual antenna which is exactly the same as branch a as shown in Fig. 5.18. Suppose that the chamber is well stirred, we have [50]

$$e_b = \frac{\sqrt{\langle |S_{11a,s}|^2 \rangle \langle |S_{22v,s}|^2 \rangle}}{\langle |S_{21va,s}|^2 \rangle} = 2 \quad (5.39)$$

where the $S_{22v,s}$ and $S_{21va,s}$ are the S -parameters of the virtual antenna. Since the virtual antenna is exactly the same as the AUT, we have $\langle |S_{11a,s}|^2 \rangle = \langle |S_{22v,s}|^2 \rangle$, this makes

$$\langle |S_{21va,s}|^2 \rangle = \frac{\langle |S_{11a,s}|^2 \rangle}{2} \quad (5.40)$$

If branch a and branch b are well isolated, which means the signal received by these two ports are not relevant. Thus the signal samples received by branch a in (5.26) can be rewritten as

$$h_{21va} = |S_{11a,s}| \sqrt{\frac{\eta_{Ref}(1 - \langle |S_{11a}|^2 \rangle)}{2T_{Ref}}} \quad (5.41)$$

And the combined signal in (5.29) becomes

$$h_{comb} = \max(h_{21va}, h_{21ab}) \quad (5.42)$$

Now the Tx antenna is eliminated. It is important to note that in (5.42) h_{21va} and h_{21ab} are not exactly in the same environment, it is easy to understand that $\langle |S_{21va,s}|^2 \rangle = \langle |S_{11a,s}|^2 \rangle / 2$ does not mean $S_{21va,s} = \sqrt{|S_{11a,s}|^2 / 2}$, but when the isolation between these two ports are good enough, h_{21va} and h_{21ab} are independent random variables, this makes (5.42) valid.

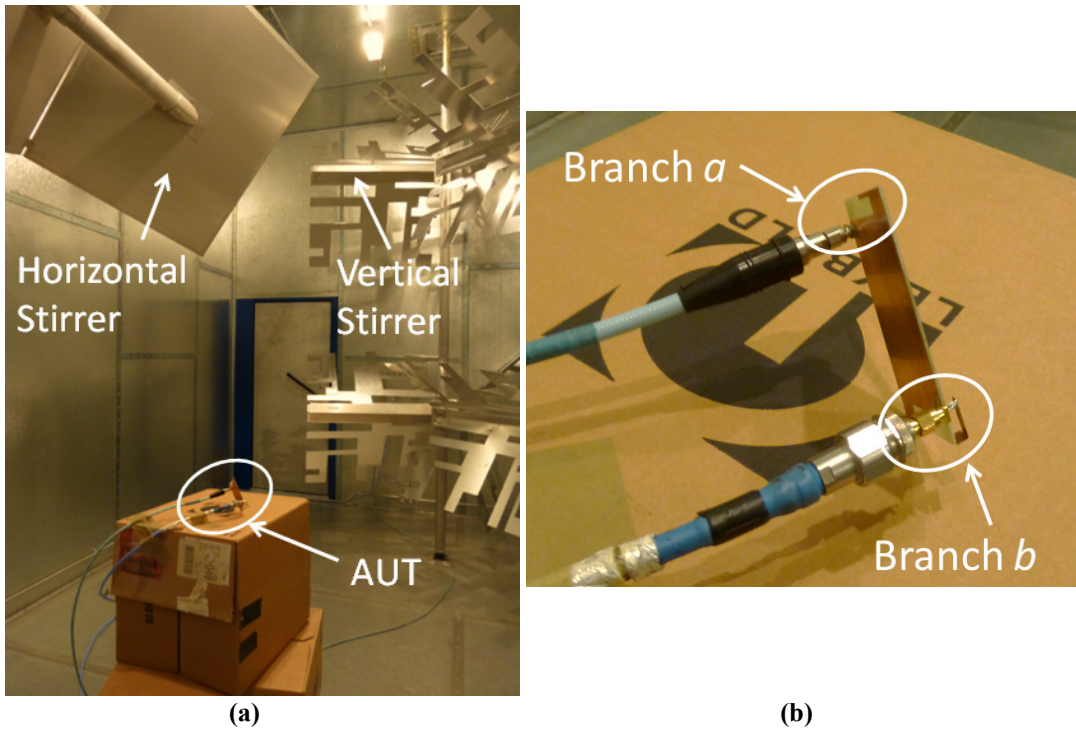


Fig. 5.19. Measurement setup in the RC using the method with no extra antennas: (a) the system view, (b) zoom in view of the AUT

The measurement setup for this method is shown in Fig. 5.19, empty cartons are used to support the AUT from the ground. Port 1 and port 2 of the VNA are connected to the branch a and branch b of the AUT. Branch a is considered as the reference antenna.

The size of the RC is $3.6 \text{ m} \times 4 \text{ m} \times 5.8 \text{ m}$. The frequency setting of the VNA is 1 GHz - 4 GHz with 10,001 sample points, this means that the time domain resolution of $\text{IFFT}(S)$ is 0.25 ns and the total time is 2,500 ns. The AUT is a homemade two-port planar inverted-L antenna (PILA) and the detailed dimensions are given in [55]. The mechanical stirring sample number is 360 with 1° step size, and the frequency stir with nearest 50 frequency samples is also used, this means $360 \times 50 = 18,000$ samples for each frequency. The measured e_b in (5.39) is shown in Fig. 5.20, compared with the measurement in the last section, they are in a very good agreement and close to 2, which means the chamber is well-stirred [3].

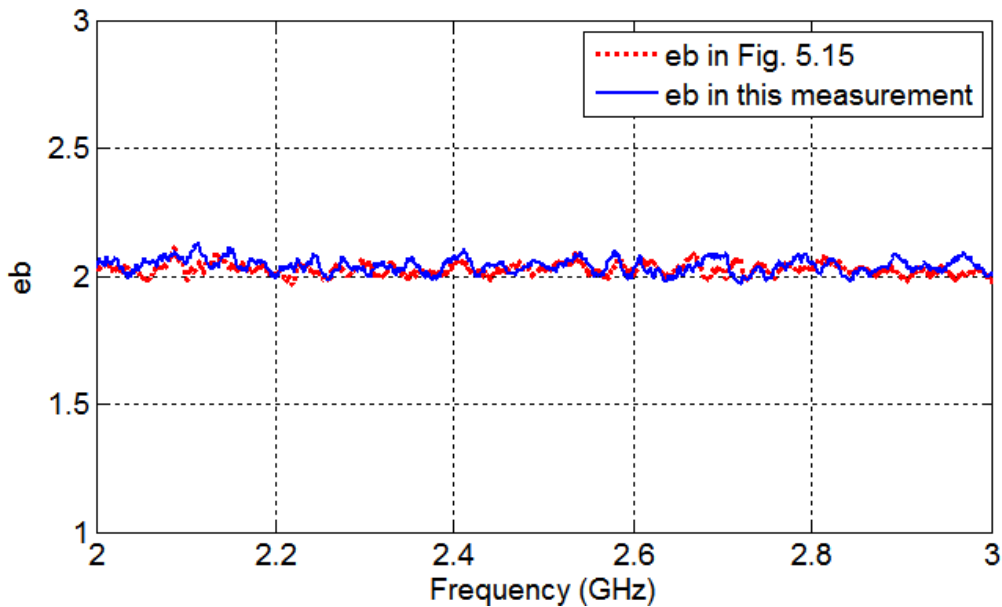


Fig. 5.20. Enhanced back scatter constant extracted from the measured S -parameters.

The radiation efficiency value of branch a has been given in Fig. 5.16(a). The chamber transfer function obtained using (5.37) is shown in Fig. 5.21. As can be seen, the chamber transfer function is larger than the previous measured value. This is because the horn antenna (as the Tx antenna) and the reference antenna (including the support structure) have been moved out from the RC which has reduced the loss of the chamber.

Finally, all the samples collected from 2 GHz to 3 GHz (the working frequency range of the AUT) are used to generate the CDF plot, and the combined CDF obtained from (5.42) is given in Fig. 5.22. The apparent DG and the effective DG at 1% are $-10.99 + 21.18 = 10.19 \text{ dB}$ and $-10.99 + 20.33 = 9.34 \text{ dB}$,

respectively. We have also checked the results using 100 MHz bandwidth; the results are similar (difference smaller than 1 dB).

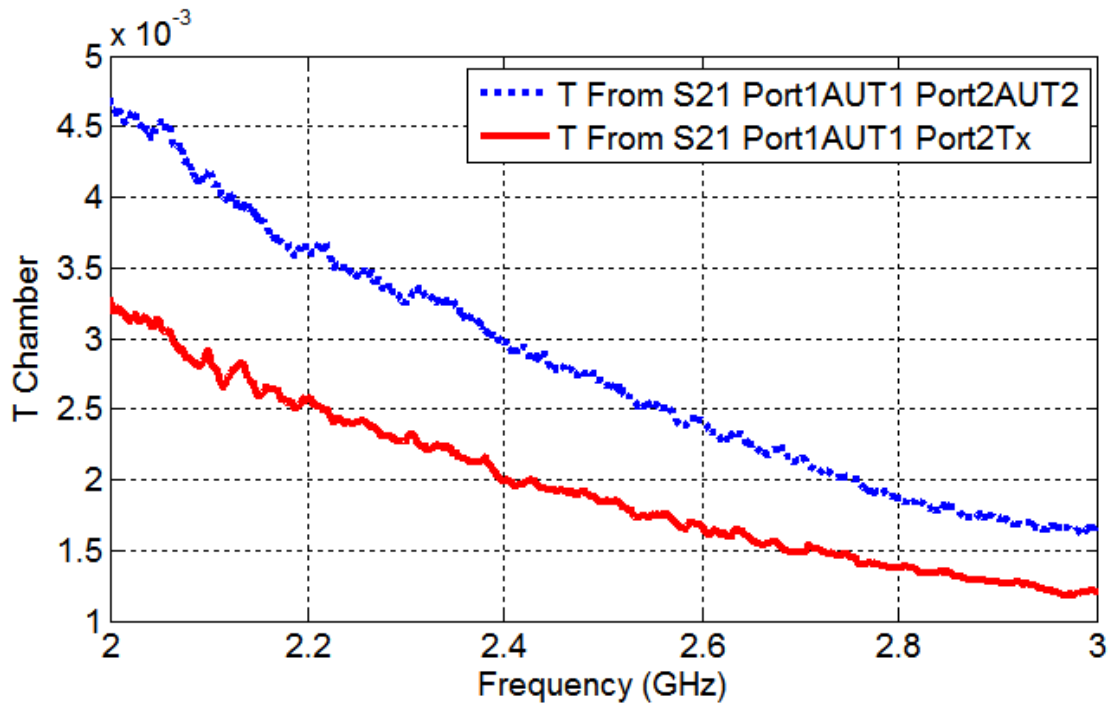


Fig. 5.21. Measured chamber transfer function using (5.37).

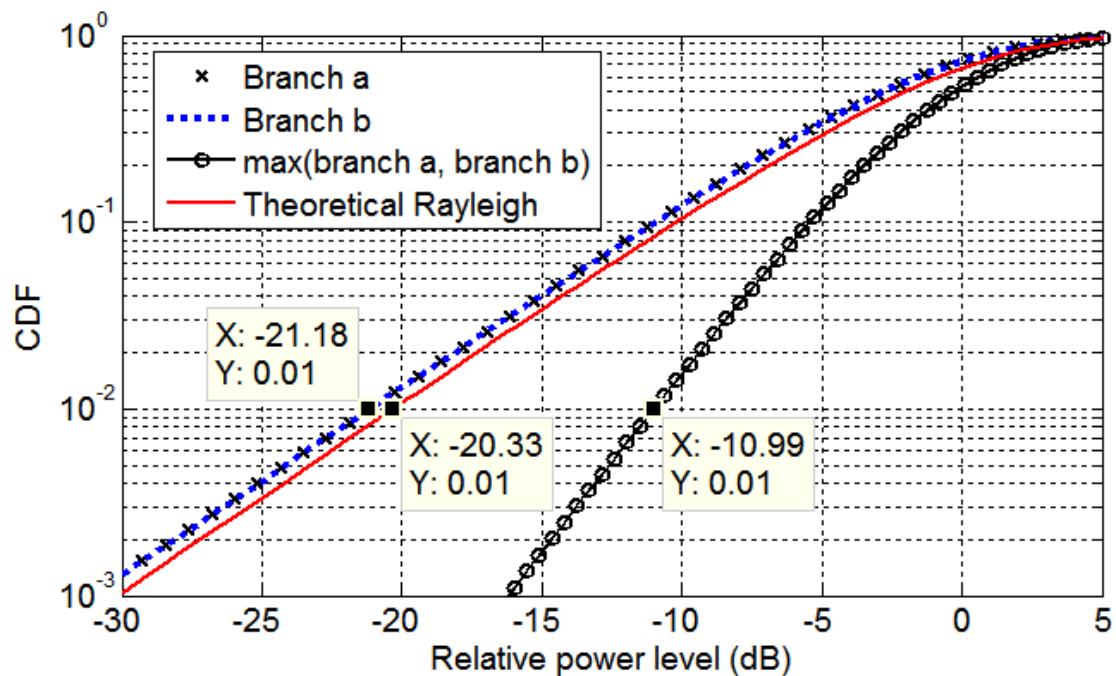


Fig. 5.22. CDF plot of both branches and the combined signal using the proposed method.

5.3.4 Short Summary of Section 5.3

It should be noted that the proposed method in Section 5.3.2 has limitations which may be easily ignored, when we use the one- or two- antenna method to extract the radiation efficiency of branch a , we assume that the assumptions in one- or two- antenna method are still valid in this environment.

Both one-antenna and two-antenna methods require that the RC is well stirred and the losses in the chamber are dominated by the chamber wall losses (including load). This means the channel is Rayleigh channel and the antenna loss will not change too much over the chamber decay time τ_{RC} . Additionally, for the one-antenna method, it requires $e_b = 2$; for the two-antenna method, it requires e_b to be identical for the AUT and Tx antenna (spatial homogeneity in the chamber), the required condition for the two-antenna method is weaker than the one-antenna method and gives high accuracy [3], and we choose the two-antenna method in this chapter. It is also possible to incorporate the three-antenna method to the DG measurement which needs one more step to connect the branch a and branch b to the port 1 and port 2 of the VNA.

The proposed method in Section 5.3.3 also has similar limitations, the method is based on the one- or two- antenna method in [3], the chamber must be well-stirred and the losses in the chamber are dominated by the chamber wall losses (including any load), the introduction of virtual antenna requires the conditions of one-antenna method to be satisfied ($e_b = 2$ and spatially uniform). It takes advantage of the enhanced back scattering effect by introducing the virtual antenna, it has been pointed out that $\langle |S_{21va,s}|^2 \rangle = \langle |S_{11a,s}|^2 \rangle / 2$ does not mean $S_{21va,s} = \sqrt{S_{11a,s}/2}$, when the mutual coupling between the MIMO branches is high, h_{21va} and h_{21ab} are no longer independent random variables, this will render the proposed method inaccurate, the distribution obtained from $S_{11a,s}$ cannot be used to predict the distribution of h_{21va} . To verify this, the mutual coupling is extracted from the unstirred part of S -parameters $\langle S_{21ab} \rangle$ and given in Fig. 5.23. It can be seen that the mutual coupling is very small, which validates the proposed method. The proposed method does not need extra antennas and the complexity of the measurement system is reduced. The S_{11} of each branch antenna and the mutual coupling between the branch antennas can also be extracted simultaneously (from the unstirred part of the S -parameters). It should be noted that the proposed method considers the radiation efficiency of branches, but decorrelates the signals when the mutual coupling is high. However, the measurement results still provide useful information (such as S -parameters, mutual coupling and radiation efficiency). The measured DG can be regarded as a practical limit when branches are well isolated.

Although a two-branch MIMO antenna is used in this chapter, the proposed method can be easily extended to an arbitrary number of branches. Thus it is an effective and general method for MIMO antenna measurements. Future work may include the degradation analysis of the proposed method with different MIMO antennas. The method proposed in this chapter can also be generalised to measure the channel capacity following a similar procedure [26-27].

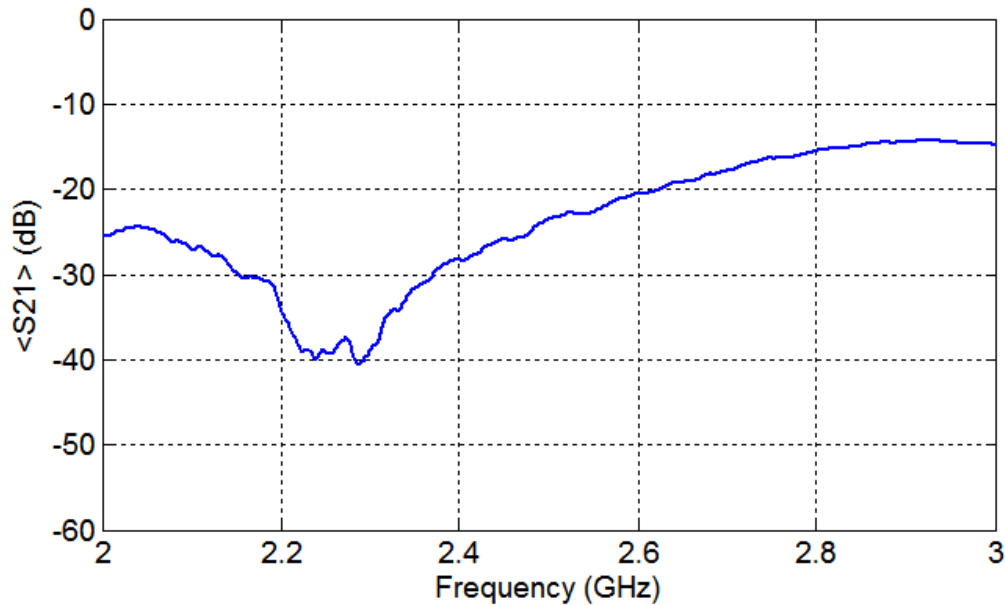


Fig. 5.23. Mutual coupling of the two branches of the MIMO AUT.

5.4 Radiated Emission Measurement in an RC

Reverberation chambers have been used to measure the radiated emission (RE) of equipment under test (EUT) since 1975 [56]. The standard procedure has been well established in IEC 6100-4-21 standard [1]. In 2006, efforts were made to simplify the measurement procedure, by measuring the received power in the time domain, the RC does not need to be calibrated in advance [18]. However, this method requires the signal generator (SG) to be switched off quickly (much smaller than the chamber decay time) and the spectrum analyser (SA) needs to work in a zero span mode to record the received power in the time domain. Moreover, the SG and the SA must be synchronised for trigger. These could be a problem for some instruments. In 2011, new methods on antenna radiation efficiency measurement without reference antenna in an RC were developed (the one-, two- and three-antenna method) [3]. This offers an opportunity to further simplify the RE measurement procedure in an RC.

In this section, two new alternative methods are proposed by incorporating the one- and/or two-antenna methods into the RE measurement. The method in the IEC standard requires a SG and a SA, while the proposed methods require a vector network analyser (VNA) and a SA. The time domain response of the RC is extracted from the inverse fast Fourier transform (IFFT) of the collected S -parameters, this eliminates the synchronization issue in [18] and the radiation efficiency of antennas could be measured at the same time. It is interesting to note that, by taking advantage of the enhanced back scattering effect [50], only one antenna is required. Both proposed methods do not need the RC to be calibrated in advance.

The method in the IEC standard is reviewed first and followed by the two proposed methods. Measurements are conducted to verify the results by using three methods (the method in IEC standard and two proposed methods). And finally, discussions and conclusions are given.

5.4.1 RE Measurement Method in the IEC Standard

The method in the IEC standard [1] is reviewed first; either averaged or maximum received power can be employed. The averaged received power is used in this section, because it has a lower uncertainty [1]. The measurement system is shown in Fig. 5.24 where the computer controls the operation of the stirrers and records the reading from the SA for each stirrer position over the frequency band of interest. In this section the stirrers rotate step by step (in mode-tuned operation [1]).

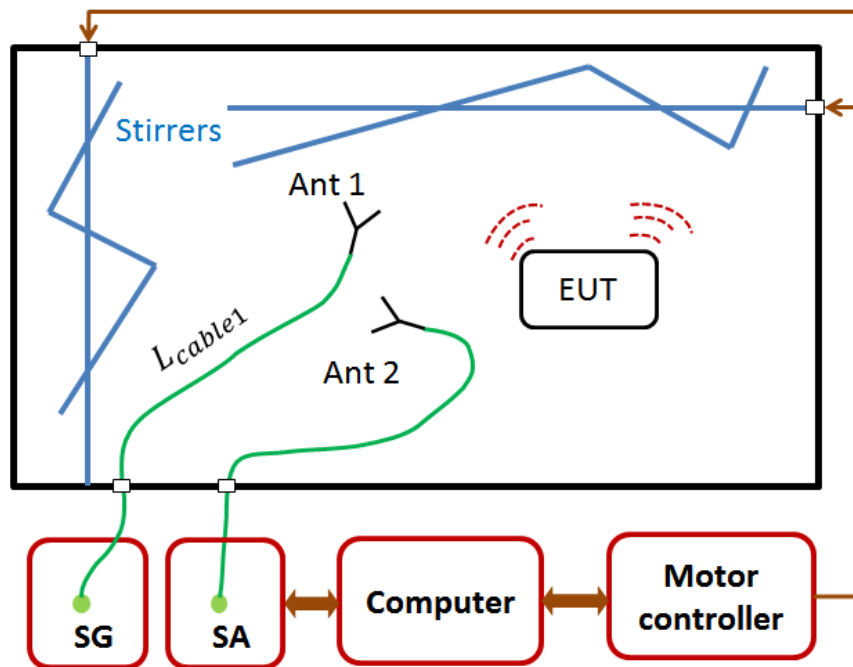


Fig. 5.24. The RE measurement system in the IEC standard.

The measurement procedure is given as follows:

- 1) The EUT is turned on; the SG is replaced with a 50 Ohm load. Then record the SA reading for each stirrer position.
- 2) Turn off the EUT, connect antenna 1 to the SG (reference source) and record the SA reading for each stirrer position.
- 3) The radiated power of the EUT (P_{radEUT}) can be obtained from

$$P_{radEUT} = \frac{\langle P_{SAEUT} \rangle}{\langle P_{SAref} \rangle} P_{rad1} \quad (5.43)$$

$$P_{rad1} = P_{ref} L_{cable1} (1 - |S_{11}|^2) \eta_1 \quad (5.44)$$

where $\langle P_{SAEUT} \rangle$ is the averaged received power (SA readings) from the EUT for all stirrer positions, $\langle P_{SAref} \rangle$ is the averaged received power (SA readings) from the reference source for all stirrer positions, P_{rad1} is the radiated power of antenna 1 when connected to the SG, P_{ref} is the output power from SG, L_{cable1} is the loss of the cable between antenna 1 and SG, S_{11} is the reflection coefficient of antenna 1, η_1 is the radiation efficiency of antenna 1.

Two issues should be noted when following the procedure in the IEC standard [1]

- 1) The loss of the cable must be known;
- 2) The performance of antenna 1 must be known (S_{11} and η_1)

Both of these measurements need a VNA: for the radiation efficiency measurement, the IEC standard also gives a standard procedure (which needs a reference antenna with known radiation efficiency), but a separate measurement needs to be conducted to characterise the performance of the antenna which is time consuming. However, by combining the one- and two- antenna methods in [3], this extra measurement is not necessary as we will see from the proposed methods below.

5.4.2 RE Measurement Using a VNA and Two Antennas

The first measurement step is the same as Step 1) in the IEC standard. For Step 2), as shown in Fig. 5.25, the EUT is turned off, we use a VNA and connect port 1 to antenna 1 and port 2 to antenna 2, respectively. The reference plane of the VNA is calibrated at the ends of cable 1 and cable 2 (at the input port of the antennas).

By applying the chamber transfer function between antenna 1 and antenna 2, we have

$$T_{21} = \frac{\langle |S_{21,s}|^2 \rangle}{(1 - \langle |S_{22}|^2 \rangle)(1 - \langle |S_{11}|^2 \rangle) \eta_1 \eta_2} \quad (5.45)$$

where $S_{21,s}$ is the stirred part of S -parameters defined in (5.8), $\langle \cdot \rangle$ means the averaged value of S -parameter using any stirring method (mechanical stir, frequency stir, source stir, *etc.*), η_1 and η_2 are the radiation efficiency of antenna 1 and antenna 2, respectively.

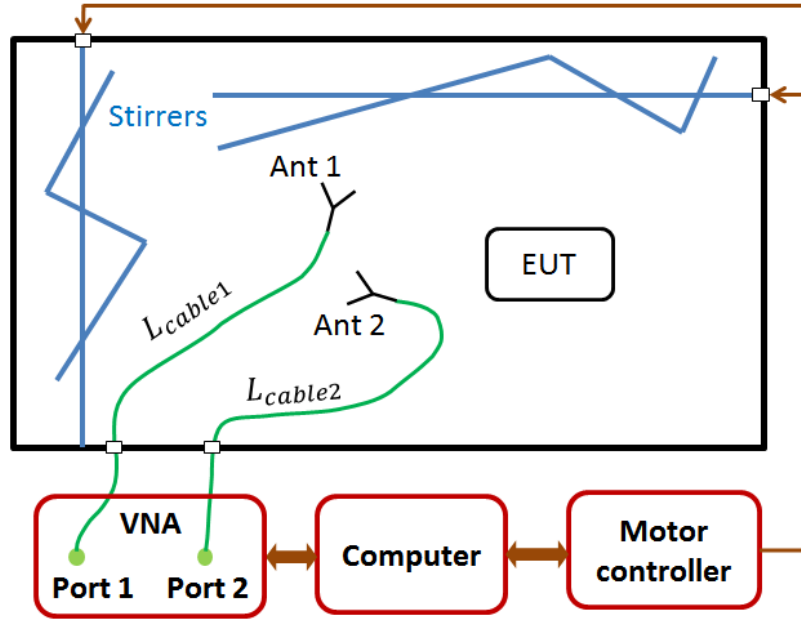


Fig. 5.25. The RE measurement system with a VNA and two antennas.

Note that the measurement setup in Fig. 5.25 is the same as in the two-antenna measurement method (the EUT can be regarded as a load), and the radiation efficiency of antenna 1 and antenna 2 can be obtained using (5.13) [3]

By applying the chamber transfer function between antenna 2 and the EUT, we have

$$T_{2EUT} = \frac{\langle P_{SAEUT} \rangle}{P_{radEUT}} \frac{1}{L_{cable2} (1 - |\langle S_{22} \rangle|^2) \eta_2} \quad (5.46)$$

If the chamber is well-stirred, $T_{21} = T_{2EUT}$, the radiated power from the EUT (P_{radEUT}) can be solved as

$$P_{radEUT} = \frac{\langle P_{SAEUT} \rangle (1 - |\langle S_{11} \rangle|^2) \eta_1}{L_{cable2} \langle |S_{21,s}|^2 \rangle} \quad (5.47)$$

η_1 can be obtained using (5.13). Thus the proposed method is mathematically derived. Compared with the method in the IEC standard [1], this method does not need a SG (but a VNA instead); the radiation efficiency of antennas and the cable loss do not need to be measured separately.

5.4.3 RE Measurement Using a VNA and One Antenna

Now we are going to introduce a virtual antenna to derive the chamber transfer function of the RC using only one antenna, as shown in Fig. 5.26.

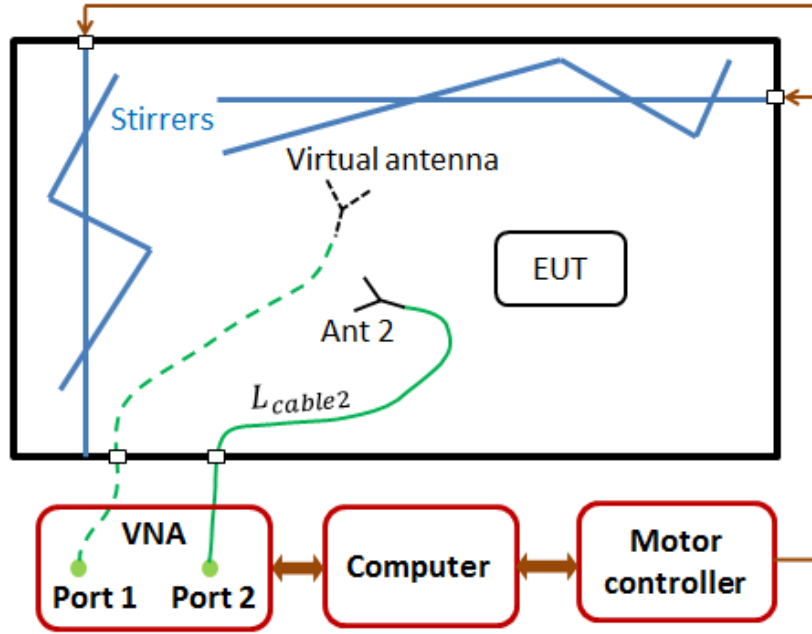


Fig. 5.26. The RE measurement system with a VNA and one antenna.

The virtual antenna is assumed to be exactly the same as antenna 2, this makes (5.45) become

$$T_{2v} = \frac{\langle |S_{21,s}|^2 \rangle}{(1 - \langle |S_{22}|^2 \rangle)^2 \eta_2^2} \quad (5.48)$$

If the chamber is well-stirred, $e_b = 2$ [3, 50], we have

$$\langle |S_{22,s}|^2 \rangle / \langle |S_{21,s}|^2 \rangle = 2 \quad (5.49)$$

From (5.48) and (5.49) the chamber transfer function is only related to the parameters of antenna 2

$$T_{2v} = \frac{\langle |S_{22,s}|^2 \rangle / 2}{(1 - \langle |S_{22}|^2 \rangle)^2 \eta_2^2} \quad (5.50)$$

Let $T_{2v} = T_{2EUT}$, the radiated power from the EUT (P_{radEUT}) can be solved as

$$P_{radEUT} = \frac{P_{SAEUT} (1 - \langle |S_{22}|^2 \rangle) \eta_2}{L_{cable2} \langle |S_{22,s}|^2 \rangle / 2} \quad (5.51)$$

If only antenna 1 is used we have

$$P_{radEUT} = \frac{P_{SAEUT}(1 - |\langle S_{11} \rangle|^2)\eta_1}{L_{cable1} \left(|S_{11,s}|^2 \right) / 2} \quad (5.52)$$

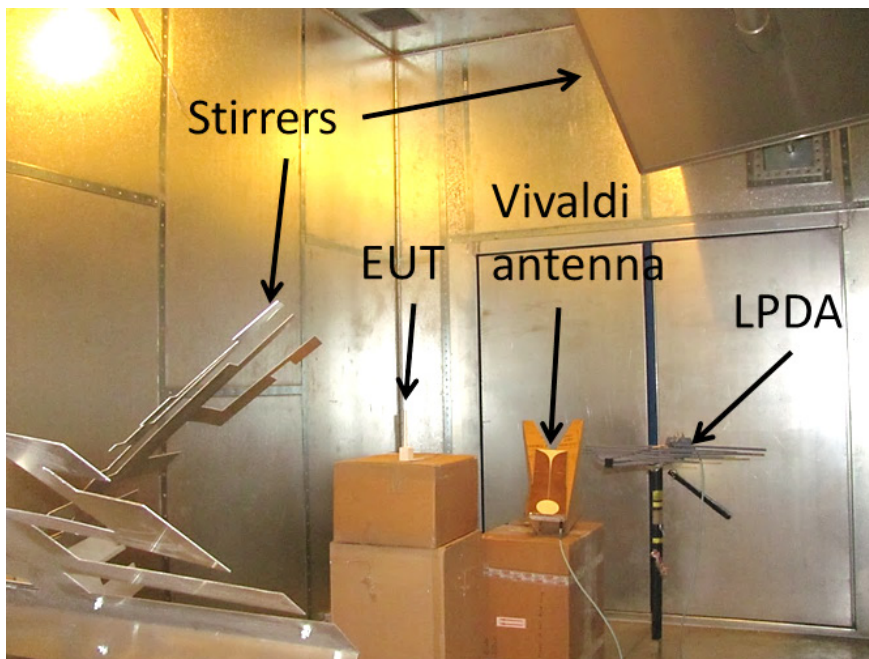
Thus the proposed method with a VNA and only one antenna is mathematically derived. Compared with the method in 5.4.2, only one antenna is needed.

Note that the measurement setup in Fig. 5.26 is the same as the one-antenna method in [3], η_1 and η_2 in (5.51) and (5.52) can be obtained using (5.12) [3]

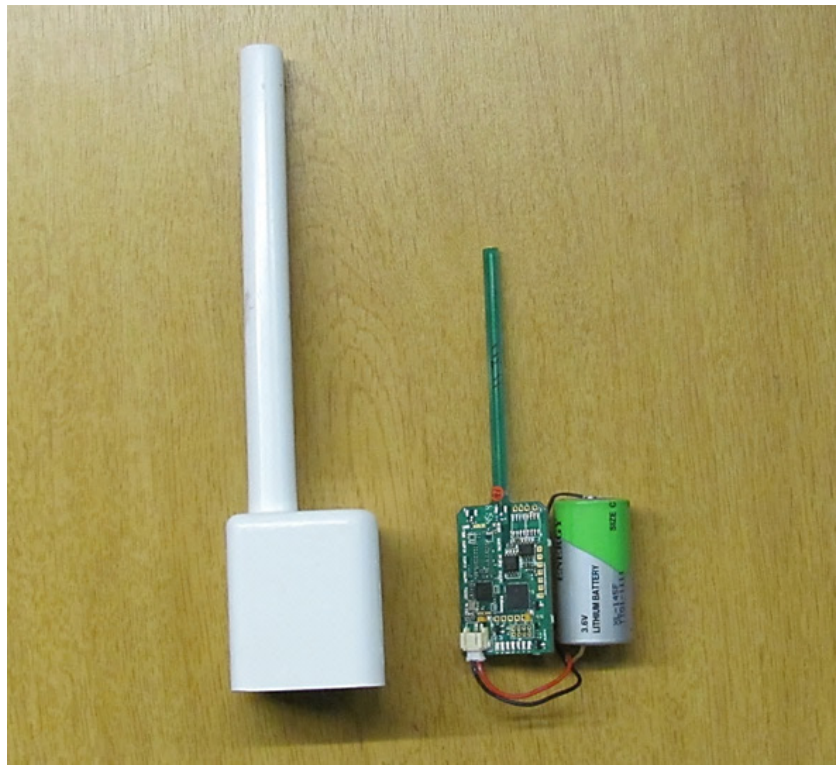
In the next section, measurements are conducted to verify the proposed methods.

5.4.4 RE Validation Measurement

The validation measurements were conducted in the RC at the University of Liverpool; the size of the RC is 3.6 m × 4 m × 5.8 m. The EUT used is from Invisible Systems [57], it is a sensor/transceiver which collects and transmits the data (temperature, electric meters, *etc.*) wirelessly. The carrier frequency of the sensor is 869.5 MHz which is much larger than the lowest usable frequency (LUF) of the RC (150 MHz in this case). The measurement system and the sensor are shown in Fig. 5.27(a) and (b), the EUT and antennas are supported by empty cartons (low loss), and are positioned with no line-of-sight paths.



(a)



(b)

Fig. 5.27. (a) The measurement system in an RC; (b) the plastic enclosure and the sensor (EUT).

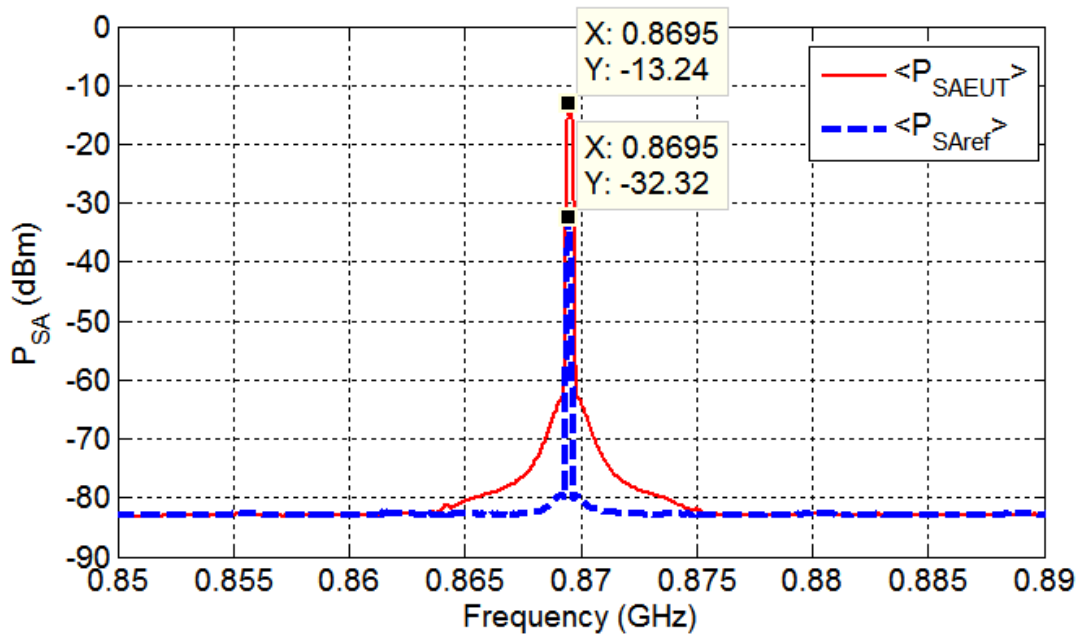


Fig. 5.28. Measured averaged SA readings.

Three methods were conducted: a log-periodic antenna (LPDA, Rohde & Schwarz HL223) was used as antenna 2, a homemade wideband Vivaldi antenna was used as antenna 1. To protect the SA, a 10 dB attenuator was connected to antenna 2 to attenuate the received signal, the reference level of SG

was set as 0 dBm ($P_{ref} = 1mW$ at 869.5 MHz), 359 stirrer locations with a step size of 1 degree were used, S -parameters with 10,001 points were collected in the range of 0.5 GHz ~ 1.5 GHz using a VNA. The reason why so many S -parameters points were collected is that we need to perform the IFFT using the S -parameters to obtain accurate τ_{RC} [34]. The frequency stirring with 100 sample points (10 MHz bandwidth) was used to provide an averaged result for each frequency, this makes $359 \times 100 = 35,900$ samples at each frequency.

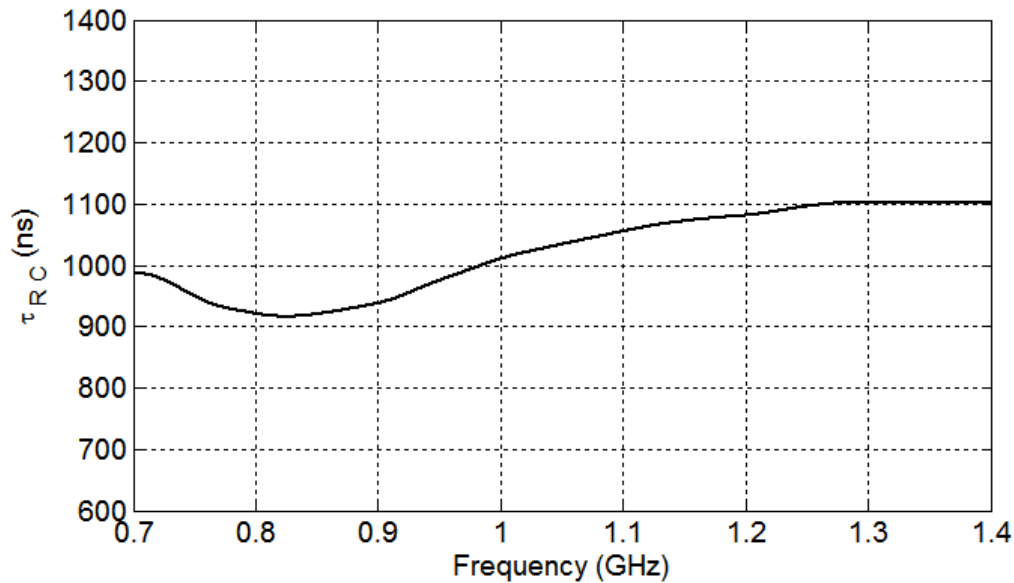


Fig. 5.29. Measured chamber decay time τ_{RC} .

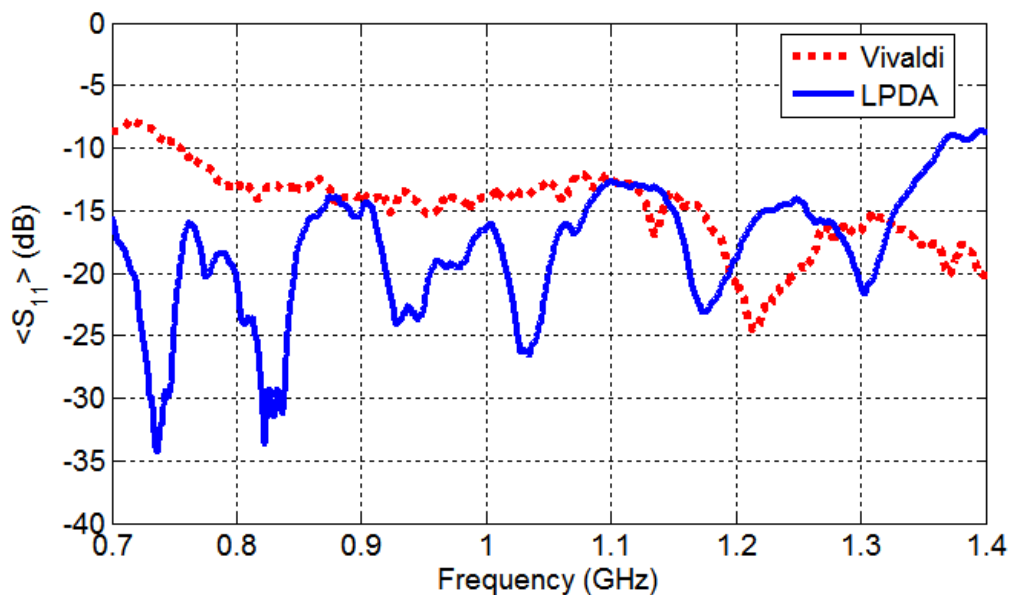


Fig. 5.30. Measured reflection coefficients of antennas.

The averaged SA readings of EUT and reference source are shown in Fig. 5.28. The peak values are -13.24 dBm and -32.32 dBm, respectively. The measured chamber decay time is extracted and shown

in Fig. 5.29 using the least square method [51]. The reflection coefficients of antennas were measured using the complex averaged S -parameters at each frequency [2] (Fig. 5.30). The radiation efficiency of antennas using two- and one-antenna methods are given in Fig. 5.31 and Fig. 5.32.

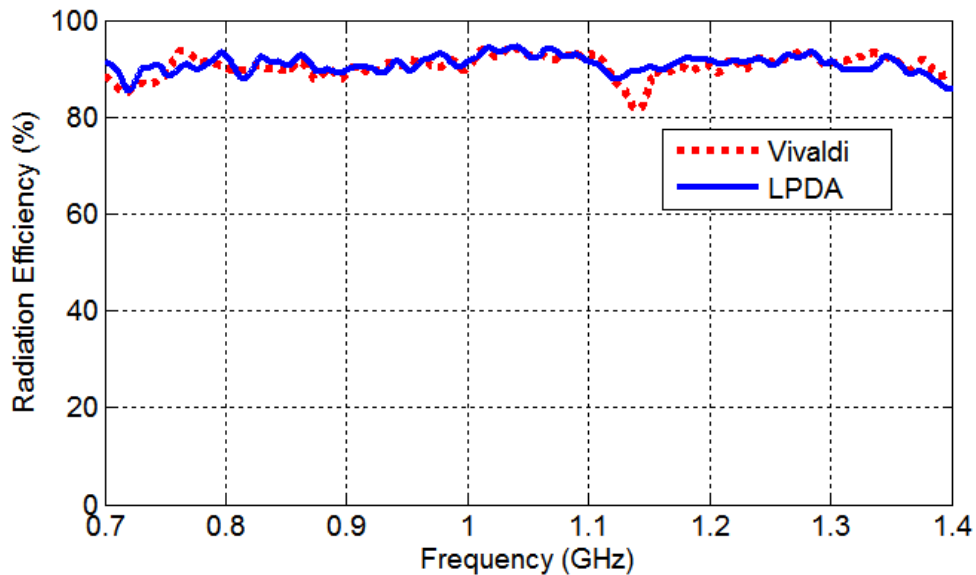


Fig. 5.31. Measured radiation efficiency of antennas using two-antenna method.

The chamber transfer functions are obtained using (5.45) or (5.48). For one antenna method, it can be obtained from either antenna 1 or antenna 2. The results are shown in Fig. 5.33, as can be seen, they are in a very good agreement.

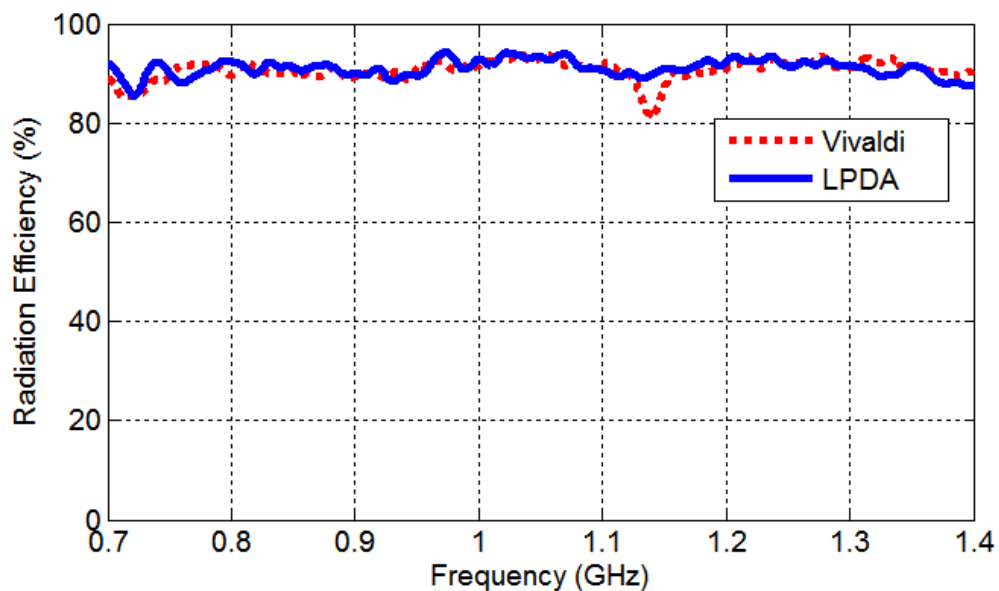


Fig. 5.32. Measured radiation efficiency of antennas using one-antenna method.

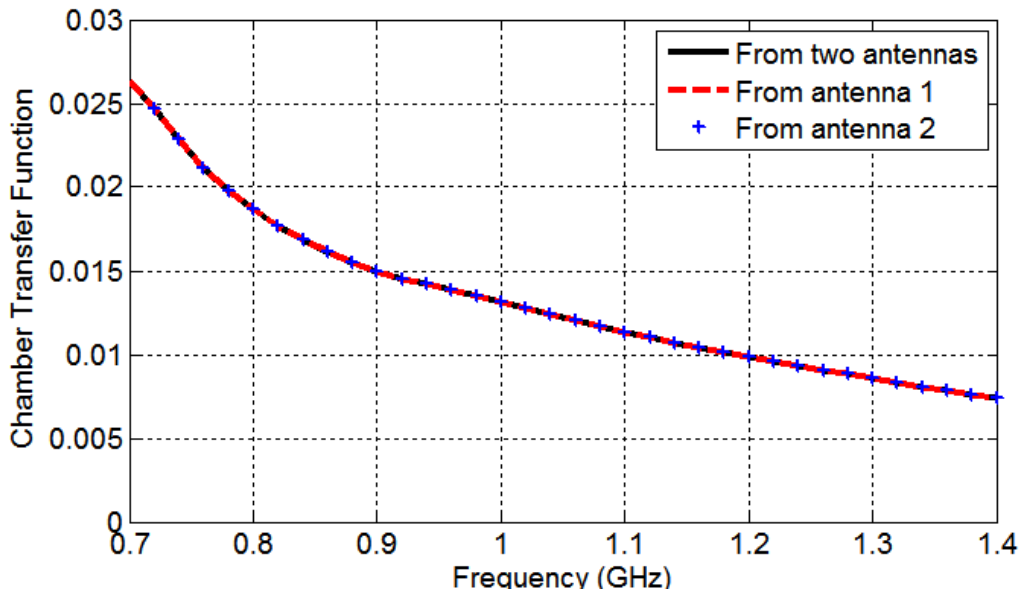


Fig. 5.33. Measured chamber transfer function.

The measured radiated power using three methods (5.43), (5.47), and (5.51),(5.52) are summarised in Table 5.3, either antenna 1 or antenna 2 can be used in the third method (1Ant + VNA + SA). As expected, a very good agreement is obtained, the difference is quite small (0.2 dB).

Table 5.3: Measured Radiated Power Using Three Methods

Method*	Measured radiated power P_{radEUT}
2Ant + SG + SA (IEC standard)	17.4 dBm
2Ant + VNA + SA	17.2 dBm
1Ant + VNA + SA (Vivaldi)	17.2 dBm
1Ant + VNA + SA (LPDA)	17.2 dBm

*2Ant + SG + SA means using 2 antennas, a signal generator and a spectrum analyser.

5.4.5 Short Summary of Section 5.4

The contribution of this section is: two new alternative methods have been proposed in this section to measure the RE of EUT. In the IEC standard method, the loss of the cable and the performance of the antenna need to be known in advance. Also a SG and two antennas are required. It has been shown that the SG is not necessary in the proposed methods, instead a VNA can be used to complete the measurement and only one antenna is enough, which simplifies the measurement system without losing accuracy. This method requires minimum number of instruments in the RE measurement in an RC. In this measurement, a two-in-one instrument was used (including both a VNA and a SA). The

one- and/or two-antenna method were incorporated into the RE measurement. The radiation efficiency of antennas, reflection coefficients, and the chamber transfer function were measured simultaneously.

Compared with the method in [18], there is no need to measure the received power in the time domain, thus no synchronization issue is involved. The chamber decay time is obtained from the IFFT of S -parameters.

There is a 0.2 dB difference in Table 5.3, if we examine the full procedure carefully, the error may come from two sources:

- 1) The measurement of cable loss: In the RC, we had a relatively long cable (around 5 meters), when measuring the loss of the cable using a VNA, the cable was bend and the route might not be exactly the same as in the RE measurement, thus the cable loss may vary.
- 2) The difference in the collected sample number: In the IEC standard method, no frequency stir is used, the averaged received power is obtained from 359 samples (mechanical stir), while using the VNA, the sample number is 35,900 (mechanical stir + frequency stir). It is also possible to calibrate the RC in a certain frequency band using a SG, but it takes more time compared with the use of a VNA.

There are issues to be treated carefully when using the proposed methods:

- 1) The proposed methods are based on the one- and/or two-antenna method. The preconditions of these methods need to be satisfied; this has been discussed in [3]. The chamber must be well-stirred and the loss of the chamber (including the EUT) is larger than the loss of antennas. However, typical values of the radiation efficiency can also be used if a higher uncertainty is acceptable (75% for LPDA and 90% for horn antenna [1]).
- 2) The transmitting time of the EUT should be much larger than the chamber decay time, in this measurement, the sensor (EUT) was reprogrammed for the measurement to keep radiating. If the EUT did not radiate continuously, it might not be easy to capture the signal using a SA, or the sweep time of the SA should be set very long.

5.5 Permittivity Measurement in an RC

Reverberation chambers (RCs) have been used for the measurement of absorption cross section (ACS) in the recent years [40-45], the ACS value can be further used to extract the material properties of dielectric objects [45]. However, this method is limited to electrically large objects. Only when the skin depth is much smaller than the sample cross dimension, the real part (ϵ_r) of the permittivity can

be obtained. When the skin depth is much larger than the cross-dimension the relationship between the conductivity and permittivity ($\sigma/\sqrt{\epsilon_r}$) can be found but not the specific values of the conductivity and permittivity. For general cases, a much more complex relationship can be obtained but hard to evaluate.

For a given frequency, the ACS is a single value, but the permittivity has a real part and an imaginary part, it is impossible to find a unique solution of two variables from one equation. That is the reason why the real part and imaginary part cannot be obtained at the same time in [45]. If we consider the frequency dependence, and assume that the permittivity and conductivity will not change much over a certain frequency range, it is possible to obtain both the real part and imaginary part. If both permittivity and conductivity are also frequency dependent, it will limit the proposed method; since we do not have enough information to solve the unknown variables (solution may not be unique).

We limit the object shape to a sphere since for a spherical object, the ACS is independent of the incident angle; this directly links the measured ACS value in a RC with the theoretical value, because the measured ACS in an RC is the averaged value of all the incident angles. By considering the ACS value at different frequencies, the real part permittivity and conductivity that satisfy the ACS value at all the frequencies can be found, an evaluation function is defined, like the probability distribution function (PDF), the PDF-like evaluation function will make the results self-explanatory, no presumptions and uncertainty analysis are needed after the measurement and calculation. The effect of the container and the limitations of the method are also discussed.

5.5.1 Theory

The measurement setup is shown in Fig. 5.34, a plastic sphere filled with water is shown in Fig. 5.34(b). The measurement process is the same as the ACS measurement in the RC. The averaged ACS of the object under test (OUT) can be obtained by comparing the measured S -parameters of the empty chamber and the chamber loaded with the OUT [43].

$$\langle ACS \rangle = \frac{\lambda^2}{8\pi} \left(\frac{1}{T_{wo}} - \frac{1}{T_{no}} \right) \quad (5.53)$$

where λ is the wavelength of the corresponding frequency, T_{wo} is the corrected transmission coefficient (chamber transfer function) with the OUT and T_{no} is the corresponding value without the OUT, the corrected transmission coefficient can be obtained from the S -parameters and the radiation efficiency of the two antennas (η_1, η_2)

$$T = \frac{\langle |S_{21,s}|^2 \rangle}{(1 - \langle |S_{11}|^2 \rangle) \eta_1 (1 - \langle |S_{22}|^2 \rangle) \eta_2} \quad (5.54)$$

where $S_{21,s}$ is the stirred part of the S -parameter which can be obtained by using the vector average subtraction in (5.8). It is also interesting to note that the radiation efficiency of the transmitting (Tx) antenna and receiving (Rx) antenna can both be measured in the same scenario at the same time [3], no extra measurement is needed.

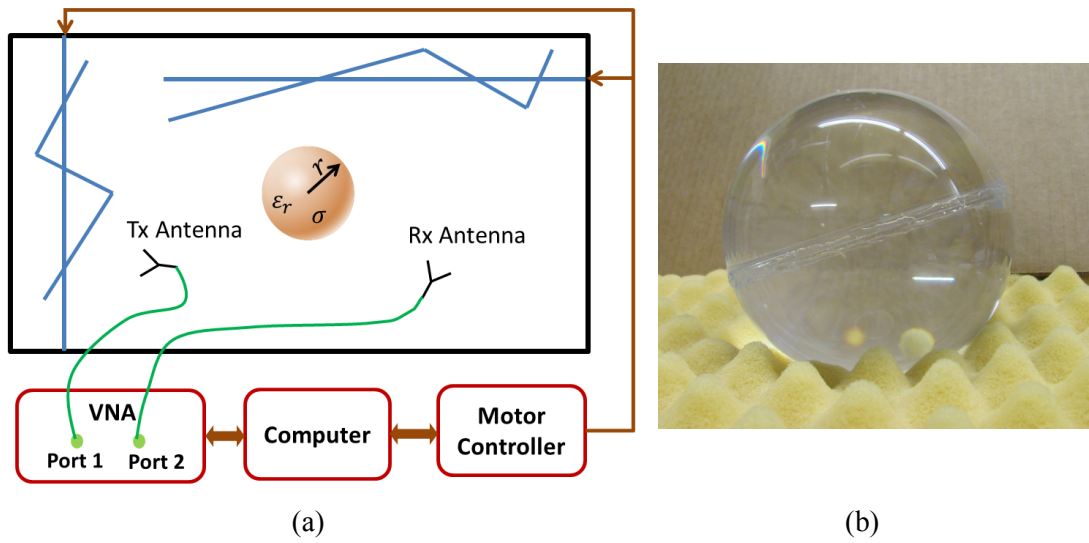


Fig. 5.34. ACS measurement system setup, (a) schematic plot, (b) a plastic sphere filled with water.

The spherical dielectric ACS value can be obtained analytically using Mie theory [58]

$$ACS_{Sphere} = \pi r^2 (Q_{ext} - Q_{sca}) \quad (5.55)$$

where r is the radius of the sphere, Q_{ext} is the extinction efficiency and Q_{sca} is the scattering efficiency

$$Q_{ext} = \frac{2}{(kr)^2} \sum_{n=1}^{\infty} (2n+1) \text{Re}(a_n + b_n) \quad (5.56)$$

$$Q_{sca} = \frac{2}{(kr)^2} \sum_{n=1}^{\infty} (2n+1) (|a_n|^2 + |b_n|^2) \quad (5.57)$$

$k = 2\pi/\lambda$ is the wave number, a_n and b_n are the Mie coefficients which are different for coated or uncoated spheres [44, 58, 59], and they will be different when considering the holder of the OUT.

Theoretically, by combining (5.53) and (5.55), and considering the frequency dependence, the permittivity ϵ_r and conductivity σ can be obtained by solving the equation system

$$ACS|_{f=f_i} = \pi r^2 (Q_{ext} - Q_{sca})|_{f=f_i}, \quad i = 1 \dots N \quad (5.58)$$

where N is the total frequency sample number. Obviously, it is a transcendental equation system which is hard to solve. In the next section, we will introduce a direct and easy way to solve (5.58).

5.5.2 Extracting the Permittivity and Conductivity

To illustrate how the ϵ_r and σ can be obtained, we assume that the OUT is the sea water in a sphere with a radius $r = 9.7 \text{ cm}$, the sea water relative permittivity is $\epsilon_r = 74$ and the conductivity is $\sigma = 3.53 \text{ S/m}$, and we assume that they do not change over the frequency of interest. A plastic spherical container is used to ensure that the water is in spherical shape, the effect of the container will be discussed later, here we assume that it has the same material property as air. Fig. 5.35 gives the ACS values calculated from Mie series.

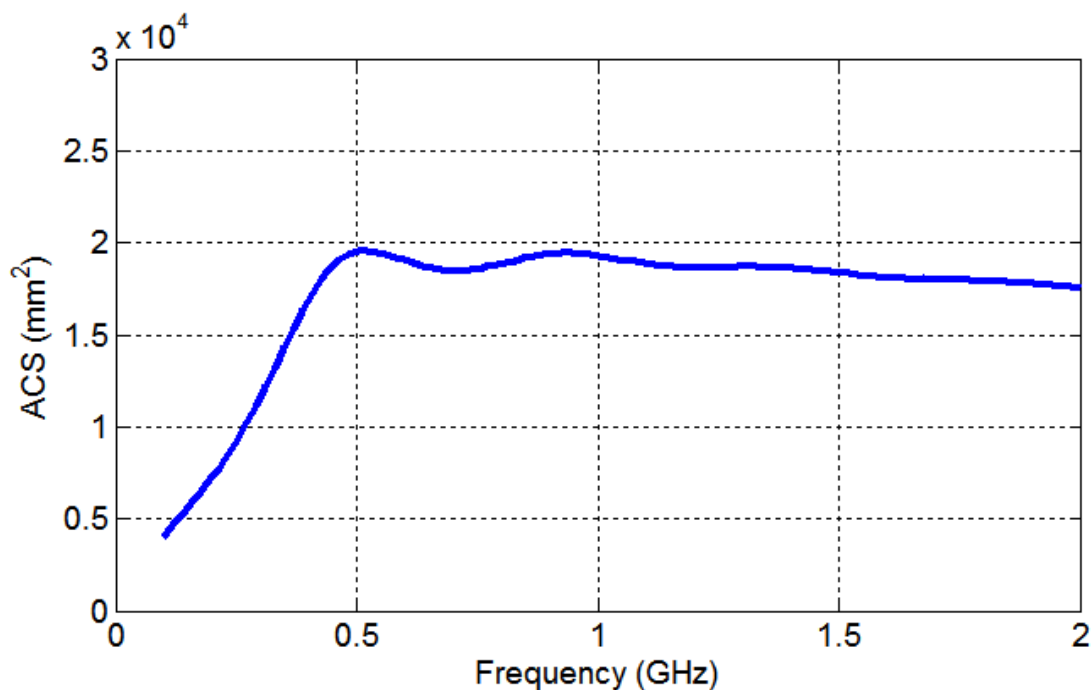


Fig. 5.35. ACS value with different frequency.

If we sweep the ϵ_r and the σ at each given frequency, the ACS value can be calculated using (5.55) and is shown in Fig. 5.36. For each frequency, we can find a contour line in Fig. 5.36 with the corresponding value in Fig. 5.35.

Next, we overlay all these contour lines together; all these contour lines will cross a common point which is the permittivity and the conductivity of the OUT. Fig. 5.37 shows the overlay plot of the contour lines at all selected frequencies. As it can be seen all the contour lines share one common

point (74, 3.53) which is exactly the point corresponding to the relative permittivity and conductivity of the OUT.

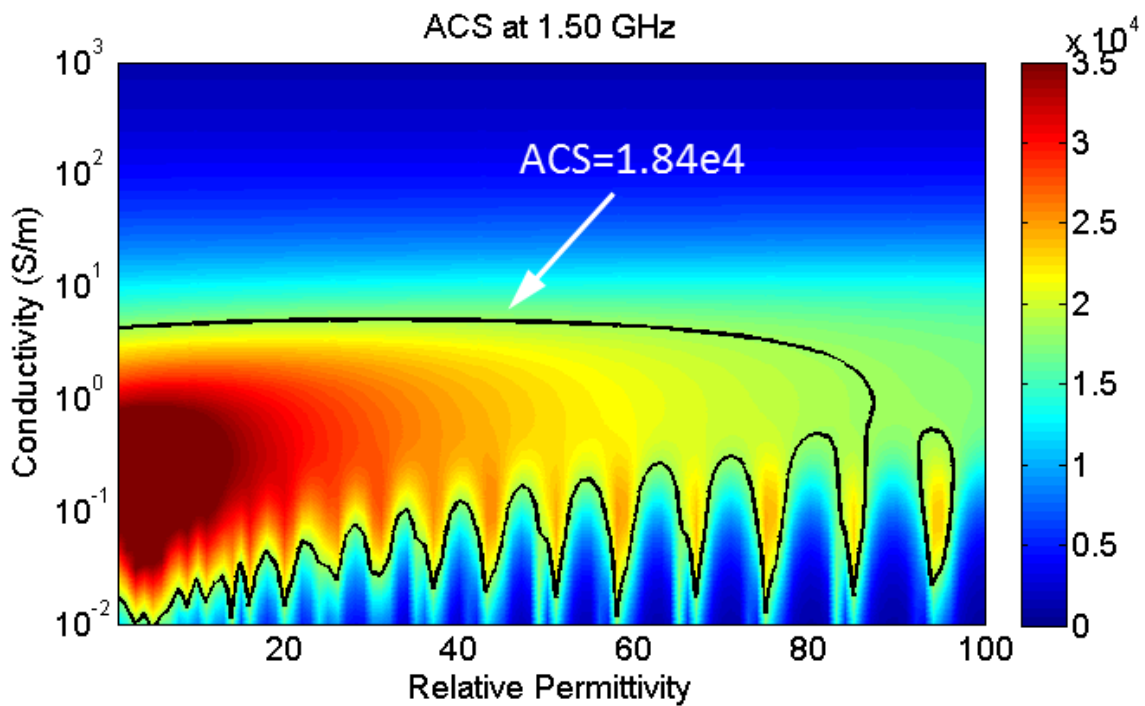
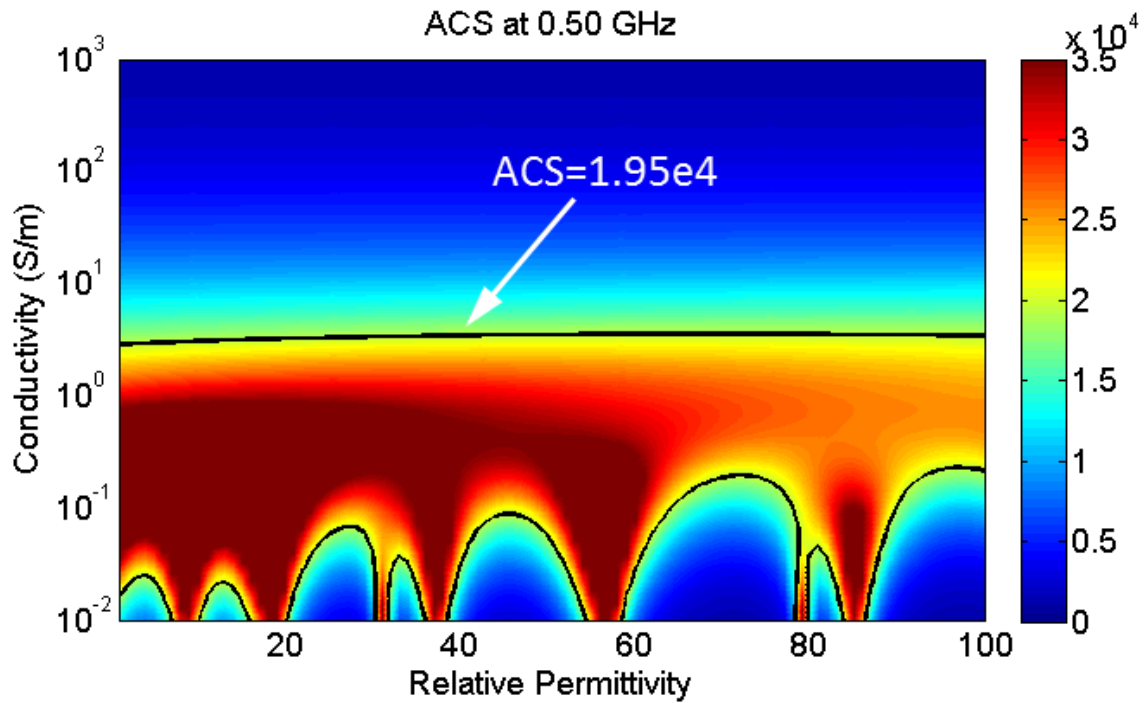


Fig. 5.36. (a) ACS value at 0.5 GHz, (b) ACS value at 1.5 GHz, unit: mm^2 .

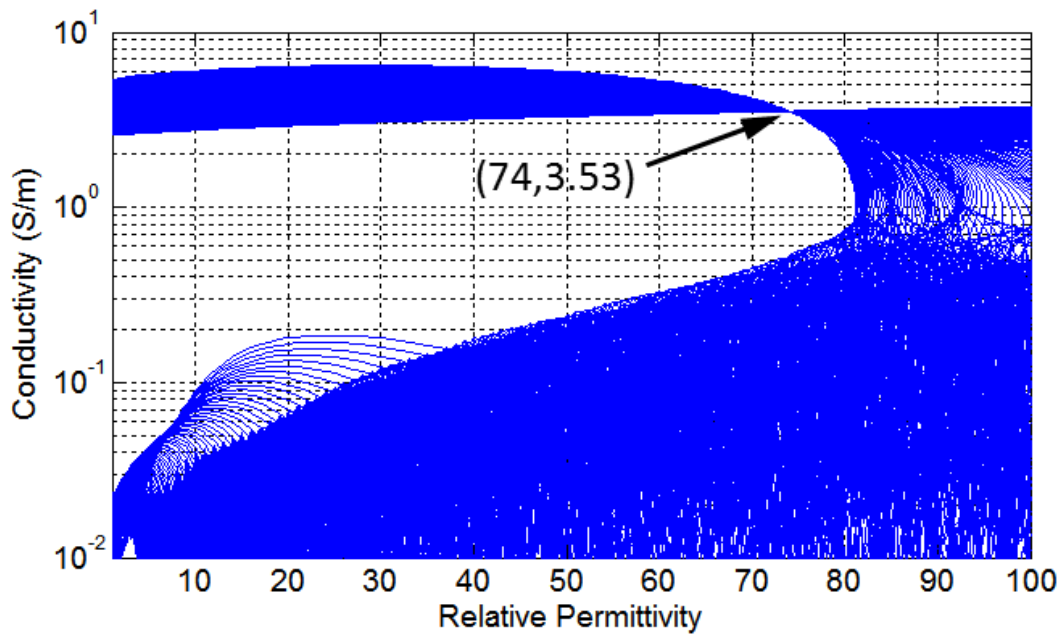


Fig. 5.37. Overlay of all the contour lines.

It is important to note that in the ideal situation, the measurement uncertainty is zero, which means the ACS value at each frequency point is exactly measured. In reality, all the measurement results have its uncertainty, and the contour lines may not always cross a common point. Thus there is an uncertainty issue.

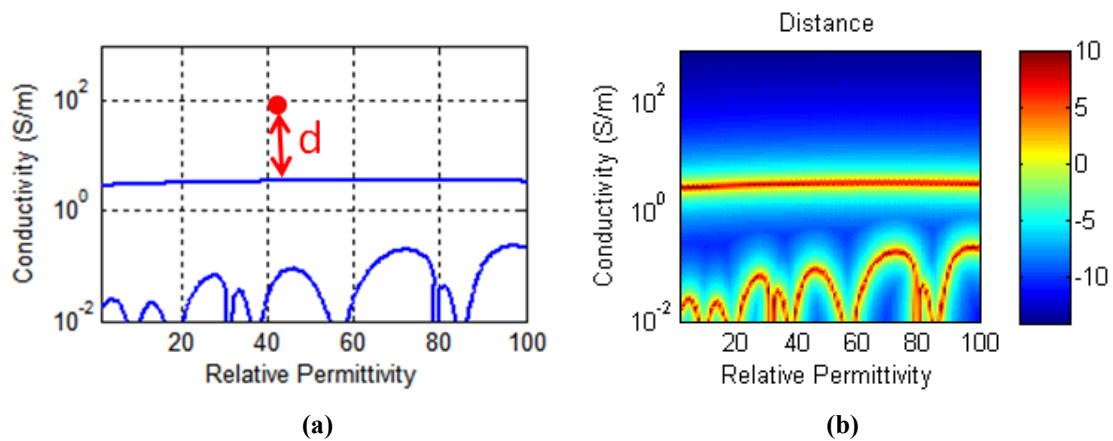


Fig. 5.38. (a) Geometric view of distance definition, (b) distance plot in dB.

Since the contour lines can be extracted from measurement as shown in Fig. 5.36 for each frequency, an evaluation function can be defined to illustrate how close the permittivity and conductivity test points are to the contour lines. We define the distance as

$$d_i = \min \sqrt{(\epsilon_r - C(x,y)_x)^2 + (10 \log_{10} \frac{\sigma}{C(x,y)_y})^2} \quad (5.59)$$

where $C(x, y)$ is the contour line equation which is described numerically by the coordinates $C(x, y)_x$ and $C(x, y)_y$. Since the logarithmic axis is used for σ value, the distance in logarithmic axis is defined, min means the nearest distance is chosen. A geometric view of (5.59) is shown in Fig. 5.38(a). As can be seen, for each grid point, a value can be found to illustrate the distance between the grid point and the contour line. 100×100 points in ϵ_r axis and σ axis are used to calculate the distance; we use $-10\log_{10}(d_i)$ to show the distance in dB scale in Fig. 5.38(b).

The same procedure can be applied to all the contour lines for all the frequency points. The average distance can be defined as

$$d_{avr} = \frac{\sum_{i=1}^N d_i}{N} \quad (5.60)$$

If 100 frequency points are chosen in the range of 200 MHz ~ 1.5 GHz to calculate the average distance using (5.60), $-10\log_{10}(d_{avr})$ in dB unit is shown in Fig. 5.39.

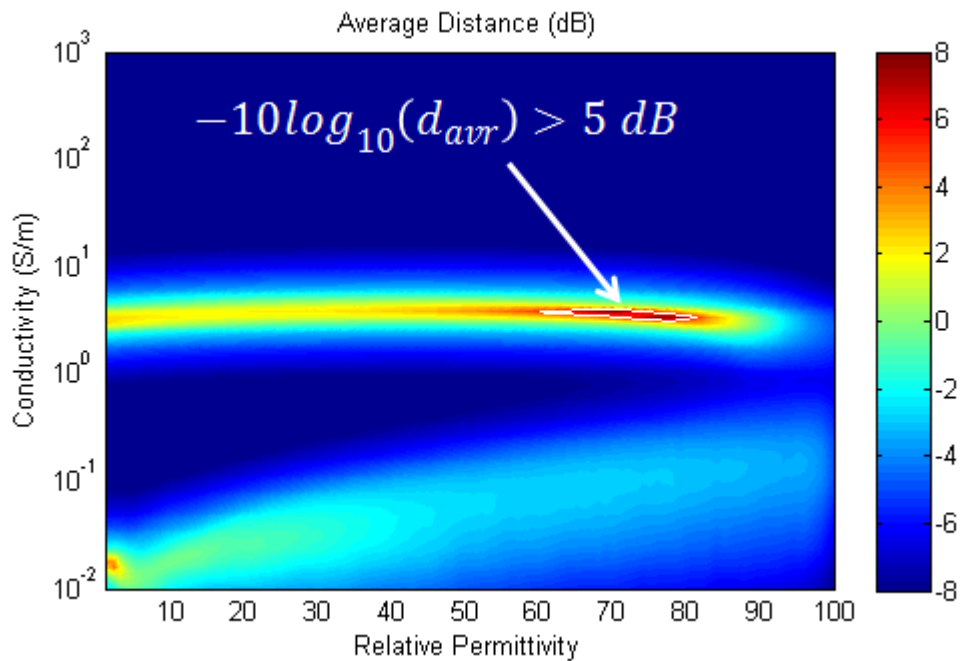


Fig. 5.39. Average distance for all the frequency points and the trust region.

We can consider d_{avr} as the evaluation function which considers all the contour lines for all the measured frequencies. It is easy to see that the point (74, 3.53) is the nearest point to all the contour lines. It can also be observed that for a given uncertainty e.g. $-10\log_{10}(d_{avr}) > 5$ dB the trust region of permittivity and conductivity can be easily found. Like PDF which is used to describe the random variables, this evaluation function explains the measurement results by using the measurement data which makes it self-explanatory.

Normally, the measured data is not as smooth as that shown in Fig. 5.35, suppose we have measured ACS values superimposed with random noise; the noise follows Gaussian distribution with mean value 0 and standard deviation 500 as shown in Fig. 5.40. The same procedure can be applied as well; the result is shown in Fig. 5.41. The trust region with different threshold value can also be easily obtained. Because of the noise, the result is less significance than Fig. 5.39. And another peak point at the left corner actually means that the object with smaller relative permittivity and conductivity may have similar results.

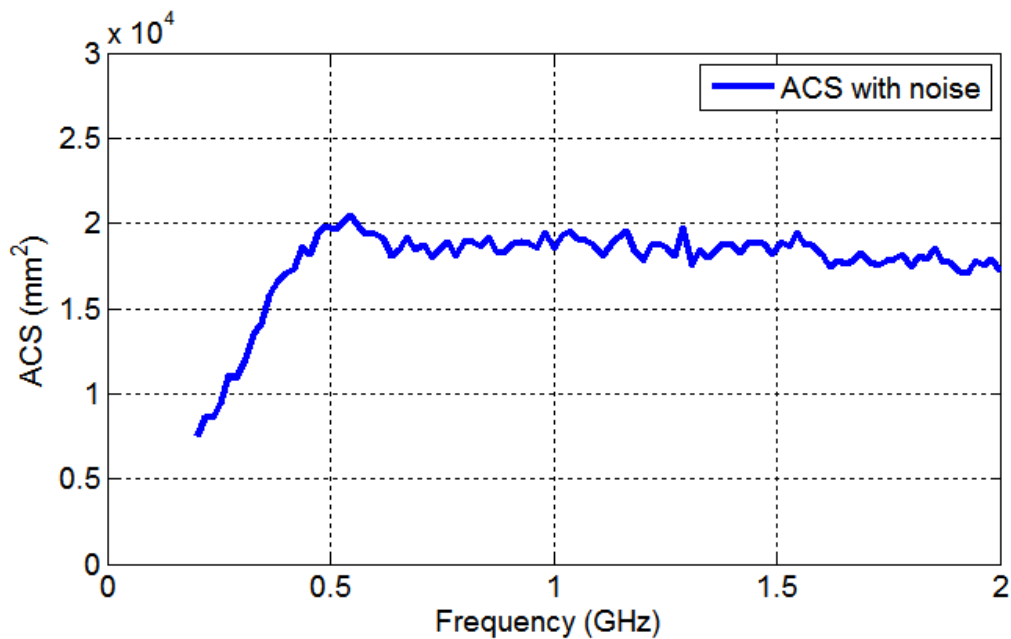


Fig. 5.40. ACS value superimposed with random noise.

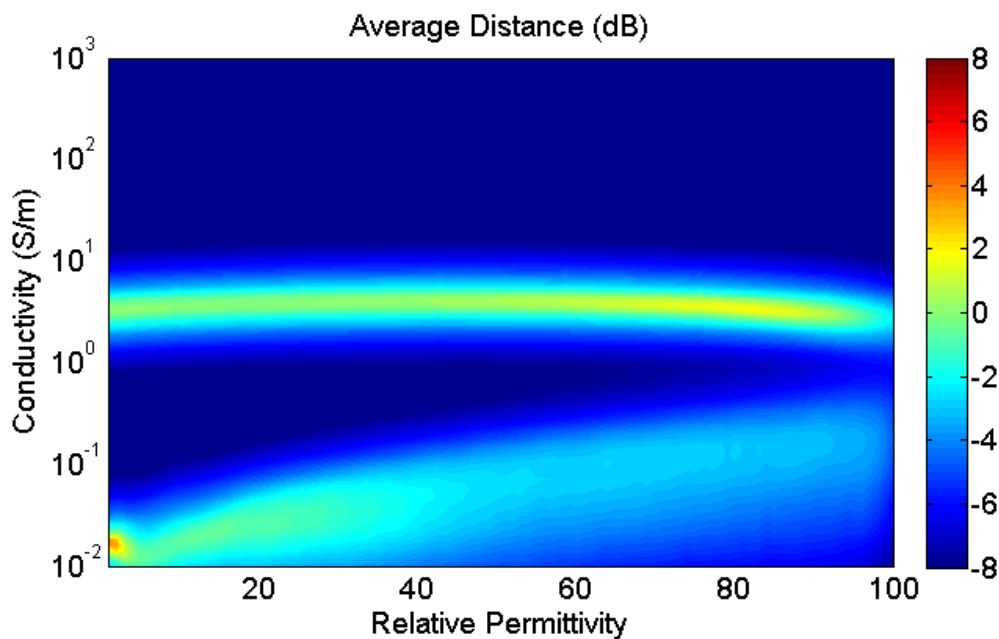


Fig. 5.41. Average distance for all the frequency points (consider random noise).

The container only affects the Mie coefficients in (5.56) and (5.57). We assume that the outer radius of the container is 10 cm, the relative permittivity is 4 and the conductivity is 0. The ACS values are calculated and shown in Fig. 5.42.

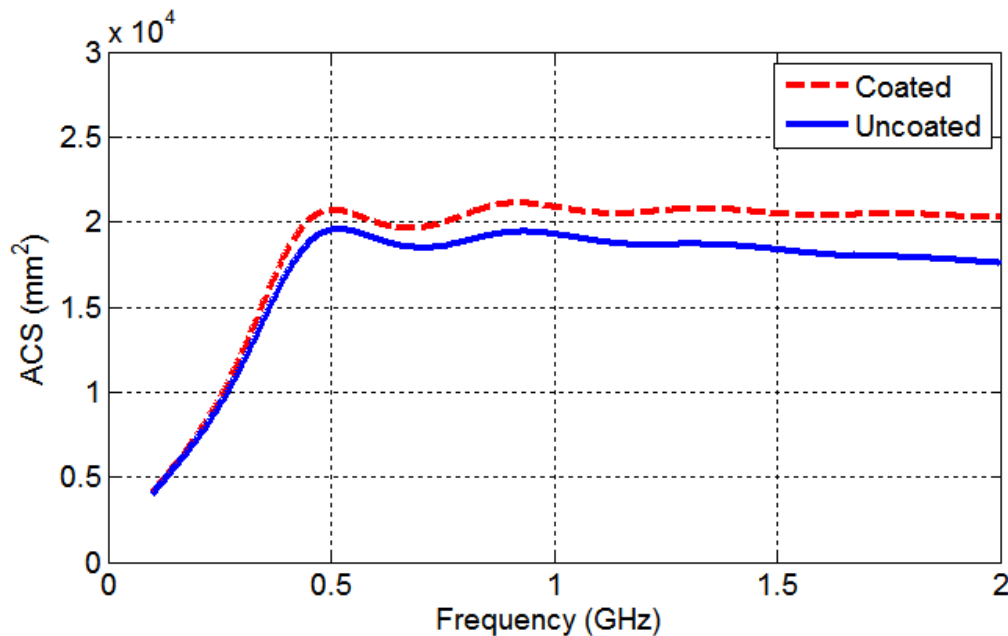


Fig. 5.42. ACS comparison of coated and uncoated sphere.

Similarly, the reference ACS value of different permittivity and conductivity needs to be updated. Fig. 5.36(b) becomes Fig. 5.43. The other procedures are the same. As can be seen, the container does not affect the proposed method, but the permittivity and conductivity of the container need to be known in advance.

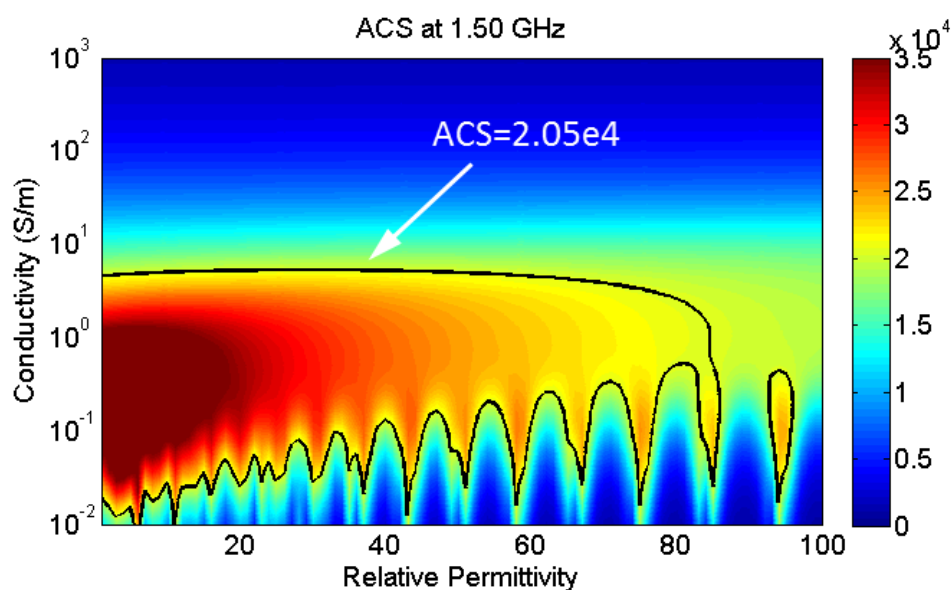


Fig. 5.43. ACS value with coated sphere at 1.5 GHz, unit: mm².

5.5.3 Short Summary of Section 5.5

The contribution of this section is: a new method has been proposed to measure the permittivity and conductivity of a spherical object. Compared with the existing method [45], the frequency dependency of ACS was considered which makes the absolute value of *both* relative permittivity and conductivity can be obtained. The effect of the container has been discussed and it did not affect the proposed method. For the practical measurement, noise may interfere with the results, an evaluation function has been defined to treat the noisy data and PDF-like results for the permittivity and conductivity have been given. The distribution of the permittivity and conductivity has made the results self-explanatory. It was also important to note that when the data was interfered by noise, the trust region may become not unique, which would reduce the significance of the results, in this case, the prior knowledge may need to help to choose the correct trust region.

Because the transmission coefficient T has been used to calculate the ACS values, limitations for T were also applied for the proposed method, obviously the RC should be well-stirred. The frequency of interest for the ϵ_r and σ should also be larger than the lowest usable frequency of the RC. Other limitations will depend on the properties of OUT, as can be seen in Fig. 5.36, if σ is very large, the ACS value will become less dependent on ϵ_r , which will increase the uncertainty for the measured ϵ_r .

5.6 Shielding Effectiveness Measurement in an RC

To protect an electronic device from unexpected signals or to reduce the emission of the device itself, an enclosure is normally employed to protect it. The shielding effectiveness (SE) is an important figure of merit to characterise the electromagnetic isolation performance of the enclosure.

Generally, the SE can be measured by following the IEEE standard 299 [1] or using a nested reverberation chamber (RC) [21]. However, this kind of method requires special facilities: an anechoic chamber (AC) or an RC, which may not be available for many companies. For an electrically large enclosure, it has been noted that the SE value is related to the Q factor of the enclosure [60]. If the apertures of the enclosure can be covered, by comparing the covered Q_c and the uncovered Q_u , the SE can be extracted.

It has been tried to obtain the SE from the Q factor in [23-24, 61], and the Q factor was obtained from the autocorrelation width of the measured S -parameters [23, 61]. However different cut-off level of the autocorrelation width may give different Q value. The selection of the cut-off level is experience based and more than one antenna is needed for the measurement. This section is aimed at solving the

above problem, results from the nested RC method and the proposed method are presented and compared, conclusions are drawn and limitations are discussed.

5.6.1 Theory

For an electrically large well-stirred enclosure, it has been shown that the SE (defined by using the ratio of the power density outside the enclosure to the power density inside the enclosure) is related to the transmission cross section (TCS) and the Q factor [60]

$$SE(dB) = 10 \log_{10} \left(\frac{S_i}{S_c} \right) = 10 \log_{10} \frac{4\pi V}{\langle \sigma_{TCS} \rangle \lambda Q_{tot}} \quad (5.61)$$

where S_i is the power density of the uniformly random incident plane wave (external), S_c is the power density inside the enclosure (internal), V is the volume of the enclosure, λ is the wavelength of the frequency of interest. $\langle \sigma_{TCS} \rangle$ is the averaged TCS of the apertures. Q_{tot} is the total Q factor of the enclosure which can be expressed as [60]:

$$Q_{tot}^{-1} = Q_{surf}^{-1} + Q_{ACS}^{-1} + Q_{ant}^{-1} + Q_{TCS}^{-1} \quad (5.62)$$

where

$$Q_{surf} = \frac{3V}{2\mu_r S \delta} \quad (5.63)$$

It is determined by the loss due to the finite conductivity of the walls of the enclosure, S is the inner surface area, μ_r is the relative permeability of the wall, δ is the skin depth.

$$Q_{ACS} = \frac{2\pi V}{\lambda \langle \sigma_{ACS} \rangle} \quad (5.64)$$

is the contribution from all the lossy materials inside the cavity, $\langle \sigma_{ACS} \rangle$ is the total averaged absorption cross section.

$$Q_{ant} = \frac{16\pi^2 V}{m\lambda^3} \quad (5.65)$$

is the contribution from the absorption of the antenna. m is the mismatch factor of the antenna.

$$Q_{TCS} = \frac{4\pi V}{\lambda \langle \sigma_{TCS} \rangle} \quad (5.66)$$

is the contribution from the averaged TCS.

It should be noted that (5.61) cannot be used directly: Q_{tot} can be extracted from the S -parameters [3], however, the averaged TCS $\langle\sigma_{TCS}\rangle$ cannot be easily measured directly.

If we assume that the aperture can be properly covered, the contribution from the aperture can be identified by using the covered and uncovered Q factors. The measurement scenarios are shown in Fig. 5.44. Let Q_{totu} be the total Q factor for the uncovered EUT and Q_{totc} be the total Q factor for the covered EUT (assume the aperture is perfectly covered, $\langle\sigma_{TCS}\rangle = 0$), Q_{TCS} should be

$$Q_{TCS}^{-1} = Q_{totu}^{-1} - Q_{totc}^{-1} \quad (5.67)$$

Using (5.61), (5.66) and (5.67), we can derive

$$SE_Q(dB) = 10\log_{10} \frac{(Q_{totu}^{-1} - Q_{totc}^{-1})^{-1}}{Q_{totu}} \quad (5.68)$$

thus the SE is now only determined by these Q factors.

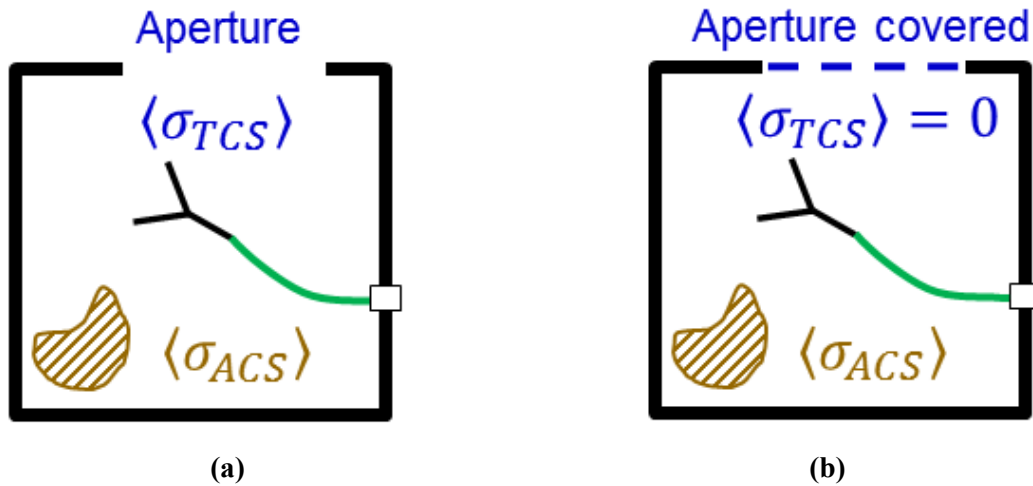


Fig. 5.44. (a) Enclosure with aperture uncovered, (b) enclosure with aperture covered.

More specifically, the Q factor can be obtained from the frequency domain and the time domain. Thus we are going to introduce another two equations for the SE in both the time and frequency domains.

In the time domain, it has been shown in [3] that $Q_{TD} = \omega\tau$, ω is the angular frequency, τ is the decay time constant of the EUT (the same as the definition of τ_{RC} used in the antenna radiation efficiency measurement). Equation (5.68) can be further expressed as

$$SE_Q(dB) = SE_{TD}(dB) = 10\log_{10} \frac{\tau_c}{\tau_c - \tau_u} \quad (5.69)$$

where τ_c is the decay time constant of the covered EUT and τ_u corresponds to the decay time constant of the uncovered EUT. Both τ_c and τ_u can be obtained from the direct measurement in the time domain [62] or from the inverse fast Fourier transform (IFFT) of the S -parameters measured in the frequency domain [51]. Note that τ is the average decay time which means the waves interact with the EUT uniformly. Imagine a high gain antenna with main lobe directs to a large aperture: the antenna cannot even see the aperture, in this case, τ cannot be accurately extracted.

It is interesting to examine the insight of the SE from the time domain. The SE value is only related to the decay time constant and independent of the volume of the EUT. As expected, when the EUT is well shielded, $\tau_u \rightarrow \tau_c$, $SE \rightarrow \infty$; when the EUT is completely open and the antenna radiates freely, $\tau_u \rightarrow 0$, $SE \rightarrow 0$.

In the frequency domain, $Q_{FD} \propto T$, where T is the chamber transfer function, we have [3]

$$Q_{FD} = \frac{16\pi^2 V \langle |S_{21,s}|^2 \rangle}{\lambda^3} \quad (5.70)$$

where $S_{*,s}$ is the stirred part of S -parameters (no line-of-sight), $\langle \cdot \rangle$ means the average value of S -parameters with any stirring method (mechanical stir, frequency stir, source stir, etc.). When the EUT is well-stirred, the enhanced backscatter constant [3, 51]

$$e_b = \sqrt{\langle |S_{11,s}|^2 \rangle \langle |S_{22,s}|^2 \rangle} / \langle |S_{21,s}|^2 \rangle = 2 \quad (5.71)$$

Assume we have two identical antennas in the EUT (not necessary in practice), we have $\langle |S_{11,s}|^2 \rangle = \langle |S_{22,s}|^2 \rangle = 2 \langle |S_{21,s}|^2 \rangle$. Now, equation (5.70) can be expressed as

$$\begin{aligned} SE_Q(dB) &= SE_{FD}(dB) = 10 \log_{10} \frac{T_c}{T_c - T_u} \\ &= 10 \log_{10} \frac{\langle |S_{11,sc}|^2 \rangle}{\langle |S_{11,sc}|^2 \rangle - \langle |S_{11,su}|^2 \rangle} \end{aligned} \quad (5.72)$$

where T_c and T_u are the chamber transfer function of the covered and uncovered EUT respectively, $S_{11,sc}$ and $S_{11,su}$ are the stirred part of the S -parameters with covered and uncovered EUT. The stirred part can be obtained from the well-known vector average subtraction [3] in (5.8)

It should be noted that (5.72) requires $e_b = 2$ for both covered and uncovered EUT. In practice, e_b depends on the shape of the cavity and stirring effectiveness. When the aperture is large and the frequency is high, the cavity could be not well-stirred and $e_b \neq 2$ [63].

To measure the stirred part of S -parameters, some kind of stirring mechanism should be involved. Normally, it is not easy to stir the EUT mechanically, but source stir and frequency stir can be easily applied which are shown in the measurement process.

5.6.2 Measurement

To verify the proposed one-antenna method, the nested RC method [21] is first used to conduct the measurement, and the results from a nested RC are compared with that from the proposed method. The measurement setup is shown in Fig. 5.45. Because there is no stirrer in the EUT, a nylon wire is fixed with antenna 1 to realise a simple source stir (by pulling the nylon wire manually), as shown in Fig. 5.45(b).

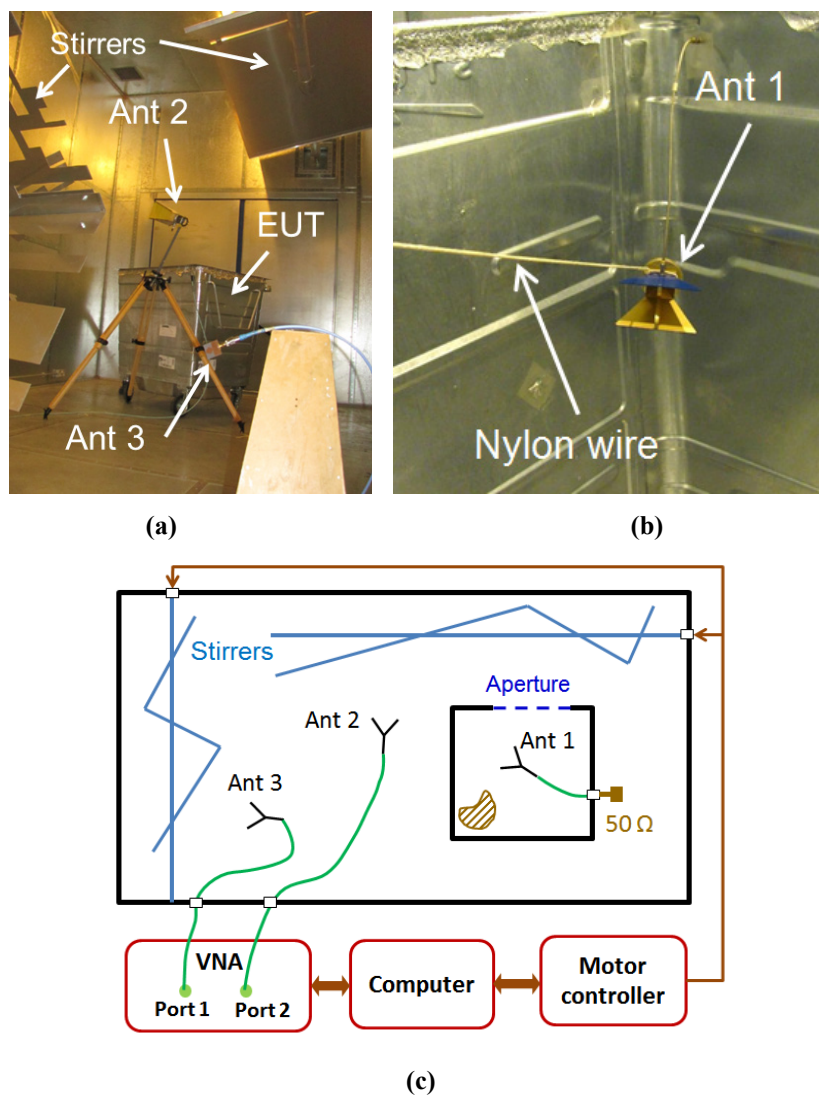


Fig. 5.45. SE measurement using nested RC: (a) measurement scenario, (b) antenna in the EUT, (c) system setup.

A wideband monopole antenna is used as antenna 3, two double-ridged waveguide horn antennas are used as antenna 2 (Rohde & Schwarz® HF 906) and antenna 1 (SATIMO® SH 2000). A vector network analyser (VNA) is employed.

After cables are connected to the VNA and two-port calibration is conducted, antenna 2 is first connected to port 2 of the VNA and antenna 1 is connected to a 50 Ohm load. Antenna 2 is then connected to a 50 Ohm load and antenna 1 is connected to port 2 of the VNA, all the S -parameters are recorded and saved for post-processing.

In this measurement we use 10,001 points in the range of 2.8 ~ 5.2 GHz and 100 rotation steps with a step size of 3 degrees. The size of the RC is 3.6 m × 4 m × 5.8 m, the size of the EUT is 0.8 m × 1 m × 1.1 m, which is about $8\lambda \times 10\lambda \times 11\lambda$ at 3 GHz. According to Weyl's law [64], the mode number is around 7,300 which is large enough. Using a nested RC, the SE value can be obtained as [21]

$$SE_{RC} = 10 \log_{10} \frac{\langle |S_{32}|^2 \rangle / (1 - \langle |S_{22}|^2 \rangle)}{\langle |S_{31}|^2 \rangle / (1 - \langle |S_{11}|^2 \rangle)} \quad (5.73)$$

Two apertures of different sizes (shown in Fig. 5.46) are tested, a foam block is used to control the aperture size and ensure its stability in the measurement process. When using the proposed method, to reduce the effect of the RC on S_{11} , the doors of the RC are kept open and only S_{11} is recorded.

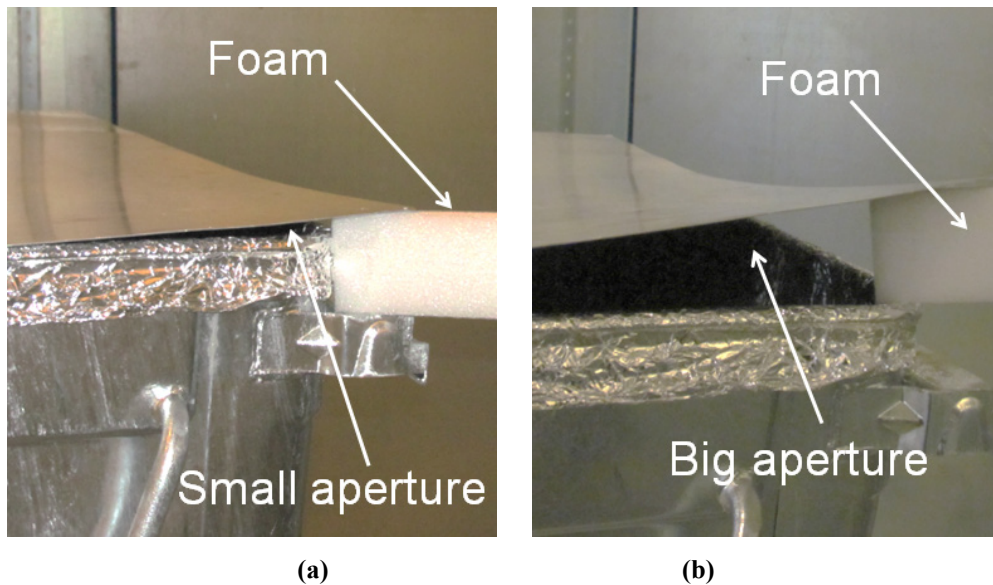


Fig. 5.46. EUT with different apertures: (a) a small aperture, (b) a big aperture.

To obtain the τ in (5.69), we need to measure the S -parameters in the frequency domain and then apply the IFFT to the measured S -parameters. 10,001 points are collected in the range of 2.8 ~ 5.2 GHz which give a resolution of 0.2 ns in the time domain with a length of 4,166 ns. Because τ is frequency dependent, a 5-order elliptic band-pass filter with 200 MHz bandwidth is used to filter the

S -parameters, as shown in Fig. 5.47(a), then the IFFT is applied to the filtered S -parameters. Because the time domain power in the cavity decays exponentially ($e^{-t/\tau}$), the least-square fit is applied to $\ln(\text{Power})$ to extract the slope ratio k , and $\tau = -1/k$ can be extracted. To avoid the fit error caused by the noise level, only part of the signal is used for least-square fit as shown in Fig. 5.47(b). By sweeping the centre frequency of the filter, τ with different centre frequencies are obtained [34].

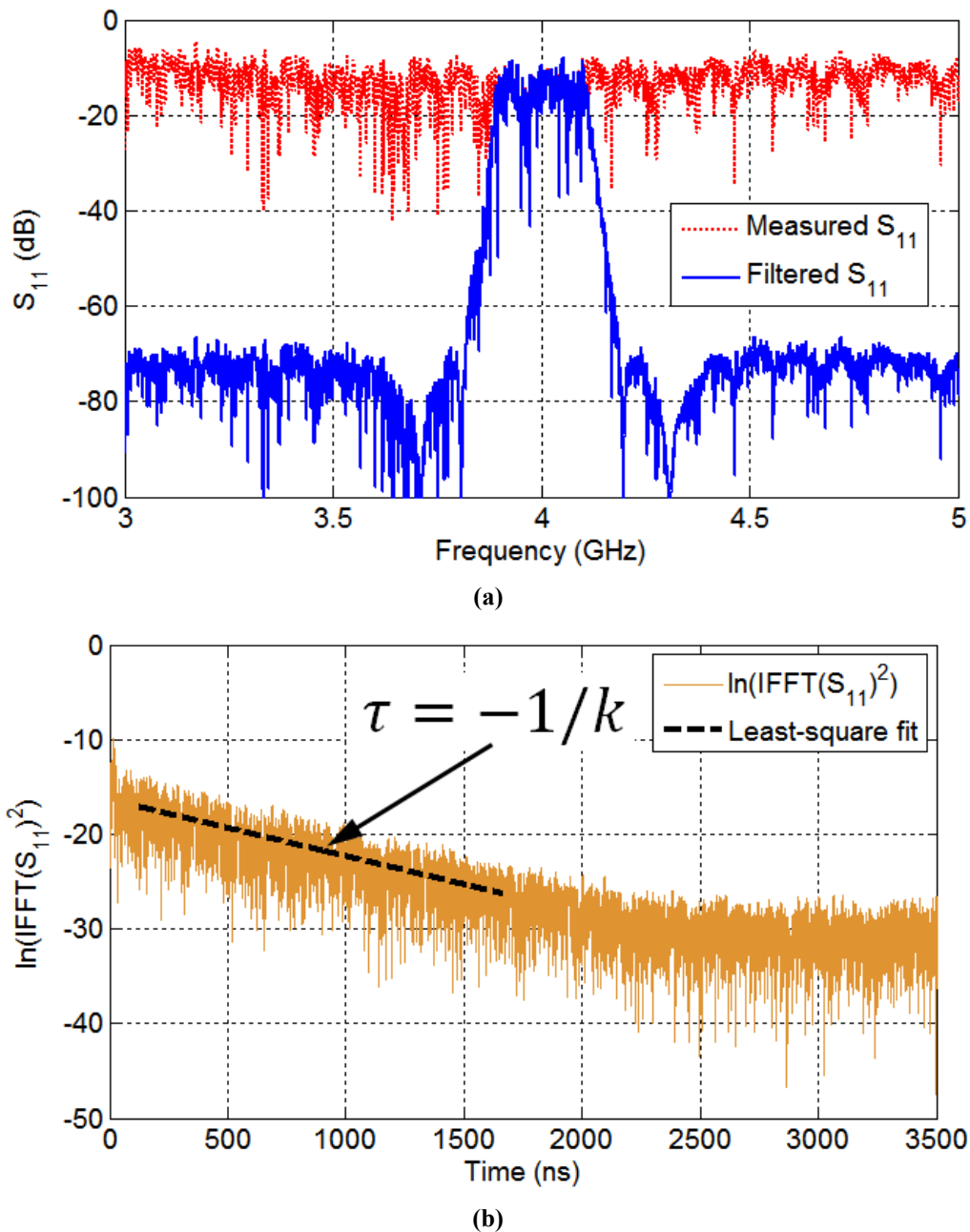
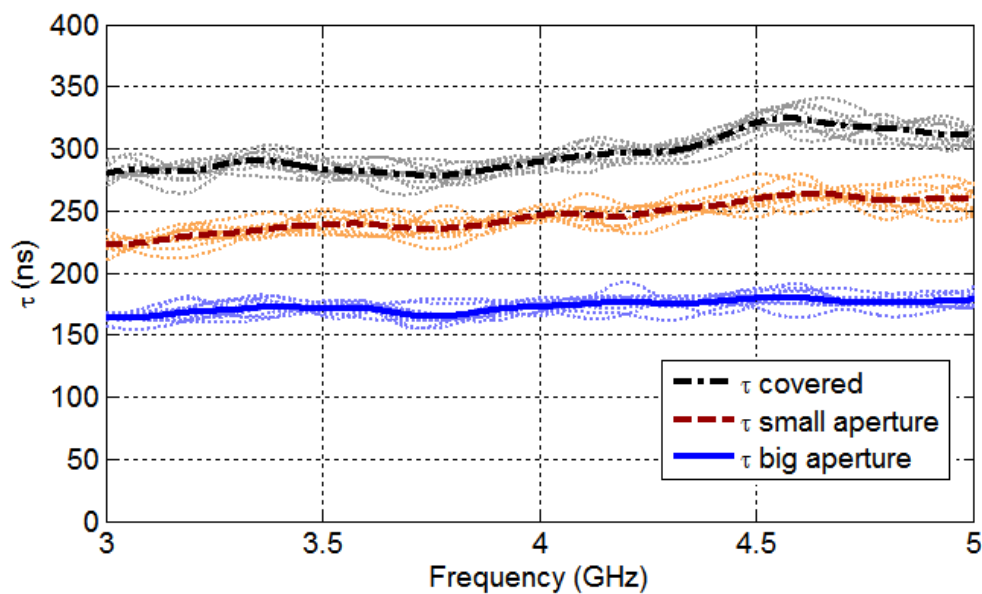


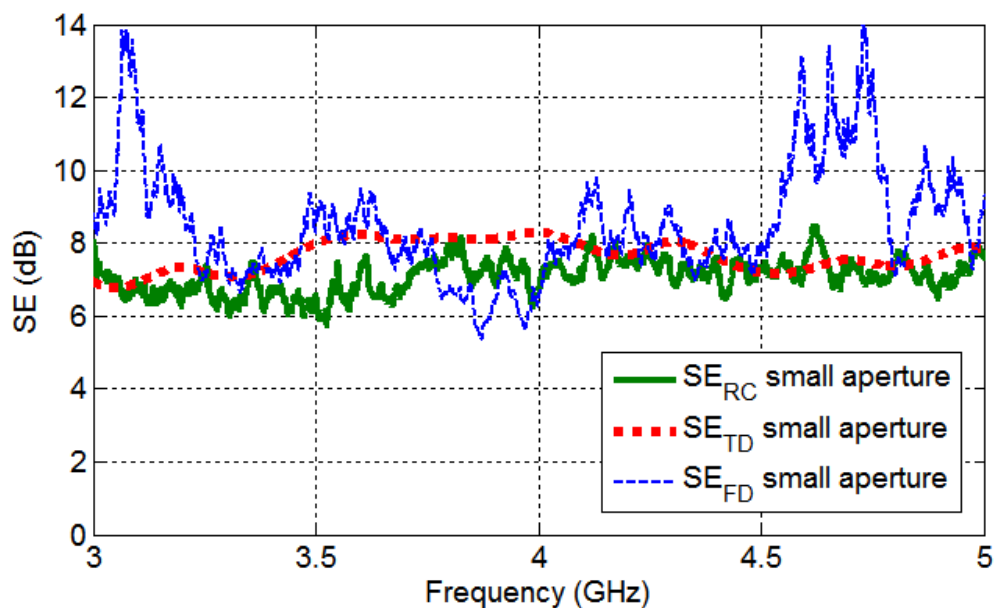
Fig. 5.47. τ extraction procedure. (a) measured S_{11} and filtered S_{11} (EUT with big aperture), (b) time domain response: $\ln(\text{IFFT}(S_{11})^2)$ and least-square fit.

To measure the stirred part of the S -parameters $S_{*,s}$ in (5.72), in practice, both source stir and frequency stir are used: for each frequency, S -parameters with 10 source positions are used, and a window of 1000 sample points (200 MHz) is used to apply the frequency stir.

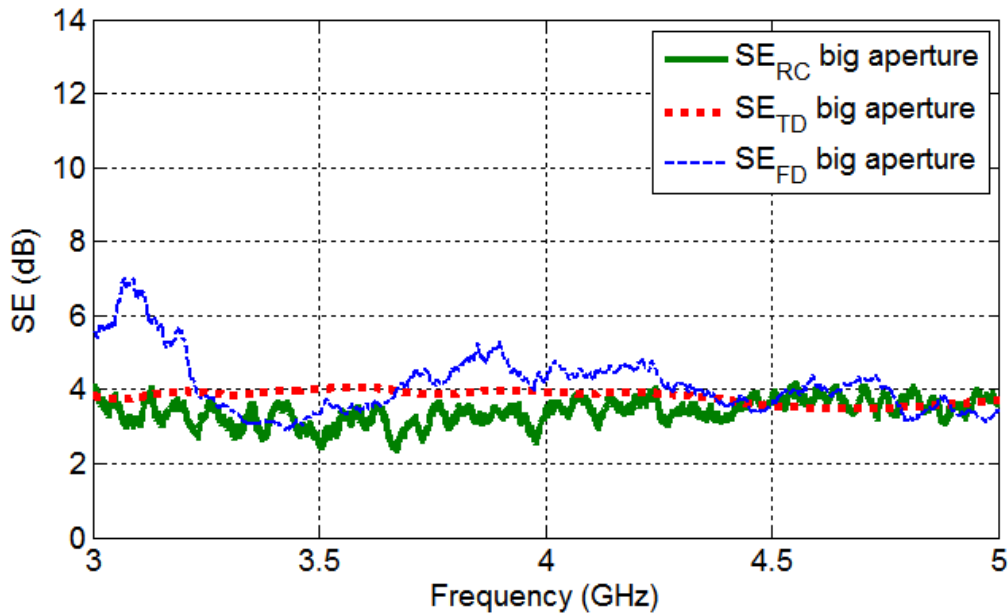
The measured decay time constants for the covered and uncovered apertures are shown in Fig. 5.48 (a): for each case, 10 source positions are used and the averaged values are used to calculate the SE_{TD} . The measured SEs of the two apertures using three equations (5.69), (5.72) and (5.73) are given in Fig. 5.48 (b) and (c).



(a)



(b)



(c)

Fig. 5.48. SE measurement results using (5.69), (5.72) and (5.73): (a) averaged τ (solid lines) and τ with different source positions (light dots), (b) SE values of EUT with a small aperture, (c) SE values of EUT with a big aperture.

The SE values are relatively small due to the aperture sizes and a good agreement between SE_{TD} and SE_{RC} is obtained. However, SE_{FD} shows peaks and troughs and has some deviations from the other two results at some frequencies, which means $e_b \neq 2$ at these frequencies (not well-stirred). More discussions are given in the next section.

5.6.3 Short Summary of Section 5.6

A one-antenna method to measure the SE of an electrically large enclosure has been presented and validated. It is interesting to note that the SE can be related only to τ or stirred S -parameter $S_{*,s}$. In addition, the following aspects should be noted.

When measuring the covered EUT and uncovered EUT, Q_{surf} , Q_{ACS} and Q_{ant} are assumed to be unchanged in the two scenarios. In reality, when the aperture is large, Q_{surf} will be different, however, if Q_{tot} is dominated by Q_{TCS} , this error becomes small. The EUT must be electrically large and well-stirred, this is the pre-condition of (5.61), in this measurement, although 10 source stir locations are used, SE_{FD} still shows bigger deviations than SE_{TD} . This is easy to understand, at a specific frequency, different electrical field distributions may have similar τ values (because the loss distribution is relatively uniform), while a small perturbation in a cavity can have totally different S -parameters. In this measurement, manually pulling the wire can change the antenna position significantly but cannot

change the orientation too much. In practice, it may not have a chance to make sure that the EUT is well-stirred, in this case, SE_{TD} is recommended to use.

In (5.69), τ_c acts as a reference value and should be carefully measured. When the aperture is not properly covered, it is likely to be overestimated when using (5.69)

$$SE_{TD}(dB) = 10 \log_{10} \left(1 + \frac{\tau_u}{\tau_c - \tau_u} \right) \quad (5.74)$$

when τ_c is smaller than the real value, the measured SE_{TD} will be larger than the real value and give an overestimated result. Equation (5.72) also has this problem, when the EUT is not perfectly shielded, T_c is smaller than the real value. This can be observed in Fig. 5.48(b) and (c). We have also checked the SE for the covered EUT using the nested RC method and the result is given in Fig. 5.49, as can be seen it is not perfectly shielded. In practice, shorting out all the apertures of a complex enclosure reliably could be difficult and time consuming, particularly if they are painted or coated in an insulating material.

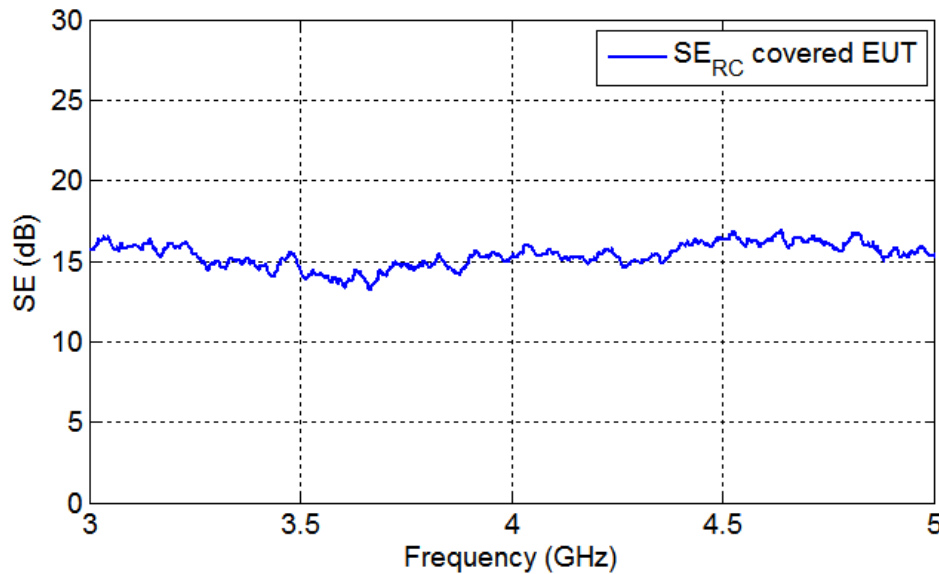


Fig. 5.49. SE values of the covered EUT using the nested RC method.

When the SE value is very large, the measurement will be very sensitive to τ_u and uncertainty will become larger as shown from the following derivative

$$\frac{\partial SE_{TD}}{\partial \tau_u} (dB) = \frac{10/\ln(10)}{\tau_c - \tau_u} \quad (5.75)$$

Suppose we use $\tau_u \approx 300$ ns in Fig. 5.48(a) and $SE_{RC} \approx 15$ dB in Fig. 5.49, τ_c can be obtained using (5.69) as $\tau_c = 309.8$ ns. Then, the SE values with different τ_u can be calculated and given in Fig.

5.50 (at a certain frequency). It can be seen that when τ_u is very close to τ_c , the SE becomes very sensitive. This could be a problem when measuring EUT with large SE values, as shown in Fig. 5.50, the difference of τ_u for SE at 20 dB and 50 dB is only 3 ns which may be smaller than the uncertainty of τ_u .

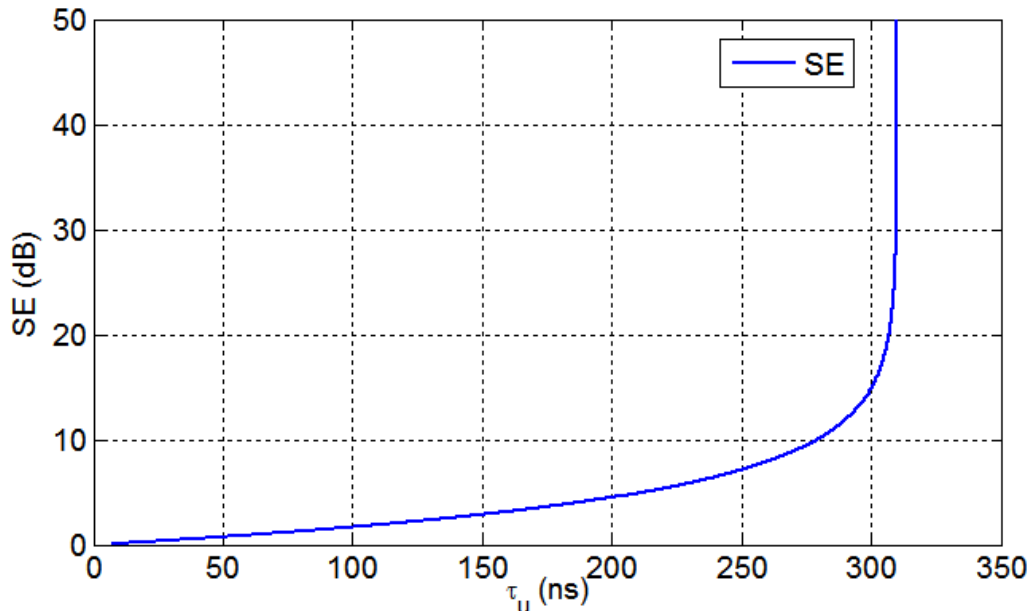


Fig. 5.50. SE values with different τ_u values ($\tau_c=309.8$ ns).

A very drastic SE change in a narrow band may be smoothed out. Both (5.69) and (5.72) can be used to calculate the SE. When using (5.69), S -parameters in a certain bandwidth are needed to calculate τ , which is an averaged τ (in the pass-band of the filter). When using (5.72), frequency stir may also smooth out the peaks and troughs; this has been discussed in [21]. However, measuring the τ in the time domain directly can eliminate this problem [62].

The main advantages of the proposed approaches are the simple measurement setup and cost effectiveness.

One can use (5.69) to calculate τ_c with known SE_{RC} and τ_u , which means that the nested RC needs only to be used once. Once the τ_c is obtained, it can be used for future measurements. This can be very cost effective for product pre-compliance evaluations.

The volume of the EUT does not need to be known, and only one antenna is used. The antenna can be homemade and the performance does not need to be known, provided that it works in the frequency band of interest (matched). Although the Q factors obtained from the time domain Q_{TD} and the frequency domain Q_{FD} are related to the total radiation efficiency of the antenna [3] $(\eta^{total})^2 = Q_{FD}/Q_{TD}$, they will not affect the SE value, because the contribution of the antenna itself Q_{ant} is

assumed to be unchanged for the two scenarios, unless the antenna is so lossy that makes Q_{ant} dominate the Q_{tot} .

There is no need for an AC or RC when using the proposed method. In the measurement, S_{11} was measured with RC doors open, it was found that the measured τ was not sensitive to the test environment, unless the SE was very small. This is easy to understand, when the leaky wave is scattered back from the environment and received by the antenna in the enclosure, the magnitude will be very small and it will not affect τ too much. To validate this, we left the doors open, fixed the EUT with a large aperture and extract τ for 100 stirrer positions. The results are given in Fig. 5.51. As can be seen, the effect caused by the outside RC is less than ± 5 ns which is much smaller than the variation caused by different antenna positions (± 20 ns in Fig. 5.48(a)). Thus the measurement can be done in a robust environment and reduce the cost.

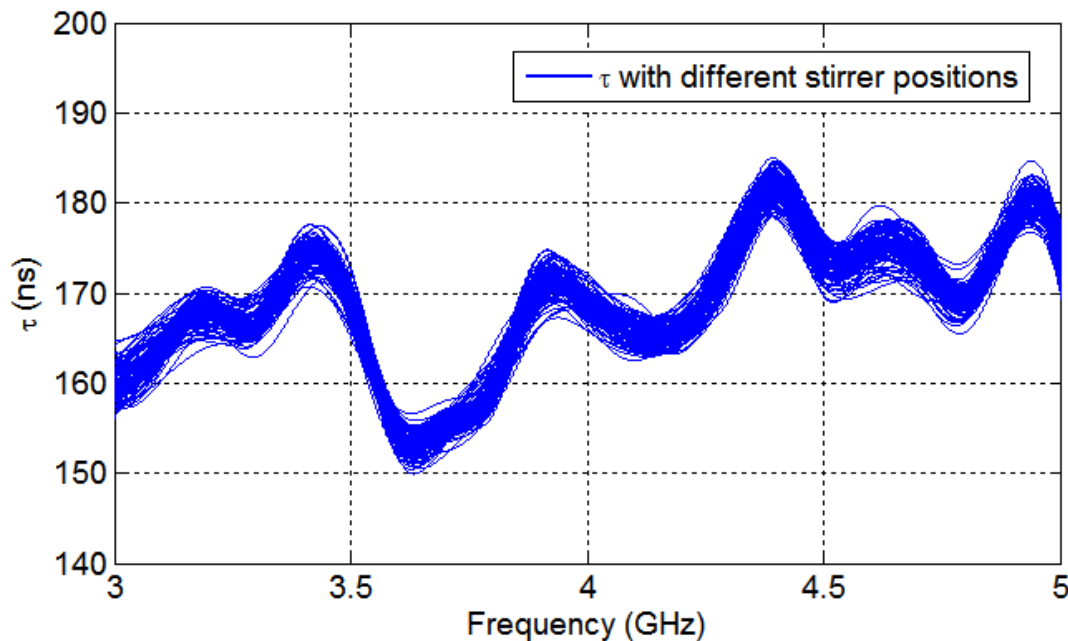


Fig. 5.51. Extracted τ for 100 stirrer positions when the RC doors are left open.

Theoretically, the three SE equations (5.69), (5.72) and (5.73) are equivalent. However, the measurement uncertainties and required facilities are different. The nested RC method (5.73) is believed to have the smallest uncertainty, because mechanical stir is used for each frequency. At the same time, the measurement setup is the most complex. For the two proposed equations (5.69) and (5.72), it has been found that the SE from τ is more stable than the SE from $S_{*,s}$ in Fig. 5.48(b) and (c). The τ value is not sensitive to the outside environment, in this measurement we used averaged τ to reduce the uncertainty. The most critical problem can be found in (5.75), when the EUT is well shielded, the uncertainty of (5.69) and (5.72) increases quickly (Fig. 5.50) which could limit the use of

them. How to measure the τ in (5.69) and $S_{*,s}$ in (5.72) with very small uncertainty/high resolution could be the future work.

5.7 Volume Measurement

It should be noted that, (5.10) can not only be used to measure the radiation efficiency of antennas but also be used to measure/sense the volume of a large cavity. This could be useful for some applications such as in the shipbuilding industry or measure the available volume of a large granary or storehouse (Fig. 5.52).

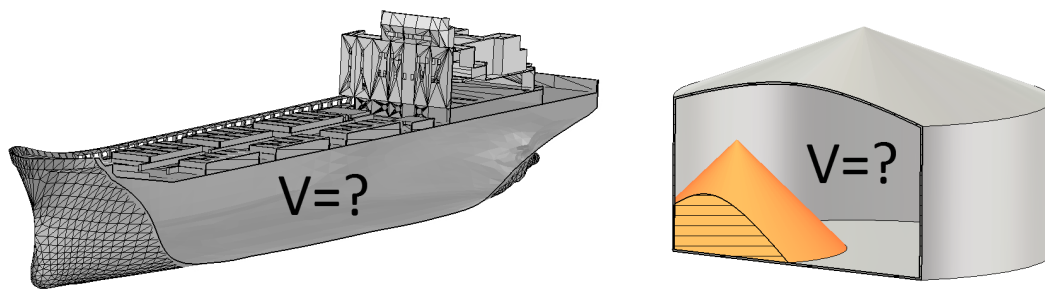


Fig. 5.52. Volume measurement requirement in practice.

In the shipbuilding industry, to measure the volume/capacity of a ship hold is important and useful. Once the available volume and weight are known, the cargos to be shipped can be optimised to maximise the efficiency/benefit of the shipment. And another application is, after a ship was built or modified, the available volume need to be measured to make sure that it is the same as expected. It is easy to obtain the weight information from the draft marks on the bow of a ship. However, the volume information below the deck is not easy to measure because of the complex environment. Conventionally, a laser is used to build a 3D model and the volume can be calculated from the 3D model which is time consuming and expensive [65]. Moreover, inside structures like tubes and stairs need to be removed to make sure that the laser can be applied. Similarly, the same problem exists in measuring the available volume of a large granary or storehouse. Since the inner structure can be complex and irregular, conventional measurement methods could be hard to implement.

If we solve (5.6) and (5.10) for the cavity volume V , we have

$$\begin{cases} C_{RC} = \frac{16\pi^2 V}{\lambda^3} \\ \eta_{1tot}\eta_{2tot} = \frac{C_{RC} \langle |S_{21,s}|^2 \rangle}{\omega\tau_{RC}} \end{cases} \quad (5.76)$$

the volume of the cavity can be obtained as

$$V = \frac{\lambda^2 c_0 \langle \tau \rangle \eta_{1tot} \eta_{2tot}}{8\pi \langle |S_{21} - \langle S_{21} \rangle|^2 \rangle} \quad (5.77)$$

where S_{21} is the transmission coefficient, $\langle \rangle$ means the average value using any stirring method (e.g. mechanical stir, frequency stir, polarisation stir, source stir, *etc.*), λ is the free-space wavelength. c_0 is the speed of light in free space (3×10^8 m/s), η_{1tot} and η_{2tot} are the total efficiency (having taken the loss and impedance matching into account) of antenna 1 and antenna 2 respectively. Here we use $\langle \tau \rangle$ instead of τ_{RC} , because we obtain τ in different scenarios and use the average value, it is not necessary in an RC so we omit the subscript RC .

If the cavity is well-stirred, $\langle |S_{11,s}|^2 \rangle = 2 \langle |S_{21,s}|^2 \rangle$, we can use the one-antenna approach [3, 50]

$$V = \frac{\lambda^2 c_0 \langle \tau \rangle \eta_{itot}^2}{4\pi \langle |S_{ii} - \langle S_{ii} \rangle|^2 \rangle}, \quad i = 1 \text{ or } 2 \quad (5.78)$$

We calibrate the total efficiency of antennas using an RC with known volume, and then we change the environment: load the RC using radio absorbing materials (RAMs), open the door of the RC. After the environment is changed we repeat the measurement to validate the proposed method.

5.7.1 Calibration Process

The measurement scenario is the same as antenna radiation efficiency measurement, shown in Fig. 5.53, two horn antennas are used as antenna 1 (Rohde & Schwarz® HF 906) and antenna 2 (SATIMO® SH2000). 100 stirrer positions with 3.5 degrees/step are used. At each stirrer position, 10001 frequency points are collected in the frequency range of 2.8 GHz to 4.2 GHz. The volume of the RC is $3.6 \text{ m} \times 4 \text{ m} \times 5.8 \text{ m} = 83.52 \text{ m}^3$.

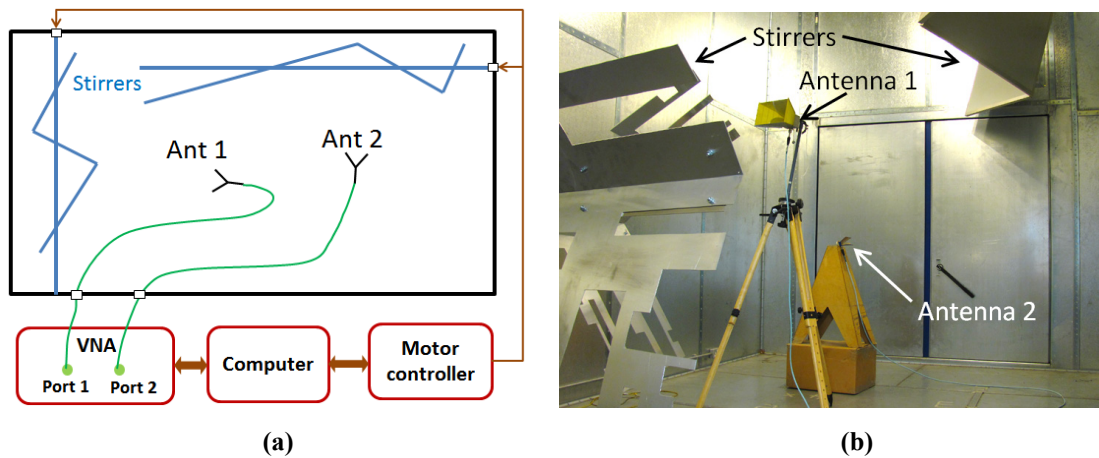


Fig. 5.53. Calibration measurement in an RC, (a) schematic view, (b) measurement setup.

If we use the two-antenna method in (5.77), the measured Q_{FD} in (5.5) is given in Fig. 5.54, at each frequency a frequency stir/window with 100 nearest frequencies are used.

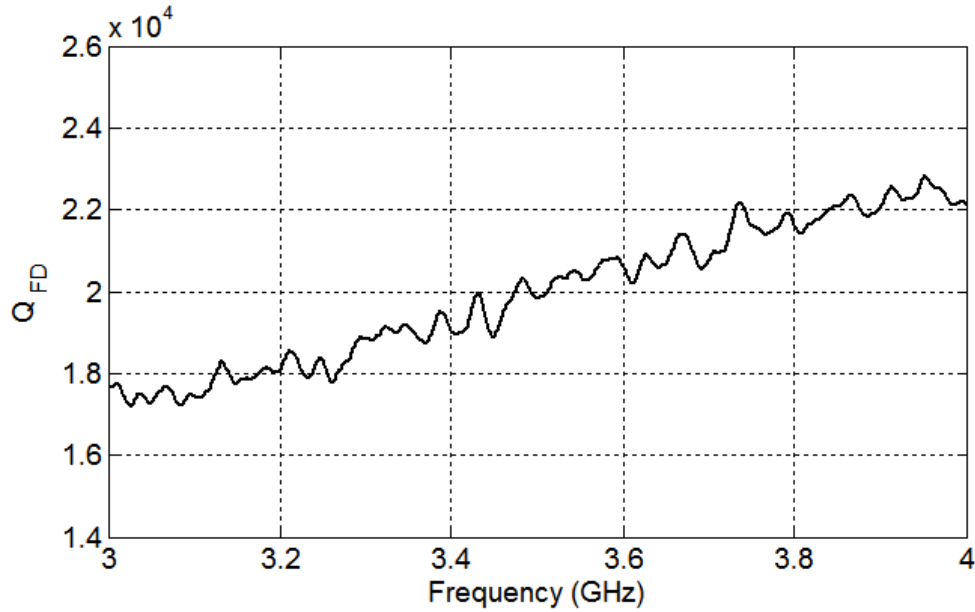


Fig. 5.54. Measured Q_{FD} in the calibration process.

Note Q_{FD} is not accurate when the total efficiency of antennas are not excluded (Q_{FD} and Q_{TD} are not the same when the total efficiencies of antennas are not 100%), but Q_{TD} is not affected by the total efficiency of antennas. We need to know Q_{TD} to obtain $\eta_{1tot}\eta_{2tot}$ [3]

$$\eta_{1tot}\eta_{2tot} = \frac{Q_{FD}}{Q_{FDCor}} = \frac{Q_{FD}}{Q_{TD}} \quad (5.79)$$

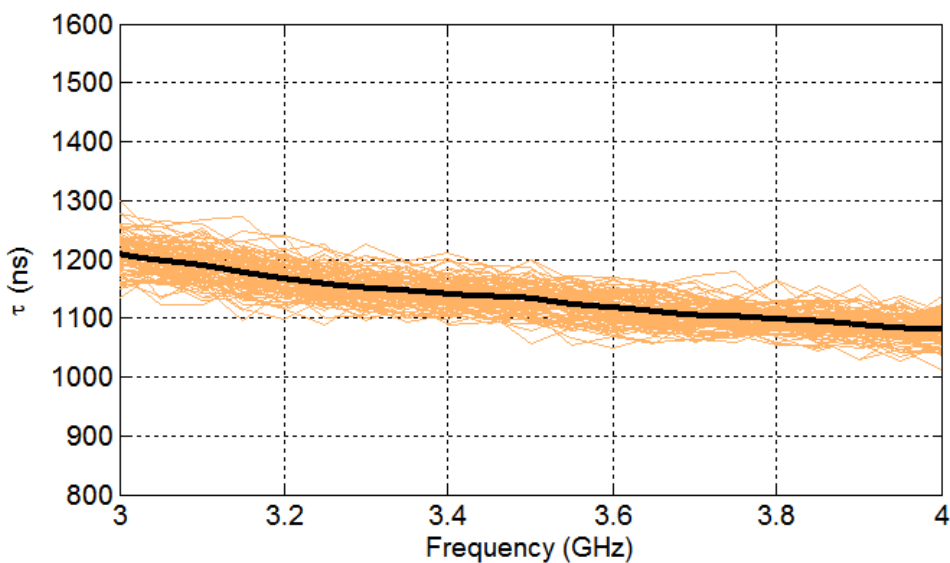


Fig. 5.55. Averaged τ (black line) and τ with different stirrer positions (light lines) in calibration process.

The same procedure in Section 5.6 is used to extract τ and Q_{TD} , shown in Fig. 5.55 and Fig. 5.56. The averaged τ is used to calculate Q_{TD} (Fig. 5.56). Finally, $\eta_{1tot}\eta_{2tot}$ can be obtained using (5.79) and shown in Fig. 5.57.

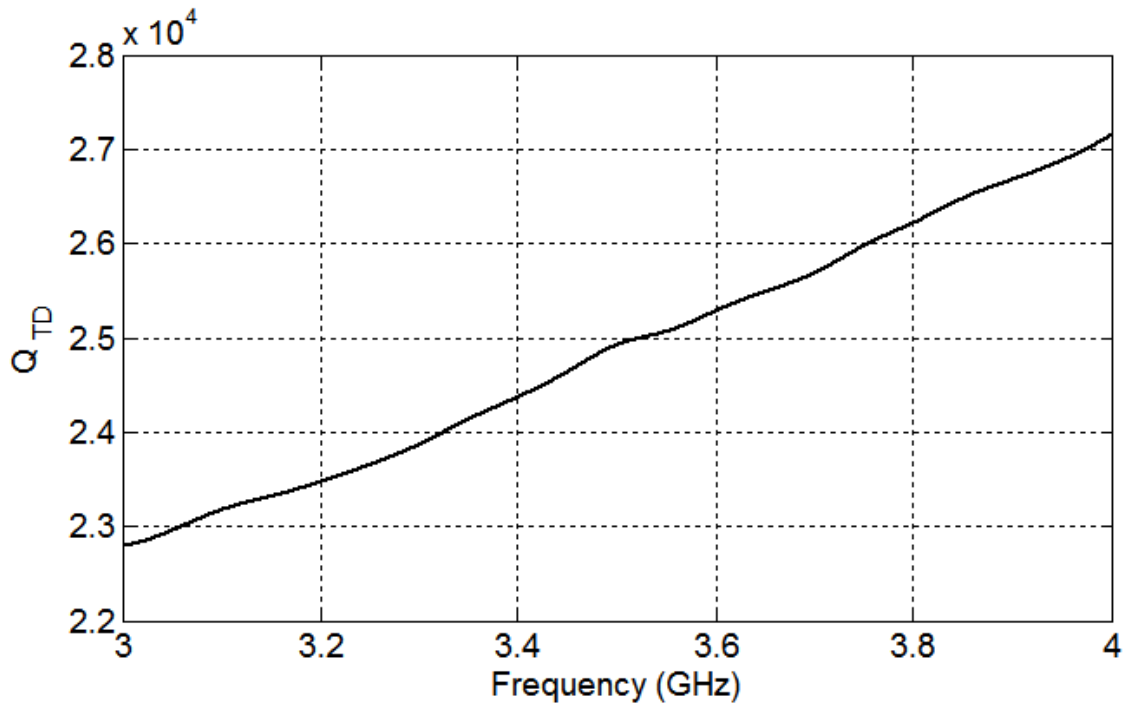


Fig. 5.56. Measured Q_{TD} in the calibration process.

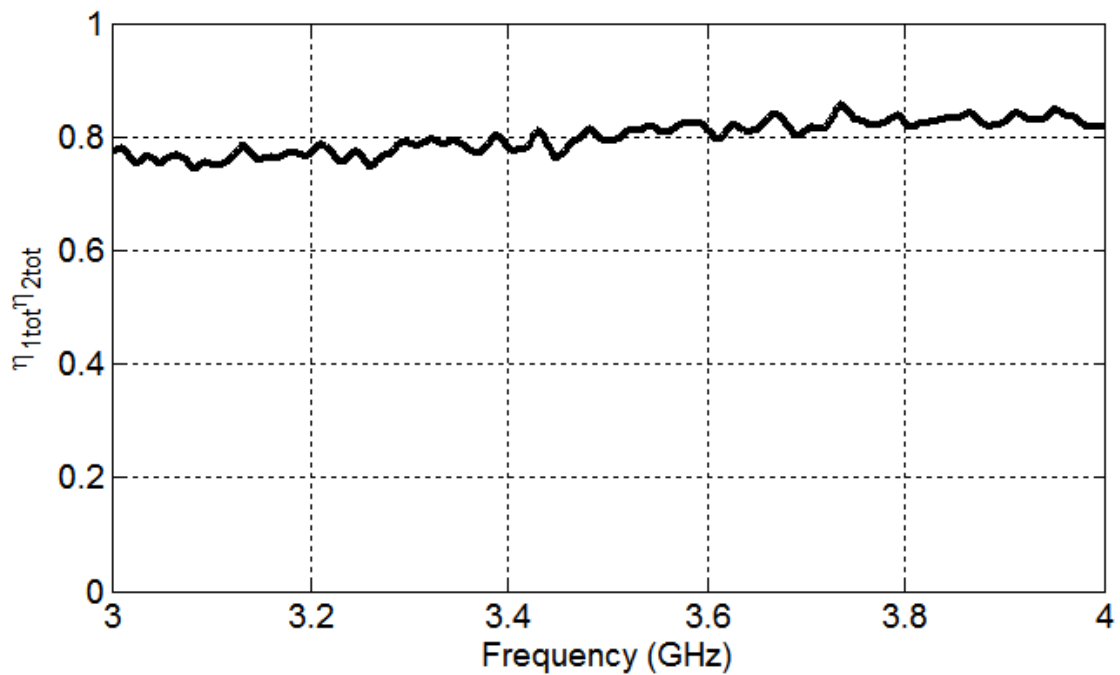
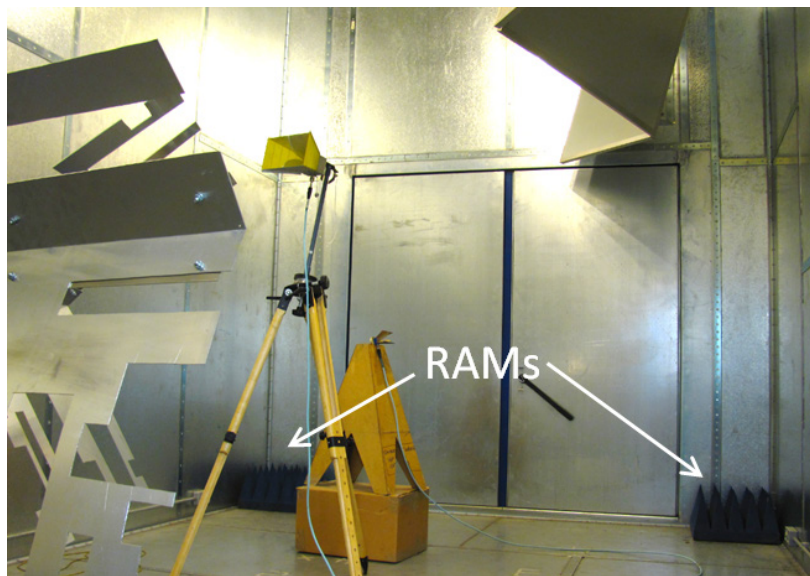


Fig. 5.57. Calibrated $\eta_{1tot}\eta_{2tot}$ in the calibration process.

5.7.2 Measurement Process

After the calibration process is finished, $\eta_{1tot}\eta_{2tot}$ is obtained, and can be used to measure other cavities. Only S_{21} and τ in (5.77) need to be measured. To validate the proposed method, we change the environment: load the RC with RAMs, open the door with 45 degrees and 90 degrees (shown in Fig. 5.58 (b) and (c) respectively). In practice, it may have an entrance without a conducting door, so we open the door to emulate an imperfect cavity.



(a)



(b)



(c)

Fig. 5.58. Measurement scenarios. (a) RC loaded with RAMs, (b) RC with 45 degrees door open, (c) RC with 90 degrees door open.

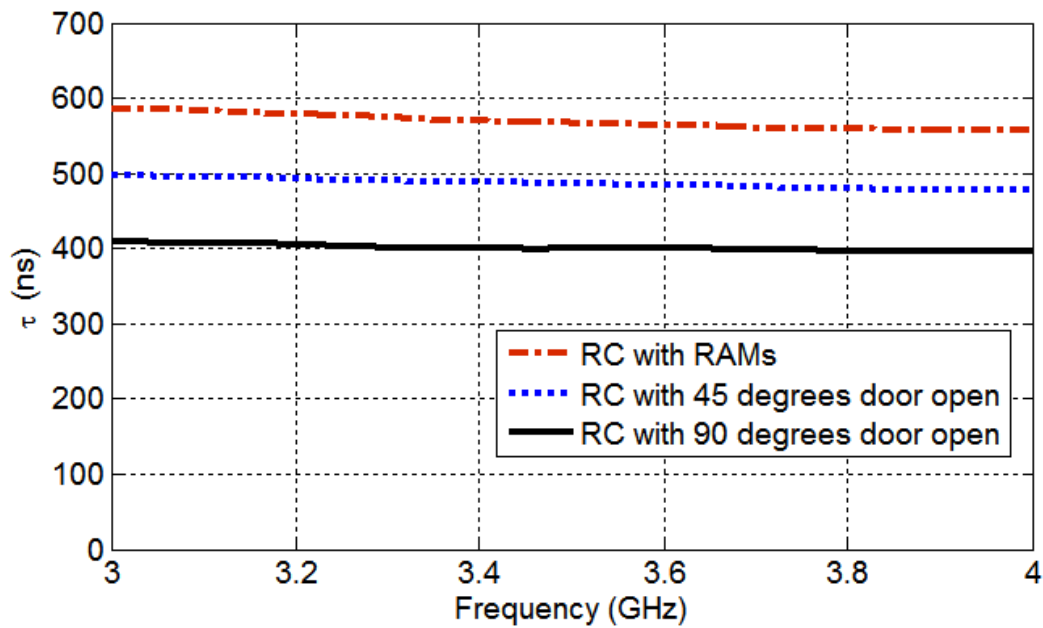


Fig. 5.59. Measured τ in three scenarios.

The same technique as in the calibration process is used to obtain the τ value in different scenarios, as shown in Fig. 5.59. The measured $\langle |S_{21,s}|^2 \rangle$ is given in Fig. 5.60. Finally we apply (5.77) to obtain the volume of the cavity, shown in Fig. 5.61. The whole calibration and measurement procedure are also repeated by using one antenna format (5.78), results are shown in Fig. 5.62 and Fig. 5.63 respectively.

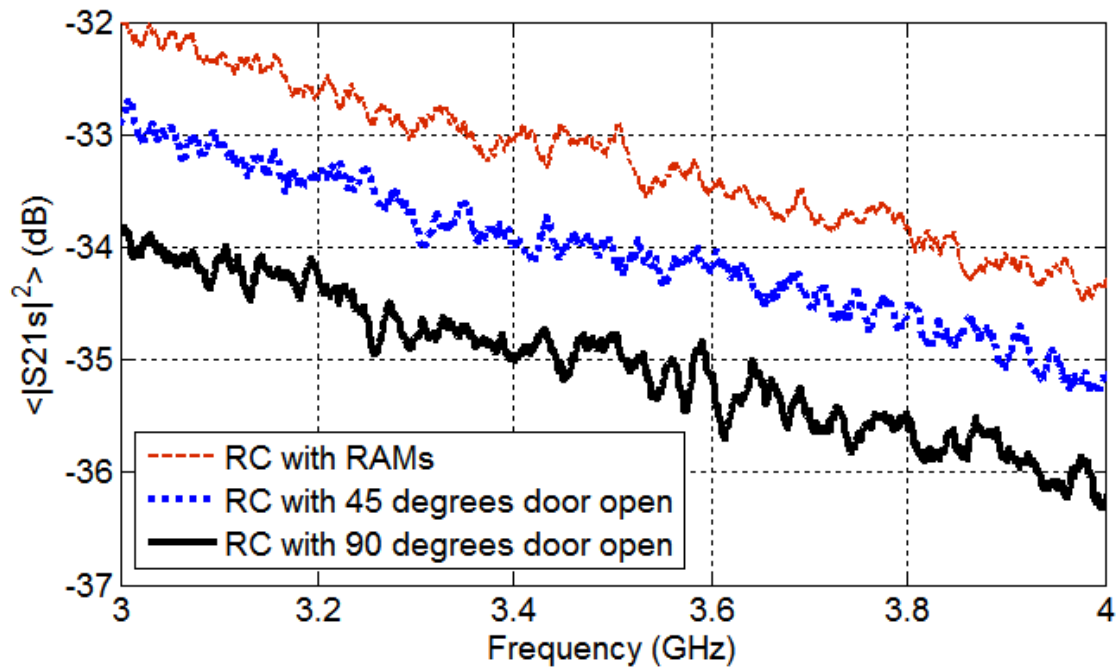


Fig. 5.60. Measured $\langle |S_{21,s}|^2 \rangle$ in three scenarios.

It should be noted that, in practice we may not have stirrers to change the field distribution in the cavity, but source stir [66] and frequency stir are also applicable. To verify it, we keep the stirrers steady; mount antenna 2 on a rotation platform (shown in Fig. 5.64) and 100 platform rotation angles with 3.5 degrees/step are used. The whole calibration and measurement procedure are repeated, results are given in Fig. 5.65 and Fig. 5.66. Note antenna 1 is not rotated, results from antenna 1 only is not available.

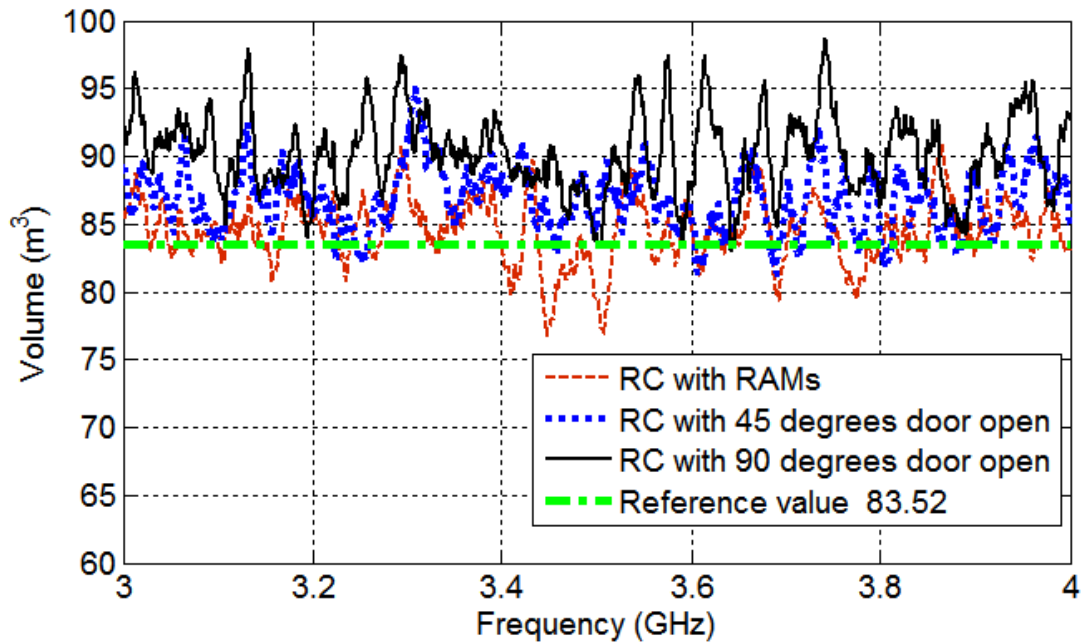


Fig. 5.61. Measured volume value in three scenarios using two-antenna method.

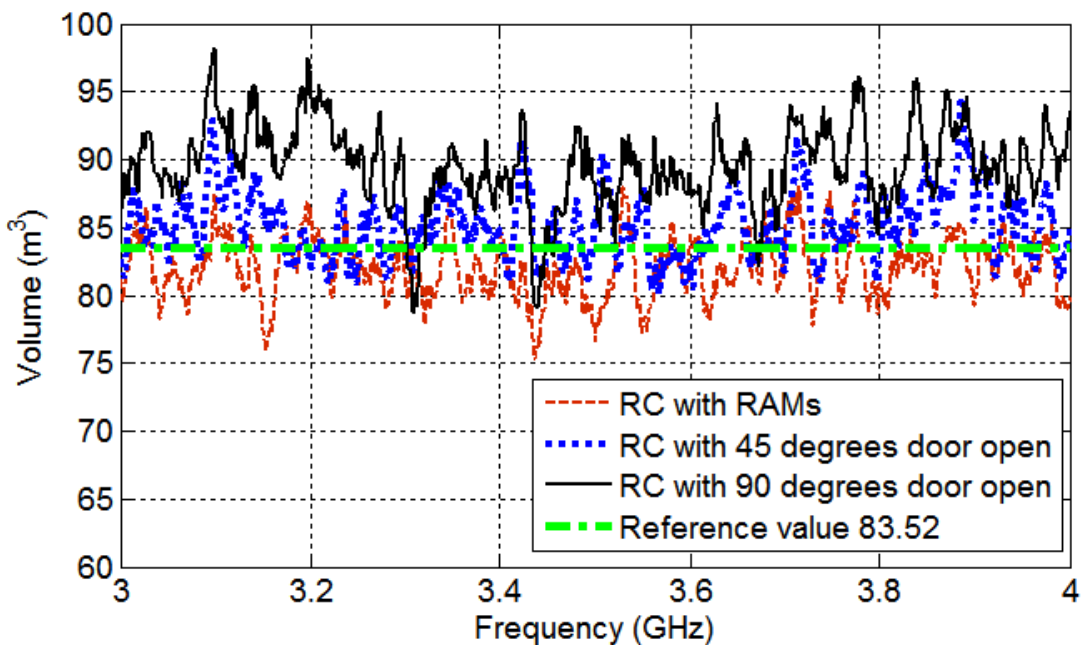


Fig. 5.62. Measured volume value in three scenarios using antenna 1 only.

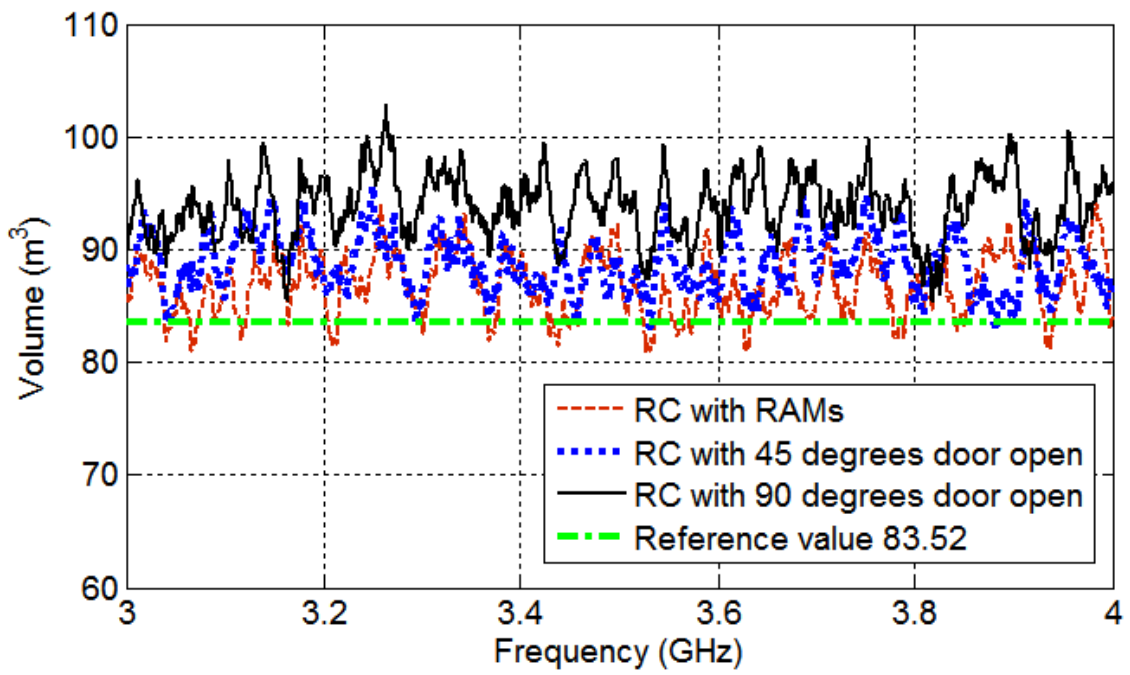


Fig. 5.63. Measured volume value in three scenarios using antenna 2 only.



Fig. 5.64. Antenna 2 mounted on a rotation platform as a source stirrer.

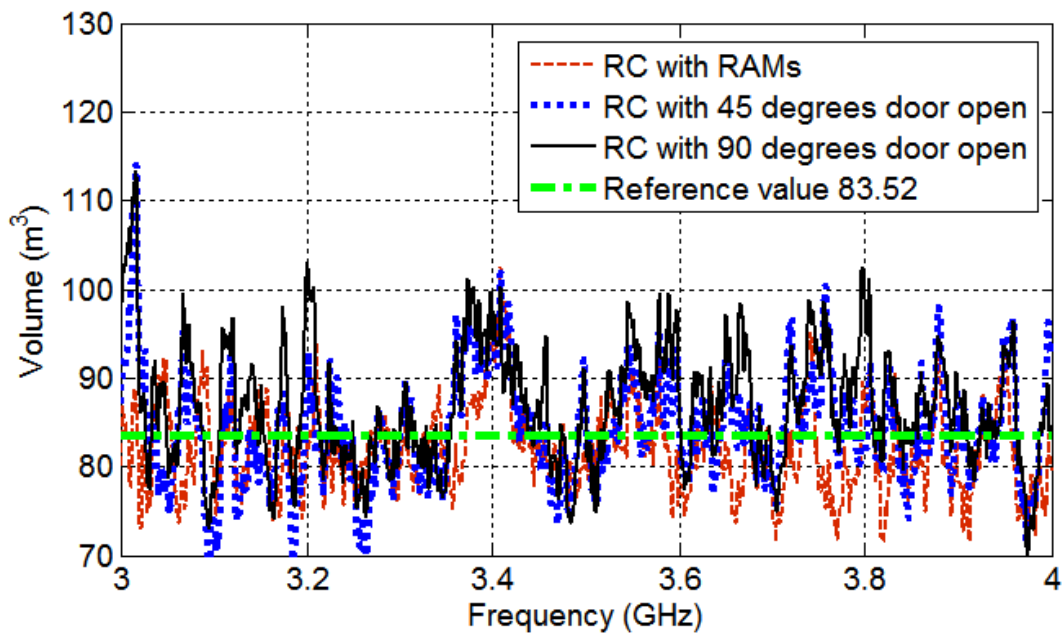


Fig. 5.65. Measured volume value in three scenarios using source stir and two-antenna method.

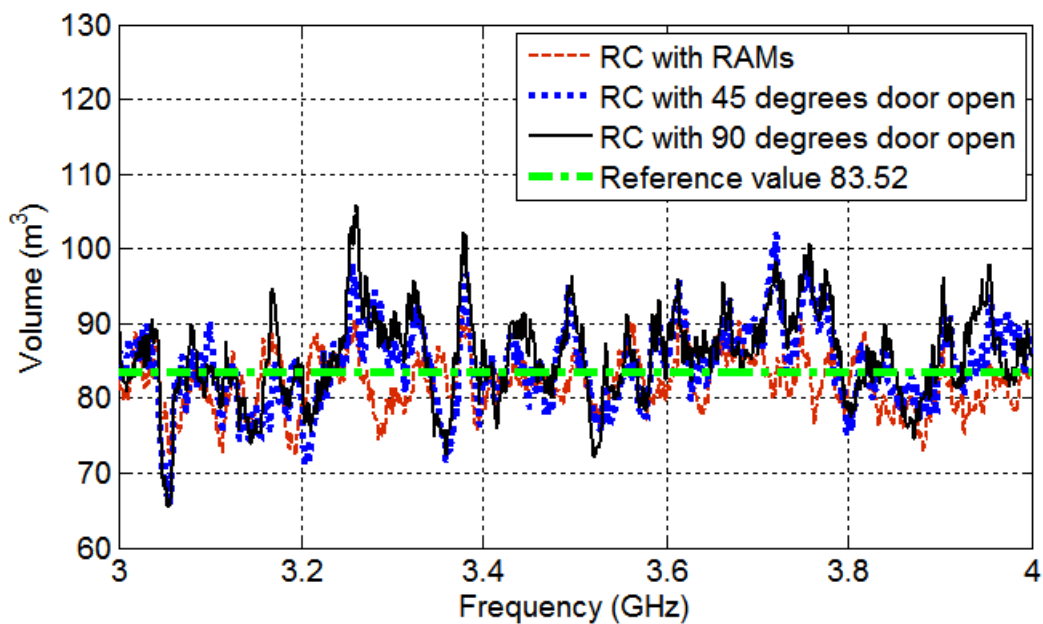


Fig. 5.66. Measured volume value in three scenarios using source stir and antenna 2 only.

The results are summarised in Table 5.4 and discussed in the next section.

5.7.3 Short Summary of Section 5.7

A fast measurement method to measure the volume of a large cavity has been proposed in this section. *Large* means the cavity is large compared with the wavelength of the used electromagnetic/acoustic wave. The method is non-destructive and the system can be assembled as a portable volume probe to

measure large cavities like ship, granary and storehouse. The measurement can be real-time and the shape of the cavity can be arbitrary (complex shape has better field uniformity). After the measurement system is calibrated, only τ and S -parameters need to be measured. Measured volume values in the frequency range of 3 GHz ~ 4 GHz are summarised in Table 5.4.

Table 5.4: Summarised Measurements Results

Measurement Method		Scenarios	Mean (Relative Error)	Standard Deviation
Mechanical stir	1 & 2*	RAMs*	84.53 (1.2%)	2.34
		45	86.90 (4.0%)	2.33
		90	90.19 (8.0%)	2.92
	1	RAMs	82.08 (-1.7%)	2.19
		45	85.23 (2.0%)	2.48
		90	89.63 (7.3%)	3.03
	2	RAMs	86.85 (4.0%)	2.71
		45	88.79 (6.3%)	2.57
		90	93.86 (12.4%)	2.84
Source stir	1 & 2*	RAMs	82.03 (-1.8%)	4.97
		45	84.34 (1.0%)	6.34
		90	86.87 (4.0%)	6.76
	2	RAMs	82.03 (-1.8%)	3.67
		45	84.42 (1.1%)	5.40
		90	85.66 (2.6%)	6.05

*1 & 2 means using the two-antenna method; 1 means using antenna 1 only; 2 means using antenna 2 only; RAMs means the RC is loaded with RAMs; 45 means the door is open with 45 degrees; 90 means the door is open with 90 degrees.

It is interesting to note that, although the proposed method does not depend on the Q factor of the cavity. Results from a small Q cavity tend to have a larger standard deviation. This is easy to understand, when the Q factor reduces, the environment degrades from RIMP to free space, and the transmission coefficient becomes highly dependent on the antenna patterns, orientations, and the distance between antennas (from Hill's equation to Friis equation). Thus, it is hard to realise a well-stirred cavity and could have a large error if the measurement sample number is small (narrow band antenna). A wideband antenna/broadband frequency sweep is better.

The relative error is calculated from the deviation from 83.52 m^3 . It can be found that when the door is open (from 45 degrees to 90 degrees), the measured volume is larger than the real value. This is because when the door is open, we have an equivalent larger cavity. This means the uncovered apertures could lead the measured volume larger than the real value. In this measurement the area of the door is 1.94 m^2 (1.6% of the surface area of the inner walls). Theoretically, the RAMs have occupied a certain volume, we can see from the results of the source stir in Table 5.4, the measured volumes for the RC with loaded RAMs are indeed smaller, but it is not clear from the results for the mechanical stir. This may be due to the total volume of RAMs used is too small ($\sim 0.1 \text{ m}^3$) to be sensed accurately.

For one-antenna method in (5.78), the condition of $e_b = 2$ should be met. If we compare the results from antenna 1 and antenna 2 in the mechanical stir, it can be found that the results from antenna 2 have a larger error than antenna 1, this should be due to the error from e_b , because the S -parameters are recorded in the same environment and system configuration.

There is an equation similar to Hill's equation in acoustics; we can also use sound/supersonic waves to detect the volume of a cavity (no longer limited to metallic cavities). A more general form can be written as

$$V = CF \frac{\lambda^2 \langle \tau \rangle}{\langle T_s \rangle} \quad (5.80)$$

where CF is the calibration factor which can be determined by using a cavity with known volume, λ is wavelength (electromagnetic or acoustic wave), $\langle T_s \rangle$ is the averaged stirred power transfer function, $\langle \tau \rangle$ is the averaged decay time. In room acoustics, it can be converted from the 60 dB reverberation time (RT_{60}) with $\tau = RT_{60}/(6 \ln 10)$ [67]

It should be noted that the method has its own limitations. Although the method is independent on Q factor, it is hard to realise a statistical uniform field in low Q cavities. Another issue is if the cavity is partially filled with liquid or dielectric materials either absorb or reflect waves completely (inhomogeneous cavity), the wave velocity is changed which could increase the measurement error. How the inhomogeneous materials affect the results could be very complex. Also if the shape of the cavity is so irregular that the power density is no longer uniform in the cavity (like the SE measurement), the volume cannot be measured accurately. Future work may include on-site measurements and validation.

5.8 Key Contributions

A series of new measurement methods have been developed in this chapter, key contributions are:

- 1) A modified two-antenna method to measure the radiation efficiency of antennas in an RC has been proposed. The proposed method does not need a reference antenna with known efficiency and the loss of the AUT can be arbitrary which offers an opportunity to measure the antenna with very low radiation efficiency (e.g. implantable antenna) in the RC. The proposed method can also be generalised to nonreciprocal antennas (active antennas), if the transmitting (Tx) efficiency and receiving (Rx) efficiency of the AUT are different (nonreciprocal).
- 2) New diversity gain measurement methods have been proposed which does not need a reference antenna and even extra antennas.
- 3) Two new alternative methods have been proposed to measure the RE of EUT. It has been shown that the signal generator is not necessary in the proposed methods, instead a VNA can be used to complete the measurement and only one antenna is enough, which simplifies the measurement system without losing accuracy. The one- and/or two-antenna method were incorporated into the RE measurement. The radiation efficiency of antennas, reflection coefficients, and the chamber transfer function can be measured simultaneously.
- 4) A new method has been proposed to measure the permittivity and conductivity of a spherical object in the RC, compared with the conventional one, the frequency dependency of ACS was considered which makes the absolute value of both relative permittivity and conductivity can be obtained. An evaluation function has been defined to treat the noisy data and PDF-like results for the permittivity and conductivity have been given. The distribution of the permittivity and conductivity has made the results self-explanatory.
- 5) A one-antenna method to measure the SE of an electrically large enclosure has been presented and validated.
- 6) A fast measurement method to measure the volume of a large cavity has been proposed. The method is non-destructive and can be real-time, the shape of the cavity can be arbitrary (complex shape has better field uniformity). The proposed method can also be realised by using acoustic waves.

5.9 References

- [1] Testing and measurement techniques – Reverberation chamber test methods, IEC 61000-4-21, 2011.
- [2] P. -S. Kildal, C. Carlsson and J. Yang, “Measurement of free-space impedances of small antennas in reverberation chambers,” *Microwave and Optical Letters*, vol. 32, no. 2, pp. 112-115, Jan. 2002.
- [3] C. L. Holloway, H. A. Shah, R. J. Pirkl, W. F. Young, D. A. Hill and J. Ladbury, “Reverberation chamber techniques for determining the radiation and total efficiency of antennas,” *IEEE Trans. Antennas Propagat.*, vol. 60, no. 4, pp. 1758-1770, Apr. 2012.
- [4] M. Piette, “Antenna radiation efficiency measurements in a reverberation chamber,” in *Proceedings of Asia-Pacific Radio Science Conference*, pp. 19-22, 24-27 Aug. 2004.
- [5] H. G. Krauthauser and M. Herbrig, “Yet another antenna efficiency measurement method in reverberation chambers,” *IEEE International Symposium on Electromagnetic Compatibility (EMC)*, pp. 536-540, 25-30 Jul. 2010.
- [6] C. L. Holloway, R. S. Smith, C. R. Dunlap, R. J. Pirkl, J. Ladbury, W. F. Young, D. A. Hill, W. R. Hansell and M. A. Shadish, “Validation of a two-antenna reverberation chamber technique for estimating the total and radiation efficiency of antennas,” *International Symposium on Electromagnetic Compatibility (EMC EUROPE)*, pp. 1-6, 17-21 Sep. 2012.
- [7] C. L. Holloway, R. S. Smith, C. R. Dunlap, R. J. Pirkl, J. Ladbury, W. F. Young, W. R. Hansell, M. A. Shadish and K. Sullivan, “Validation of a one-antenna reverberation-chamber technique for estimating the total and radiation efficiency of an antenna,” *IEEE International Symposium on Electromagnetic Compatibility (EMC)*, pp. 205-209, 6-10 Aug. 2012.
- [8] G. A. Conway, W. G. Scanlon, C. Orlenius and C. Walker, “In situ measurement of UHF wearable antenna radiation efficiency using a reverberation chamber,” *IEEE Antennas and Wireless Propagation Letters*, vol. 7, pp. 271-274, 2008.
- [9] S. J. Boyes, P. J. Soh, Y. Huang, G. A. E. Vandenbosch, N. Khiabani, “Measurement and performance of textile antenna efficiency on a human body in a reverberation chamber,” *IEEE Transactions on Antennas and Propagation*, vol. 61, no. 2, pp. 871-881, Feb. 2013.
- [10] S. J. Boyes, P. J. Soh, Y. Huang, G. A. E. Vandenbosch, N. Khiabani, “On-body performance of dual-band textile antennas,” *IET Microwaves, Antennas & Propagation*, vol. 6, no. 15, pp. 1696-1703, Dec. 2012.
- [11] X. Chen, “On statistics of the measured antenna efficiency in a reverberation chamber,” *IEEE Transactions on Antennas and Propagation*, vol. 61, no. 11, pp. 5417-5424, Nov. 2013.

-
- [12] X. Chen, "Measurement uncertainty of antenna efficiency in a reverberation chamber," *IEEE Transactions on Electromagnetic Compatibility*, vol. 55, no. 6, pp. 1331-1334, Dec. 2013.
- [13] X. Chen, "Generalized statistics of antenna efficiency measurement in a reverberation chamber," *IEEE Transactions on Electromagnetic Compatibility*, vol. 62, no. 3, pp. 1504-1507, Dec. 2013.
- [14] C. Lemoine, E. Amador, P. Besnier, J. -M. Floc'h and A. Laisné, "Antenna directivity measurement in reverberation chamber from Rician K-factor estimation," *IEEE Transactions on Antennas and Propagation*, vol. 61, no. 10, pp. 5307-5310, Oct. 2013.
- [15] P. Besnier, C. Lemoine, J. Sol, and J. -M. Floc'h, "Radiation pattern measurements in reverberation chamber based on estimation of coherent and diffuse electromagnetic fields," *IEEE Conference on Antenna Measurements & Applications (CAMA)*, pp. 1-4, 16-19 Nov. 2014.
- [16] M. A. Garcia-Fernandez, D. Carsenat and C. Decroze, "Antenna gain and radiation pattern measurements in reverberation chamber using Doppler effect," *IEEE Transactions on Antennas and Propagation*, vol. 62, no. 10, pp. 5389-5394, Oct. 2014.
- [17] V. Fiumara, A. Fusco, V. Matta and I. M. Pinto, "Free-space antenna field/pattern retrieval in reverberation environments," *IEEE Antennas and Wireless Propagation Letters*, vol. 4, pp. 329-332, 2005.
- [18] H. G. Krauthauser, "On the measurement of total radiated power in uncalibrated reverberation chambers," *IEEE Transactions on Electromagnetic Compatibility*, vol. 49, no. 2, pp. 270-279, May 2007.
- [19] P. Wilson, G. Koepke, J. M. Ladbury, C. L. Holloway, "Emission and immunity standards: replacing field-at-a-distance measurements with total-radiated-power measurements," *IEEE International Symposium on Electromagnetic Compatibility*, vol. 2, pp. 964-969, 2001.
- [20] C. L. Holloway, D. A. Hill, J. M. Ladbury, G. Koepke, R. Garzia, "Shielding effectiveness measurements of materials using nested reverberation chambers," *IEEE Transactions on Electromagnetic Compatibility*, vol. 45, no. 2, pp. 350-356, May 2003.
- [21] C. L. Holloway, D. A. Hill, M. Sandroni, J. M. Ladbury, J. Coder, G. Koepke, A. C. Marvin and Y. He, "Use of reverberation chambers to determine the shielding effectiveness of physically small, electrically large enclosures and cavities," *IEEE Transactions on Electromagnetic Compatibility*, vol. 50, no. 4, pp. 770-782, Nov. 2008.
- [22] A. Gifuni and M. Migliaccio, "Use of nested reverberating chambers to measure shielding effectiveness of nonreciprocal samples taking into account multiple interactions," *IEEE Transactions on Electromagnetic Compatibility*, vol. 50, no. 4, pp. 783-786, Nov. 2008.
- [23] R. Armstrong, A. Marvin and J. Dawson, "An experimental investigation of the use of Q-

- factor to determine the shielding effectiveness of electrically large equipment enclosures with apertures,” in *Proc. 10th Int. Symposium on Electromagn. Compat. (EMC Europe 2011)*, York, UK, Sep. 26-30, pp. 148-152, 2011.
- [24] A. Gifuni, A. Sorrentino, A. Fanti, G. Ferrara, M. Migliaccio, G. Mazzarella and F. Corona, “On the evaluation of the shielding effectiveness of an electrically large enclosure,” *Advanced Electromagnetics*, vol. 1, no. 1, pp. 84-91, 2012.
- [25] P. –S. Kildal, K. Rosengren, J. Byun and J. Lee, “Definition of effective diversity gain and how to measure it in a reverberation chamber,” *Microwave and Optical Technology Letters*, vol. 34, no. 1, 2002.
- [26] K. Rosengren and P. –S. Kildal, “Radiation efficiency, correlation, diversity gain and capacity of a six-monopole antenna array for a MIMO system: theory, simulation and measurement in reverberation chamber,” *IEE Proceedings Microwaves, Antennas and Propagation*, vol. 152, no. 1, pp. 7-16, 2005.
- [27] P. –S. Kildal, K. Rosengren, “Correlation and capacity of MIMO systems and mutual coupling, radiation efficiency, and diversity gain of their antennas: simulations and measurements in a reverberation chamber,” *IEEE Communications Magazine*, vol. 42, no. 12, pp. 104-112, Dec. 2004.
- [28] M. Mouhamadou, C. A. Tounou, C. Decroze, D. Carsenat, T. Monediere, “Active measurements of antenna diversity performances using a specific test-bed, in several environments,” *International Journal of RF and Microwave Computer-Aided Engineering*, vol. 20, pp. 264–271, 2010.
- [29] C. L. Holloway, D. A. Hill, J. M. Ladbury, P. F. Wilson, G. Koepke and J. Coder, “On the use of reverberation chambers to simulate a Rician radio environment for the testing of wireless devices,” *IEEE Transactions on Antennas and Propagation*, vol. 54, no. 11, pp. 3167-3177, Nov. 2006.
- [30] C. Lemoine, E. Amador, P. Besnier, “On the K-factor estimation for Rician channel simulated in reverberation chamber,” *IEEE Transactions on Antennas and Propagation*, vol. 59, no. 3, pp. 1003-1012, March 2011.
- [31] M. I. Andries, P. Besnier, C. Lemoine, “Estimating K-factor and time spread parameters from a transient response of a pulse modulated sine wave in reverberation chamber,” *IEEE Transactions on Antennas and Propagation*, vol. 61, no. 1, pp. 380-389, Jan. 2013.
- [32] H. A. Shah, “Wireless channel characterization of the reverberation chamber at NIST,” Master Thesis, Dept. of Signals and System, Chalmers University of Technology, Gothenburg, Sweden, 2011.
- [33] X. Chen, P. –S. Kildal, C. Orlenius and J. Carlsson, “Channel sounding of loaded

- reverberation chamber for over-the-air testing of wireless devices: coherence bandwidth versus average mode bandwidth and delay spread,” *IEEE Antennas and Wireless Propagation Letters*, vol. 8, pp. 678-681, 2009.
- [34] E. Genender, C. L. Holloway, K. A. Remley, J. M. Ladbury, G. Koepke, and H. Garbe, “Simulating the multipath channel with a reverberation chamber: application to bit error rate measurements,” *IEEE Transactions on Electromagnetic Compatibility*, vol. 52, no. 4, pp. 766-777, Nov. 2010.
- [35] K. Karlsson, X. Chen, P. –S. Kildal and J. Carlsson, “Doppler spread in reverberating chamber predicted from measurements during step-wise stationary stirring,” *IEEE Antennas and Wireless Propagation Letters*, vol. 9, pp. 497-500, 2010.
- [36] P. Hallbjorner, A. Rydberg, “Maximum Doppler frequency in reverberation chamber with continuously moving stirrer,” *Antennas and Propagation Conference (LAPC)*, Loughborough, pp. 229-232, 2007.
- [37] X. Chen, “Evaluation and measurement of the Doppler spectrum in a reverberation chamber,” *Progress in Electromagnetics Research M*, vol. 26, pp. 267-277, 2012.
- [38] C. Orlenius, P. –S. Kildal, G. Poilasne, “Measurements of total isotropic sensitivity and average fading sensitivity of CDMA phones in reverberation chamber,” *IEEE Antennas and Propagation Society International Symposium*, vol. 1A, pp. 409-412, 3-8 Jul. 2005.
- [39] A. Hussain, P. –S. Kildal, A. A. Glazunov, “Interpreting the total isotropic sensitivity and diversity gain of LTE-enabled wireless devices from over-the-air throughput measurements in reverberation chambers,” *IEEE Access*, vol. 3, pp. 131-145, 2015.
- [40] U. Calberg, P. –S., Kildal, A. Wolfgang, O. Sotoudeh and C. Orlenius, “Calculated and measured absorption cross sections of lossy objects in reverberation chamber,” *IEEE Transactions on Electromagnetic Compatibility*, vol. 46, no. 2, pp. 146-154, May 2004.
- [41] G. Gradoni, D. Micheli, F. Moglie and V. M. Primiani, “Absorbing cross section in reverberation chamber: experimental and numerical results,” *Progress In Electromagnetics Research B*, vol. 45, pp. 187-202, 2012.
- [42] E. Amador, M. I. Andries, C. Lemonie and P. Besnier, “Absorbing material characterization in a reverberation chamber,” *Proc. of the 10th Int. Sympos. on Electromagnetic Compatibility (EMC Europe 2011)*, York, UK, Sep. 26-30, 2011.
- [43] G. C. R. Melia, I. D. Flintoft and M. P. Robinson, “Absorption cross-section of the human body in a reverberant environment,” *Int. Sympos. on Electromagnetic Compatibility (EMC Europe 2012)*, Rome, Italy, Sep. 2012.
- [44] C. L. Holloway, D. A. Hill and J. M. Ladbury and G. Koepke, “Requirements for an effective reverberation chamber: unloaded or loaded,” *IEEE Transactions on Electromagnetic*

- Compatibility*, vol. 48, no. 1, pp. 187-194, Feb. 2006.
- [45] P. Hallbjorner, U. Calberg, K. Madsen and J. Andersson, "Extracting electrical material parameters of electrically large dielectric objects from reverberation chamber measurements of absorption cross section," *IEEE Transactions on Electromagnetic Compatibility*, vol. 47, no. 2, pp. 291-303, May 2005.
- [46] S. Lallechere, I. E. Baba, P. Bonnet and F. Paladian, "Total scattering cross section improvements from electromagnetic reverberation chambers modeling and stochastic formalism," *Proceedings of the 5th European Conference on Antennas and Propagation (EUCAP)*, pp. 81-85, 11-15 April 2011.
- [47] I. E. Baba, S. Lallechere, P. Bonnet, J. Benoit and F. Paladian, "Computing total scattering cross section from 3-D reverberation chambers time modeling," *Asia-Pacific Symposium on Electromagnetic Compatibility (APEMC)*, pp. 585-588, 21-24 May 2012.
- [48] G. Lerosey and J. Rosny, "Scattering cross section measurement in reverberation chamber," *IEEE Transactions on Electromagnetic Compatibility*, vol. 49, no. 2, pp. 280-284, May 2007.
- [49] I. E. Baba, S. Lallechere and P. Bonnet, "Numerical total scattering cross section from reverberating electromagnetic experiments," *Progress in Electromagnetics Research Letters*, vol. 19, pp. 127-135, 2010.
- [50] J. M. Ladbury and D. A. Hill, "Enhanced backscatter in a reverberation chamber: Inside every complex problem is a simple solution struggling to get out," in *Proc. IEEE Int. Symp. on Electromagnetic Compatibility*, pp. 1-5, Jul. 9-13, 2007.
- [51] C. L. Holloway, H. A. Shah, R. J. Pirkl, K. A. Remley, D. A. Hill and J. Ladbury, "Early time behavior in reverberation chambers and its effect on the relationships between coherence bandwidth, chamber decay time, RMS delay spread, and the chamber buildup time," *IEEE Transactions on Electromagnetic Compatibility*, vol. 54, no. 4, pp. 717-725, Nov. 2012.
- [52] A. K. Skrivervik, "Implantable antennas: The challenge of efficiency," *7th European Conference on Antennas and Propagation (EUCAP)*, pp. 3627-3631, 8-12 Apr. 2013, 2013.
- [53] R. Alrawashdeh, Y. Huang and P. Cao, "A flexible loop antenna for total knee replacement implants in the MedRadio band," *Loughborough, Antennas and Propagation Conference (LAPC)*, pp. 225-228, Nov. 2013.
- [54] L. Huitema, T. Reveyrand, J. -L. Mattei, E. Arnaud, C. Decroze and T. Monediere, "Frequency tunable antenna using a magneto-dielectric material for DVB-H application," *IEEE Trans. Antennas Propagat.*, vol. 61, no. 9, pp. 4456-4466, Sep. 2013.
- [55] S. S. Alja'afreh, Y. Huang and L. Xing, "A compact, wideband and low profile planar inverted-L antenna," in *Proc. 8th European Conference on Antennas and Propagation (EuCAP)*, Netherlands, April. 2014.

- [56] P. Corona, G. Latmiral, E. Paolini and L. Piccioli, "Use of reverberating enclosure for measurements of radiated power in the microwave range," *IEEE Transactions on Electromagnetic Compatibility*, vol. 18, pp. 54–59, 1976.
- [57] [Online]. Available: <http://www.invisible-systems.com/>.
- [58] C. F. Bohren and D. R. Huffman, *Absorption and Scattering of Light by Small Particles*, John Wiley, New York, 1983.
- [59] C. Matzler, Matlab functions for Mie scattering and absorption, research report, Institute of Applied Physics, University of Bern, no. 2002-11, Aug. 2002.
- [60] D. A. Hill, M. T. Ma, A. R. Ondrejka, B. F. Riddle, M. L. Crawford and R. T. Johnk, "Aperture excitation of electrically large, lossy cavities," *IEEE Trans. Electromagn. Compat.*, vol. 36, no. 3, pp.169-178, Aug. 1994.
- [61] R. Armstrong, "Measurement of shielding in electrically large metallic enclosures," Ph.D. dissertation, Dept. of Electronics., University of York, York, UK, 2013.
- [62] E. Amador, C. Lemonie, P. Besnier and A. Laisné, "Reverberation chamber modeling based on image theory: Investigation in the pulse regime," *IEEE Trans. Electromagn. Compat.*, vol. 52, no. 4, pp.778-789, Nov. 2010.
- [63] C. R. Dunlap, "Reverberation chamber characterization using enhanced backscatter coefficient measurements," Ph.D. dissertation, Dept. of Electrical, Computer and Engineering, University of Colorado, Boulder, USA, 2013.
- [64] D. A. Hill, "Electromagnetic fields in cavities: Deterministic and statistical theories," Wiley-IEEE Press, 2009.
- [65] S. S. Bhat and D. J. Smith, "Laser and sound scanner for non-contact 3D volume measurement and surface texture analysis," *Physiological Measurement*, vol. 15, no. 1, pp.79-88, 1994.
- [66] Y. Huang and D. J. Edwards, "A novel reverberating chamber: source-stirred chamber", *Proc. of IEE 8th International Conference on Electromagnetic Compatibility*, pp.120-124, Edinburgh, UK, September 1992.
- [67] M. Kleiner, J. Tichy, "Acoustics of small rooms," CRC Press, 2014.

Chapter 6: B-Scan in a Reverberation Chamber

6.1 Introduction

In this chapter, we investigate the reverberation chamber in the time domain. The time domain behaviour of an RC has been observed in [1, 2] to investigate the statistical isotropy of the RC. The information extracted from the time domain can be combined with that from the frequency domain, and a series of applications become possible, such as measuring the radiation efficiency of antennas without using a reference antenna [3], absorption cross section measurement [4], Q factor extraction and chamber decay time control [5], *etc.* B-scan is a two-dimensional time domain impulse scan and has been widely used in many applications such as radar, medical imaging, non-destructive testing [6], *etc.* However, a complete B-scan has not yet been implemented in an RC. Some relevant work has been done in [1, 2], which provides important insight from the time domain, and the synthetic-aperture technique is used with 9 stirrer positions [1, 2]. In the time domain, the arrived signal with different time and angle (anisotropy of the RC) can be observed directly which provides important guidelines and insights for the future measurement setup.

The statistical behaviour in the frequency domain has been well investigated [7, 8], and the statistical distributions of the electric field in the frequency domain are well-known. However, there are limited studies in the time domain statistical distribution, which is one of the main contributions of this chapter. An important definition is the stirrer efficiency, which is hard to quantify in the frequency domain (even impossible). Many efforts have been made to discuss it [9-12], which provided important practical guidelines and experience. It has been found that, the stirrer efficiency (if defined by using K -factor) could be changed by load or antenna positions [13-15]. Thus, it is related to too many variables and hard to characterise in the frequency domain. In this chapter, it has been found that the stirrer efficiency can be well defined in the time domain and only related to the equivalent total scattering cross section (TSCS) of the stirrers. The equivalent TSCS of stirrers is determined by the geometric properties of the stirrers (shape, position, *etc.*) and how the stirrers are moved; it is not sensitive to the load and antenna position. Like the efficiency definition in other applications, the stirrer efficiency defined in this chapter is in the range of 0% to 100% which corresponds to an RC with no stirrer and well-stirred RC respectively. The definition in this chapter provides a universal way to compare the performance between different RCs or different stirrer designs in one RC. Moreover, the time-gating technique has been used to remove the early-time behaviour in the chamber decay constant extraction [3, 16], it has been found in this chapter that the time-gating technique can also be used in an RC to filter the unwanted signals to correct the chamber transfer function. By removing the unwanted signals, the stirrer efficiency can be increased without changing the stirrers.

This chapter is organised as follows: the measurement setup and theory are given first, followed by the understanding and discussion of the results where three main aspects are addressed: the statistical behaviour, stirrer efficiency quantification and time-gating technique. Finally, discussions and conclusions are summarised.

6.2 B-Scan Measurement and Theory

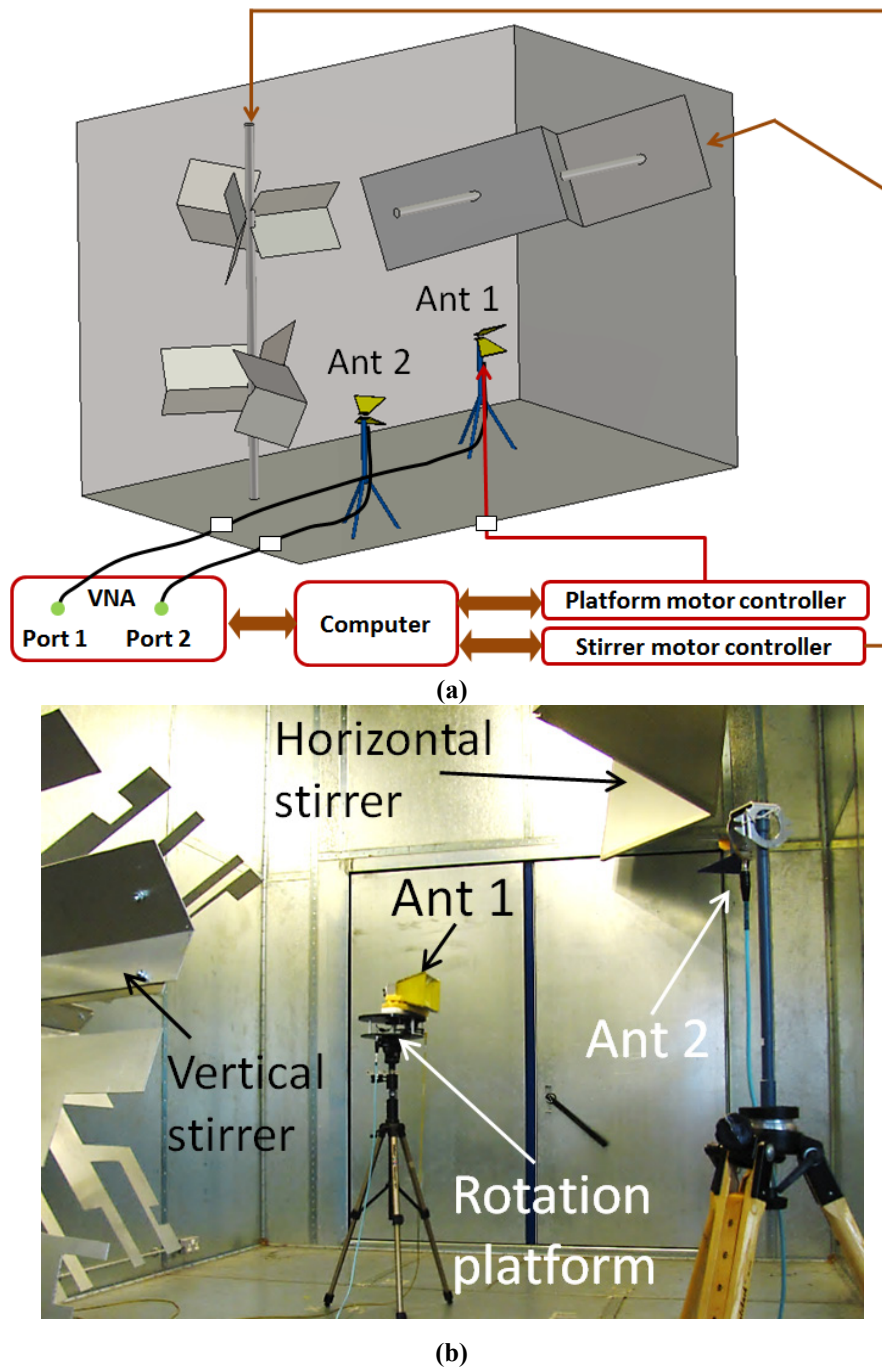


Fig. 6.1. B-scan measurement setup in an RC: (a) schematic measurement setup, (b) measurement setup in the RC at the University of Liverpool.

To realise a B-scan in an RC, it is possible to measure the time domain response directly using an impulse source and an oscilloscope [17]. Another method is to measure the system response in the frequency domain and apply the inverse fast Fourier transform (IFFT) to obtain the time domain response. Measuring the frequency domain response using a vector network analyser (VNA) is simpler and can provide larger dynamic range [18]. In this chapter, frequency domain measurement method is used to obtain the time domain response.

The measurement setup is shown in Fig. 6.1, the size of the RC is 3.6 m (W) \times 5.8 m (L) \times 4 m (H). Two horn antennas are used as antenna 1 (Rohde & Schwarz® HF 906) and antenna 2 (SATIMO® SH 2000), both antennas are well-matched from 2 GHz. The rotation platform, stirrers and VNA are synchronised and controlled by a computer. S -parameters with 10001 sample points in the frequency range of 2 GHz to 4 GHz are recorded for different platform angles and stirrer positions; this corresponds to the time domain (after IFFT) resolution of 0.25 ns and duration of 5000 ns. For each platform angle, 100 stirrer positions are used with 3.5 degrees/step. The platform is rotated with 2 degrees/step for one complete revolution to have a good angular resolution. Thus we have $180 \times 100 = 18000$ set of S -parameters in total.

The time domain response can be obtained from the IFFT of the measured S -parameters, and a 10th order elliptic band pass filter is applied to reduce the ripples caused by a rectangular window [19], of which the pass band is set as 2.4 GHz \sim 3.6 GHz. We denote the electric field at the receiving antenna as

$$E(t, \theta, n) = IFFT[\tilde{S}(\theta, f, n)] \quad (6.1)$$

where \tilde{S} represents the filtered S -parameters depends on the rotation angle of antenna 1 (θ), frequency (f) and stirrer position (n). The plots of $IFFT[\tilde{S}_{11}(\theta, f, n)]$ and $IFFT[\tilde{S}_{21}(\theta, f, n)]$ give a monostatic and bistatic B-scan map respectively. Although the electric field obtained from the IFFT of S -parameters is not the actual E-field in space, it does not affect our study in this chapter; we can consider it as *equivalent* E-field and it has been shown that the statistical behaviour of received voltage and electric field are the same [7]. The gain of antenna 1 in the measured frequency range is around 10 dBi (half-power beamwidth $\approx 60^\circ$), thus a good angular resolution can be obtained. Obviously, rotating an omnidirectional (low gain) antenna is meaningless.

Since the measured S -parameters include unstirred part \tilde{S}_{us} and stirred part \tilde{S}_s [3]

$$\tilde{S} = \tilde{S}_{us} + \tilde{S}_s = \langle \tilde{S} \rangle + \tilde{S}_s \quad (6.2)$$

where $\langle \cdot \rangle$ means the average using any stirring method (e.g. mechanical stir, frequency stir, source stir, *etc.*). Applying the IFFT to both sides of (6.2)

$$IFFT(\tilde{S}) = IFFT(\langle \tilde{S} \rangle) + IFFT(\tilde{S}_s) \quad (6.3)$$

$IFFT(\tilde{S})$ is the total time domain response and $IFFT(\langle \tilde{S} \rangle)$ is the unstirred part in the time domain. For an ideal/well-stirred reverberation chamber, $\langle \tilde{S} \rangle$ is the free-space S -parameter and $\langle \tilde{S} \rangle = \tilde{S}_{FreeSpace}$ [20]. As can be seen later, when the RC is not ideal (stirrer efficiency is not 100%), the unstirred part $\langle \tilde{S} \rangle$ does not only include the free-space response, but also include the contribution of equivalent TSCS of stirrers (the moving objects in the RC). It is not rigorous to consider $\langle \tilde{S} \rangle$ as just the unstirred part of the free-space response in the RC.

6.2.1 Statistical Behaviour in the Time Domain

If we consider the statistical behaviour of the impulse response in the time domain, the E-field can be regarded as a non-stationary stochastic process. For a specific time, because the incident wave superimpose randomly, by applying the Lindberg central limit theorem, the rectangular E-field follows normal distribution at each specific time. If the early time response and the unstirred part are ignored, the probability distribution function (PDF) can be expressed as

$$PDF[E(t)] = PDF[E_x(t)] = PDF[E_y(t)] = PDF[E_z(t)] = e^{-\frac{x^2}{2\sigma^2}} / (\sigma\sqrt{2\pi}) \quad (6.4)$$

with a mean value $\langle E(t) \rangle = 0$, and σ is a time dependent variable. An expression for $\sigma(t)$ needs to be known, if we consider the power decay $P(t)$, it decays exponentially which can be expressed as

$$\langle P(t) \rangle \propto \langle E(t)^2 \rangle = P_0 e^{-t\tau_{RC}^{-1}} \quad (6.5)$$

where τ_{RC} is the decay constant of the RC, P_0 is a constant which determines the initial power. From (6.4), the PDF of $E(t)^2$ which follows chi-square distribution with one degree of freedom can be obtained

$$PDF[E(t)^2] \sim \chi_1^2 = e^{-\frac{x^2}{2\sigma^2}} / (\sigma\sqrt{2\pi x}) \quad (6.6)$$

From (6.6), the mean value can be obtained as

$$\langle E(t)^2 \rangle = \sigma^2 \quad (6.7)$$

If we compare (6.5) and (6.7), the time dependent σ can be obtained as

$$\sigma(t) = \sqrt{P_0 e^{-t\tau_{RC}^{-1}}} \quad (6.8)$$

Thus the statistical behaviour of the impulse response E-field is well characterised. Note that τ_{RC} is frequency dependent and can be considered as the average value in the spectrum range of the excitation impulse.

6.2.2 Stirrer Efficiency

If we check the TSCS measurement in [21], the stirrers can be considered as an object under test, and it has been used to characterise the TSCS of stirrers in simulation [22, 23]. It should be noted that, in the TSCS measurement, the object under test is required to be moved freely in space. However, in practice, the stirrers are rotating around fixed axes (cannot be moved freely), thus the measured TSCS is actually the *equivalent* TSCS. Since only the equivalent TSCS plays a part in the measurement, we are not interested in the real value TSCS of stirrers. We denote the equivalent TSCS as \widetilde{TSCS} , thus \widetilde{TSCS} of stirrers can be obtained from the difference of the decay speed of $\langle E(t)^2 \rangle$ and $\langle E(t) \rangle^2$ [21-23]

$$\langle E(t)^2 \rangle = P_0 e^{-t\tau_{RC}^{-1}} \quad (6.9)$$

$$\langle E(t) \rangle^2 = P_0 e^{-t(\tau_{RC}^{-1} + \tau_s^{-1})} \quad (6.10)$$

The least-square fit can be applied to extract the chamber decay time τ_{RC} and the scattering damping time τ_s [21], and \widetilde{TSCS} of stirrers can be obtained as [21]

$$\widetilde{TSCS} = \frac{V}{\tau_s c_0} \quad (6.11)$$

Thus $\tau_s = V/(\widetilde{TSCS} \times c_0)$, where V is the volume of the RC, c_0 is the speed of light. If we check (6.9) - (6.11) carefully, it can be found that the contribution of τ_s is independent of the load of the chamber, because the load of the chamber has been included in τ_{RC} . The contribution of τ_s can be extracted by

$$\frac{\langle E(t) \rangle^2}{\langle E(t)^2 \rangle} = e^{-t\tau_s^{-1}} \quad (6.12)$$

If we check (6.3), it can be found that, τ_s and \widetilde{TSCS} actually describe how fast the unstirred part decays compared with the total signal strength (PDP). If we define the *stirrer efficiency* as the residual of the ratio in (12) caused by the scattering damping time τ_s , we have

$$\eta_s = 1 - e^{-t_0 \tau_s^{-1}} \quad (6.13)$$

where t_0 is a typical/reference time (similar to the concept of typical physical dimension in [17, 24]). The stirrer efficiency becomes in the range of 0% to 100%. It can be seen that when a very small stirrer is used, the stirrer efficiency is small, as there is no significant difference between (6.9) and (6.10), $\tau_{RC}^{-1} \approx (\tau_{RC}^{-1} + \tau_s^{-1})$, $\tau_s \rightarrow +\infty$, $\eta_s \rightarrow 0\%$. When the RC is well-stirred, $\langle E(t) \rangle^2$ decays to zero very fast and $\tau_{RC}^{-1} + \tau_s^{-1} \rightarrow +\infty$, $\tau_s \rightarrow 0$, $\eta_s \rightarrow 100\%$. In this thesis we choose $t_0 = 12 \sqrt[3]{V}/c_0$ which means the wave is allowed to interact with the walls of the RC at least twice, more discussions on t_0 are given in Appendix A3. Then η_s in (6.13) becomes

$$\eta_s = 1 - e^{-12 \sqrt[3]{V}/(c_0 \tau_s)} \quad (6.14)$$

(6.13) can also be written in the TSCS form using (6.11)

$$\eta_s = 1 - e^{-12 \overline{TSCS}/V^{2/3}} \quad (6.15)$$

It is only related to the ratio between the equivalent TSCS of the stirrers and the surface area of the RC.

The definition in (6.13) confirms that τ_s is only related to \overline{TSCS} of stirrers which is not sensitive to the load and the antenna positions in the RC.

6.2.3 Time-Gating Technique

In the frequency domain, it is well-known that the chamber transfer function T can be corrected by removing the unstirred part of S -parameters [3]

$$T_{CFD} = \langle |S_{21} - \langle S_{21} \rangle|^2 \rangle \quad (6.16)$$

where T_{CFD} denotes the chamber transfer function is corrected in the frequency domain. Correspondingly, in the time domain, if we check (6.9) and (6.10), because of τ_s , $(\tau_{RC}^{-1} + \tau_s^{-1}) > \tau_{RC}^{-1}$, the unstirred part $\langle E(t) \rangle^2$ decays faster than $\langle E(t) \rangle^2$. This is easy to understand, as the longer the wave travels, the more times it interacts with stirrers. Filtering the signals in the time domain can also correct the unstirred part

$$T_{CTD} = \langle |FFT\{TG[IFFT(\tilde{S}_{21})]\}|^2 \rangle \quad (6.17)$$

where TG means the time-gating operation, FFT denotes the fast Fourier transform, T_{CTD} is the chamber transfer function corrected in the time domain. The philosophy is similar to what is done in the reflectivity measurement of radio absorbing material [25]: to measure the S -parameter in the

frequency domain, transfer it to the time domain, then apply the time domain truncation to select the wanted signals, and finally, transfer the selected signals back to the frequency domain.

6.3 Measurement Results

We first rotate antenna 1 but keep the stirrer positions fixed, so there is no variable n in (6.1). The top view of the measurement setup inside the chamber is shown in Fig. 6.2(a), and typical filtered S -parameters S_{21} and S_{11} are shown in Fig. 6.2(b). Then antenna 1 is rotated with 2 degrees/step, and the IFFT is applied to all filtered S -parameters. We denote the bistatic and monostatic time domain responses as $E_{21}(t, \theta)^2 = \{IFFT[\tilde{S}_{21}(\theta, f)]\}^2$ and $E_{11}(t, \theta)^2 = \{IFFT[\tilde{S}_{11}(\theta, f)]\}^2$ respectively.

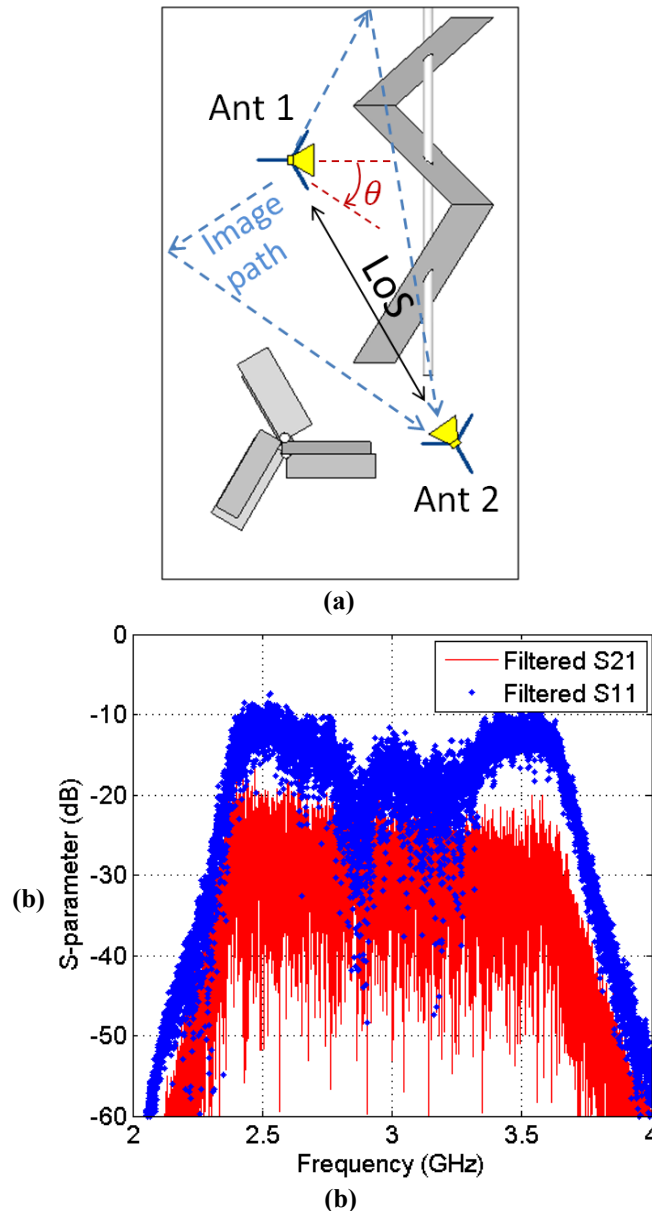


Fig. 6.2. (a) Top view of B-scan measurement setup inside an RC, (b) typical filtered S -parameters.

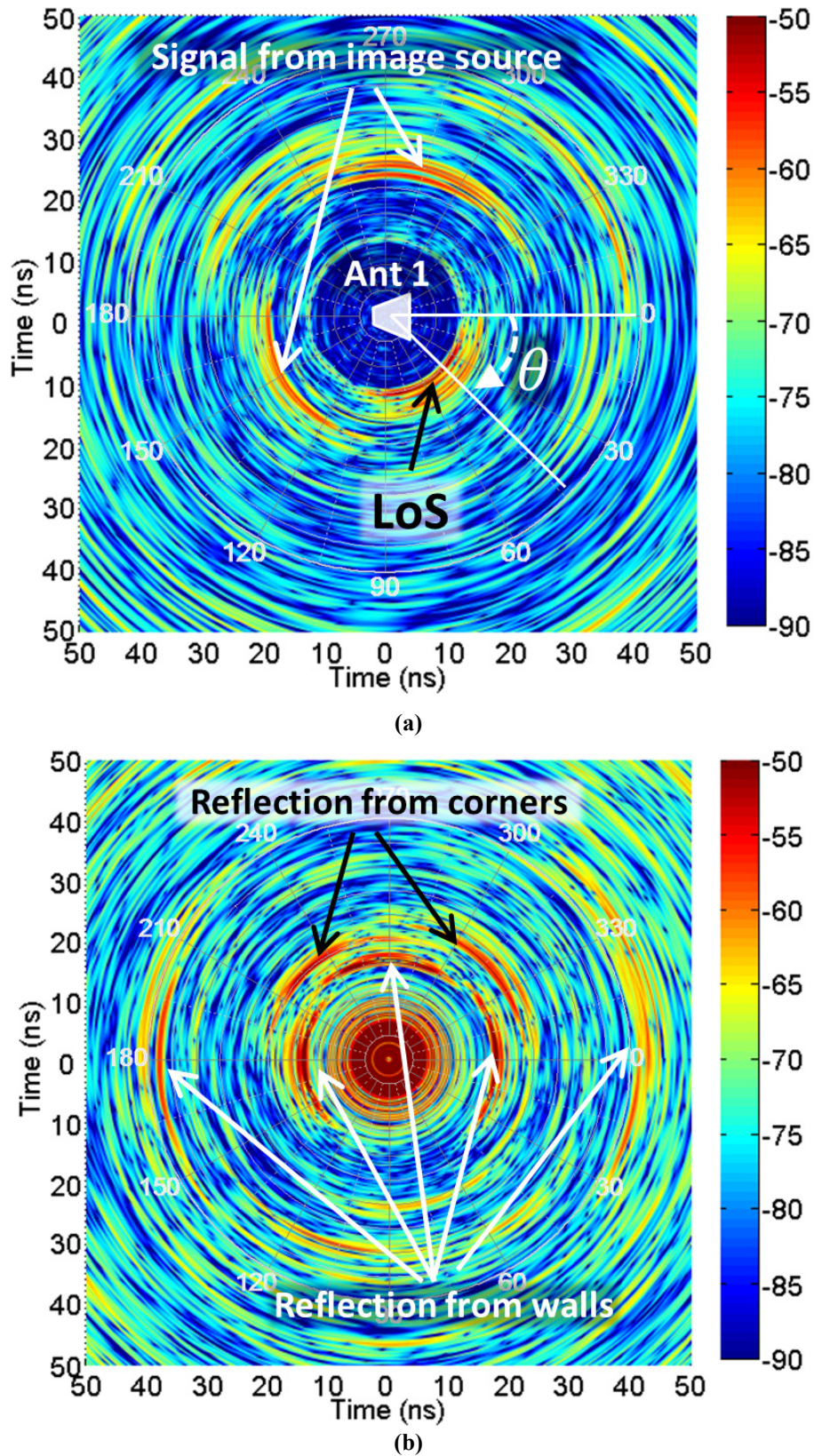


Fig. 6.3. B-scan in the range of 0 ~ 50 ns with stirrers fixed, (a) bistatic map, $E_{21}(t, \theta)^2$ in dB, all the figures in this chapter share the same θ definition given in Fig. 6.2(a), (b) monostatic map, $E_{11}(t, \theta)^2$ in dB.

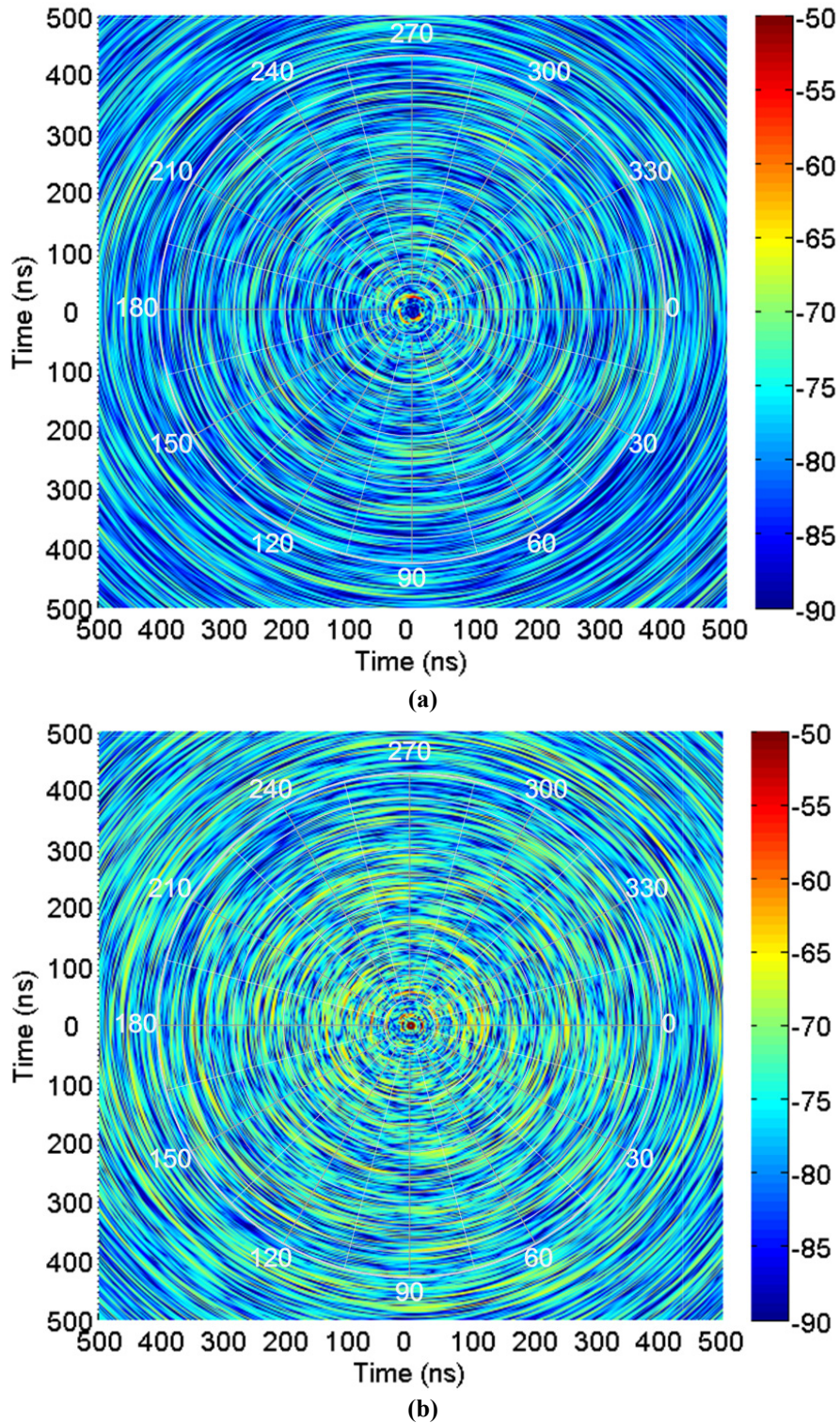


Fig. 6.4. B-scan in the range of 0 ~ 500 ns with stirrers fixed, (a) bistatic map, $E_{21}(t, \theta)^2$ in dB, (b) monostatic map, $E_{11}(t, \theta)^2$ in dB.

The bistatic and monostatic B-scan power maps in the range of 0 to 50 ns are shown in Fig. 6.3. In Fig. 6.3(a), the line-of-sight (LoS) component which can be seen clearly arrived first ($\theta \approx 45^\circ$, the

distance is 3 m between antenna 1 and antenna 2, the travelling time is 10 ns), followed by signals from the image sources ($\theta \approx 135^\circ$, $\theta \approx 280^\circ$) which are also significant; In Fig. 6.3(b), reflections from walls and corners are easily identified (for monostatic map, the time need to be divided by 2 when calculating the distance). Note the reflected wave from $\theta = 90^\circ$ is diffused because of the vertical stirrer. The concentric circles in the centre are the reflection from the antenna itself which is independent of rotation angle. The bistatic and monostatic B-scan power maps in the range of 0 to 500 ns are given in Fig. 6.4. As expected, the field is diffused as it travels in the RC.

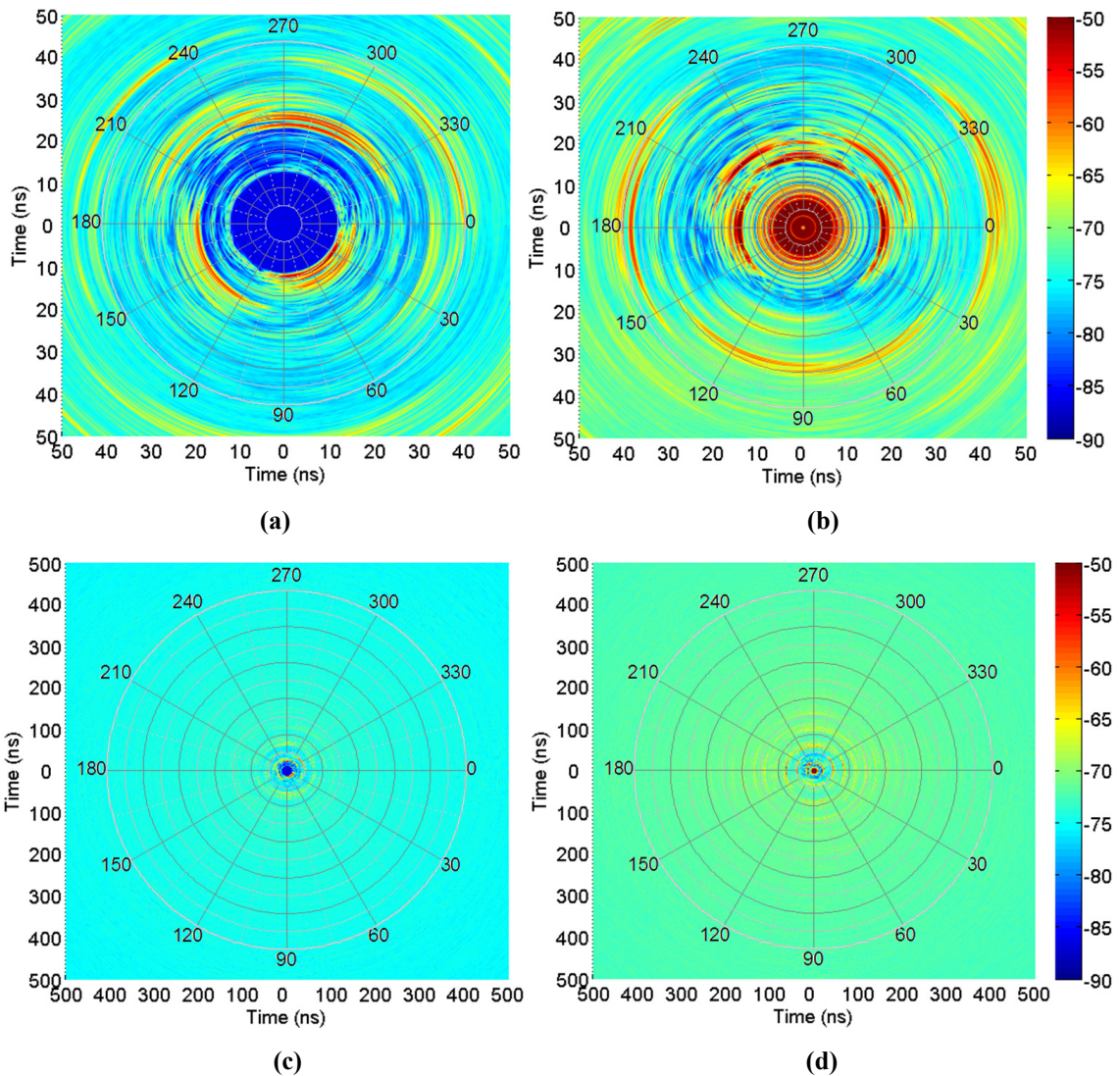


Fig. 6.5. PDP plot, (a) $\langle E_{21}(t, \theta)^2 \rangle$ in the range of 0 to 50 ns, (b) $\langle E_{11}(t, \theta)^2 \rangle$ in the range of 0 to 50 ns, (c) $\langle E_{21}(t, \theta)^2 \rangle$ in the range of 0 to 500 ns, (d) $\langle E_{11}(t, \theta)^2 \rangle$ in the range of 0 to 500 ns.

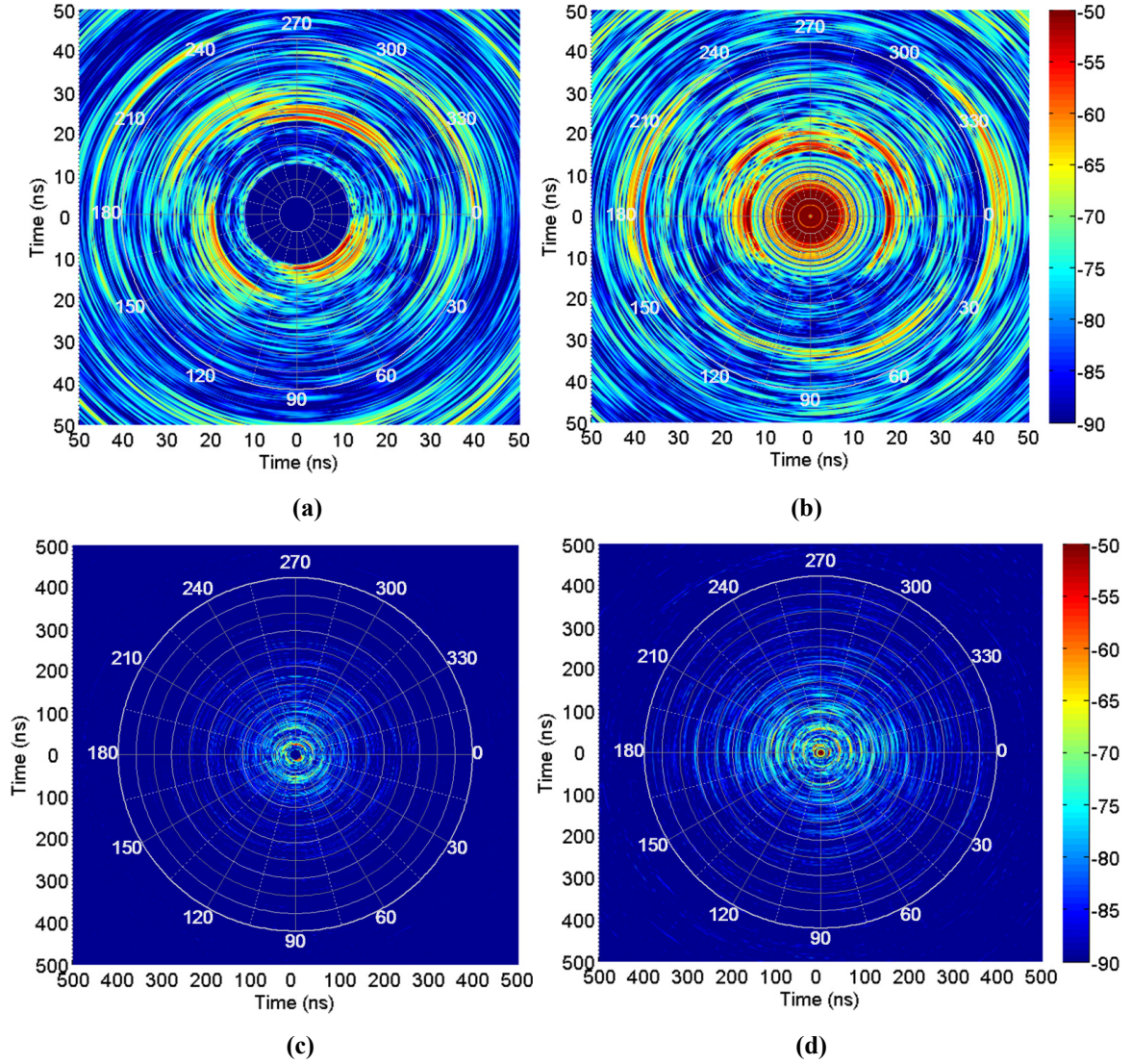


Fig. 6.6. Unstirred time-domain response, (a) $\langle E_{21}(t, \theta) \rangle^2$ in the range of 0 to 50 ns, (b) $\langle E_{11}(t, \theta) \rangle^2$ in the range of 0 to 50 ns, (c) $\langle E_{21}(t, \theta) \rangle^2$ in the range of 0 to 500 ns, (d) $\langle E_{11}(t, \theta) \rangle^2$ in the range of 0 to 500 ns.

To investigate the angle dependency of the stirrer efficiency, 100 stirrer positions are used for each angle of antenna 1. $\langle E_{21}(t, \theta) \rangle^2$ and $\langle E_{11}(t, \theta) \rangle^2$ are shown in Fig. 6.5, while the unstirred part $\langle E_{21}(t, \theta) \rangle^2$ and $\langle E_{11}(t, \theta) \rangle^2$ are shown in Fig. 6.6. $\langle E_{21}(t, \theta) \rangle^2$ is actually the power delay profile (PDP), as expected, (6.10) decays faster than (6.9), and the early time response from the walls cannot be cancelled, since the waves have not interacted with the stirrers yet. $\langle E_{21}(t) \rangle^2$ and $\langle E_{21}(t, \theta) \rangle^2$ for a fixed angle are shown in Fig. 6.7. It can be seen from Fig. 6.7 that, because the value of $(\tau_{RC}^{-1} + \tau_s^{-1})$ in (6.10) is not infinite, η_s is not 100%, $IFFT(\langle \tilde{S} \rangle) \neq IFFT(\tilde{S}_{FreeSpace})$. This explains the difference between the S -parameter measurement in the anechoic chamber and reverberation chamber [20]. The difference between $\langle \tilde{S} \rangle$ and $\tilde{S}_{FreeSpace}$ is due to the unstirred part which can be observed in the time domain, it does not only include the free-space response but also includes the contribution of \overline{TSCS}

(decay exponentially). In practice, if η_s is high, the difference between $\langle \tilde{S} \rangle$ and $\tilde{S}_{FreeSpace}$ is small, $\tilde{S}_{FreeSpace}$ can still be measured in the RC.

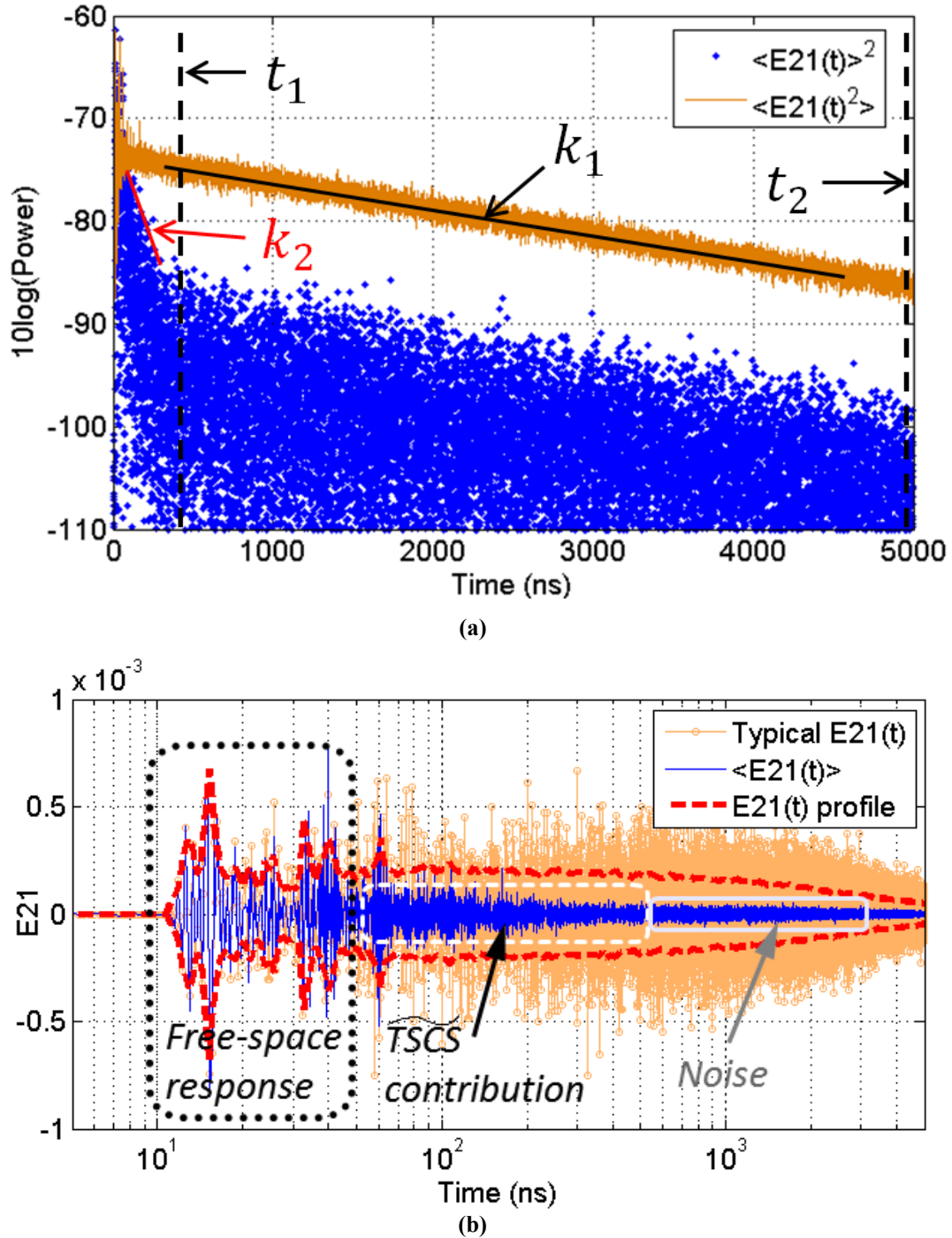


Fig. 6.7. (a) Typical $\langle E_{21}(t)^2 \rangle$ and $\langle E_{21}(t) \rangle^2$ at a specific θ angle in dB scale, (b) typical $E_{21}(t)$, $\langle E_{21}(t) \rangle$ and E_{21} profile (square root of the PDP) plot in linear scale, dominated response in different time range are also marked.

The least-square fit is applied to extract τ_s in (6.10). As shown in Fig. 6.7, the slope of $\langle E_{21}(t)^2 \rangle$ and $\langle E_{21}(t) \rangle^2$ are k_1 and k_2 , respectively. From (6.9) and (6.10), we have

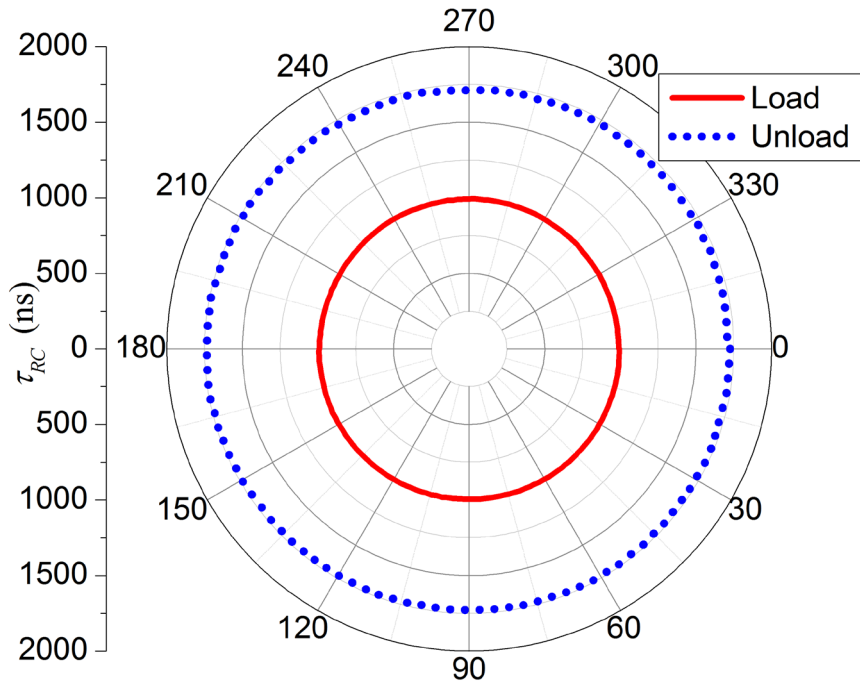
$$\tau_{RC}^{-1} = -k_1 \ln 10 / 10 \quad (6.18)$$

$$\tau_{RC}^{-1} + \tau_s^{-1} = -k_2 \ln 10 / 10 \quad (6.19)$$

τ_s can be obtained as

$$\tau_s = \frac{10}{(k_1 - k_2) \ln 10} \quad (6.20)$$

or directly from the least-square fit using the ratio between $\langle E_{21}(t) \rangle^2$ and $\langle E_{21}(t)^2 \rangle$ in (6.12). In Fig. 6.7(b), $E_{21}(t)$ and $\langle E_{21}(t) \rangle$ are also shown with time in log scale and magnitude in linear scale. As can be seen, at the beginning, the time domain response is dominated by the free-space response (first arrived waves), because of the contribution of \widetilde{TSCS} , $\langle E_{21}(t) \rangle$ decays faster than $E_{21}(t)$ in a few hundred nanoseconds, the decay speed is determined by τ_s in (20). For an ideal RC we have $IFFT(\langle \tilde{S} \rangle) = IFFT(\tilde{S}_{FreeSpace})$ which means $\langle E_{21}(t) \rangle$ decays so fast that $\tau_s \rightarrow 0$.



(a)

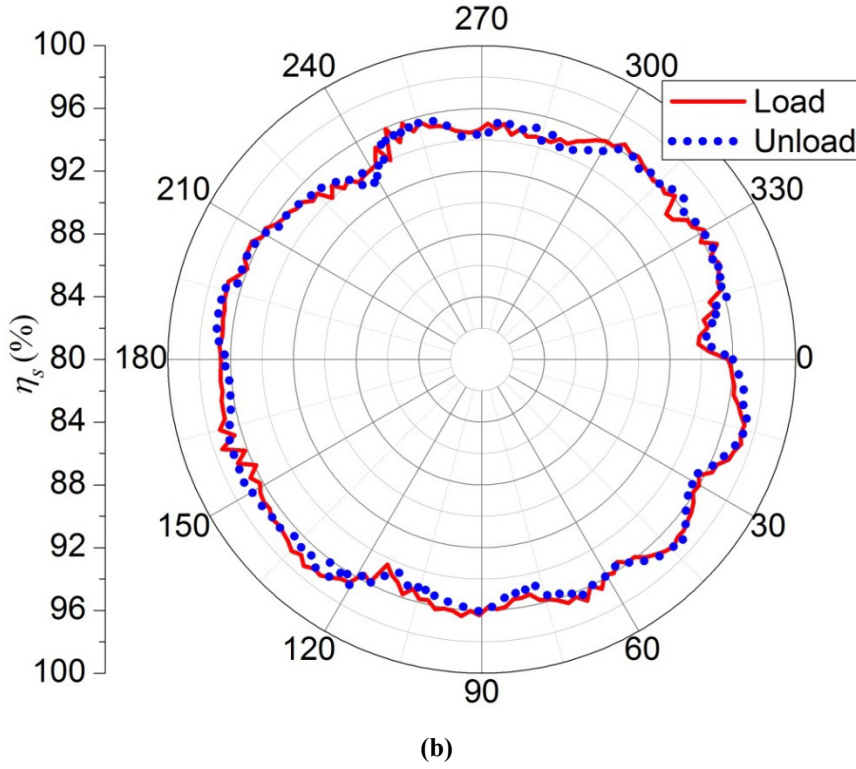


Fig. 6.8. Loaded and unloaded τ_{RC} (a) and η_s (b) with different rotation angles.

In order to investigate the load effect on the stirrer efficiency, we have repeated the whole measurement with the RC loaded with radio absorbing materials. Loaded and unloaded τ_{RC} , η_s with different rotation angles are shown in Fig. 6.8. Obviously, τ_{RC} is not sensitive to antenna positions, we have $\tau_{RCload} = 993 \text{ ns}$, $\tau_{RCunload} = 1726 \text{ ns}$. Although τ_{RC} are different, we still have the same η_s , and η_s remaining insensitive to the rotation angles ($95.8 \pm 2 \%$) as expected. As discussed previously, η_s depends only on the equivalent TSCS of stirrers.

Next we investigate the corrected chamber transfer function in the frequency domain (6.16) and time domain (6.17). Suppose the time gate is from t_1 to t_2 , for the loaded and unloaded RC, the power range must be the same, which means that we have the same initial and dissipated powers for the loaded and unloaded RC during the time gate (energy conservation). Otherwise, T_{CTD} in different scenarios cannot be compared. If the chamber buildup time is ignored [19], we have $P_0 e^{-t_{1unload} \tau_{RCunload}^{-1}} = P_0 e^{-t_{1load} \tau_{RCload}^{-1}}$, thus

$$t_{1unload} \tau_{RCunload}^{-1} = t_{1load} \tau_{RCload}^{-1} \quad (6.21)$$

$$t_{2unload} \tau_{RCunload}^{-1} = t_{2load} \tau_{RCload}^{-1} \quad (6.22)$$

As can be seen in Fig. 6.7, after 500 ns, the unstirred part is quite small, we use $t_{1unload} = 500$ ns, $t_{2unload} = 5000$ ns for the unloaded RC and $t_{1load} = 288$ ns, $t_{2load} = 2876$ ns for the loaded RC respectively.

The results are shown in Fig. 6.9, a frequency stir with nearest 100 frequency points is used. The uncorrected chamber transfer function $\langle |S_{21}|^2 \rangle$ is given first in Fig. 6.9(a), because of the unstirred part, it shows angle dependency. The angle dependency of K -factor in dB is also shown in Fig. 6.9(b). At each rotation angle, the K -factor is calculated using the unbiased estimator [10]

$$K = \frac{N-2}{N-1} \left\langle \frac{|S_{21}|^2}{|S_{21} - \langle S_{21} \rangle|^2} \right\rangle - \frac{1}{N} \quad (6.23)$$

where $N = 100$ with a frequency stir with 100 nearest frequencies.

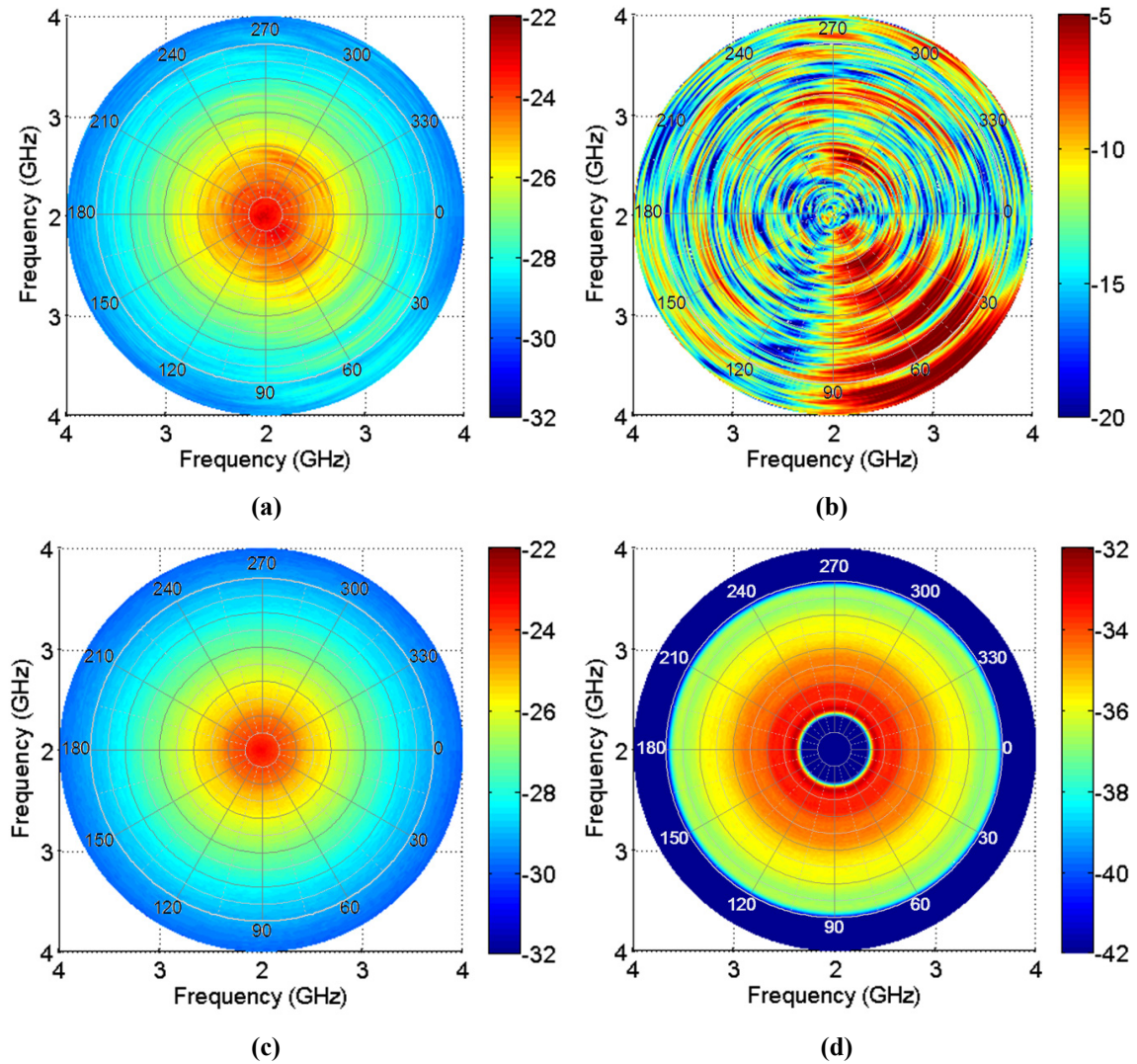


Fig. 6.9. (a) Uncorrected chamber transfer function $\langle |S_{21}|^2 \rangle$, (b) K -factor, (c) T_{CFD} , (d) T_{CTD} , the RC is unloaded.

The corrected chamber transfer function using (6.16) and (6.17) are given in Fig. 6.9(c)(d). As expected, no angle dependency is observed which means both methods can remove the unstirred component. A comparison between T_{CFD} and T_{CTD} is given in Fig. 6.10, because part of the time domain signal is filtered by using time gating, this results in $T_{CTD} < T_{CFD}$. It is not an issue, because normally we are interested in the relative T rather than the absolute T , and it can be seen in Fig. 6.10(b) that there is a very good agreement between $T_{CFDload} - T_{CFDunloaded}$ and $T_{CTDload} - T_{CTDunloaded}$. The small deviation (< 0.2 dB) could be due to the ignorance of the different chamber buildup time in (6.21) and (6.22), which leads to slightly different total energy for the loaded and unloaded RC in the time gate.

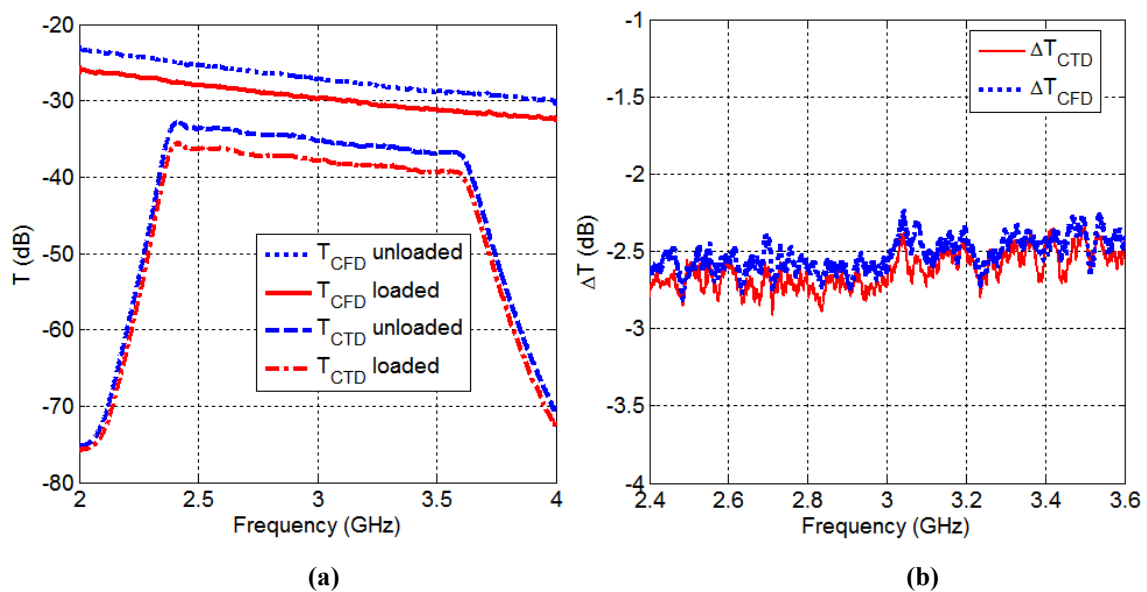


Fig. 6.10. (a) Corrected chamber transfer functions, (b) difference between loaded and unloaded T .

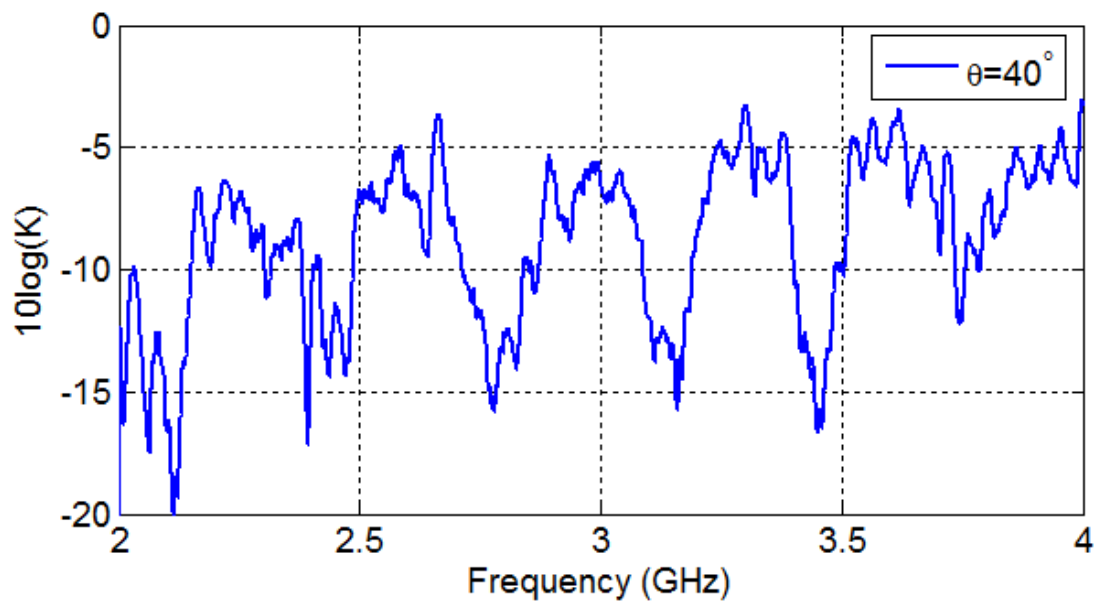


Fig. 6.11. K -factor in dB at $\theta = 40^\circ$, the RC is unloaded.

It is interesting to note that, even two antennas are positioned in LoS, the K -factor (smoothed with frequency stir) can still be very small at some specific frequencies (Fig. 6.11). Remember the unstirred part is not only from the LoS, it can be also from the walls (specular reflection [2]) and other structures (also the contribution of \overline{TSCS}), when the waves from these sources cancel each other at some frequencies, a small K -factor is observed.

6.4 Discussion and Conclusions

In this chapter, a very fine B-scan measurement has been performed in an RC. Measurement scenarios are summarised in Table 6.1. Based on the B-scan results, this chapter is focused on three aspects: the statistical behaviour of the E-field in the time domain, the stirrer efficiency quantification, and the time gating technique.

Table 6.1: Measurement Scenarios

Scenario	Stirrer Position No.	Platform Position No.	Load/Unload	Measurement Time
1	1	180	Unload	4 hours
2	100	180	Unload	402 hours
3	100	180	Load	402 hours

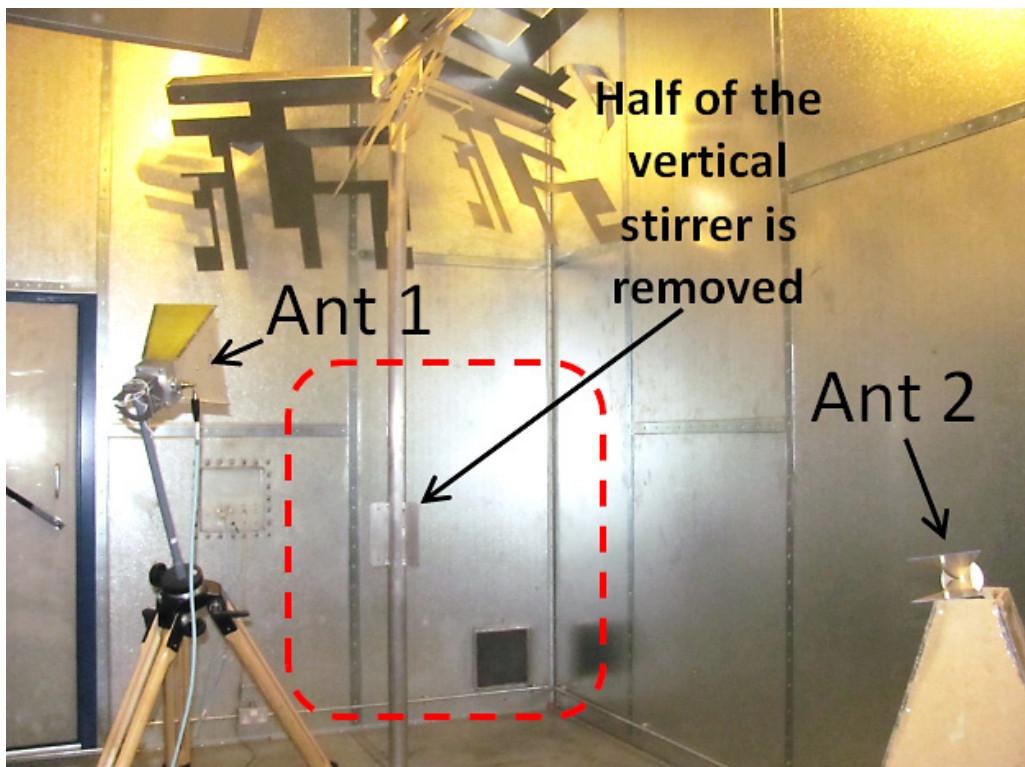
It has been shown in this chapter that the late-time E-field can be regarded as a non-stationary stochastic process with Gaussian distribution; the standard deviation is time dependent and related to the chamber decay time (6.8).

For the stirrer efficiency, we have measured it in a bandwidth of 1.2 GHz (2.4 GHz ~ 3.6 GHz) with different angle of antenna 1 (Fig. 6.8(b)). Since τ_{RC} and τ_s are frequency dependent, η_s is also frequency dependent. If we use a smaller bandwidth (200 MHz) and sweep the centre frequency, a frequency dependency of stirrer efficiency can be observed (like the extraction of τ_{RC} in [3]). Further measurement scenarios are given in Table 6.2, we rotate only the horizontal stirrer, only the vertical stirrer and both stirrers. Because of the limitation of the maximum sample number of the VNA, the frequency range of 0.2 GHz ~ 4.1 GHz is divided into three bands with 10001 sample points in each band, thus we have total 30003 sample points. Finally, we remove half of the vertical stirrer (Fig. 6.12) and repeat the measurement with 10 random antenna positions, one of them is LoS to check if there is any relation between the K -factor and η_s .

Table 6.2: Further Measurement Scenarios

Scenario	Stirrer Position No.	Load/Unload	Antenna Position No.	Frequency Range
Only H	360	Load	1	0.2 GHz ~ 4.1 GHz (30003 points)
Only V	360	Load	1	0.2 GHz ~ 4.1 GHz (30003 points)
H & V	360	Load	1	0.2 GHz ~ 4.1 GHz (30003 points)
Small V*	360	Load	10	1.9 GHz ~ 4.1 GHz (10001 points)

* Small V means half of the vertical stirrer is removed shown in Fig. 6.12.

**Fig. 6.12. Measurement with half of the vertical stirrer.**

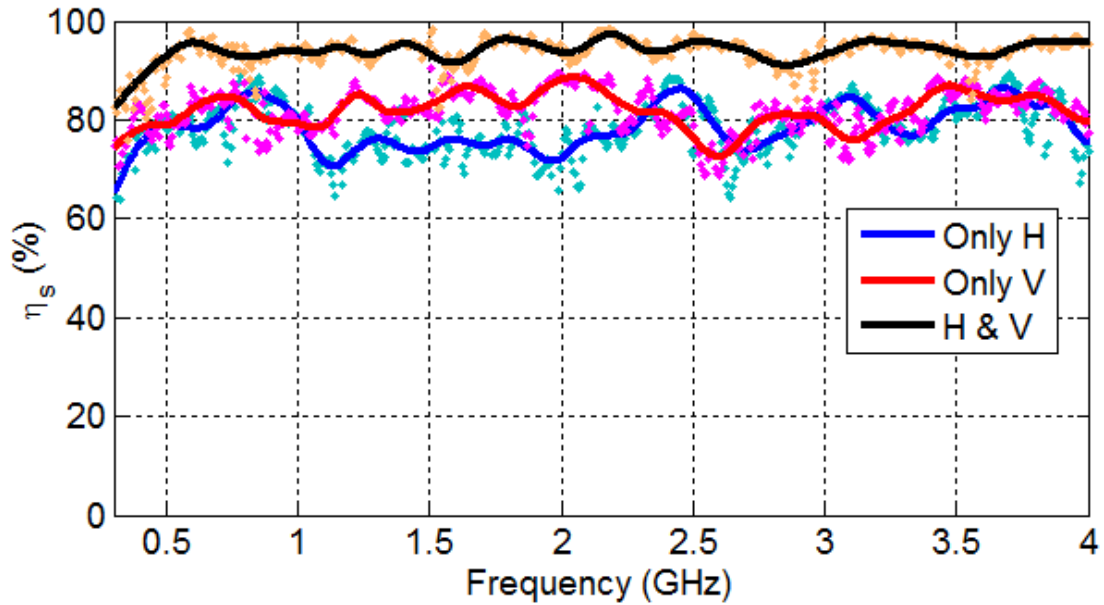


Fig. 6.13. Stirrer efficiency with different stirrer rotation, light dot is the measured result; solid line is the smoothed result.

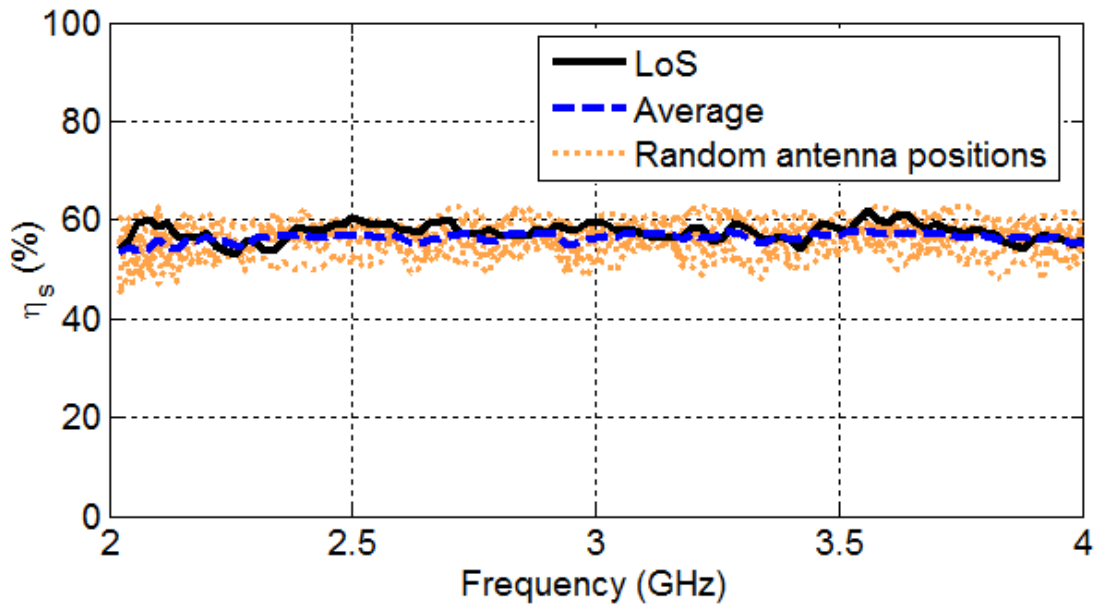


Fig. 6.14. Stirrer efficiency with half of the vertical stirrer (10 random antenna positions are used with 1 LoS).

The results are given in Fig. 6.13 and Fig. 6.14, and K -factors with random antenna positions are given in Fig. 6.15. As expected, when both stirrers are used, we have the highest stirrer efficiency and a smaller stirrer gives small stirrer efficiency. Although the K -factor has a large variation (~ 15 dB), they do not affect the stirrer efficiency. The LoS component only affects the initial response in a few

nanoseconds, but the decay speed in a few hundred nanoseconds (Fig. 6.16) is determined by the equivalent TSCS of the stirrers and not sensitive to the antenna position.

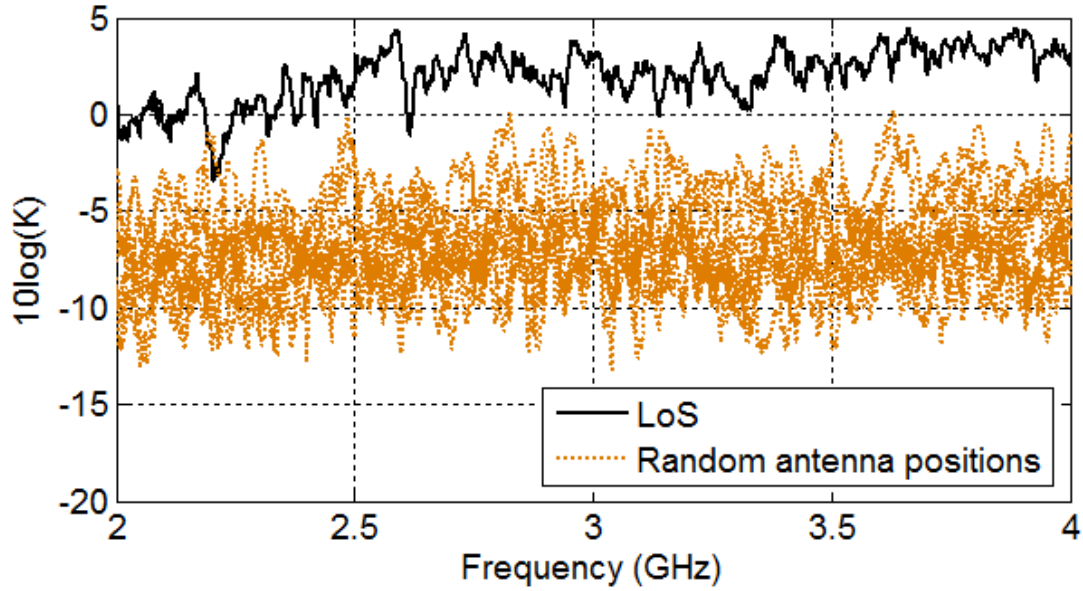


Fig. 6.15. K -factor in dB with half of the vertical stirrer (10 random antenna positions are used with 1 LoS).

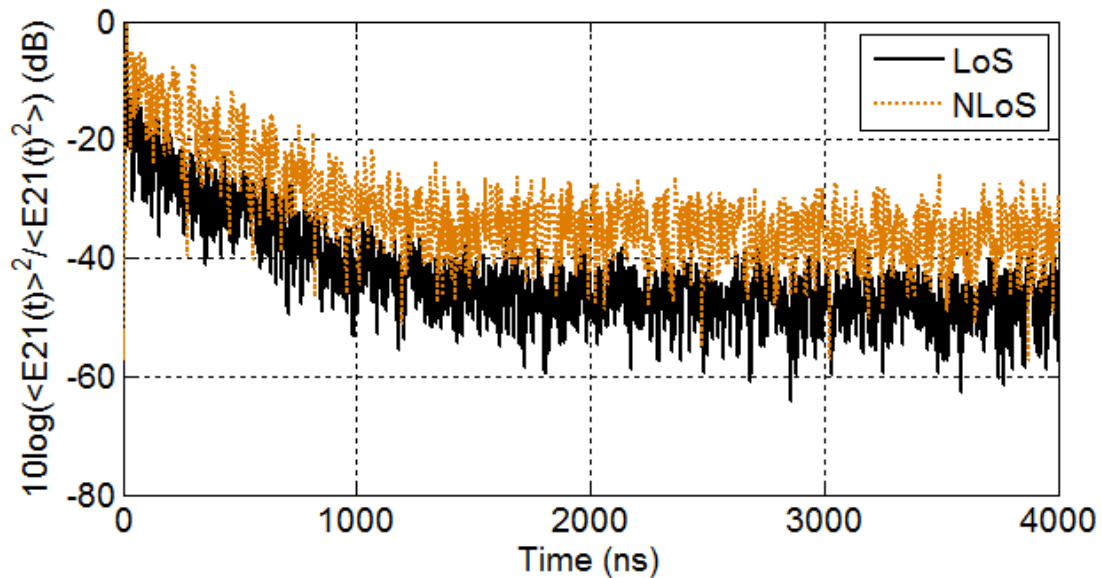


Fig. 6.16. $\langle E(t) \rangle^2 / \langle E(t)^2 \rangle$ in dB with half of the vertical stirrer, a comparison between LoS and non-line-of-sight (NLoS).

If we check the mean value of η_s , it can be found that the mean value of η_s of the half vertical stirrer is around 55%, this corresponds to the \overline{TSCS} of $0.0665V^{2/3}$ in (6.15). Because the TSCS can be superimposed under the dilute approximation [21, 26], if a whole vertical stirrer is used, the \overline{TSCS} is roughly $2 \times 0.0665V^{2/3}$, this corresponds to the stirrer efficiency of 80% which agrees well in Fig.

6.13. We also have comparable stirrer efficiency between horizontal and vertical stirrer in Fig. 6.13. The \overline{TSCS} of the two stirrers is around $2 \times 2 \times 0.0665V^{2/3}$, this corresponds to the stirrer efficiency of 96% which agrees well with the H & V in Fig. 6.13. Thus from (6.15) we have

$$\eta_{stot} = 1 - \prod_{i=1}^N (1 - \eta_{si}) \quad (6.24)$$

where η_{si} is the stirrer efficiency with only i -th stirrer, η_{stot} is the stirrer efficiency when all N stirrers are moving together.

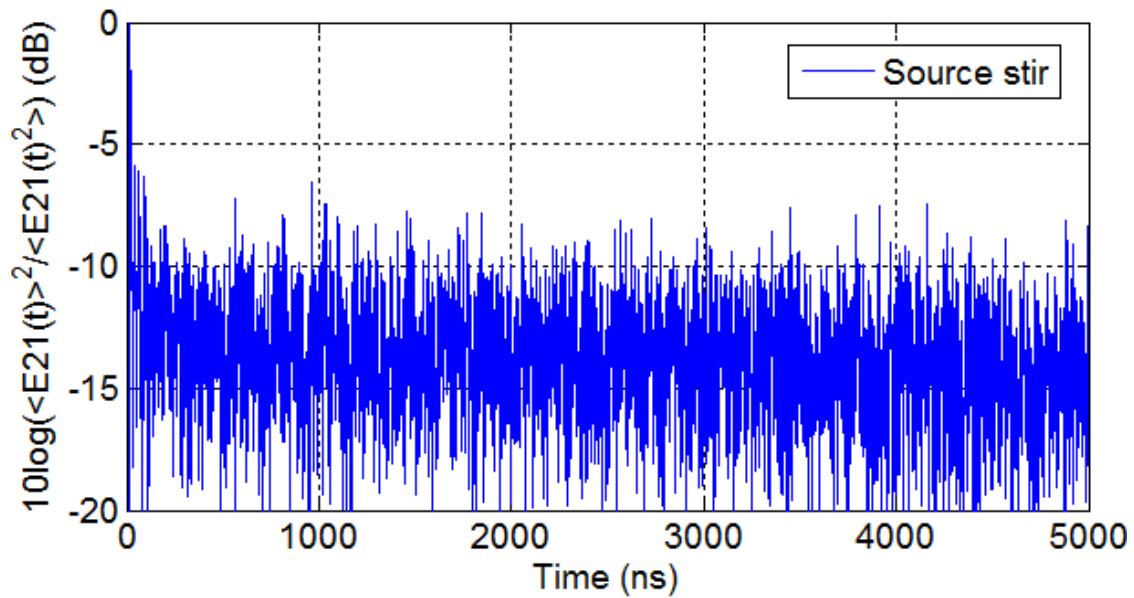


Fig. 6.17. $\langle E(t) \rangle^2 / \langle E(t)^2 \rangle$ in dB using the source stir method.

An important question is: how to increase the stirrer efficiency? From (6.24), we can conclude that a big stirrer or many stirrers working together is obviously better, but the trade-off is a reduction of the test volume. The source stir is a proven method to improve the performance of the RC [27, 28]. Actually, if we consider the moving antenna as the stationary coordinate frame, rotating the antenna is actually rotating the whole RC, which obviously has a large \overline{TSCS} . We have also tried to aim the antenna to the stirrer (in 10 random antenna positions in Fig. 6.12), because there are always leaky waves (from side lobes, back lobes, scattering from rotation axis and stationary object) which do not fully interact with the moving stirrer, thus waves from the antenna have not fully interacted with the stirrer except for the extreme case (source stir). Note the TSCS contribution dominates the time domain response in a few hundred seconds, in this time scale the leaky wave dominates the unstirred part. Otherwise the stirrer and the antenna can be considered as an integrated big antenna and the moving of the stirrer becomes the moving of the source (source stir). To verify this, we use the data from scenario 1 in Table 6.1 to calculate the stirrer efficiency (keep the stirrers steady and rotate the

antenna), a nearly 100% stirrer efficiency is obtained in the frequency range of 2.4 GHz ~ 3.6 GHz. The ratio between $\langle E(t) \rangle^2$ and $\langle E(t) \rangle^2$ is shown in Fig. 6.17, it drops down to the noise level in 100 ns.

To summarise, the stirrer efficiency in this chapter is highly related to the equivalent TSCS of stirrers (the moving object in the RC), which is not sensitive to the antenna position and the load of the RC, thus it provides a general way to compare the performance of different RCs or one chamber with different stirrers. The proposed definition is intuitive and can be understood from another point of view: a small stirrer means the wave needed to travel a relatively long time and interact with stirrers more times to be random enough (a slow $\langle E(t) \rangle^2$ decay), while a big stirrer means the wave can become random quickly (a fast $\langle E(t) \rangle^2$ decay). Because the \widetilde{TSCS} can be superimposed, which means the stirrer efficiency is predictable, this is important for the RC design, the designer can evaluate how large a stirrer is enough (or how many stirrers are needed) based on the existing design using (6.24).

A time-gating technique in the RC has been proposed, which provides an alternative method to correct the unstirred part in the time domain. It should be noted that when using this time-gating technique to compare the transfer functions in the unloaded and loaded RCs, the start time and the end time of the time gate are different. The time-gating technique can be used to improve the stirrer efficiency: by filtering the early time response, a uniform chamber transfer function can be obtained. For antenna measurement the time domain response can be easily truncated, for other measurements if the time domain response cannot be easily separated (radiated susceptibility or radiated emission measurement), physically high stirrer efficiency is still required.

It would be necessary to clarify the difference between the stirrer efficiency and the field uniformity (FU). The FU is determined by the measured average E-field in the frequency domain [15] which includes both the unstirred part and stirred part. Stirrer efficiency describes how fast the unstirred part decays compared with the total response or how fast the total signal is dominated by the stirred part. It also describes the difference between $\langle \tilde{S} \rangle$ and $\tilde{S}_{FreeSpace}$, as discussed before, $\langle \tilde{S} \rangle$ does not only include free-space response (in a few nanoseconds), but also include the contribution of \widetilde{TSCS} of moving objects (in a few hundred nanoseconds), we need $\langle E(t) \rangle^2$ to decay very fast make sure the unstirred part is dominated by the free space response (a few nanoseconds), that is when $\eta_s \rightarrow 100\%$, $\langle \tilde{S} \rangle \rightarrow \tilde{S}_{FreeSpace}$.

To have a good RC, we need the stirred part to be as uniform as possible and the unstirred part as small as possible. The use of diffusers [29, 30] on the specular reflection wall actually diffuse the unstirred part to improve the field uniformity, but the stationary diffusers cannot change the \widetilde{TSCS} of the stirrers thus cannot change the stirrer efficiency (the decay speed of $\langle E(t) \rangle^2$). However, if only the

field uniformity is used as the standard it is already a good RC, unless for some special applications (e.g. measure the free space S -parameters in an RC) we need $IFFT(\langle \tilde{S} \rangle) = IFFT(\tilde{S}_{FreeSpace})$ ($\langle \tilde{S} \rangle = \tilde{S}_{FreeSpace}$).

High stirrer efficiency does not necessarily mean a good FU (when a high directivity antenna direct to the test region) and a good FU does not necessarily mean high stirrer efficiency (both stirred part and unstirred part are uniform but the unstirred part decays slowly in time domain). Normally, if the stirrer efficiency is high and the K -factor is small, the field in the test region is dominated by the stirred part, if the stirred part is uniform, a good FU is obtained (except some special cases the stirred part can also be non-uniform [31]).

6.5 Key Contributions

In this chapter, B-scan has been applied to a reverberation chamber (RC) for the first time to characterise the time domain behaviour of the chamber. Based on the understanding of B-scan measurement results, three aspects have been mainly discussed:

- 1) The statistical behaviour of the fields in the time domain is investigated, it has been found that the received power of the impulse response follows chi-square distribution with one degree of freedom;
- 2) The stirrer efficiency is first quantified based on the equivalent total scattering cross section (TSCS) of stirrers; this definition is not sensitive to the antenna position and load in an RC. The quantified stirrer efficiency provides a universal way to evaluate the stirrer design and the chamber performance;
- 3) Time-gating technique in an RC is proposed which provides an alternative method to eliminate the early time response and correct the chamber transfer function of the RC, this could be potentially used to increase the stirrer efficiency without changing the stirrers.

6.6 References

- [1] R. J. Pirkl and K. A. Remley, "Experimental evaluation of the statistical isotropy of a reverberation chamber's plane-wave spectrum," *IEEE Trans. EMC*, vol. 46, no. 3, pp. 498-509, Jun. 2014.

-
- [2] R. J. Pirkl, J. M. Ladbury and K. A. Remley, "The reverberation chamber's unstirred field: A validation of the image theory interpretation," IEEE International Symposium on EMC, pp. 670-675, Long Beach, USA, Aug. 2011.
- [3] C. L. Holloway, H. A. Shah, R. J. Pirkl, W. F. Young, D. A. Hill and J. Ladbury, "Reverberation chamber techniques for determining the radiation and total efficiency of antennas," *IEEE Trans. Antennas Propagat.*, vol. 60, no. 4, pp. 1758-1770, Apr. 2012.
- [4] U. Calberg, P. -S., Kildal, A. Wolfgang, O. Sotoudeh and C. Orlenius, "Calculated and measured absorption cross sections of lossy objects in reverberation chamber," *IEEE Trans. EMC*, vol. 46, no. 2, pp. 146-154, May 2004.
- [5] E. Genender, C. L. Holloway, K. A. Remley, J. M. Ladbury, G. Koepke and H. Garbe, "Simulating the multipath channel with a reverberation chamber: application to bit error rate measurements," *IEEE Trans. EMC*, vol. 52, no. 4, pp. 766-777, Nov. 2010.
- [6] D. J. Daniels, *Ground Penetration Radar*, 2nd Ed, The IEE Press, 2004.
- [7] D. A. Hill, *Electromagnetic Fields in Cavities: Deterministic and Statistical Theories*, Wiley-IEEE Press, 2009.
- [8] D. A. Hill, "Uniqueness of plane wave integral representation for idealized fields in reverberation chambers," *IEEE Trans. EMC*, vol. 57, no. 3, pp. 584-586, June 2015.
- [9] O. Lunden and M. Backstrom, "Stirrer efficiency in FOA reverberation chambers. Evaluation of correlation coefficients and chi-squared tests," IEEE International Symposium on EMC, pp. 11-16, Washington DC, USA, Aug. 2000.
- [10] C. Lemoine, E. Amador and P. Besnier, "Mode-stirring efficiency of reverberation chambers based on Rician K-factor," *Electronic Letters*, vol. 47, no. 20, Sep. 2011.
- [11] C. Lemoine, P. Besnier and M. Drissi, "Evaluation of frequency and mechanical stirring efficiency in a reverberation chamber," International Symposium on Electromagnetic Compatibility – EMC Europe, pp. 1-6, Hamburg, German, Sep. 2008,
- [12] J. Clegg, A. C. Marvin, J. F. Dawson and S. J. Porter, "Optimization of stirrer designs in a reverberation chamber," *IEEE Trans. EMC*, vol. 47, no. 4, pp. 824-832, Nov. 2005.
- [13] C. L. Holloway, D. A. Hill, J. M. Ladbury and G. Koepke, "Requirements for an effective reverberation chamber: unloaded or loaded," *IEEE Trans. EMC*, vol. 48, no. 1, pp. 187-194, Feb. 2006.
- [14] C. L. Holloway, D. A. Hill, J. M. Ladbury, P. F. Wilson, G. Koepke and J. Coder, "On the use of reverberation chambers to simulate a Rician radio environment for the testing of wireless devices," *IEEE Trans. Antennas Propagat.*, vol. 54, no. 11, pp. 3167-3177, Nov. 2006.
- [15] Electromagnetic compatibility (EMC) – Part 4-21: Testing and measurement techniques – Reverberation chamber test methods, IEC 61000-4-21, Ed 2.0, 2011.

-
- [16] W. T. C. Burger, C. L. Holloway and K. A. Remley, "Proximity and orientation influence on Q-factor with respect to large-form factor loads in a reverberation chamber," Proc. of the 2013 International Symposium on Electromagnetic Compatibility, pp. 369-374, Brugge, Belgium, Sep. 2013.
- [17] E. Amador, C. Lemonie, P. Besnier and A. Laisné, "Reverberation chamber modeling based on image theory: Investigation in the pulse regime," *IEEE Trans. EMC*, vol. 52, no. 4, pp.778-789, Nov. 2010.
- [18] S. M. H. A. Shah, "Wireless channel characterization of the reverberation chamber at NIST," M.S. thesis, Department of Signals and System, Chalmers University of Technology, Gothenburg, Sweden, 2011.
- [19] C. L. Holloway, H. A. Shah, R. J. Pirkl, K. A. Remley, D. A. Hill and J. Ladbury, "Early time behavior in reverberation chambers and its effect on the relationships between coherence bandwidth, chamber decay time, RMS delay spread, and the chamber buildup time," *IEEE Trans. EMC*, vol. 54, no. 4, pp.717-725, Nov. 2012.
- [20] P. -S. Kildal, C. Carlsson and J. Yang, "Measurement of free-space impedances of small antennas in reverberation chambers," *Microwave and Optical Technology Letters*, vol. 32, no. 2, pp. 112-115, Dec. 2001.
- [21] G. Lerosey and J. de Rosny, "Scattering cross section measurement in reverberation chamber," *IEEE Trans. EMC*, vol. 52, no. 2, pp.280-284, May. 2007.
- [22] S. Lallechere, I. E. Baba, P. Bonnet and F. Paladian, "Total scattering cross section improvements from electromagnetic reverberation chambers modelling and stochastic formalism," in Proceeding of the 5th European Conference on Antennas and Propagation (EUCAP), pp. 81-85, Rome, Italy, Apr. 2011.
- [23] I. E. Baba, S. Lallechere, P. Bonnet, J. Benoit and F. Paladian, "Computing total scattering cross section from 3-D reverberation chambers time modelling," Asia-Pacific Symposium on Electromagnetic Compatibility (APEMC), Singapore, May 2012.
- [24] E. Amador, C. Lemoine and P. Besnier, "An empirical statistical detection of non-ideal field distribution in a reverberation chamber confirmed by a simple numerical model based on image theory," *Ann. Telecommun.*, vol. 66, pp. 445-455, Aug. 2011.
- [25] IEEE recommended practice for radio-frequency (RF) absorber evaluation in the range of 30 MHz to 5 GHz, IEEE Standard 1128-1998, Apr. 1998.
- [26] A. Ishimaru, *Wave Propagation and Scattering in Random Media*, vol. 2, New York: Academic, 1978, ch. 14, pp. 253-294.

-
- [27] Y. Huang and D. J. Edwards, "A novel reverberating chamber: source-stirred chamber," Proc. Of IEE 8th International Conference on Electromagnetic Compatibility, pp. 120-124, Edinburgh, UK, Sep. 1992.
- [28] K. Rosengren, P. -S. Kildal, C. Carlsson and J. Carlsson, "Characterization of antennas for mobile and wireless terminals in reverberation chambers: improved accuracy by platform stirring," *Microwave and Optical Technology Letters*, vol. 39, no. 6, pp. 391-397, Sep. 2001.
- [29] J. -C. Yun, J. -G. Rhee and S. -Y. Chung, "An improvement of field uniformity of reverberation chamber by the variance of diffuser volume ratio," Asia-Pacific Microwave Conference (APMC), vol. 3, pp. 1123-1126, Taipei, Dec. 2001.
- [30] A. C. Marvin and E. Karadimou, "The use of wave diffusers to reduce the contribution of specular wall reflections to the unstirred energy in a reverberation chamber," IEEE International Symposium on Electromagnetic Compatibility, pp. 227-231, Denver, USA, Aug. 2013.
- [31] J. A. D. Toorn, K. A. Remley, C. L. Holloway, J. M. Ladbury and C. Wang, "Proximity-effect test for lossy wireless-device measurements in reverberation chambers," *IET Science, Measurement & Technology*, vol. 9, no. 5, pp. 540-546, 2015.

Chapter 7: Conclusions and Future Work

In this thesis, two different chambers are discussed: the anechoic chamber and the reverberation chamber. Key contributions have been listed in each chapter, there are also work could be done in the future.

Contributions in each chapter are identified:

In Chapter 1, introduction and motivations of this thesis are given.

In Chapter 2, the GO theory is presented with two forms; a number of computational electromagnetics (CEM) algorithms are discussed and compared for anechoic chamber simulation. It has been shown that GO combined with FEM could be the best choice.

In Chapter 3, a CAD tool is developed; the development details of the CAD tool for the anechoic chamber design are given, including 3D model description, preprocessing, material definition, boundary definition, post processing, etc. Two algorithms (forward and inverse) are developed with acceleration techniques respectively. Adaptive octree is proposed in the forward algorithm, and convex acceleration technique is proposed in the inverse algorithm. Both these two techniques improve the computation efficiency significantly.

In Chapter 4, the definitions of NSA, SVSWR and FU have been given; measurement results and simulation results are compared. It has been found that, for the NSA values, the difference between the simulated values and measurement values can be smaller than ± 2 dB in the whole frequency range (30 MHz ~ 1 GHz). For the SVSWR values, a good agreement has been obtained when the frequency is between 1 GHz ~ 14 GHz, and the difference is smaller than 2 dB when frequency is lower than 8 GHz. For the FU values, the difference is smaller than 2 dB in the frequency range of 300 MHz ~ 8 GHz. Possible error sources and the limit of the proposed method are also discussed.

In Chapter 5, the applications of the reverberation chamber are reviewed, a series of measurement methods in the RC are developed including antenna radiation efficiency measurement, diversity gain measurement, radiated emission measurement, material characterisation, shielding effectiveness, and volume measurement:

- 1) A modified two-antenna method to measure the radiation efficiency of antennas in an RC has been proposed. The proposed method offers an opportunity to measure the antenna with very low radiation efficiency (e.g. implantable antenna) in the RC without the need for reference antenna.

- 2) By applying the non-reference antenna method to the diversity gain and radiated emission measurement, the measurement process can be simplified without losing accuracy.
- 3) A new method has been proposed to measure the permittivity and conductivity of a spherical object. The frequency dependency of ACS was considered which makes both relative permittivity and conductivity can be obtained. The effect of the container has been discussed and it did not affect the proposed method. The proposed method has self-explanatory results which gives a PDF-like distribution of permittivity and conductivity.
- 4) A new method is proposed to measure the shielding effectiveness (SE) of an electrically large enclosure. In the proposed method, only one antenna is needed in the whole measurement procedure. There is no requirement to use a reference antenna. If the aperture of the enclosure under test (EUT) can be covered, the SE can be measured quickly by comparing the Q factor or the decay time of the covered and uncovered EUT. The results are compared with those obtained using the nested reverberation chamber method. The proposed method does offer a new understanding of SE from both time domain and frequency domain.
- 5) An efficient method to measure the volume of a large conducting cavity. The proposed method is based on Hill's equation. By measuring the Q factor in the time and frequency domains, the volume of the cavity can be extracted. In the time domain, the Q factor can be extracted directly from the time domain response. While in the frequency domain, the Q factor depends on the volume of the cavity and the transferred power, the transferred power can be measured directly. By correcting the frequency domain Q with the radiation efficiency of antennas, the Q factors obtained from both the time domain and frequency domains are equal in a well-stirred chamber; this provides an opportunity to measure the volume of the cavity. Acoustic waves can also be used which will not limit this method to only conducting cavities.

In Chapter 6, B-scan has been applied to a reverberation chamber (RC) for the first time to characterise the time domain behaviour of the chamber, three aspects have been investigated:

- 1) It has been found that the received power of the impulse response follows chi-square distribution with one degree of freedom;
- 2) The stirrer efficiency is first quantified based on the equivalent total scattering cross section (TSCS) of stirrers; this definition is not sensitive to the antenna position and load in an RC. The quantified stirrer efficiency provides a universal way to evaluate the stirrer design and the chamber performance;
- 3) Time-gating technique in an RC is proposed which provides an alternative method to eliminate the early time response and correct the chamber transfer function of the RC.

There are also possible future work:

From Chapter 2 to Chapter 4, we developed a CAD tool for the design of an anechoic chamber. It has also been shown that the tool is efficient and accurate for the anechoic chamber simulation and suitable for real world chamber design. It is important to note that the GO is a high frequency approximation method, in the measurement part we have compared the simulation and measurement results which were in good agreement, and the error was smaller than ± 2 dB. A potential problem is, at higher frequencies, the tip scattering of RAM becomes significant and it is not considered in the model, when the tip scattering becomes the major contribution for the unexpected field (in millimetre wave), it will limit the boundary of the high frequency of this method. This could be in the region of statistical electromagnetics but not deterministic electromagnetics. Another issue is the diffraction or scattering of the rays, if the tip scattering effect is considered, the ray number will be huge and outside the ability of standard computers. For example, if the scattered ray no. is 1000, every time the ray is reflected, 1000 extra rays need to be generated, which will increase the simulation time drastically (1000 times) and make the ray tracing algorithm useless. There has been some research [1] using inverse algorithm to consider only part (but not all) of the diffracted waves. How to deal with the scattered field is still a challenging problem not just in EM community but also in computer graphics community.

In the Chapter 5, we have developed a series of new applications of the RC. We proposed a method which does not need extra antennas, and it was also pointed out that the proposed method decorrelates the signals when the mutual coupling is high. How to estimate this degradation could be the future work. For the permittivity measurement, there are also limitations, when the conductivity is very large, the ACS value will become less dependent on ϵ_r , which will increase the uncertainty for the measured ϵ_r . How to measure the object with high conductivity could be the future work. And also the proposed method is limited to the spherical object, is it possible to extend it to arbitrarily shaped object? For the SE measurement using one antenna, when the EUT is well shielded the uncertainty of increases quickly. How to measure the decay time constant τ with very small uncertainty/high resolution could be challenging. For the volume measurement, if the cavity is partially filled with liquid or dielectric materials either absorb or reflect waves completely (inhomogeneous cavity), the wave velocity is changed which could increase the measurement error. How the inhomogeneous materials affect the Hill's equation could be an interesting problem.

In Chapter 6, we have quantified the stirrer efficiency. Enhanced back scatter coefficient (e_b) can be used to judge if the RC is well-stirred or not [2, 3], is there any relationship between e_b and η_s ? τ_{RC} can be regarded as a random variable [4-6], thus τ_s could also be considered as a random variable.

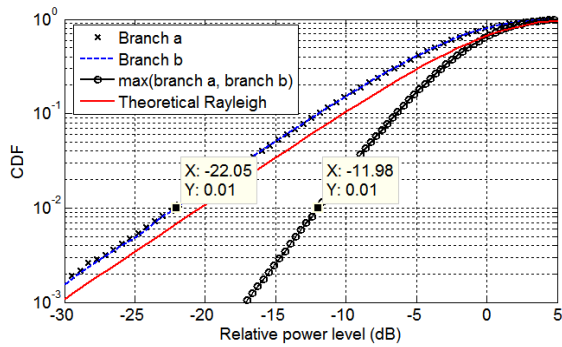
What is the probability distribution function (PDF) of \widetilde{TSCS} , τ_s and η_s , and what factors could affect these PDFs are still unknown.

References

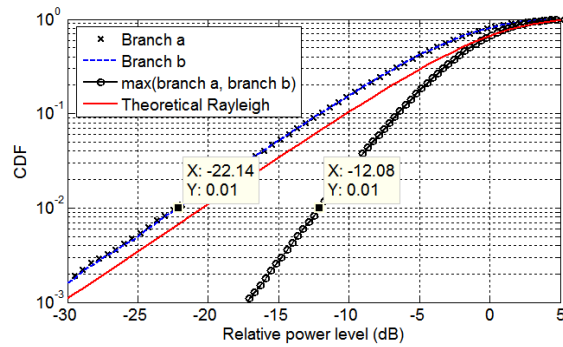
- [1] B. Choudhury, H. Singh, J. P. Bommer and R. M. Jha, "RF field mapping inside a large passenger-aircraft cabin using a refined ray-tracing algorithm," *IEEE Antennas and Propagation Magazine*, vol. 55, no. 1, pp.276-288, Feb, 2013.
- [2] C. R. Dunlap, "Reverberation chamber characterization using enhanced backscatter coefficient measurements," Ph.D. dissertation, Dept. of Electrical, Computer and Engineering, University of Colorado, Boulder, USA, 2013.
- [3] J. M. Ladbury and D. A. Hill, "Enhanced backscatter in a reverberation chamber: Inside every complex problem is a simple solution struggling to get out," in *Proc. IEEE Int. Symp. Electromagn. Compat.*, pp. 1-5, Jul. 9-13, 2007.
- [4] L. R. Arnaut, "Statistics of the quality factor of a rectangular reverberation chamber," *IEEE Trans. Electromagn. Compat.*, vol. 45, no. 1, pp. 61–76, Feb. 2003.
- [5] L. R. Arnaut and G. Gradoni, "Probability distribution of the quality factor of a mode-stirred reverberation chamber," *IEEE Trans. Electromagn. Compat.*, vol. 55, no. 1, pp. 35–44, Feb. 2013.
- [6] A. Gifuni, G. Ferrara, M. Migliaccio and A. Sorrentino, "Estimate of the probability density function of the quality factor of mode tuned, source stirred and mode stirred reverberation chambers," *IEEE Trans. Electromagn. Compat.*, accepted and available online, DOI: 10.1109/TEM.2015.2430525.

Appendix A1

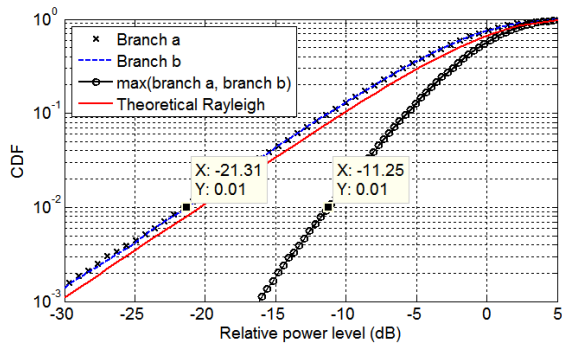
The measured diversity gain using traditional method and the proposed method in Chapter 5.3.2 are given in Fig. A.1, the DG values are listed in Table A.1.



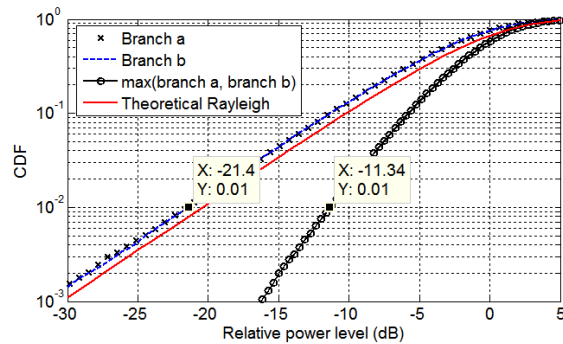
(a)



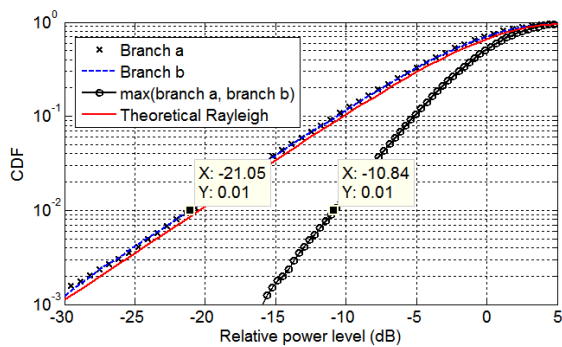
(b)



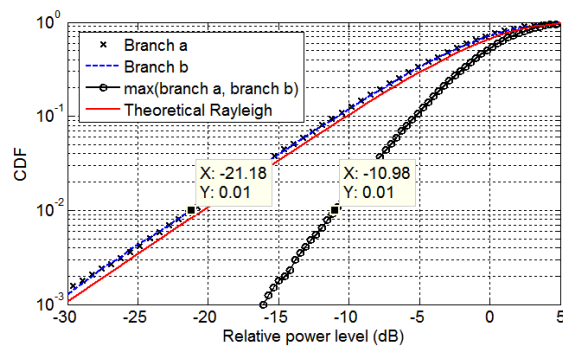
(c)



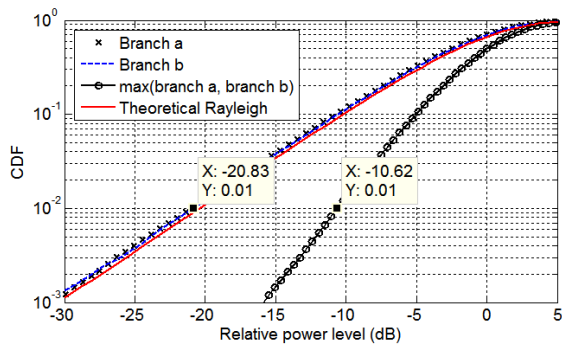
(d)



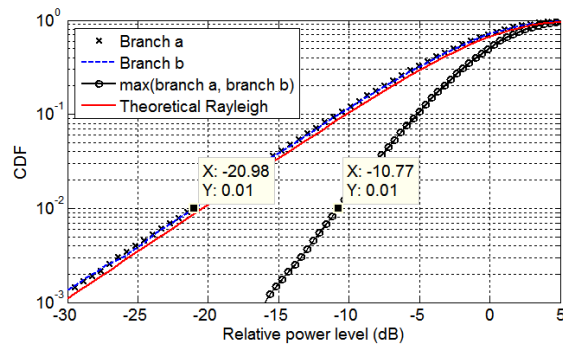
(e)



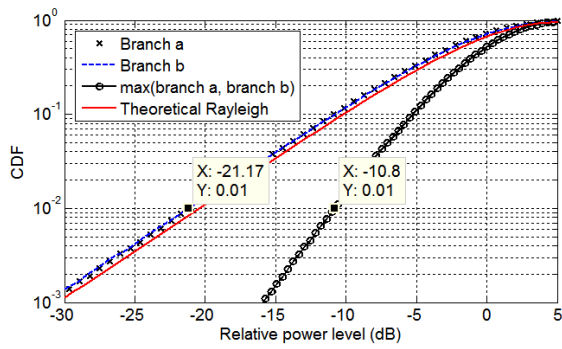
(f)



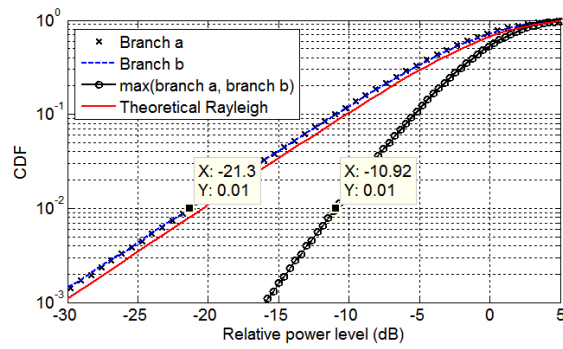
(g)



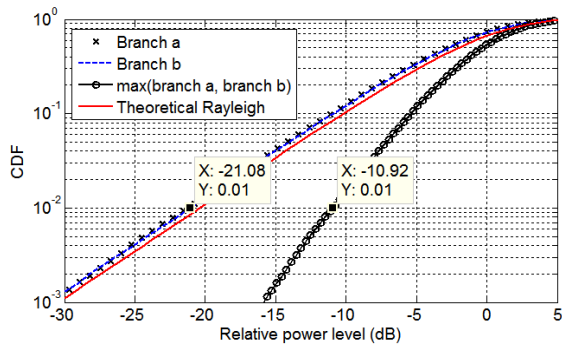
(h)



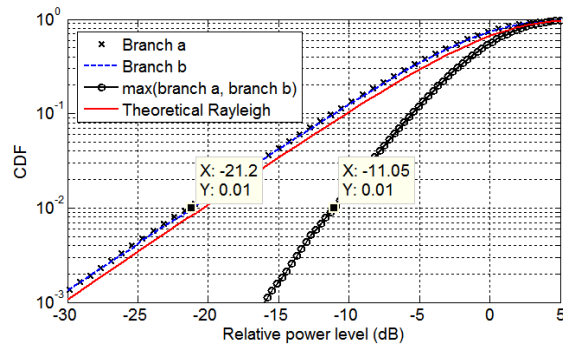
(i)



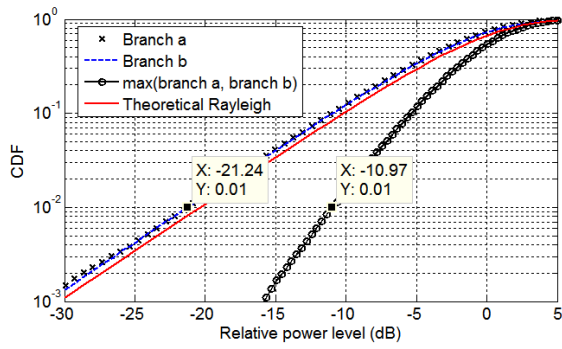
(j)



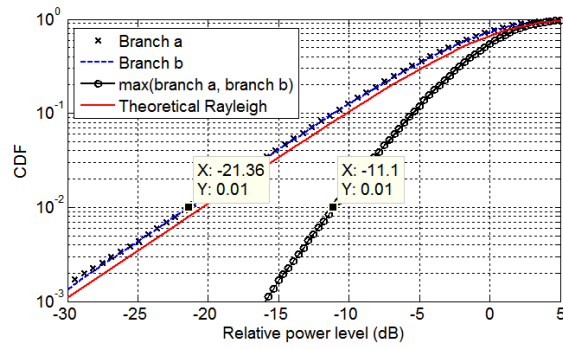
(k)



(l)



(m)



(n)

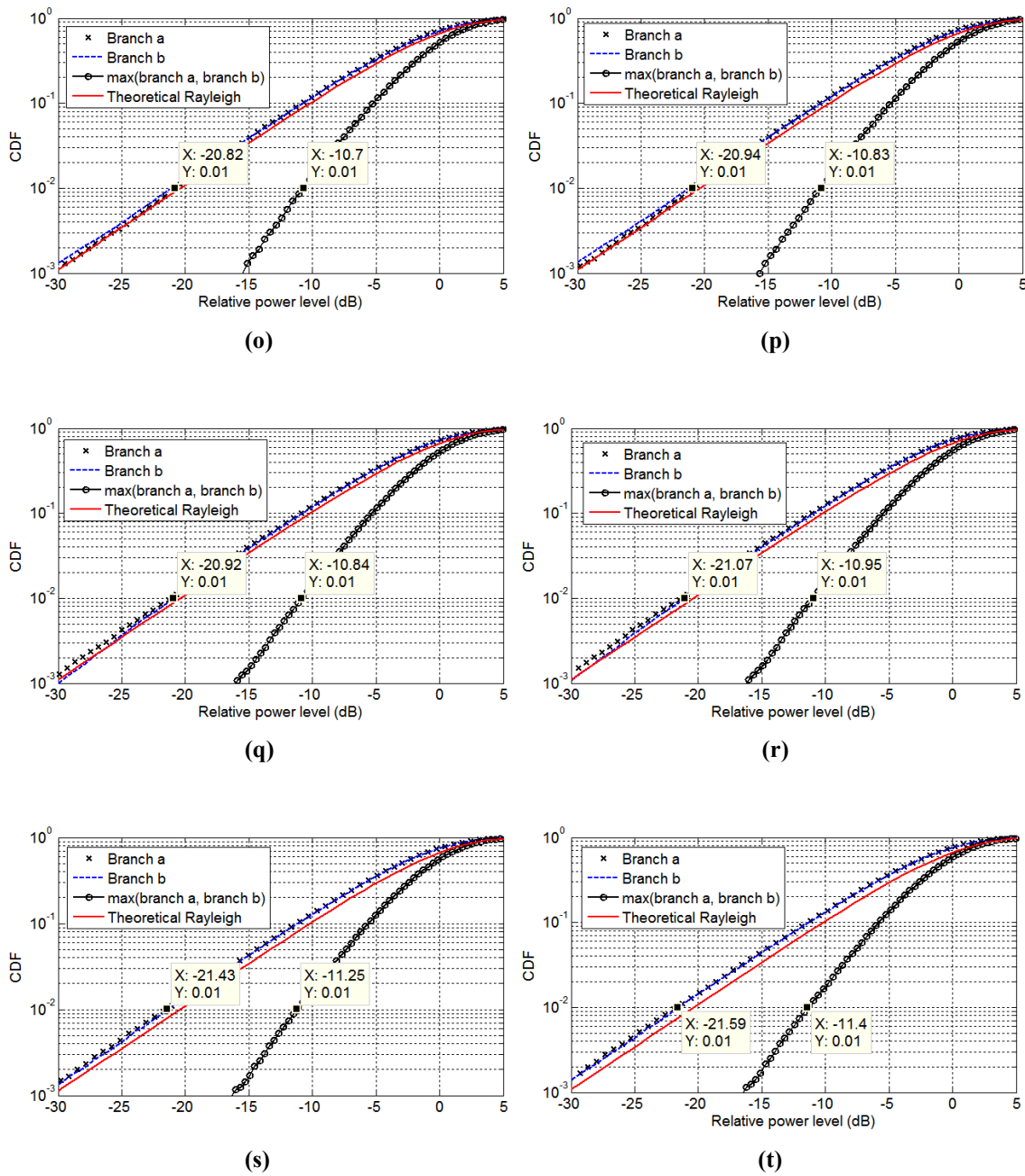


Fig. A1.1. CDF plot of branches, combined signal and theoretical Rayleigh distribution in the frequency range of 2 GHz ~ 3 GHz, DG values are listed in Table A.1.

Table A.1: Measured DG using the traditional method and the proposed method

Frequency Range	DG	Traditional Method	Proposed Method
2.0 ~ 2.1 GHz	Apparent DG (a)	-11.98+22.05=10.07 dB	-12.08+22.14=10.06 dB
	Effective DG (b)	-11.98+20.33=8.35 dB	-12.08+20.33=8.25 dB
2.1 ~ 2.2 GHz	Apparent DG (c)	-11.25+21.31=10.06 dB	-11.34+21.4=10.06 dB
	Effective DG (d)	-11.25+20.33=9.08 dB	-11.34+20.33=8.99 dB
2.2 ~ 2.3 GHz	Apparent DG (e)	-10.84+21.05=10.21 dB	-10.98+21.18=10.2 dB
	Effective DG (f)	-10.84+20.33=9.49 dB	-10.98+20.33=9.35 dB
2.3 ~ 2.4 GHz	Apparent DG (g)	-10.62+20.83=10.21 dB	-10.77+20.98=10.21 dB
	Effective DG (h)	-10.62+20.33=9.71 dB	-10.77+20.33=9.56 dB
2.4 ~ 2.5 GHz	Apparent DG (i)	-10.8+21.17=10.37 dB	-10.92+21.3=10.38 dB
	Effective DG (j)	-10.8+20.33=9.53 dB	-10.92+20.33=9.41 dB
2.5 ~ 2.6 GHz	Apparent DG (k)	-10.92+21.08=10.16 dB	-11.05+21.2=10.15 dB
	Effective DG (l)	-10.92+20.33=9.41 dB	-11.05+20.33=9.28 dB
2.6 ~ 2.7 GHz	Apparent DG (m)	-10.97+21.24=10.27 dB	-11.1+21.36=10.26 dB
	Effective DG (n)	-10.97+20.33=9.36 dB	-11.1+20.33=9.23 dB
2.7 ~ 2.8 GHz	Apparent DG (o)	-10.7+20.82=10.12 dB	-10.83+20.94=10.11 dB
	Effective DG (p)	-10.7+20.33=9.63 dB	-10.83+20.33=9.5 dB
2.8 ~ 2.9 GHz	Apparent DG (q)	-10.84+20.92=10.08 dB	-10.95+21.07=10.12 dB
	Effective DG (r)	-10.84+20.33=9.49 dB	-10.95+20.33=9.38 dB
2.9 ~ 3.0 GHz	Apparent DG (s)	-11.25+21.43=10.18 dB	-11.4+21.59=10.19 dB
	Effective DG (t)	-11.25+20.33=9.08 dB	-11.4+20.33=8.93 dB

The details of how the theoretical Rayleigh curve is generated are also given. Suppose X is the magnitude of the receiving signal, and it follows Rayleigh distribution

$$PDF(X) = \frac{x}{\sigma^2} e^{-x^2/2\sigma^2}, x \geq 0 \quad (A1.1)$$

the CDF of X is

$$CDF(X) = 1 - e^{-\frac{x^2}{2\sigma^2}} \quad (A1.2)$$

X^2 is the power of the receiving signal, it follows exponential distribution

$$PDF(X^2) = \frac{1}{2\sigma^2} e^{-x/2\sigma^2}, x \geq 0 \quad (A1.3)$$

The mean value of X^2 is

$$\text{Mean}(X^2) = 2\sigma^2$$

If we normalise the signal to the mean power value, $\sigma = \sqrt{1/2}$, (A1.2) becomes $CDF(X) = 1 - e^{-x^2}$, the theoretical Rayleigh curve can be obtained from the following Matlab code.

```
% Plot theoretical Rayleigh distribution.  
RayleighMagdB = -30:0.1:10;  
RayleighMag = 10.^( RayleighMagdB /20);  
RayleighCDF= 1 - exp(-RayleighMag.^2);  
figure;  
semilogy(RayleighMagdB, RayleighCDF,'color','r','LineWidth', 2);  
figure(gcf);
```

Appendix A2

Derivations of the one-, two- and three-antenna method are given. From (5.7) and (5.9) we have

$$Q_{FDCor} = \frac{C_{RC} \langle |S_{21,s}|^2 \rangle}{\eta_{1tot} \eta_{2tot}} = \omega \tau_{RC} = Q_{TD} \quad (A2.1)$$

thus

$$\eta_{1tot} \eta_{2tot} = \frac{C_{RC} \langle |S_{21,s}|^2 \rangle}{\omega \tau_{RC}} \quad (A2.2)$$

We apply this relation (A2.2) to antenna 1 only and let $\langle |S_{11,s}|^2 \rangle / e_{b1} = \langle |S_{21,s}|^2 \rangle$, we have

$$\eta_{1tot}^2 = \frac{C_{RC} \langle |S_{11,s}|^2 \rangle / e_{b1}}{\omega \tau_{RC}} \quad (A2.3)$$

Then we apply (A2.2) to antenna 2 only and let $\langle |S_{22,s}|^2 \rangle / e_{b2} = \langle |S_{21,s}|^2 \rangle$, we have

$$\eta_{2tot}^2 = \frac{C_{RC} \langle |S_{22,s}|^2 \rangle / e_{b2}}{\omega \tau_{RC}} \quad (A2.4)$$

As can be seen from (A2.2) – (A2.4), if $e_{b1} = e_{b2} = 2$, we solve (A2.3) and (A2.4) for η_{1tot} and η_{2tot} respectively, we have the one-antenna method

$$\eta_i = \frac{\eta_{itot}}{(1 - |\langle S_{ii} \rangle|^2)} = \frac{1}{(1 - |\langle S_{ii} \rangle|^2)} \sqrt{\frac{C_{RC}}{2\omega \tau_{RC}} \langle |S_{ii,s}|^2 \rangle} \quad (i = 1 \text{ or } 2) \quad (A2.5)$$

If we have only $e_{b1} = e_{b2} = e_b$ (not necessarily 2), we solve the equation system (A2.2) – (A2.4) for η_{1tot} , η_{2tot} and e_b , the two-antenna method is obtained

$$\eta_i = \frac{\eta_{itot}}{(1 - |\langle S_{ii} \rangle|^2)} = \frac{1}{(1 - |\langle S_{ii} \rangle|^2)} \sqrt{\frac{C_{RC}}{\omega e_b \tau_{RC}} \langle |S_{ii,s}|^2 \rangle} \quad (i = 1 \text{ or } 2) \quad (A2.6)$$

$$e_b = \frac{\sqrt{\langle |S_{11,s}|^2 \rangle \langle |S_{22,s}|^2 \rangle}}{\langle |S_{21,s}|^2 \rangle} \quad (A2.7)$$

If there are three antennas, besides (A2.2) we have

$$\eta_{1tot}\eta_{3tot} = \frac{C_{RC} \langle |S_{31,s}|^2 \rangle}{\omega\tau_{RC}} \quad (A2.8)$$

$$\eta_{2tot}\eta_{3tot} = \frac{C_{RC} \langle |S_{32,s}|^2 \rangle}{\omega\tau_{RC}} \quad (A2.9)$$

Combine (A2.2), (A2.8) and (A2.9), then solve the equation system for η_{1tot} , η_{2tot} and η_{3tot} respectively, there is no requirement for e_b , the three-antenna method is obtained

$$\eta_1 = \frac{\eta_{1tot}}{(1 - |S_{11}|^2)} = \frac{1}{(1 - |S_{11}|^2)} \sqrt{\frac{C_{RC} \langle |S_{21,s}|^2 \rangle \langle |S_{31,s}|^2 \rangle}{\omega\tau_{RC} \langle |S_{32,s}|^2 \rangle}} \quad (A2.10)$$

$$\eta_2 = \frac{\eta_{2tot}}{(1 - |S_{22}|^2)} = \frac{1}{(1 - |S_{22}|^2)} \sqrt{\frac{C_{RC} \langle |S_{21,s}|^2 \rangle \langle |S_{32,s}|^2 \rangle}{\omega\tau_{RC} \langle |S_{31,s}|^2 \rangle}} \quad (A2.11)$$

$$\eta_3 = \frac{\eta_{3tot}}{(1 - |S_{33}|^2)} = \frac{1}{(1 - |S_{33}|^2)} \sqrt{\frac{C_{RC} \langle |S_{31,s}|^2 \rangle \langle |S_{32,s}|^2 \rangle}{\omega\tau_{RC} \langle |S_{21,s}|^2 \rangle}} \quad (A2.12)$$

Results are the same as in [3] in Chapter 5.

Appendix A3

An appropriate typical/reference time t_0 need to be chosen to determine η_s . Assume the shape of the RC is a cube, if the wave is allowed to interact with all the walls inside the RC at least twice (the wave follows the red dot line in Fig. A3.1), the travel time is $12 \sqrt[3]{V}/c_0$.

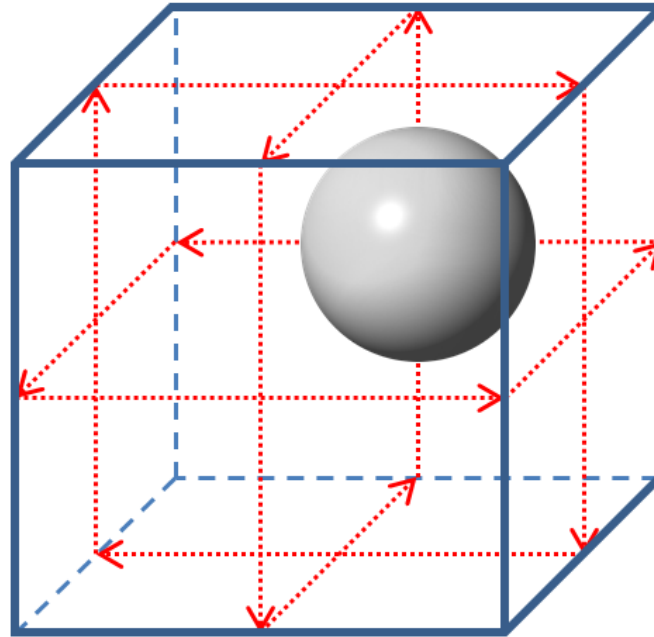


Fig. A3.1. An intuitive explanation of the wave interaction with the boundaries in a cubic RC, a sphere with radius $r = V^{1/3}/\sqrt{8\pi}$ is also shown.

As can be seen, when $\overline{TSCS} = V^{2/3}/4$ (a quarter of the surface area of a face in Fig. A3.1), $\eta_s = 1 - e^{-3} = 95.0\%$. This is a reasonable value to our knowledge, if we have such a large sphere with radius $r = V^{1/3}/\sqrt{8\pi}$ which can move freely in the RC, the stirrer efficiency should be high (the TSCS of the sphere is $2\pi r^2 = V^{2/3}/4$ when the electrical size is large [1]). Normally, the stirrers are rotating around fixed axes, the equivalent TSCS is smaller than the real TSCS of the stirrers.

It should be noted that, theoretically there are infinite ways to map $\overline{TSCS}/V^{2/3}$ to the range of 0% to 100%. If we use a variable α to control the allowed travel time and let $t_0 = \alpha \sqrt[3]{V}/c_0$, η_s with different α values are shown in Fig. A3.2. As can be seen, when α is small, high stirrer efficiency becomes hard to achieve, which means a very short time is allowed for the waves to travel to become random. In practice, we need an appropriate value to have an intuitive understanding and it is not reasonable to have a too small (high η_s can never be achieved) or too large α (always give a high η_s). In this thesis, $\alpha = 12$ is recommended.

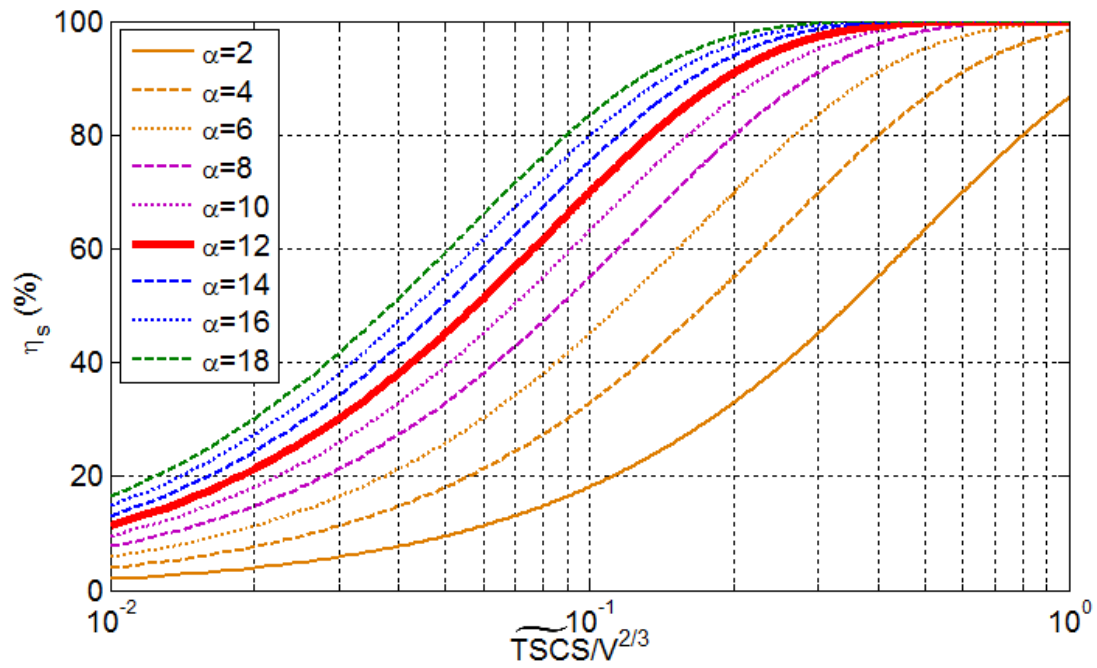


Fig. A3.2. η_s curves with different α values.

References

- [7] G. Lerosey and J. de Rosny, "Scattering cross section measurement in reverberation chamber," *IEEE Trans. EMC*, vol. 52, no. 2, pp.280-284, May. 2007.